Summer 8-15-2016

A Study of the Effects of Pair Production and Axionlike Particle Oscillations on Very High Energy Gamma Rays from the Crab Pulsar

Avery Michael Archer
Washington University in St. Louis

Recommended Citation

Archer, Avery Michael, "A Study of the Effects of Pair Production and Axionlike Particle Oscillations on Very High Energy Gamma Rays from the Crab Pulsar" (2016). *Arts & Sciences Electronic Theses and Dissertations*. 828.
https://openscholarship.wustl.edu/art_sci_etds/828

WASHINGTON UNIVERSITY IN ST. LOUIS

Department of Physics

Dissertation Examination Committee:
James Buckley, Chair
Francesc Ferrer
Viktor Gruev
Henric Krawzcynski
Michael Ogilvie

A Study of the Effects of Pair Production and Axionlike Particle Oscillations on Very High Energy Gamma Rays from the Crab Pulsar

by

Avery Michael Archer

A dissertation presented to the
Graduate School of Arts and Sciences
of Washington University in
partial fulfillment of the
requirements for the degree of

Doctor of Philosophy

August 2016
Saint Louis, Missouri

Contents

List of Tables **v**

List of Figures **vi**

Acknowledgments **xvi**

Abstract **xix**

1 Introduction **1**
- 1.1 Gamma-Ray Astronomy . . . 1
- 1.2 Pulsars . . . 3
- 1.3 Axions and Axionlike Particles . . . 5
- 1.4 Dissertation Overview . . . 6

2 Pulsars and Radiative Emission/Absorption Mechanisms **8**
- 2.1 Introduction . . . 8
- 2.2 Multiwavelength Observations of Pulsars . . . 9
- 2.3 Pulsar Properties . . . 12
  - 2.3.1 Pulsar Energetics . . . 13
  - 2.3.2 Pulsar Magnetosphere . . . 15
- 2.4 Radiative Emission Mechanisms . . . 18
  - 2.4.1 Synchrotron Radiation . . . 18
  - 2.4.2 Curvature Radiation . . . 20
  - 2.4.3 Inverse Compton Scattering . . . 21
  - 2.4.4 Pair Production . . . 23
- 2.5 Magnetosphere Gap Models . . . 25
  - 2.5.1 Polar Cap Models . . . 26
  - 2.5.2 Slot Gap Models . . . 28
  - 2.5.3 Outer Gap Models . . . 31

3 Axions **35**
- 3.1 Introduction . . . 35
- 3.2 Theoretical Basis for Axions . . . 36
- 3.3 Axions as Dark Matter . . . 40
- 3.4 Astrophysical Axion Constraints . . . 42
  - 3.4.1 Constraints from Globular Clusters . . . 42

    - 3.4.2 Constraints from White Dwarf Cooling Times . . . 43
    - 3.4.3 Constraints from SN 1987A . . . 44
  - 3.5 Searches for Axions/ALPs . . . 44
    - 3.5.1 Helioscope Searches . . . 46
    - 3.5.2 Haloscopes . . . 48
    - 3.5.3 Light Shining Through Wall Searches . . . 49
    - 3.5.4 AGN/Blazar Searches . . . 50
    - 3.5.5 Constraints from Neutron Stars . . . 55

4 VERITAS Instrument and Analysis Techniques 58
  - 4.1 Imaging Atmospheric Cherenkov Technique . . . 58
  - 4.2 Analysis Technique . . . 62
    - 4.2.1 Summary of Standard Data Analysis Methods . . . 62
    - 4.2.2 Spectral Reconstruction . . . 65
    - 4.2.3 Periodic Analysis . . . 66

5 VERITAS Analysis of Crab Pulsar Up to TeV Energies 72
  - 5.1 VERITAS Data on the Crab . . . 72
  - 5.2 MAGIC Observations . . . 72
  - 5.3 Data Selection . . . 75
  - 5.4 Cut Selection for Pulsed Analysis . . . 76
  - 5.5 Crab Pulsar Light Curve . . . 77
  - 5.6 Crab Pulsar Spectrum . . . 80
  - 5.7 Height of Pulsed Emission Site . . . 82
  - 5.8 Results Summary and Discussion . . . 83

6 Effect of Geometry and Pair Opacity on Light Curves 85
  - 6.1 Simulation of Photon Propagation through Pulsar Magnetospheres . . . 86
    - 6.1.1 Pulsar Magnetosphere and Geometry . . . 86
    - 6.1.2 Photon Emission . . . 88
  - 6.2 Results . . . 94
    - 6.2.1 Effects of Geometric Considerations on Simulated Light Curves . . . 94
    - 6.2.2 Effect of Pair Creation on Simulated Light Curves . . . 95

7 Axion-like Particle Oscillations in Pulsar Magnetospheres 105
  - 7.1 Pair-Opacity of Pulsar Magnetospheres . . . 106
  - 7.2 Distance Scales . . . 110
  - 7.3 ALP-Photon Mixing in Pulsar Magnetospheres . . . 112
    - 7.3.1 Mixing without Pair Production . . . 112
    - 7.3.2 Mixing with Pair Production . . . 117
    - 7.3.3 Monte Carlo Simulation of Photons . . . 123
  - 7.4 Results . . . 123

8 Conclusion 130

Appendix A List of Crab Data Run **133**

Appendix B Monte Carlo Simulations of VHE Emission and Propagation Results **135**

Appendix C ALP-mixing Results **141**

References **151**

List of Tables

5.1 VERITAS Data Analysis Cuts 76
5.2 Crab Pulsar Differential Energy Spectrum 81
5.3 Results of Spectral Fit to Power Law Function 82

6.1 Pulsar Parameters Used in Simulations 95

7.1 Results of Spectral Fit with Power Law Function 124

A.1 Crab Pulsar Run List 134

C.1 Results of Spectral Fit with Power Law Function ($\xi = \pi/12$) 141
C.2 Results of Spectral Fit with Power Law Function ($\xi = \pi/6$) 143
C.3 Results of Spectral Fit with Power Law Function ($\xi = \pi/4$) 145
C.4 Results of Spectral Fit with Power Law Function ($\xi = \pi/3$) 147
C.5 Results of Spectral Fit with Power Law Function ($\xi = 5\pi/12$) 149

List of Figures

1.1 Catalog of known VHE sources created using TeVCat online TeV catalog: http://tevcat2.uchicago.edu/. The top plot maps the known VHE emitters in Galactic coordinates and is color-coded by source type. The middle plot shows the number of known VHE sources over time. The bottom plot shows the breakdown of the VHE catalog by source type. Pulsars (PSR) are the main topic for this thesis and only comprise 1.1% of known sources with only the Crab being detected above 100 GeV. 2

1.2 Composite image of optical and x-ray observations of the Crab Nebula. Image taken from: http://hubblesite.org/newscenter/archive/releases/2002/24/image/a/ 4

2.1 Phase-averaged Vela spectral energy distribution. Fermi-LAT data are shown with blue circles and EGRET data are shown with unfilled diamonds for reference. The Fermi-LAT data are fit with a power-law with an exponential cutoff, shown by the solid line. Figure taken from (Abdo et al., 2009) 11

2.2 Combined spectral energy distribution for Crab pulsar. VERITAS data are given by red circles. Fermi-LAT data are given by green circles. The VERITAS and Fermi-LAT data are fit with an power-law with an exponential cutoff, shown with a dashed line, and a broken power-law, shown with a solid line. χ^2 values are shown below to illustrate the deviations from the Fermi-LAT and VERITAS flux measurements. Figure taken from (VERITAS Collaboration et al., 2011) 12

2.3 The corotating magnetosphere described by Goldreich and Julian is shown. Protons and electrons escape the magnetosphere streaming along open magnetic field lines. The null-surface defines separation between regions where electrons flow and protons flow. Figure adapted from (Goldreich and Julian, 1969). . . 17

2.4 Feynman diagrams for pair creation processes. (a) shows the Feyman diagram for photon-photon pair creation. (b) shows Feyman diagram for pair creation where a magnetic field acts as a virtual photon. 23

2.5 Illustration of the geometry of the various gap models in a pulsar magnetosphere out to the light cylinder. The polar cap region is shaded in red. The slot gap region is shaded in blue and includes the polar cap region. The outer gap region is shaded in gray. The dotted line indicates the null charge surface, where $\Omega \cdot B = 0$. 28

2.6 Results from a two-pole caustic model simulation for a pulsar with inclination angle $\xi = 60°$. (A) shows the photon mapping as a function of the line of sight angle ζ_{obs} and phase angle ϕ, as measured in the observer's frame. Magnetic polar caps are depicted as blank circles. Two caustics can be seen as dark arches trailing the polar caps. Caustics form as a result of special relativistic effects. A light curve can be produced by taking a horizontal cut of the diagram for some constant observation angle, ζ, as depicted in (B)-(F). Each figure (B)-(F) corresponds to a constant viewing angle depicted as dotted lines in (A). Figure taken from (Dyks and Rudak, 2003). 30

2.7 Schematic of 3 possible charge-depleted gap regions in the outer gap model. Gamma rays are produced by electrons accelerated by $E_{\parallel}$, and thus are beamed along field lines.' In regions (B) and (C) gamma rays emitted from other regions can penetrate and pair-produce filling the region with charge carriers and closing the gap region. Region (A), however, cannot be penetrated by gamma rays emitted from other regions, e.g. (B) and (C), showing a stable gap forms along the last closed field line. Figure taken from (Cheng et al., 1986). 32

2.8 Phase-folded spectral energy distribution of the Crab pulsar for peaks P1 and P2 from MAGIC (closed circles) and *Fermi*-LAT (open circles). Dashed line shows power-law with exponential cut-off fit to *Fermi*-LAT data. Solid line shows fit using a broken power-law to *Fermi*-LAT and MAGIC data. Figure taken from (Ansoldi et al., 2016). 34

3.1 Feynmann diagram for axion coupling to photons 39

3.2 Summary of current constraints, future prospects and hints in axion/ALP parameter space. The classical QCD axion parameter space is shown by a yellow band. Axionic dark matter parameter space is shown by orange bands. In the region labeled "WIMP-axion CDM" axions would only comprise a fraction of the dark matter energy density. Prospects for IAXO and ADMX are shown by hatched regions. Figure taken from Carosi et al. (2013). 45

3.3 Feynmann diagram for the Primakoff effect. 46

3.4 Exclusion limits on the axion/ALP coupling constant and mass from the first two OSQAR data runs. The exclusion limits from ALPS is shown for comparison in red. Figure taken from Pugnat et al. (2014). 50

3.5 Illustration of ALP oscillation scenarios near the source and in the intergalactic magnetic field. Figure taken from Sánchez-Conde et al. (2009). 51

3.6 Left: Effect of ALP-photon oscillations inside source and in IGMF on the spectrum of 3C 279 and PKS 2155-304 for two EBL models: Kneiske (dashed line) and Primack (solid line). Expected photon flux without ALP mixing is shown for comparison (dotted line for Kneiske model and dot-dashed line for Primack model). Right: Boost in intensity of photon flux due to ALP mixing. Figure taken from Sánchez-Conde et al. (2009). 53

3.7 ALP parameter space with lower limits on the axion-photon coupling constant found by studying 15 AGNs with various ground-based gamma-ray telescopes. Several magnetic field scenarios are considered. Limits from each scenario are in different shades of blue. Only the FRV EBL model results are shown. Figure taken from Meyer et al. (2013). 54
3.8 Left: Observed and expected 95% confidence limits on ALP mass and coupling derived from 6 years of *Fermi*-LAT observations of NGC 1275. Expected limits are from 400 Monte Carlo simulations. Right: Comparison of constraints from *Fermi*-LAT to other constraints from other works. Figure taken from Ajello et al. (2016). 55
3.9 Excluded regions of ALP parameter space (m_a, f_a) from a study of 5 years of *Fermi*-LAT data for 4 neutron stars (labeled NS). Excluded parameter space from studies of SN 1987A are labeled SN 1987A. Allowed parameters for the classical Peccei-Quinn axion are shown with a black line. Figure taken from (Berenji et al., 2016). 57

4.1 The VERITAS array located at the Fred Lawrence Whipple Observatory near Tucson, AZ 59
4.2 Model of electromagnetic cascade induced by VHE gamma ray interaction in the Earth's atmosphere 60
4.3 Figures showing the shower geometry as an image in an IACT. (a) depicts how a shower forms a projection in the IACT camera. (b) is a schematic of a gamma ray shower imaged by 4 VERITAS telescopes and the geometry of the images is used to reconstruct the shower direction. 61

5.1 Phase-folded spectral energy distribution of the Crab pulsar for peaks P1 and P2 from MAGIC (closed circles) and *Fermi*-LAT (open circles). Dashed line shows power-law with exponential cut-off fit to *Fermi*-LAT data. Solid line shows fit using a broken power-law to *Fermi*-LAT and MAGIC data. Figure taken from (Ansoldi et al., 2016). 73
5.2 Phase-folded light curve, or phaseogram, of the Crab pulsar from MAGIC observations in the energy ranges $100 < E < 400$ GeV (top) and $E > 400$ GeV (bottom). The region used for background subtraction is shaded gray. The peak intervals are shown highlighted in yellow. Figure taken from (Ansoldi et al., 2016). 74
5.3 Crab Nebula differential spectrum for $100 < E < 30000$ GeV using the three standard VERITAS source cuts. *Soft*-source cuts are shown in blue. *Medium*-source cuts are shown in black. *Hard*-source cuts are shown in red. Each SED is fit using a power-law function shown as a solid line. The pink dashed line is the power-law function that was fit to HEGRA observations of the Crab Nebula and is shown for comparison (Aharonian et al., 2004). 77

5.4 VERITAS phaseogram of the Crab pulsar plotted over two phase intervals for all energies observed. Two pulses can be seen at phases 0.0 and 0.4 and are referred to as P1 and P2, respectively. The highlighted regions are the signal regions used in the significance calculation for a pulsed signal. The signal regions were defined based on the previous 2011 VERITAS analysis of the Crab. The background region is indicated by black arrows. The red, dashed line indicates the background level estimated from the background region. . 78
5.5 VERITAS integral phaseogram of Crab pulsar with an energy threshold of $E > 501$ GeV. Signal region (highlighted) and background region (indicated by arrows) are the same as Figure 5.4. The pulsed signal has a significance of 2.6σ as given by the Li & Ma formula. 79
5.6 Growth of excess (left) and signifance (right) against cumulative photon events. 80
5.7 The phase-folded differential energy spectrum of the Crab pulsar for P1 and P2 combined measured by VERITAS between 100 GeV and 500 GeV. The Crab pulsar spectrum is well fit by a power law function (black line). The best-fit parameters are given in Table 5.3. The power law fit to the 2011 VERITAS observations is shown (dashed, blue) and the 2016 MAGIC observations are shown for P1 (dot-dashed, red) and P2 (dashed, green) for comparison. . . . 81
5.8 Plot of the minimum emission height (i.e. minimum distance between the Crab pulsar stellar surface and the emission location) of a VHE photon for a given energy. The strong magnetic fields in the magnetosphere allow the absorption of VHE photons due to pair creation. As a result of pair attenuation, photons observed at various energies must have been emitted a minimum distance above the stellar surface to survive propagation through the magnetosphere. The exact location of emission cannot be known but a bound may be set on the emission height. For the Crab pulsar, the spectrum is reconstructed up to 500 GeV by the analysis in this chapter. This yields a minimum emission height of 12 R_s. 83

6.1 Schematic of the geometry used for pulsar simulations. The axis of rotation $\hat{\Omega}$ lies along the z-axis. 87
6.2 Outer gap region used for simulation shown in orange shaded region with the boundaries of the light cylinder shown. Photons are given randomly seeded initial positions throughout the OG region. 90
6.3 Slot gap region used for simulation shown in orange shaded region with the boundaries of the light cylinder shown. Photons are given randomly seeded initial positions throughout the SG region. 90
6.4 Example of the distributions of photon emission locations for one simulation with $\xi = \pi/4$. 91

6.5 (a) shows the light curves from one simulation with $\xi = \pi/3$ and $\zeta = \pi/4$ for both the SG model (black) and the OG model (blue). The top plot is the light curve before any time of flight corrections are applied to the emission phase ϕ_i. The bottom plot in (a) is the light curve for the same set of propagated photons with phase-corrections ϕ_c applied. (b) is the distribution of values for phase-corrections applied to the propagated photons. 92
6.6 Distribution of photon energies used in simulations. Energies range from 100 GeV to 10 TeV. Photon energies are generated using a smoothly-broken power law function and parameters that have been fit to *Fermi*-LAT and VERITAS observations of the Crab Pulsar from VERITAS Collaboration et al. (2011). 93
6.7 Lightcurves from simulations for SG and OG models with inclination angle $\xi = 5\pi/12$ and a range of viewing angles ζ. 96
6.8 Lightcurves from simulations for SG and OG models with inclination angle $\xi = \pi/3$ and a range of viewing angles ζ. 97
6.9 Plot of the mean free path of photons at various energies (100 GeV [black], 1 TeV [red] and 10 TeV [blue]) at any point from the stellar surface to the light cylinder. The mean free path was calculated for a pulsar with inclination angle $\xi = \pi/4$ and photons traveling along the $+\hat{x}$-direction. The mean free path changes as a function of distance from the pulsar due to the falling magnetic field strength. The x, y values are given in units of pulsar radii (R_s). The dashed gray line is the remaining distance to the light cylinder from a given $x-$coordinate. Once the mean free path value exceeds the distance to the light cylinder photons are expected to survive propagation. From this plot the one can get an idea of the distance from the stellar surface that higher energy photons must be emitted to be observed. 99
6.10 Schematic of the geometry used for calculation of pair production opacity. The emission point (red point) is identified in the diagram. The photon momentum vector $\vec{k}$ showing the direction of photon propagation is a dashed red arrow. Initially $\vec{k}$ is tangential to the field line but as the the photon propagates the angle β_{ph} between $\vec{k}$ and $\vec{B}$ increases. $\vec{B}$ is shown by a dashed gray arrow at one point along the photon's path. The line of sight to the observer is shown by the solid black arrow. An angle cut is applied for the angle ϑ to determine if a photon will be observed. The dipole magnetic field lines are shown as solid black lines. 100

6.11 Light curves from simulations for SG and OG models with inclination angle $\xi = 5\pi/12$, a range of viewing angles ζ and an energy threshold $E > 600$ GeV. The light curves resulting only from geometric considerations with no pair absorption are depicted in black for both SG and OG models. Some photons that are capable of being observed due to geometry are not observed due to pair attenuation in the strong magnetic fields of the magnetosphere. The light curves showing the effect of pair attenuation on VHE gamma rays are shown in blue. Light curves for some viewing angles, ζ, are more strongly affected than others. For viewing angles of similar value to the magnetic inclination angle the light curves are less affected as seen for both SG and OG models. 101

6.12 Light curves from simulations for SG and OG models with inclination angle $\xi = \pi/3$, a range of viewing angles ζ and an energy threshold $E > 600$ GeV. The light curves resulting only from geometric considerations with no pair absorption are depicted in black for both SG and OG models. Some photons that are capable of being observed due to geometry are not observed due to pair attenuation in the strong magnetic fields of the magnetosphere. The light curves showing the effect of pair attenuation on VHE gamma rays are shown in blue. Light curves for some viewing angles, ζ, are more strongly affected than others. For viewing angles of similar value to the magnetic inclination angle the light curves are less affected as seen for both SG and OG models. . 102

6.13 Results of photon propagation with and without pair production. The distribution of radial distances to the emission location of photons is shown in (a). The energy distribution of simulated photons is shown in (b). The full distributions of emitted photons is shown in black with gray shading. The blue distributions shows "observed" photons. The red distribution shows photons that underwent pair production during propagation. 103

6.14 3D visualization of the emission locations of simulated photons in the magnetosphere for SG (top) and OG (bottom) models where the inclination angle $\xi = \pi/3$. "Observed" photons are shown in white and pair-attenuated photons are depicted in red. The size of the points are weighted by the energy of the photon emitted. The light cylinder is shown as a nearly transparent cylinder. The pulsar is shown in black with an exaggerated size. The pulsar spin direction $\hat{\Omega}$ is along the $z-$axis. The line of sight to the observer is depicted by an arrow ($\zeta = \pi/12$). 104

7.1 Plot of the fraction of simulated, emitted VHE photons that undergo pair production while propagating through the pulsar magnetosphere for $\xi = \pi/4$ (top), $\xi = \pi/4$ (bottom) and the range of simulated ζ values over the range of energies used. The plots demonstrate the range in effects of pair attenuation on the propagation of photons. For $\xi = \pi/4$ most photons do not pair produce until high energies are reached. For $\xi = \pi/3$ between $0 - 20\%$ of photons in the 600 GeV energy bin are attenuated (for $\zeta \leq \pi/3$) while at higher energies, for some viewing angles, all photons are attenuated. 107

7.2 Plot of the fraction of simulated, emitted VHE photons that undergo pair production while propagating through the pulsar magnetosphere for $\xi = \pi/4$ (top), $\xi = \pi/4$ (bottom) and the range of simulated ζ values over the range of emission location radial distances. The plots demonstrate the range in effects of pair attenuation on the propagation of photons. 108

7.3 The mean free path of a 100 GeV photon emitted at a distance $6R_s$ (in the $\hat{x}-$direction) above the stellar surface is shown for the full range of phase values. The mean free path is calculated for several possible inclination angles to illustrate the range of phase dependence for all simulated inclination angles. The photons are assumed to propagate in the $+\hat{x}-$direction. The distance to the light cylinder R_{lc} is shown (red). Photons with mean free path values less than this distance imply (gray region) the photons will be attenuated. Photons with mean free path values greater than R_{lc} will be observed. 109

7.4 Comparison of relevant distance scales for pair-production and ALP oscillation probability for a pulsar with $\xi = \pi/4, \zeta = \pi/2$. The horizontal axis is the emission location of photons in units of stellar radii (R_s) and goes from the stellar surface out to the light cylinder radius. The vertical axis is the distance scale for the two considered physical processes in units of stellar radii (R_s). The mean free path for the range of energies considered (100 GeV to 10 TeV) is bounded by blue lines and shaded. The distance scale that maximizes ALP oscillation probability ($d = \pi/(Bg)$ for the relevant range of coupling constant, g, (10^{-11} to 10^{-7}) is bounded by black lines and hashed. The distance from the radial position to the light cylinder R_{lc} is shown in red to indicate what distance scales are of interest for pulsar magnetospheres. From this figure it can be seen that there is a range of photon energies and coupling constants for which the distance scale relevant to pair production and ALP oscillation probability are comparable. This range lies naturally in the VHE regime for photon energies. 111

7.5 Feynman diagrams of the Primakoff effect (a) and the inverse Primakoff effect (b). Axions and ALPs are coupled to photons and in the presence of an external magnetic field, an ALP may convert into a photon. This interaction is key for many searches for ALPs including the work presented in this chapter. 113

7.6 Probability of photon-ALP oscillation at locations through a pulsar magnetosphere calculated using Equation 7.6 where $m_a = 10^{-4}$ eV, $d = L$. $P_{a\gamma}$ is shown for $E_\gamma = 100$ GeV (top), $E_\gamma = 1$ TeV (center) and $E_\gamma = 10$ TeV (bottom) and various values of g. The $x-$axis gives the emission location of the considered photon, d is measured from this distance. Not all values of g are shown for each energy due to the rapid oscillations of the function that obscure the graph. For each considered energy, smaller values of g give lower frequencies of oscillation for the probability function. For any values of g, E_γ the probability of oscillation never exceeds 0.5. 115

7.7 ALP parameter space relevant to pulsar magnetospheres where we fix $E_{\text{crit}} = 10$ GeV to allow for strong mixing to occur in the VHE regime. The effective axion mass is limited, in part, by the particle density, n_{GJ}, in the magnetosphere. The coupling constant range is limited to values where ALP-photon oscillation distance scales are comparable to the pair-attenuation mean free path of VHE photons (as seen in Figure 7.4). The left and right edges of the parameter space are determined by the magnitude of the magnetic field at the stellar surface (right) and the light cylinder (left). 116

7.8 Probability of photon-ALP oscillation at locations through a pulsar magnetosphere calculated using Equation 7.16 where $m_a = 10^{-4}$ eV and d is the distance to the light cylinder from the initial position. $P_{a\gamma}$ is shown for $E_\gamma = 100$ GeV (top), $E_\gamma = 1$ TeV (bottom) with various values of g. The $x-$axis gives the emission location of the considered photon, d is measured from this distance. Both graphs show that the probability of oscillation is negligible until beyond $10R_s$. In general lower energy photons have a larger probability of oscillation for the parameters considered. The suppression of the ALP-photon oscillations near the stellar surface is due to inclusion of the vacuum polarization term, Δ_{QED}, and the oscillation probability becomes nonnegligible once the other terms are of the same order of magnitude as Δ_{QED}. Including Δ_{QED} inside of the pair producing region is clearly not rigorously correct, but is shown here to bound the possible effects of vacuum polarization. 121

7.9 Probability of photon-ALP oscillation (top) and probability of photon survival (bottom) at locations through a pulsar magnetosphere calculated using Equation 7.15 with Δ_{QED} set to zero where $m_a = 10^{-4}$ eV, $E_\gamma = 1$ TeV d is the distance to the light cylinder from the initial position. The $x-$axis gives the emission location of the considered photon. The graph of $P_{a\gamma}$ shows that the probability of oscillation negligible until beyond $5R_s$. The suppression of ALP-photon oscillations near the stellar surface is due to the strength of the pair absorption term in this region. ALP-photon oscillations are limited to a narrow region of the magnetosphere. 122

7.10 Results of simulations of photon emission and propagation in a pulsar magnetosphere with inclination angle $\xi = \pi/3$ and various viewing angles. Light curves are shown (left) for the observed photons with considerations for geometry only (black), geometry and pair attenuation (red) and geometry, pair attenuation and ALP-photon mixing (blue). For many viewing angles variations in light curves are negligible. More pronounced effects are seen for $\zeta = \pi/12$ and $\zeta = \pi/2$. Differential spectra are shown (right) for the observed photons with consideration for geometry only (black), geometry and pair attenuation (red) and geometry, pair attenuation and ALP-photon mixing (blue). Each distribution is fit with a power law function (solid line) and 95% confidence bands (dotted line) are shown. The best-fit spectral indices for each viewing angle are shown in Table 7.1. 125

7.11 Results of simulations of photon emission and propagation in a pulsar magnetosphere with inclination angle $\xi = \pi/3$ and $\zeta = \pi/12$. The light curve is shown (above) for the observed photons with considerations for geometry only (black), geometry and pair attenuation (red) and geometry, pair attenuation and ALP-photon mixing (blue). The differential spectrum is shown (bottom) for the observed photons with consideration for geometry only (black), geometry and pair attenuation (red) and geometry, pair attenuation and ALP-photon mixing (blue). Each distribution is fit with a power law function (solid line) and 95% confidence bands (dotted line) are shown. The best-fit spectral indices are shown in Table 7.1. 126

B.1 Light curves from simulations for SG and OG models with inclination angle $\xi = \pi/12$ and a range of viewing angles ζ. The light curves with only resulting only from geometric considerations are depicted in black for both SG and OG models. Some photons that are capable of being observed due to geometry are not observed due to pair attenuation in the strong magnetic fields of the magnetosphere. The light curves showing the effect of pair attenuation on VHE gamma rays are shown in blue. Some the light curves for some viewing angles, ζ, are more strongly affected than others. For viewing angles of similar value to the magnetic inclination angle the light curves are less affected as seen for both SG and OG models. 136

B.2 Light curves from simulations for SG and OG models with inclination angle $\xi = \pi/6$ and a range of viewing angles ζ. The light curves with only resulting only from geometric considerations are depicted in black for both SG and OG models. Some photons that are capable of being observed due to geometry are not observed due to pair attenuation in the strong magnetic fields of the magnetosphere. The light curves showing the effect of pair attenuation on VHE gamma rays are shown in blue. Some the light curves for some viewing angles, ζ, are more strongly affected than others. For viewing angles of similar value to the magnetic inclination angle the light curves are less affected as seen for both SG and OG models. 137

B.3 Light curves from simulations for SG and OG models with inclination angle $\xi = \pi/4$ and a range of viewing angles ζ. The light curves with only resulting only from geometric considerations are depicted in black for both SG and OG models. Some photons that are capable of being observed due to geometry are not observed due to pair attenuation in the strong magnetic fields of the magnetosphere. The light curves showing the effect of pair attenuation on VHE gamma rays are shown in blue. Some the light curves for some viewing angles, ζ, are more strongly affected than others. For viewing angles of similar value to the magnetic inclination angle the light curves are less affected as seen for both SG and OG models. 138

B.4 Light curves from simulations for SG and OG models with inclination angle $\xi = \pi/3$ and a range of viewing angles ζ. The light curves with only resulting only from geometric considerations are depicted in black for both SG and OG models. Some photons that are capable of being observed due to geometry are not observed due to pair attenuation in the strong magnetic fields of the magnetosphere. The light curves showing the effect of pair attenuation on VHE gamma rays are shown in blue. Some the light curves for some viewing angles, ζ, are more strongly affected than others. For viewing angles of similar value to the magnetic inclination angle the light curves are less affected as seen for both SG and OG models. 139

B.5 Light curves from simulations for SG and OG models with inclination angle $\xi = 5\pi/12$ and a range of viewing angles ζ. The light curves with only resulting only from geometric considerations are depicted in black for both SG and OG models. Some photons that are capable of being observed due to geometry are not observed due to pair attenuation in the strong magnetic fields of the magnetosphere. The light curves showing the effect of pair attenuation on VHE gamma rays are shown in blue. Some the light curves for some viewing angles, ζ, are more strongly affected than others. For viewing angles of similar value to the magnetic inclination angle the light curves are less affected as seen for both SG and OG models. 140

Acknowledgments

I owe a great sum of gratitude to a number of people for all of the support and guidance that has been given to me in course of writing this dissertation. I have been blessed by having such a wonderful support system. I would certainly like to thank everyone but I might double the size of this dissertation in doing so and still not express ample gratitude to all those that have encouraged my throughout my academic career thus far.

First, I must thank my wonderful wife, Christine Archer. She has been everything to me in the last five years. She has been incredibly patient as she listened to me talk through various physics problems, despite her field of studying being far removed from physics. She has been a source of encouragement any time that I needed an optimism and motivation. She has been the captain of our ship when I was too busy and for that I will always be thankful.

Second, I need to thank my advisor, Jim Buckley. Jim has been the best mentor a student could ask for. Your insight, support, patience and humor have made graduate school a great experience. You have always been supportive of my long term goals, even if that meant me spending time on work away from research. I am grateful for the confidence you have had in me to allow me to have near free reign over outreach activities at WUSTL. Working with you and Dan in the lab has been a wholly worthwhile experience.

I owe many thanks to Dan Leopold, who unfortunately passed away in December 2015. Dan was a second unofficial mentor to me over the years. I had the good fortune to work side by side with Dan in the lab and his experience was incredibly helpful as I learned the ins and outs of the lab. He is certainly missed and I am grateful I had the opportunity to work with and learn from him.

Thank you to the members of my mentoring committee, Francesc Ferrer and Henric Krawzcynski. Your feedback and insight over the last several years has proved invaluable. Also, many thanks to Mike Ogilivie and Viktor Gruev for being a part of my dissertation committee and providing useful comments on my dissertation. Thanks to Shmuel Nussinov for the discussion of the validity of the main topic of this dissertation your comments and encouragement were very helpful.

I would like to thank my VERITAS collaborators for the combined efforts to keep such a great instrument running. Thanks to those that I have had the pleasure of sharing the long nights of observing shifts with. Good company makes the nights go by quickly.

I would like to thank all of the friends that I made over the years in St. Louis. Many thanks to all of my WUSTL friends who I have commiserated with through classes, qualifying exams and research woes. Ryan, Tom, Tony, Matt, Nathan, Wenlei, Nick, Nara, Kelsey, Brendan, Gus, Joben, and so many others, you all made my time at WUSTL an unforgettable experience. To all my non-WUSTL friends, thank you for helping to find a place in St. Louis and discover what a wonderful city St. Louis truly is.

Last, but certainly not least, I need to thank all of my family. My mom and dad are largely responsible for me entering graduate school. They have always encouraged me to push myself and not shy away from a challenge. My brother, Josh, and sister, Abby, have been incredibly patient with my lack of consistent communication while in graduate school. Despite regularly poking fun at each other, I am confident that I have the best siblings. You guys are the best. Thanks to the Walker family for keeping Christine sane while I have been more or less absent. Particular thanks to my octo-buddy Katherine.

I could not have done this without the love and support from all those mentioned and so many more. Thank you all.

Avery Michael Archer

Washington University in Saint Louis

August 2016

ABSTRACT OF THE DISSERTATION

A Study of the Effects of Pair Production and Axionlike Particle Oscillations on Very High Energy Gamma Rays from the Crab Pulsar

by

Avery Michael Archer

Doctor of Philosophy in Physics

Washington University in St. Louis

Professor James Buckley, Chair

Pulsars are highly-magnetized rapidly-rotating neutron stars that emit energy throughout the electromagnetic spectrum. Despite decades of study, the emission mechanisms of pulsars are not well understood. New observations at the highest energy end of the spectrum can provide strong constraints on theoretical models of pulsar emission. The strong magnetic fields of pulsar magnetospheres accelerate charged particles to relativistic energies and these particles emit very high energy (VHE; $E > 100$ GeV) gamma rays. In addition to creating conditions to emit gamma rays, the magnetic fields are powerful enough to attenuate gamma rays through pair production. The attenuation of gamma rays limits the photon energies that may escape the magnetosphere, unless an additional physical process decreases the opacity of the magnetosphere to these photons. The interaction of axions or axionlike particles (ALPs) with magnetic fields is one such process.

Some extensions of the Standard Model suggest the existence of axions, which are light pseudoscalar bosons with a two-photon coupling. As a result of this coupling photon-ALP oscillations can occur in the strong fields of a pulsar magnetosphere. For typical parameters of pulsar magnetospheres, VHE photons fall within the strong mixing-regime for oscillations when the axion mass is 10^{-3} eV $< m_a <$ 10 eV and the axion-photon coupling constant is $10^{-11} < g_{a\gamma} < 10^{-6}$. Axion-photon oscillations within the inner magnetosphere would decrease its opacity as axions would propagate unimpeded by pair attenuation.

In this dissertation, the VHE photon emission and propagation from pulsars is studied in detail. New observations and analysis of the Crab pulsar from the VERITAS experiment are presented which extend the Crab spectrum to higher energies. The magnetospheres of pulsars are simulated using a retarded vacuum dipole solution for the magnetic field. VHE photon emission and propagation is studied using a Monte Carlo method. The emission regions are defined using the slot gap and outer gap models. The effects of pair production and axion-photon mixing are considered and light curves and spectra are produced to illustrate the influence of both processes on the observations of pulsars. For some geometries, VHE photons are heavily attenuated by pair production. Axion-photon mixing is shown to reduce the opacity of pulsar magnetospheres allowing a larger fraction of VHE photons to survive propagation. However, we find that the inclusion of QED effects on the effective photon mass limit the conversion probability over much of the region where strong pair attenuation is expected.

Chapter 1

Introduction

1.1 Gamma-Ray Astronomy

Gamma-ray astronomy is the study of celestial objects at the most energetic end of the electromagnetic spectrum. While the field of astronomy is one of the oldest natural sciences, gamma-ray astronomy is one of the youngest forms of astronomy. The relative youth of the field is due almost entirely to the opacity of the Earth's atmosphere to gamma rays. Gamma-ray astronomy did not become possible until the 1960s when satellite experiments provided our first look at the gamma-ray sky.

The study of very high energy (VHE; $E \geq 100$ GeV) gamma rays from the ground arguably began with the first detection of VHE gamma rays from the Crab Nebula by the *Whipple* Observatory in 1987. These observations were made possible by a technique of imaging the atmospheric air showers with multiple PMT pixels to distinguish these from cosmic-ray induced hadronic showers. The Crab Nebula now serves as a standard candle for the field of VHE astronomy. The number of known VHE sources has increased greatly since the first detection of the Crab, now with over 150 detected VHE emitters (see Figure 1.1). Gamma-ray astronomy plays a unique role in understanding non-thermal radiative processes. Such processes occur in the most extreme environments in the universe where particles are

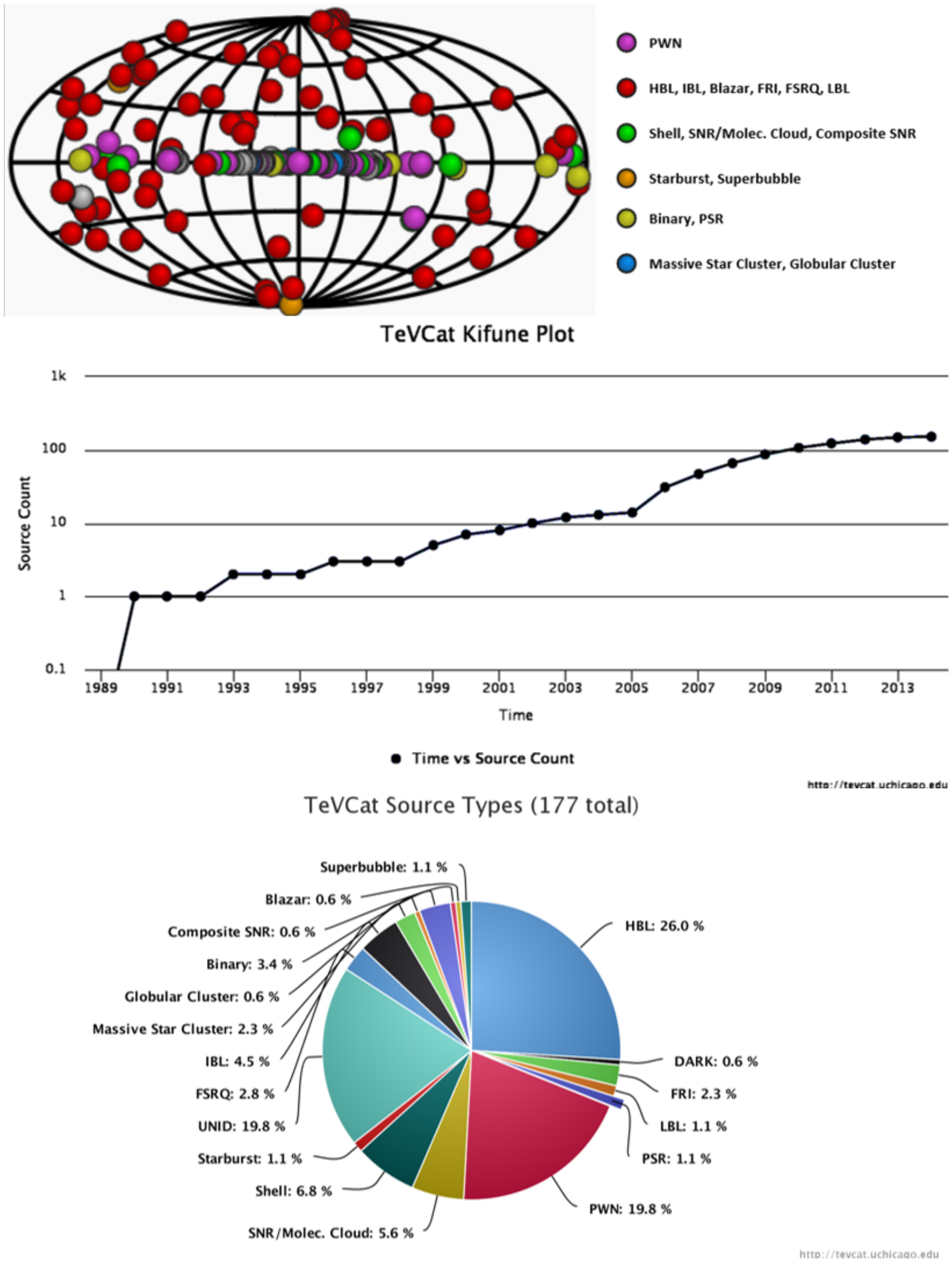

Figure 1.1: Catalog of known VHE sources created using TeVCat online TeV catalog: http://tevcat2.uchicago.edu/. The top plot maps the known VHE emitters in Galactic coordinates and is color-coded by source type. The middle plot shows the number of known VHE sources over time. The bottom plot shows the breakdown of the VHE catalog by source type. Pulsars (PSR) are the main topic for this thesis and only comprise 1.1% of known sources with only the Crab being detected above 100 GeV.

accelerated to relativistic energies. Gamma-ray astronomy provides a unique and powerful tool for probing relativistic processes in astrophysics in a variety of environments. The gamma-ray catalog has a number of galactic and extra-galactic sources from a variety of sources including supernova remnants, pulsar wind nebulae, active galaxies and x-ray binaries as shown in Figure 1.1. This work will focus on a galactic source class with currently only one source in the VHE catalog, pulsars.

There are currently three major ground-based imaging atmospheric Cherenkov telescopes (IACTs) in operation. The High Energy Stereoscopic System (H.E.S.S.) is an array of five telescopes located in Namibia and went into operation in 2002 with only four telescopes, a larger fifth telescope was added in 2012. The Major Atmospheric Gamma Imaging Cherenkov (MAGIC) system is a pair of 17 meter telescopes located in La Palma. MAGIC began observations in 2004 with one telescope and the second was added in 2009. The Very Energetic Radiation Imaging Telescope Array System (VERITAS) is an array of four 12 meter telescopes located near Tucson, AZ. VERITAS began full array observations in 2007 and had a major camera system upgrade in 2012. Observations made by VERITAS of the Crab pulsar (see Figure 1.2) between 2007 and 2015 are one major topic discussed in this work.

1.2 Pulsars

Pulsars are highly-magnetized rapidly rotating neutron stars. Pulsars are compact objects with characteristic masses of 1.4 $M_{\odot}$ and characteristic radii of 10 km. These peculiar objects were first discovered in serendipitous fashion in 1967 and the known pulsar catalog now contains over 1800 objects. Pulsars' defining observational characteristic is the high-frequency periodic or pulsed emission observed across the electromagnetic spectrum. A

Figure 1.2: Composite image of optical and x-ray observations of the Crab Nebula. Image taken from: http://hubblesite.org/newscenter/archive/releases/2002/24/image/a/

pulsar results from a magnetized neutron strar, typically with its magnetic poles misaligned with respect to the rotation axis. Such magnetized neutron stars are surrounded by powerful, corotating, dipole-like magnetic fields as well as strong electric fields capable of accelerating particles to very high energies. The name pulsar comes from an early idea that they were pulsating stars. Pulsars do not actually *pulse* to radiate, but rather their periodic signal comes from a beam of electromagnetic radiation sweeps across the observers line of sight as the star rotates. Pulsars are often referred to as "cosmic lighthouses" because of the similarity between the beam of radiation of a pulsar and the light emanating from a light house.

Though there are nearly 2000 known pulsars, the number of gamma-ray emitters is drastically smaller with 117 gamma-ray pulsars in The Second Fermi Large Area Telescope Catalog of Gamma-Ray Pulsars (Abdo et al., 2013). The VHE pulsar catalog is smaller still with only one known VHE emitter, the Crab pulsar. Due to the interactions between VHE photons and the strong magnetic fields of pulsars, gamma-ray observations of pulsars provide a unique probe into the structure of the pulsar magnetosphere and the emission mechanisms at work in these extreme astrophysical environments. VHE observations can place constraints on the emission locations and help shape theoretical models of pulsar magnetopsheres. In addition to providing insight in to pulsars themselves, VHE observations of pulsars can serve as a tool to investigate fundamental physics. The magnetic fields of pulsars (reaching 10^{12} Gauss) are far more powerful than any laboratory-based experiment could achieve and the propagation of VHE photons through such fields allows for an extreme environment to be used as an astrophysical laboratory to investigate effects of quantum electrodynamics not easily produced in a terrestrial lab. Moreover, these unique systems may even provide a window into physics beyond the Standard Model.

1.3 Axions and Axionlike Particles

A solution (the Peccei-Quinn (PQ) mechanism) to the strong CP problem in QCD results in the prediction of a pseudo-Nambu Goldstone boson resulting from the new CP symmetry (Weinberg, 1978; Wilczek, 1978). This particle known as an axion, obtains a mass at the QCD phase transition in the early universe. Axions couple to photons, allowing axion-photon oscillations to occur, amongst other processes. These oscillations require the presence of an external magnetic field. Since they may be born nonrelativistic, such axions provide a good candidate for cold dark matter. One can envision a broader class of axion-like particles (ALPs) that couple to electrogamnetism like the axion (with the ALP coupling to two photons) that may solve the strong CP problem, or contribute to dark matter

The axion is a theoretical particle that arises from a solution to the strong CP problem in quantum chromodynamics (QCD) first postulated by Roberto Peccei and Helen Quinn in 1977. The strong CP problem is a well-known and unresolved issue with the Standard

Model. QCD does not break charge parity symmetry and there is no known reason for CP-symmetry to be conserved, creating a “fine-tuning” problem. The proposed solution known as the Peccei-Quinn mechanism introduces a new global symmetry that can be spontaneously broken, which results in a new particle, the axion, as demonstrated by Frank Wilczek and Steven Weinberg. The QCD axion has a direct relation between its mass and the energy scale at which the Peccei-Quinn symmetry is violated. A more general class of particle, referred to as axion-like particles (ALPs), are not restricted to such a direct relationship and are assumed to only couple to photons. ALPs also serve as a solution to the strong CP problem.

The coupling of ALPs to photons allows for ALP-photon oscillations to occur, amongst other processes. These oscillations require the presence of an external magnetic field. Oscillations occur in weak fields over large distances or they can occur over shorter distances in the presence of powerful magnetic fields. The oscillation of photons between an ALP state and a photon state would affect well-known and studied physical processes, in particular, astrophysical processes. Studies have been conducted on a number of different astrophysical sources which would be affected by the existence of axions or ALPs. Several studies have been conducted investigating the effects of ALP-photon oscillations on the VHE spectra of distant blazars. In this dissertation we present a new method of probing ALP parameter space by investigating ALP-photon oscillations that may occur as VHE photons propagate through the powerful magnetic fields of pulsar magnetospheres.

1.4 Dissertation Overview

This dissertation is organized into three primary sections. The first section (Chapters 2 and 3) reviews the background physics of pulsars and axion-like particles necessary for understanding and performing the analysis presented in later chapters. The second section (Chapters 4 and 5) of the dissertation describes the VERITAS experiment and analysis techniques, then discusses: observations of the Crab pulsar from 2007-2015, analysis performed on this data and the results of that analysis. The third section (Chapters 6 and 7) describes Monte Carlo simulations of VHE emission and propagation of VHE photons through a pulsar magnetosphere with currently understood physics (Chapter 6). The effect of including ALP-photon oscillations in the propagation simulations is described in Chapter 7. The final chapter discusses conclusions reached by the analysis and simulations performed and future work to be pursued.

Chapter 2

Pulsars and Radiative Emission/Absorption Mechanisms

2.1 Introduction

James Chadwick famously discovered the neutron in 1932 by scattering alpha particles off of beryllium atoms. Only a few years later in 1934, Walter Baade and Fritz Zwicky proposed the existence of stars comprised primarily of these newfound particles stating:

> *"With all reserve we advance the view that a supernova represents the transition of an ordinary star into a new form of star, the neutron star, which would be the end point of stellar evolution. Such a star may possess a very small radius and an extremely high density"* (Baade and Zwicky, 1934).

The first evidence of the existence of neutron stars came in 1967 with the discovery of pulsars. Pulsars were first discovered in serendipitous fashion by Anthony Hewish and Jocelyn Bell on November 28, 1967 using a radio telescope designed to search for distant quasars (Hewish et al., 1968). The short-timescale periodicity of the signal was unprecedented and did not have an immediate, known natural explanation. As a result of the peculiar nature of the signal the object was initially nicknamed LGM-1, for Little Green Men, implying a sentient extraterrestrial being was responsible for the signal. After a similar signal was detected from elsewhere in the sky, the notion of alien contact was eliminated since it was highly unlikely that intelligent lifeforms would contact humans at the same time using the same method. This first pulsar discovered took on the more formal name CP 1919 and has since been designated the name PSR 1919+21. We know now that pulsars are rapidly-rotating highly-magnetized neutron stars. Since this initial discovery at radio wavelengths pulsars have been found to emit radiation throughout the electromagnetic spectrum up to, and including, gamma ray wavelengths. As of 2016 there are more than 2500 known pulsars[1] (Manchester et al., 2005). This chapter will briefly discuss the history of observations of pulsars, the basic known properties of pulsars, the radiative emission mechansims relevant to pulsar physics, different theoretical models used to explain observed high energy emission and finally discussing these models in the context of recent observations of the Crab Pulsar.

2.2 Multiwavelength Observations of Pulsars

Since the initial discovery in 1967, pulsars have been studied in great detail across the electromagnetic spectrum. Within one year's time 21 more pulsars had been discovered, including the well-known Crab pulsar (Comella et al., 1969) and the Vela pulsar (Large et al., 1968). The following decades have been filled with detailed studies adding new insight into these objects and adding more known pulsars to the catalog. This thesis is mainly concerned with the highest energy end of the spectrum covering observations from 10 GeV to 1 TeV.

The first gamma-ray observations of pulsars came in the 1970s from NASA's Small Astronomy Satellite 2 (SAS-2) launched in 1972 and the European Space Research Organisation's Cos-B satellite launched by NASA in 1975. These two missions were able to detect pulsed

---

[1] http://www.atnf.csiro.au/research/pulsar/psrcat/

gamma-ray emission from the Crab pulsar and the Vela pulsar (Bennett et al., 1977); (Thompson et al., 1975). SAS-2 was the first to detect gamma-ray emission from Geminga, a source that could not be associated with other known objects at the time (Fichtel et al., 1975) and was only later confirmed to be a pulsar by x-ray observations. The gamma-ray pulsar catalog was further expanded with observations from the *Energetic Gamma Ray Experiment Telescope* (EGRET) telescope aboard the *Compton Gamma-Ray Observatory* (CGRO), one of NASA's "Great Observatories" satellites, launched in 1991. By 1999 the EGRET catalog included five pulsars (Hartman et al., 1999) and by the end of the satellite's mission in 2001 EGRET identified a total of 7 gamma-ray pulsars and several more likely sources. With these observations EGRET discovered pulsed emission as high as 30 GeV (Thompson, 2008). In 2008 the *Gamma-ray Large Area Space Telescope* (GLAST), now known as the *Fermi Gamma-ray Space Telescope* (*Fermi*), was launched by NASA. Within 6 months of the launch date, *Fermi* had detected an additional 39 new gamma-ray emitting pulsars, bringing the total known gamma-ray pulsars to 46 (Abdo et al., 2010b). By 2011 *Fermi* increased that number to 101. Currently *Fermi* has detected a total of 205[2] pulsars.

These observations of many gamma-ray emitting pulsars, some with observed emission as high as 10 GeV, have had a large impact on the theoretical understanding of where the broadband radiation is being emitted within the pulsar magnetosphere. In particular the *Fermi* observations of energies above a few GeV disfavor one model for the pulsed nonthermal, the *polar cap model*. The polar cap model requires emission to occur within altitudes (radial distances from the stellar surface) of $1-2$ stellar radii. With energies of a few GeV, photons would have to occur at altitudes higher than 2 stellar radii, due to the strong attenuation from $B+\gamma \rightarrow e^{+}e^{-}$ absorption in the strong magnetic field of the star(Abdo et al., 2010a). Other models such as the *slot-gap* or *outer-gap* models allow for high altitude emission and are therefore favored by the *Fermi* results. The spectral energy

---

[2] https://confluence.slac.stanford.edu/display/GLAMCOG/Public+List+of+LAT-Detected+Gamma-Ray+Pulsars

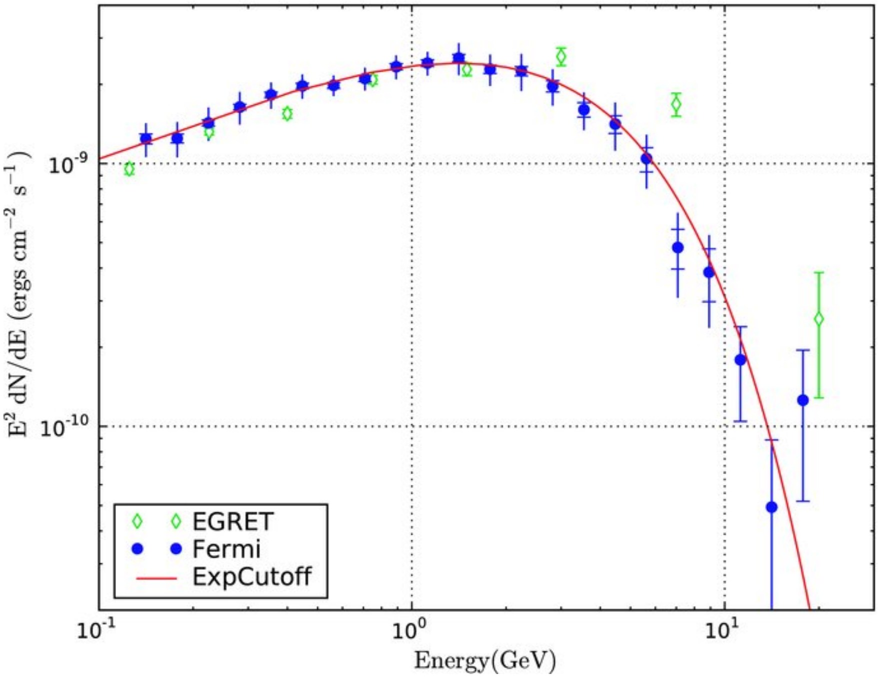

Figure 2.1: Phase-averaged Vela spectral energy distribution. Fermi-LAT data are shown with blue circles and EGRET data are shown with unfilled diamonds for reference. The Fermi-LAT data are fit with a power-law with an exponential cutoff, shown by the solid line. Figure taken from (Abdo et al., 2009)

distributions (SEDs) of the pulsed emission also provide constraints on the emission models. The SED for the Vela pulsar is shown in Fig 2.1. The spectra of the *Fermi* pulsars in the gamma-ray band exhibit an exponential cutoff that bolsters the curvature radiation scenario incorporated in the gap models, see Section 2.5, furthering support for such emission models (Romani, 1996). Until 2011 these seemed to be the favored description of radiative emission from pulsars.

In 2011 VERITAS reported a detection of pulsed gamma rays coming from the Crab pulsar at energies above 100 GeV, the first detection of pulsed emission at such energies. The combined spectral energy distribution from *Fermi*-LAT and VERITAS, shown in Fig 2.2, over the energy range of 100 MeV to several hundred GeV favors a broken power law of the form $A \times (E/E_0)^{\alpha} / \left[1 + (E/E_0)^{\alpha-\beta}\right]$ (VERITAS Collaboration et al., 2011). The exponential cut-off expected by the curvature radiation scenario is disfavored. Curvature radiation alone

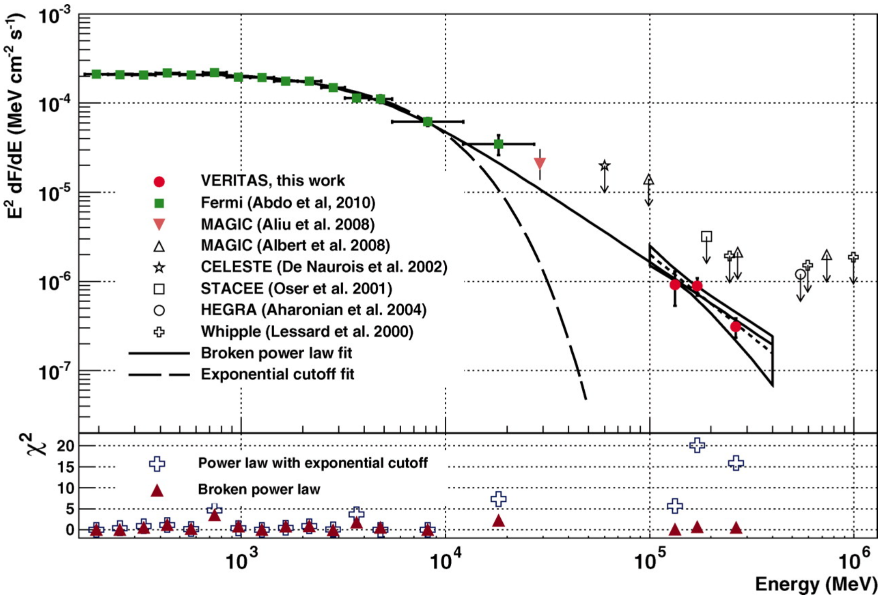

Figure 2.2: Combined spectral energy distribution for Crab pulsar. VERITAS data are given by red circles. Fermi-LAT data are given by green circles. The VERITAS and Fermi-LAT data are fit with an power-law with an exponential cutoff, shown with a dashed line, and a broken power-law, shown with a solid line. χ^2 values are shown below to illustrate the deviations from the Fermi-LAT and VERITAS flux measurements. Figure taken from (VERITAS Collaboration et al., 2011)

cannot adequately explain the $\gtrsim$ 100 GeV emission. An additional or alternative mechanism is necessary to explain the spectral shape seen in the Crab pulsar.

2.3 Pulsar Properties

Pulsars are highly-magnetized rapidly-rotating neutron stars. Pulsars are the compact remnant left after the catastrophic gravitational collapse and supernova explosion of massive ($M > 8M_{\odot}$) main sequence stars. These objects are identifiable by their distinct short timescale periodic signals. Pulsars have been observed with pulse periods ranging from milliseconds to a few seconds. These stellar remnants can be divided into three categories: rotation-powered pulsars, accretion-powered pulsars and magnetars. The first category are characterized by rotational energy losses powering the emission. The second category are characterized by powering emission through the gravitational potential energy of accreted matter from a companion object. The third category are characterized by powering emission through the decay of the extremely powerful magnetic field of the star. This thesis will concentrate on the description and characteristics of rotation-powered pulsars.

2.3.1 Pulsar Energetics

The canonical neutron star has a mass of $1.4M_\odot$, a radius of 10 km and a magnetic field strength at the stellar surface of 10^{12} G. The magnetic field of a pulsar takes the form of a rapidly rotating dipole with the magnetic axis of the star typically misaligned with respect to the rotation axis. The magnetic flux density at the surface of the star then takes the dipole form:

$$\vec{B} = \frac{m}{r^3}\left[2\cos\theta\hat{r} + \sin\theta\hat{\theta}\right] \tag{2.1}$$

The rotational energy of a pulsar is given by the angular velocity, Ω, and the moment of inertia, I in the form

$$E_{\text{rot}} = \frac{1}{2}I\Omega^2 \quad \text{where} \quad \Omega = 2\pi/P,\ I = MR^2 \tag{2.2}$$

$$\text{giving} \quad E_{\text{rot}} = \frac{2\pi^2 MR^2}{P^2} \tag{2.3}$$

For the Crab pulsar which has a period $P = 0.033$ s, the rotational energy is

$$E_{\text{rot}} = \frac{2\pi^2 \cdot 1.4M_\odot \cdot 10^2\ \text{km}^2}{(0.033\ \text{s})^2} = 2.5 \times 10^{42}\ \text{J} \tag{2.4}$$

Pulsar spin-rates decrease very slowly over large timescales with a period derivative, dP/dt, generally greater than zero. The rate of energy loss can be determined given a pulsar's spin period, P, and the time derivative of the period, $dP/dt = \dot{P}$.

$$\frac{dE_{\text{rot}}}{dt} = \frac{d}{dt}\frac{2\pi^2 MR^2}{P^2} = 2\pi^2 MR^2 \frac{d}{dt}\frac{1}{P^2} = -4\pi^2 MR^2 \frac{\dot{P}}{P^3} \tag{2.5}$$

The age of a pulsar, τ, can also be estimated from a few basic parameters and assuming the magnetic field strength does not change significantly over time. To see this we begin with the formula for radiation from a rotating magnetic dipole:

$$\frac{dE}{dt} = \frac{2}{3}\frac{\ddot{m}_{\perp}^2}{c^3} \tag{2.6}$$

where $m_{\perp}$ is the component of the magnetic dipole perpendicular to the rotation axis. For an inclined dipole rotating with some angular velocity, Ω:

$$\ddot{m}_{\perp} = \Omega^2 m \tag{2.7}$$

which gives

$$\frac{dE}{dt} = \frac{2}{3}\frac{\Omega^4 m_{\perp}^2}{c^3} \tag{2.8}$$

a pulsar is approximately a uniformly magnetized sphere with radius, R, magnetic field strength at the stellar surface, B_s, one can write the magnetic dipole moment in terms of this surface field:

$$m = B_s R^3 \quad \text{and} \quad m_{\perp} = B_s R^3 \sin\theta \tag{2.9}$$

and for an inclined magnetic dipole with angular velocity Ω:

$$\begin{aligned} m &= m_0 e^{-i\Omega t} \\ \Longrightarrow \ddot{m} &= \Omega^2 m_0 e^{-i\Omega t} = \Omega^2 m \end{aligned} \tag{2.10}$$

combining Equations 2.9 and 2.10 and substituting into Eq. 2.5 gives

$$\frac{dE}{dt} = \frac{2}{3}\left(\frac{2\pi}{P}\right)^4 \frac{R^6 \left(B_s \sin\theta\right)^2}{c^3} \tag{2.11}$$

combining the previous formula with the rotational energy loss formula Eq. 2.5 to find:

$$P\dot{P} = \frac{8\pi}{3}\frac{R^4 \left(B_s \sin\theta\right)^2}{Mc^3} \tag{2.12}$$

thus $P\dot{P}$ is a constant that depends on the mass, radius, magnetic field strength and misalignment angle. The characteristic age can be determined by integrating:

$$\int_{P_0}^{P} PdP = P\dot{P}\int_0^{\tau} dt \tag{2.13}$$

$$\tau = \frac{P}{2\dot{P}} \tag{2.14}$$

It can also be shown from the previous relation for $P\dot{P}$ that the surface strength of the magnetic field is approximately:

$$B_s \approx \sqrt{\frac{3}{8\pi}\frac{Mc^3}{R^6}P\dot{P}} \approx 2.12 \times 10^{15}\sqrt{P\dot{P}} \quad \mathrm{G} \tag{2.15}$$

which for values of the Crab pulsar, $P = 0.033$ s and $\dot{P} \approx 10^{-12.4}$ s^{-1}, gives $B_s \approx 2 \times 10^{12}$ G.

2.3.2 Pulsar Magnetosphere

In a well-known paper published in Peter Goldreich and William H. Julian (Goldreich and Julian, 1969) argued that the region surrounding pulsars, the *pulsar magnetosphere*, cannot exist as a vacuum. Goldreich and Julian argued that a strong electric field exists at the stellar surface as a result of the stellar matter being an excellent electrical conductor. In the stationary frame of the spinning star the interior electric field $\vec{E}'$ must vanish so in the lab frame that field would take a form that satisfies the condition:

$$\vec{E}' = \vec{E} + \frac{\vec{v} \times \vec{B}}{c} = \vec{E} + \frac{\vec{\Omega} \times \vec{r}}{c} \times \vec{B} = 0 \tag{2.16}$$

It is easy to show that the Coulomb force of such a field on a charged particle would be strong enough to overcome the gravitational pull of the star and strip the charged particles from the stellar surface into the magnetosphere resulting in a charged, conducting plasma surrounding the star. Up to a point, this plasma corotates with the star but has an outer boundary past which corotation would require velocities greater than the speed of light and is therefore no longer physically viable. This outer boundary is known as the light cylinder and is defined by a radius of $r_{lc} = c/\Omega$ and bounded above and below by the planes $z = \pm c/\Omega$. Magnetic field lines contained within the light cylinder boundary are closed while magnetic field lines that pass through the light cylinder boundary are open. While particles moving perpendicular to the field lines rapidly gyrate (and radiate), the charged particles in this plasma move relatively freely along the magnetic field lines thus making these lines act as essentially equipotential lines. In the stationary frame a Lorentz transformation of the dipole field results in an electric field

$$\vec{E} = \frac{\Omega B_s R_s^5}{c r^4} \left(\frac{1}{2} \left(3\cos^2\theta - 1 \right) \hat{r} - \cos\theta \sin\theta \hat{\theta} \right) \tag{2.17}$$

where ϕ is the azimuthal unit vector and B_s is the field strength at the magnetic pole. Substituting into Gauss' law one obtains the space-charge density of the corotating plasma, commonly referred to as the Goldreich-Julian density, given by:

$$\rho_{GJ} = \frac{\nabla \cdot \vec{E}}{4\pi} = \frac{-\vec{\Omega} \cdot \vec{B}}{2\pi c} \frac{1}{\left[1 - (\Omega r/c)^2 \sin^2\theta\right]} \tag{2.18}$$

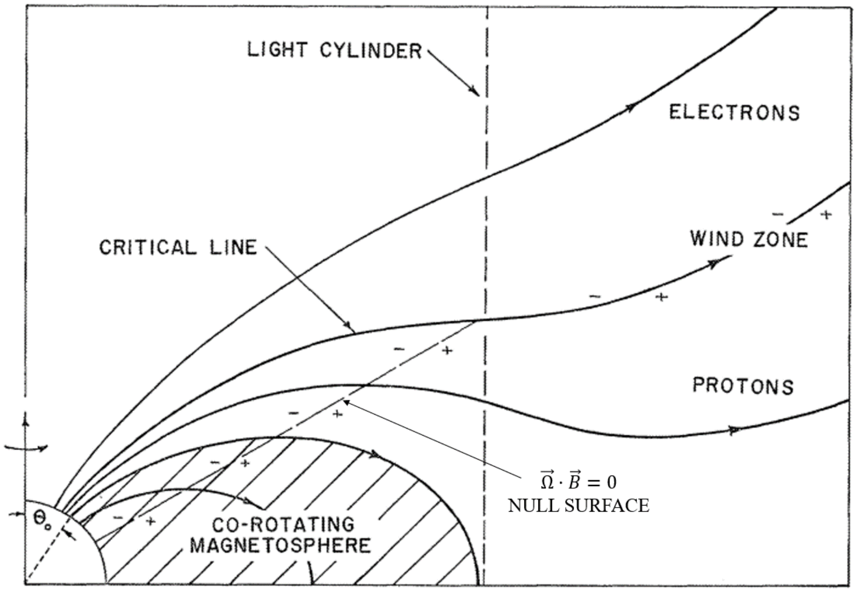

Figure 2.3: The corotating magnetosphere described by Goldreich and Julian is shown. Protons and electrons escape the magnetosphere streaming along open magnetic field lines. The null-surface defines separation between regions where electrons flow and protons flow. Figure adapted from (Goldreich and Julian, 1969).

This expression only applies to the plasma bounded by the light cylinder. Charged particles of the plasma stream along open field lines and escape the magnetosphere. Protons and electrons escape the magnetosphere in roughly equal number so that the star suffers no net charge loss. Protons will travel and escape the magnetosphere along magnetic field lines which are at higher electrostatic potentials than the surrounding interstellar gas, while electrons will follow field lines at electrostatic potentials lower than the surrounding interstellar gas. Figure 2.3 illustrates the structure of the pulsar magnetosphere as described by Goldreich and Julian. The *null surface*, defined by $\vec{\Omega} \cdot \vec{B}$, is the surface separates the electron lines from the proton lines and divides the magnetosphere into separate charge regions (Goldreich and Julian, 1969). The model presented by Goldreich and Julian is the primary basis used for subsequent explanations of various pulsar radiative emission mechanisms which will be discussed in the following section.

2.4 Radiative Emission Mechanisms

The current understanding of the precise physical mechanisms at work in a pulsar magnetosphere is best summed up by Werner Becker of the Max-Planck Institut, “The theory of how pulsars emit their radiation is still in its infancy” (Schartel). Despite nearly 50 years of observations the mechanisms behind pulsar radiation are still not entirely agreed upon. The radiative emission of pulsars is generally divided into two categories, coherent and incoherent emission. The radio regime is typically narrow-band and has a high luminosity both of which are indicative of coherent emission. The high-energy regime is very broad-band and much more indicative of synchrotron, curvature radiation and inverse Compton scattering. This section will focus on outlining some of the basic mechanisms likely responsible for the high-energy emission from pulsars.

2.4.1 Synchrotron Radiation

A charged particle traveling through a magnetic field will be accelerated in the direction perpendicular to the particle’s velocity and perpendicular to the magnetic field line. As a result of the acceleration the charged particles emit radiation as they gyrate about the field line. For non-relativistic velocities this radiation is known as *cyclotron radiation* and for a particle with charge e and mass m this radiation is emitted at the Larmor- or gyro- frequency:

$$\nu_L = \frac{eB}{mc}$$

When the charged particles are significantly relativistic, the gyrofrequency is modified by a time dilation factor giving the relativistic gyrofrequency, $\nu_r = \nu_g/\gamma$. In addition to this time dilation effect on the gyrofrequency, the geometric features of radiation are affected by special relativity. At high Lorentz factors, relativistic beaming of the radiation plays an important role. The radiation is beamed forward in the direction of motion of the charged particle. This has the effect of producing an emission cone with a pitch angle, a, which is determined by the velocity of the particle:

$$\alpha \approx \frac{1}{\gamma}$$

This results in a narrow (temporal) pulse whose Fourier decomposition yields spectral components at harmonics at the relativistic gyrofrequency. At sufficiently high velocities the emission of each of the harmonics is broadened due to special relativistic effects and the radiation observed is a continuous spectrum rather than a single frequency or series of discrete harmonics. This continuous spectrum exhibits an exponential cut-off above a frequency known as the *critical angular frequency*:

$$\omega_c = \frac{3c\gamma^3}{2a}$$

where γ is the Lorentz factor of the charged particle and a is the radius of curvature of the charged particle's spiral orbit. Folding this with the electron energy spectrum gives the spectrum of the resulting synchrotron radiation.

The average energy loss rate for these particles can be found by starting with the relativistic Larmor formula for power radiated by an accelerating charge:

$$-\left(\frac{dE}{dt}\right) = \frac{2}{3}\frac{e^2}{c^3}\gamma^4 a^2 \tag{2.19}$$

where $a = e\beta \sin \alpha B / \left(\gamma m_e\right)$. Averaging over all pitch angles α, to determine the average energy loss rate, and rewriting in terms of the Thomson cross section, $\sigma_T = 8\pi r_e^2/3$, and the classical electron radius, $r_e = e^2/\left(m_e c^2\right)$, gives:

$$-\left(\frac{dE}{dt}\right) = \frac{4}{3}\sigma_T c \frac{B^2}{8\pi}\left(\frac{v}{c}\right)^2 \gamma^2 \tag{2.20}$$

The salient features of this equation are: the energy loss rate (1) is proportional to the magnetic energy density, (2) is proportional to the Lorentz factor squared, and (3) is inversely proportional to the square of the particle's rest mass

2.4.2 Curvature Radiation

Pulsars have extremely strong magnetic fields and thus charged particles gyrating about the field lines rapidly lose the velocity component perpendicular to the field lines due to synchrotron losses resulting in the particles streaming along the field lines. However, since the magnetic field lines of the pulsar are curved due to the dipolar shape of the field, as charged particles stream along these curved field lines they emit *curvature radiation*. The formalism for curvature radiation follows that for synchrotron radiation, with the radius, a of the spiral orbit of the charged particle being replaced by the radius of curvature, ρ_c of the magnetic field line. In section 2.5 we will discuss the possibility of a parallel component of the electric field existing in regions of low charge density. Such electric fields can accelerate particles along the field lines. The cut-off energy for curvature radiation of electrons whose acceleration is balanced by radiative losses is given by:

$$E_c = 0.64\pi\lambdabar\left(\frac{E_\parallel}{e}\right)^{3/4}\rho_c^{1/2} \tag{2.21}$$

where $\lambdabar \equiv \hbar/m_e c$ is the electron Compton wavelength and $E_\parallel$ is the electric field that accelerates the electrons parallel to the magnetic field (Zheleznyakov, 1996). Above this cutoff energy, E_c, the spectrum falls off exponentially. For an acceleration region in the outer gap of a pulsar magnetosphere the parallel component of the electric field takes the form $E_\parallel \sim eB_{lc}/\left(r_e \lambdabar \chi^2 B_\hbar\right)$, where, by convention, we scale the magnetic field at the light cylinder $B_{lc} = B_s \left(R_s/R_{lc}\right)^3$ by the critical field for pair creation $B_\hbar \equiv m_e^2 c^3/\left(e\hbar\right)$. χ is a scaling parameter such that the scaled radius of curvature $\rho_\chi = \rho_c/(\chi R_{lc})$. Using the formula for $E_\parallel$, setting $P = 0.1P_{-1}$ and since $R_{lc} = Pc/(2\pi)$ one can rewrite Eq. 2.21 for a pulsar magnetosphere as:

$$E_c \approx \frac{8\rho_\chi^{1/2}}{\chi}\left(\epsilon_\parallel B_{12}\right)^{3/4}\left(P_{-1}\right)^{-7/4} \quad \text{(GeV)} \tag{2.22}$$

where $\epsilon_\parallel$ is an electrostatic decrement factor $\epsilon_\parallel \leq 1$ and $B_{12} = B_0/10^{12}$ Gauss (Baring, 2011).

Curvature radiation within a pulsar magnetosphere is predicted to have a cut-off energy on the order of a few GeV, which is consistent with the measured values from *Fermi*-LAT detected pulsars (Abdo et al., 2010a), but an unlikely explanation for the VERITAS observations of pulsed emission above 100 GeV from the Crab pulsar (VERITAS Collaboration et al., 2011).

2.4.3 Inverse Compton Scattering

In the classical Compton scattering process an incoming high energy photon collides with an electron and transfers some of its energy and momentum to the electron. The scattered photon has a lower energy and momentum than the initial photon while the scattered electron has gained the lost energy and momentum. Inverse Compton scattering occurs when ultra-relativistic electrons collide with a low-energy photon. The photon gains energy from the electron. For the case where $\gamma\hbar\omega \ll m_e c^2$, the Thomson scattering cross-section, σ_T, can be used to describe the scattering. (This constraint defines a low energy regime called the Thomson regime.)

The energy gained by low photons by scattering in the Thomson regime is given by:

$$\frac{dE}{dt} = \frac{4}{3}\sigma_T c u_{\text{rad}} \left(\frac{v^2}{c^2}\right) \gamma^2 \tag{2.23}$$

where u_{rad} is the energy density of radiation in the laboratory frame (Longair, 2011). The number of photons scatter per unit time is given by $\sigma_T c u_{\text{rad}} / (\hbar\omega)$, using this with Eq. 2.23 gives the average energy of scattered photons

$$\bar{E_\gamma} = \frac{4}{3} E_{\gamma 0} \left(\frac{v}{c}\right)^2 \gamma^2 \tag{2.24}$$

Equation 2.24 shows that photons upscattered by the inverse Compton process is proportional to γ^2 in the Thomson regime, this is important in high energy astrophysics since this process allows low energy ambient or synchrotron photons to be upscattered to gamma-ray energies. Energy conservation limits the maximum energy of the inverse Compton photon to $\lesssim \gamma m_e c^2$. It should be noted that Eq. 2.23 is valid for only in the limit $\gamma\hbar\omega \ll m_e c^2$. Many of these types of interactions in astrophysical conditions happen in the extreme relativistic regime, also known as the Klein-Nishina regime. The full expression for inverse Compton scattering uses a cross section that includes proper relativistic corrections called the Klein-Nishina formula:

$$\sigma_{KN} = \sigma_T \frac{3}{4} \left[\frac{1+x}{x^3} \left\{ \frac{2x(1+x)}{1+2x} - \ln(1+2x) \right\} + \frac{1}{2x} \ln(1+2x) - \frac{1+3x}{(1+2x)^2} \right] \tag{2.25}$$

where $x \equiv \hbar\omega / m_e c^2$. This cross section reduces to the Thomson cross section in the limit $x \ll 1$. In the Klein-Nishina regime the cross section decreases with increasing photon energy making collisions less likely. In the ultra-relativistic limit $\gamma \gg 1$, the Klein-Nishina cross section simplifies to: $\sigma_{KN} = (3/8)\, \sigma_T x^{-1} (\ln 2x + 1/2)$.

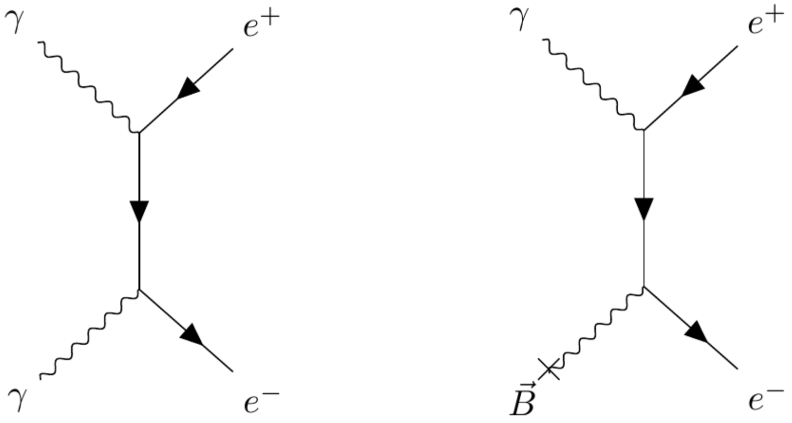

Figure 2.4: Feynman diagrams for pair creation processes. (a) shows the Feyman diagram for photon-photon pair creation. (b) shows Feyman diagram for pair creation where a magnetic field acts as a virtual photon.

2.4.4 Pair Production

If a photon has energy of at least $2m_ec^2$, it is possible for the photon to interact with a second photon to produce an electron-positron pair. A single photon cannot pair produce since energy and momentum can not be simultaneously conserved, But one can think of the Coulomb field of an atom on a magnetic field as providing off-shell, virtual photons allowing conservation of momentum and pair production by single gamma rays in the presence of a field. The process of pair creation can lead to the substantial attenuation of gamma rays in certain astrophysical scenarios, such as the extra-galactic background light attenuation of TeV gamma rays from distant blazars as disucssed in Chapter 3. The Feynman diagram for standard photon-photon pair creation is shown in Fig. 2.4(a). In some considerations of pulsar physics the interaction of two high-energy photons can be important as discussed in the sections on pulsar gap models.

For a photon propagating through a magnetic field, the field appears as a virtual photon allowing for pair creation to occur. This magnetic pair production becomes significant for gamma rays above $E_\gamma = 2m_ec^2$ and in magnetic fields with strengths comparable to the quantum critical field $B_\hbar = m_e^2 c^3/e\hbar \approx 4.4 \times 10^{13}$ G. Pair creation cannot occur in a vacuum due to the requirement of four-momentum conservation; however, an external magnetic field can absorb photon momentum perpendicular to the field, while energy and momentum along the field is still conserved. Because of the absorption of momentum perpendicular to $\vec{B}$ the pair creation threshold takes a slightly different form which can easily be found by considering the conservation of energy and longitudinal momentum and gives the relation:

$$\sin^2 \beta_p = \frac{k^2 \sin^2 \beta_{ph} - 4}{k^2 - 4} \tag{2.26}$$

where $\vec{k}$ is the photon momentum vector defined to be dimensionless with respect to $\lambdabar$ (i.e. $k' = k\lambdabar$). β_p is the angle between the magnetic field and the momentum vector $\vec{p}_{e^\pm}$ of the produced particle. From this it can be seen that the threshold for pair creation depends on the orthogonal component of the photon momentum:

$$k_{\perp 0} = \left(k \sin \beta_{ph}\right)_0 = 2 \tag{2.27}$$

The probability, per unit time, of producing an electron-positron pair by a photon with momentum $\vec{k}$ moving in a magnetic field $\vec{B}$ is given by the expression:

$$W\left(\vec{k}\right) = \frac{3^{3/2}}{2^{9/2}} \frac{\alpha_\hbar c}{\lambdabar} b_0 |\sin \beta_{ph}| \exp\left(-\frac{8}{3kb_0 |\sin \beta_{ph}|}\right) \Theta\left[k|\sin \beta_{ph}| - k_{\perp 0}\right] \tag{2.28}$$

where $\alpha_\hbar$ is the fine-structure constant, $b_0 = B/B_\hbar$, $\Theta(x)$ is a step-function and $k_{\perp 0}$ is the minimal value of the photon momentum component orthogonal to $\vec{B}$ for pair production to be possible.

From the equation for W it is clear that the likelihood of pair production scales with the perpendicular component of the magnetic field, with respect to the path of the photon.

The mean free path, l, can be found to be:

$$l = \frac{8\rho_c}{3kb_0}\left[\ln\frac{\alpha_\hbar\rho_c}{2\sqrt{6}\lambdabar k^2 b_0} - 3\ln\left[\frac{1}{2}\ln\left[\frac{\alpha_\hbar\rho_c}{2\sqrt{6}\lambdabar k^2 b_0}\right]\right]\right] \tag{2.29}$$

(Beskin et al., 1993). This pair attenuation makes some altitudes of the pulsar magnetosphere opaque to high energy photons, depending on the exact energy of a given photon. A limit can be placed on how near the stellar surface a detected photon may originate to avoid to pair attenuation. For a polar cap model the restriction placed on the location of emission is:

$$r \geq \left(\frac{E_c B_{12}}{1.76\ \mathrm{GeV}}\right)^{2/7} P^{-1/7} 10^6\ \mathrm{cm} \tag{2.30}$$

where B_{12} is the magnetic field in units of 10^{12} G.

2.5 Magnetosphere Gap Models

Following the description outlined by Goldreich and Julian (Goldreich and Julian, 1969) the charge density that builds up in the pulsar magnetosphere is such that charges are able to rearrange themselves and short out the electric field component parallel to the magnetic field, except in a few limited regions. The two general locations of these regions where $\vec{E}\cdot\vec{B} \neq 0$ are the region just above the polar cap and the region along the null surface boundary, where $\vec{\Omega}\cdot\vec{B} = 0$. In these areas there can exist a nonzero $E_{\parallel}$ that would accelerate charged particles allowing radiative emission, but this is a necessary not sufficient condition. It has been exceedingly challenging to pinpoint the gap from first principles and typically one postulates plausible locations for the gap and then turns to experimental constraints to either support or contradict these ansatz.

2.5.1 Polar Cap Models

Polar cap (PC) models, in general, propose that high-energy emission from pulsars originates from charged particles being accelerated by a nonzero $E_\parallel$ which forms near the magnetic poles in a region that is called the polar cap. The first versions of PC models to explain pulsar emission date back the work of Sturrock (Sturrock, 1971) and Ruderman and Sutherland (Ruderman and Sutherland, 1975). Much work has gone into updating and providing ever greater detail to these first models but the bulk of the basic principles remain the same.

PC models fall into two categories: *vacuum gap* models and *space charge-limited flow* models. Binding forces act on charged particles in the surface layer of a pulsar due to the lattice structure of the particles in a strong magnetic field. These charged particles are considered free (ignoring gravitational considerations discussed in Sec. 2.3.2 only if the surface temperature of the pulsar is above the thermal emission temperature for electrons T_e and ions T_i. If the surface temperature of the neutron star, T, exceeds the thermal emission temperature, $T_{e,i}$, free emission of charged particles will occur and the flow of particles is only limited by the space-charge. Such PC models are known as *space charge-limited flow* (SCLF) models. Alternatively if T is less than the thermal emission temperature, $T_{e,i}$, then charges are trapped in the surface of the neutron star and a vacuum gap will form at the surface creating a region in which particles can be accelerated, such models are referred to as *vacuum gap* models.

Sturrock first defines the polar cap region in his SCLF model in 1971. Any field line that extends as far as the light cylinder, $r\cos\theta = R_{lc}$ must be an open field line. Any field lines within a radius θ_p as measured from the magnetic pole will be open field lines. This region is defined as the polar cap. The angular radius of the polar cap is given by:

$$\theta_p \approx \sqrt{R/R_{lc}} = 10^{-4.8} R^{1/2} T^{-1/2}$$

and the radius of this cap is

$$R_p \approx R\theta_p = 10^{-4.8} R^{3/2} T^{-1/2}.$$

It is along these open field lines that charged particles stream outward (Sturrock, 1971). Fig 2.5 shows the geometry of the polar cap region. In the Ruderman and Sutherland PC model, the space charge along these open field lines just above the stellar surface is less than the Goldreich-Julian corotating charge density due to the outflow of charged particles, while surface charges are trapped as previously described. With the deficit of charge in relation to the Goldreich-Julian charge density, a nonzero $E_{\parallel}$ forms which will accelerate charged particles. The accelerating particles can radiate via curvature radiation or in some models they may scatter via the inverse Compton process with thermal X-rays. Through either radiative mechanism the produced photons will undergo pair production in the pulsars strong magnetic field. As the charged particles produced stream outward they also gyrate around B-field lines and emit coherent synchrotron radiation. The secondary photons travel to higher altitudes and eventually pair produce and this continues creating a cascade. Such a mechanism predicts a sharp cutoff at hard gamma-ray energies due to pair attenuation off of the strong B-field at lower altitudes (Baring, 2011). In addition to difficulty in describing the VHE gamma-ray emission PC models also have difficulty in reproducing the pulse profile; PC models rely on relatively low altitude emission and, as a result, the predicted beam size is too small to produce some observed wider pulse profiles.

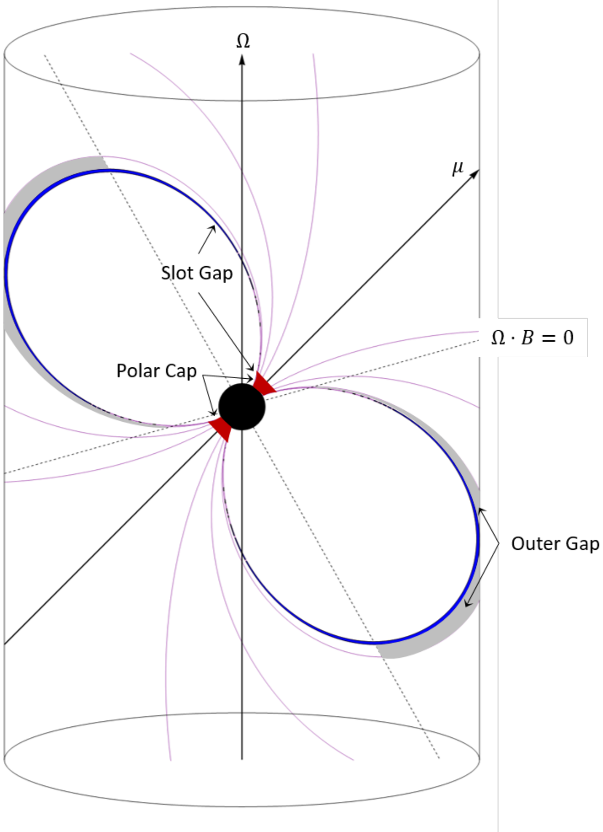

Figure 2.5: Illustration of the geometry of the various gap models in a pulsar magnetosphere out to the light cylinder. The polar cap region is shaded in red. The slot gap region is shaded in blue and includes the polar cap region. The outer gap region is shaded in gray. The dotted line indicates the null charge surface, where $\Omega \cdot B = 0$.

2.5.2 Slot Gap Models

Jonathon Arons first proposed the physical possibility of an acceleration/emission region at high-altitudes within pulsar magnetospheres (Arons, 1983). This acceleration region known as the *slot gap* (SG), comes as a consequence that the pair plasma, from PC models, above the pair formation front occurs at higher altitudes close to the edge of the polar flux tube, i.e. the surface described by the last open field lines (Arons and Scharlemann, 1979). This is allowed by the lower strength electric field near the edge of the PC boundary. With a lower strength electric field, particles must be accelerated greater distances before reaching sufficient Lorentz factors to radiate photons capable of pair production. The pair plasma that forms is responsible for screening the accelerating electric field. Since this pair plasma does not occur for higher and higher altitudes (relative to the stellar surface) as the last open field line is approached, the gap region is, accordingly, extended as a thinning layer bounded by the last open field line. Near this last open field line and at high altitude nearly all gamma rays radiated can escape. This thin layer can extend out to the light cylinder of the magnetosphere as shown in Figure 2.5. The width of the slot gap is a function of pulse period and surface magnetic field given by $\Lambda = PB_{s12}^{-4/7}$ where B_{12} is given in units of 10^{12} G (Muslimov and Harding, 2003).

The charged particles that accelerate in the slot gap will radiate via curvature, inverse Compton, and synchrotron processes at high altitudes. The Lorentz factors of these particles will ultimately be limited to $\gamma \approx 10^7$ when the cooling rate of curvature radiation is equal to the acceleration rate in the electric field. This peak energy of curvature radiation spectrum has been calculated to be approximately 30 GeV for typical pulsar parameters (Harding, 2007). It is also likely that inverse Compton scattering of the charged particles off low energy radio photons in the slot gap will occur. The IC spectrum would extend to a maximum energy of a few GeV (Harding, 2007).

The geometry of the slot gap becomes strongly influenced by special relativistic effects at high altitude. Aberration, time-of-flight and time retardation of the magnetic field play an important role in the emission signature. Aberration is taken into account by Lorentz transforming the unit vector of the photon propagation direction $\boldsymbol{\hat{k}'}$ from the corotating frame to the inertial observer (unprimed) frame:

$$\hat{k} = \frac{\hat{k}' + \left[\gamma + (\gamma - 1)\left(\boldsymbol{\beta} \cdot \boldsymbol{\hat{k}'}\right)/\beta^2\right]\boldsymbol{\beta}}{\gamma\left(1 + \boldsymbol{\beta} \cdot \boldsymbol{\hat{k}'}\right)} \tag{2.31}$$

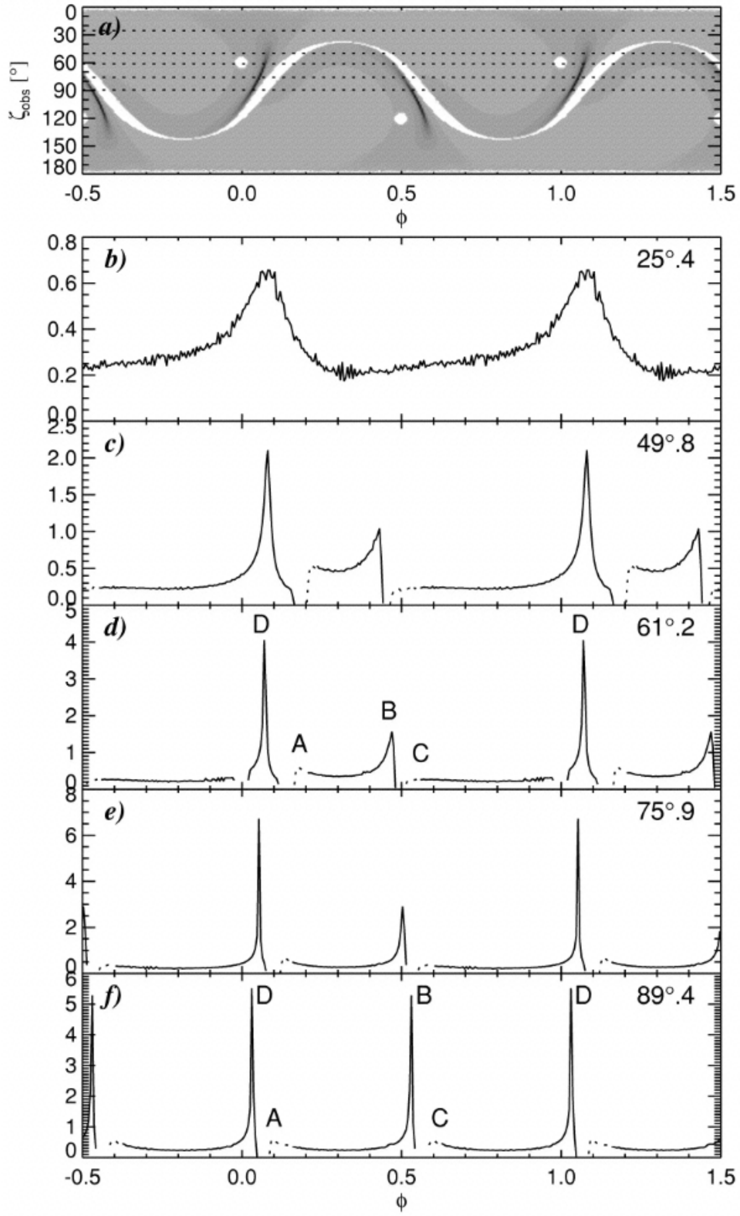

Figure 2.6: Results from a two-pole caustic model simulation for a pulsar with inclination angle $\xi = 60°$. (A) shows the photon mapping as a function of the line of sight angle ζ_{obs} and phase angle ϕ, as measured in the observer's frame. Magnetic polar caps are depicted as blank circles. Two caustics can be seen as dark arches trailing the polar caps. Caustics form as a result of special relativistic effects. A light curve can be produced by taking a horizontal cut of the diagram for some constant observation angle, ζ, as depicted in (B)-(F). Each figure (B)-(F) corresponds to a constant viewing angle depicted as dotted lines in (A). Figure taken from (Dyks and Rudak, 2003).

where $\boldsymbol{\beta}$ is the local corotation velocity in natural units. The effect of time-of-flight considerations can be seen as a shift in the observed phase of $\delta\phi = -\vec{r} \cdot \hat{k}/R_{lc}$, where $\hat{k}$ is the unit vector corresponding to the photon propagation direction in the observer's frame. The effects of special relativity also cause photons emitted at different altitudes to bunch together in phase creating caustics as depicted in Fig. 2.6. These caustics naturally create double-peaked light curves seen in gamma-ray pulsars as demonstrated in Fig. 2.6. Single-peaked curves can be reproduced at small viewing angles (Dyks and Rudak, 2003).

2.5.3 Outer Gap Models

In addition to gap regions that originate at or near the polar cap of the pulsar, another category of emission models was proposed in 1986 that exists in the outer region of the magnetosphere. These models are referred to as *outer-gap* (OG) models. The OG model was first presented by Cheng, Ho, and Ruderman who postulated the existence of a charge depletion region that would form with boundaries beginning on the outside of the last closed field line and bounded on the other side by a charge layer on a surface of an open field line. The innermost boundary of the region is the null surface, $\vec{\Omega} \cdot \vec{B} = 0$ and the region extends to the light cylinder (Cheng et al., 1986). This region is depicted in Fig 2.5 and Fig. 2.7.

At the null surface, the net Goldreich-Julian charge is zero, but there can still be a non-negligible but neutral density of charged particles. A gap can form near the null surface. Electrons streaming outward along the open field lines passing through this surface will escape through the light cylinder leaving behind a negative charge-depleted region, relative to the corotating charge density, ρ_{GJ}. If left unimpeded, this outward flow of negatively-charged particles would allow the gap region to continue to grow, depleting the outer magnetosphere of charge. The depletion of charge gives rise to a nonzero electric field, $E_{\parallel}$. The associated potential which accelerates charges is roughly that expected by Faraday's

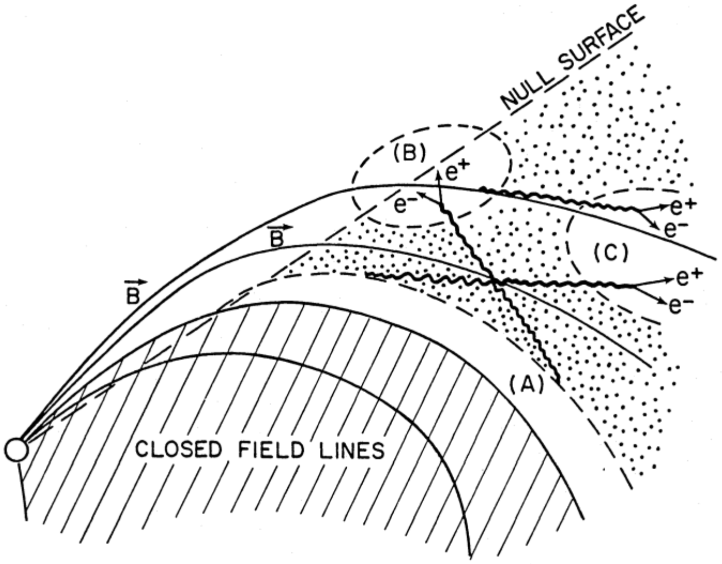

Figure 2.7: Schematic of 3 possible charge-depleted gap regions in the outer gap model. Gamma rays are produced by electrons accelerated by $E_{\|}$, and thus are beamed along field lines.‘ In regions (B) and (C) gamma rays emitted from other regions can penetrate and pair-produce filling the region with charge carriers and closing the gap region. Region (A), however, cannot be penetrated by gamma rays emitted from other regions, e.g. (B) and (C), showing a stable gap forms along the last closed field line. Figure taken from (Cheng et al., 1986).

law or Eq. 2.17 $\Delta V \approx \Omega^2 B_s R^3/c^2$. As charged particles are accelerated in this newly formed charge-depletion region, they may emit gamma-ray photons via curvature radiation, inverse Compton scattering and synchrotron radiation. Some of these gamma-ray photons will pair-produce within the gap region. The newly formed electron-positron pairs will limit the growth of the gap to a thin slab along the last closed field line.

The strength of this accelerating potential in the gap can reach 10^{15} V depending on the rotation speed of the pulsar, the length of accelerating gap, the radius of curvature of the magnetic field lines, the ratio between the width and breath of the gap and the magnetic flux though the gap region. The electric field generated has been shown to become strong enough to accelerate charged particles to Lorentz factors which allow curvature radiation gamma rays to be emitted. As stated in Section 2.5.2 the maximum Lorentz factor possible is reached when the energy gain rate from acceleration in the gap equals the energy loss rate due to radiative cooling. These gamma rays will generate further electron-positron pairs via photon-photon pair production. The only stable gap region that can be formed is one that ends extends to the light cylinder allowing the created pairs to escape the magnetosphere and preventing the gap from being quenched (Cheng et al., 1986).

As with the SG models, since the emission in the OG models take place at high altitudes near the light cylinder special relativistic effects become prominent. Aberration and time-of-flight delays play a large role and when accounted for can produce the wide separation double-peak light curves typical of gamma ray pulsars (Romani, 1996). OG models are capable of producing light curves which fit a wide variety of pulsars and are broadly accepted as the location of high energy emission from pulsars. Many OG models assume the curvature radiation plays the dominant role in the generation of gamma rays and many of the *Fermi*-LAT detected pulsars exhibit light curves that can be replicated using the geometry of the outer gap and spectral energy distributions which exhibit a power-law with an exponential cutoff relation as predicted by curvature radiation.

Curvature radiation in an outer gap was the consensus explanation for gamma ray emission pulsars until the 2011 VERITAS detection of pulsed emission from the Crab pulsar above 100 GeV (VERITAS Collaboration et al., 2011) and the MAGIC detection of pulsed emission from the Crab up to 1 TeV (Ansoldi et al., 2016). The gamma-ray spectrum of the Crab pulsar has a break at 6 GeV but the flux beyond that break does not fall off exponentially as predicted by curvature radiation models. This can be seen in Fig 2.2 and Fig 2.8. This feature in the spectrum of the Crab could be explained by invoking a different emission mechanism than curvature radiation and (Lyutikov et al., 2012b) argue that inverse Compton scattering in the Klein-Nishina regime provides a consistent picture with current observations. However, even if IC scattering can provide an explanation of the radiation mechanism for the $>$ 100 GeV gamma rays, the effects of pair absorption of these high

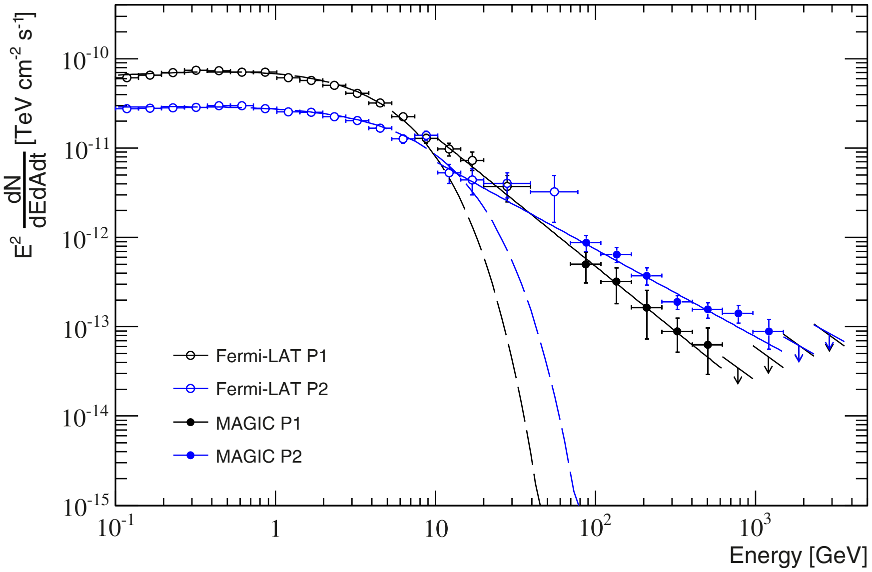

Figure 2.8: Phase-folded spectral energy distribution of the Crab pulsar for peaks P1 and P2 from MAGIC (closed circles) and *Fermi*-LAT (open circles). Dashed line shows power-law with exponential cut-off fit to *Fermi*-LAT data. Solid line shows fit using a broken power-law to *Fermi*-LAT and MAGIC data. Figure taken from (Ansoldi et al., 2016).

energy gamma rays lead to other constraints on the location of the emission region (and field geometry) that are, in part, the subject of this thesis and will be addressed in Chapter 6.

Chapter 3

Axions

3.1 Introduction

Axions are theoretical pseudoscalar bosons which were first postulated in 1978 (Weinberg; Wilczek) as a biproduct of the solution to the strong CP (charge conjugation (C) and parity inversion (P)) problem with the theory of quantum chromodynamics (QCD). The axion could result from a phase transition in the early universe and provide a natural candidate for cold dark matter. A violation in CP-symmetry in strong interactions has not been observed experimentally and has tight experimental upper bounds. In particular even a relatively small CP violating term in the QCD Lagrangian would lead to a detectable neutron electric dipole moment. Given the existence of a neutron *magnetic* dipole moment one can readily constrain the neutron *electric* dipole moment. This can be done be measuring the Larmor precession of the neutron spin in the presence of parallel and anti-parallel electric and magnetic fields. The precession frequency for both cases is then:

$$h\nu = 2\mu_B B \pm 2d_n E \tag{3.1}$$

where d_n is the neutron electric dipole moment. d_n can then be measured from the frequency difference

$$d_n = \frac{h\Delta\nu}{4E} \tag{3.2}$$

Experiments such as the RAL-Sussex-ILL experiment measure the Larmor precession frequency using NMR on ultracold neutrons trapped inside a storage cell. The current limit set on the neutron electric dipole moment is $d_n < 3.0 \times 10^{-26} e$ cm (Baker et al., 2006).

A fine-tuning problem arises with QCD since a CP-violating term is not precluded and is generally quite large. The solution to this issue was proposed by Roberto Peccei and Helen Quinn and is known as the Peccei-Quinn (PQ) mechanism (Peccei and Quinn, 1977). Since the proposal of the axion many laboratory and astrophysical searches have been developed to confirm the existence of this particle. This chapter will discuss the theoretical basis for the existence of axions and axion-like particles, the current state of terrestrial-based searches for axions, and the current state of astrophysical searches for axions.

3.2 Theoretical Basis for Axions

The strong-CP problem of QCD represents a fine-tuning problem that is considered by some theorists to be one of the most significant shortcomings of the theory. Here I focus on the Peccei-Quinn solution to serve as a template for a broader class of models that predict new axion-like particles.

In QCD, imposing a non-Ableian gauge symmetry results in a term in the Lagrangian $-1/4 G^a_{\mu\nu} G^{a\mu\nu}$ where $G^a_{\mu\nu}$ is the color field strength tensor given by

$$G^a_{\mu\nu} \equiv \partial_\mu G^a_\nu - \partial_\nu G^a_\mu - g_a f_{abc} G^b_\mu G^c_\nu \tag{3.3}$$

and where the G^i_ν terms are the gluon fields. This is closely analogous to electromagnetism where the field tensor $F_{\mu\nu} = \partial_\mu A_\nu - \partial_\nu A_\mu$, with G^i_ν corresponding to the electromagnetic potential vector A_μ. The final term in Equation 3.3 comes from the nonvanishing commutator of the non-Abelian gauge field and results in coupling of gluons to each other. Following the usual prescription, local gauge invariance requires that one replaces the derivative operator ∂^a_μ with

$$D_\mu \equiv \partial_\mu + iT_a G^a_\mu \tag{3.4}$$

where T_a are the generators of the SU(3) group. This leads to the QCD Lagrangian in the form

$$\mathcal{L}_{QCD} = \frac{1}{4g^2} G^a_{\mu\nu} G^{a\mu\nu} + \sum_j \bar{q}_j \left(i\gamma^\mu D_\mu + m_j \right) q_j \tag{3.5}$$

where q_j is the quark field of the jth flavor and m_j is the jth quark mass.

However, QCD couples to the (CP-violating) electroweak sector through loop corrections. These can be modeled by adding a CP-violating term to the effective QCD Lagrangian of the form:

$$\mathcal{L}_{\bar{\theta}} = \bar{\theta} \frac{g^2}{32\pi^2} G^a_{\mu\nu} \tilde{G}^{\mu\nu}_a \tag{3.6}$$

where $G^a_{\mu\nu}$ is the QCD gluon field strength tensor for the eight color degrees of freedom, a, and $\tilde{G}^{\mu\nu}_a$ is the dual tensor. Much like $F_{\mu\nu}\tilde{F}^{\mu\nu}$ constructed from the electromagnetic field tensor $F_{\mu\nu}$ and its dual $\tilde{F}^{\mu\nu}$, this tensor product ($4\vec{E} \cdot \vec{B}$ for the electromagnetic case) is CP odd.

To solve the strong-CP problem in the Peccei-Quinn theory, the $\bar{\theta}$ term is promoted to a field rather than static parameter by adding a kinetic term $1/2\partial_\mu a)^2$ to the Lagrangian and introducing a global, chiral symmetry $U(1)_{PQ}$, which is spontaneously broken at the Peccei-Quinn energy scale, f_a. A pseudo-Nambu-Goldstone boson with a nonzero mass arises as a result (Wilczek, 1978; Weinberg, 1978). This pseudoscalar boson is known as the axion. After introducing the new symmetry, the Lagrangian term takes the form:

$$\mathcal{L}_a = \frac{g^2}{32\pi^2}\frac{a\xi}{M}G^a_{\mu\nu}\tilde{G}^{\mu\nu}_a \tag{3.7}$$

where ξ is a model-dependent parameter, g is the coupling constant, M is the Peccei-Quinn scale and a is the axion field. The axion, which begins life as a massless Nambu-Goldstone boson acquires mass after the QCD phase transition through its coupling to gluons and hence to pions. The mass can be calculated using approximate methods giving

$$m_{a0} = \frac{F_\pi}{M}\frac{\sqrt{m_d m_u}}{m_d + m_u} \simeq \frac{13\ \mathrm{MeV}}{M[\mathrm{GeV}]} \tag{3.8}$$

where $F_\pi = 184$ MeV is the pion decay amplitude and m_d, m_u are the masses of the down and up quarks, respectively.

The Peccei-Quinn mechanism works for any value of M, thus many orders of magnitude are to be explored. Many different models of the axion exist which solve the strong CP problem but produce different couplings of the axion to Standard Model particles. In general one predicts a similar coupling to electromagnetism by virtue of triangle diagrams (see Figure 3.1) that naturally result from the coupling of axions to charged fermions, and the coupling of charged fermions to photons. The Lagragian for this interaction is:

$$\mathcal{L}_{a\gamma\gamma} = -\frac{1}{4}g_{a\gamma}F_{\mu\nu}\tilde{F}^{\mu\nu}a = g_{a\gamma}\vec{E}\cdot\vec{B}a \tag{3.9}$$

where $F_{\mu\nu}$ is the electromagnetic field tensor, $\tilde{F}^{\mu\nu}$ is the dual tensor, and $g_{a\gamma}$ is the axion-photon coupling which is given by:

$$g_{a\gamma} = \frac{\alpha}{\pi M} \tag{3.10}$$

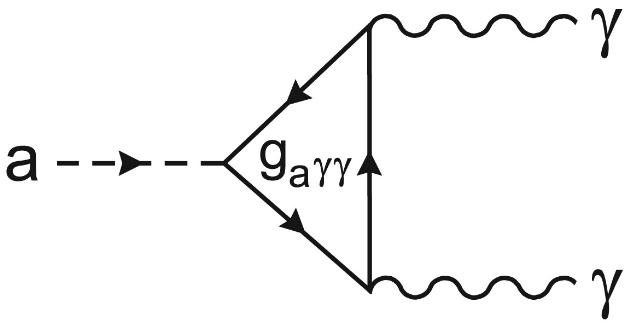

Figure 3.1: Feynmann diagram for axion coupling to photons

independent of the fermion mass.

Pierre Sikivie in a 1983 paper demonstrated the axions could be detected in a laboratory setting by exploiting the two-photon coupling of the axion (Sikivie, 1983). Experiments that take advantage of this coupling suggested by Sikivie have also been shown to be capable of detecting a broader class of particle, an axion-like pseudoscalar ϕ, that couples to photons in a fashion which mirrors Eq. 3.9 (Massó and Toldrà, 1995):

$$\mathcal{L}_{\phi\gamma\gamma} = -\frac{1}{4} g_{\phi\gamma} F_{\mu\nu} \tilde{F}^{\mu\nu} \phi = g_{\phi\gamma} \vec{E} \cdot \vec{B} \phi \tag{3.11}$$

Such a class of particle is often assumed to only couple to two photons, unlike the axion which couples to other Standard Model particles. This breaks the relationship between the axion mass, the symmetry breaking scale, and thus the relationship between $g_{a\gamma}$ and M (see Equation 3.10. A $\phi-$particle does not require the relation between the mass m_ϕ and the coupling g that the axion has. The mass and coupling to photons are independent parameters. This broader class of particles is referred to as axion-like particles (ALPs) to distinguish these from the classical QCD axions discussed. ALPs arise from the basic physical mechanism, the Peccei-Quinn mechanism, that provides a solution to the strong CP problem. ALPs can provide a candidate for the dark matter problem but unlike classical axions can not solve both problems.

There have been a number of searches conducted since 1977 in hopes of finding either axions or axion-like particles. To date none of the efforts have successfully identified axions or ALPs. The search efforts are easily divided into two categories: laboratory-based seraches and astrophysical searches. The following sections will discuss past efforts and the current constraints on axions and ALP parameter space.

3.3 Axions as Dark Matter

Axions have been considered as one possible dark matter candidate. Axions satisfy two necessary criteria for cold dark matter (CDM): (1) Axions are effectively collisionless and (2) a population of non-relativistic (cold) axions may exist in an abundance which would provide the necessary dark matter density. The mass of axions at temperatures 10^{12} K is related to the PQ–symmetry breaking energy scale M by Equation 3.8. Here and elsewhere in this chapter we closely follow the discussion in (Weinberg, 2008). Cosmological considerations of axions provide an upper bound on M and thus a lower bound on m_a.

Cold axions may be produced by three different mechanisms: vacuum realignment, string decay and domain wall decay (for a review on axion cosmology and descriptions of the cold axion production mechanisms see Sikivie (2008)). The cosmological axion field is predicted to be spatially homogeneous. The energy density and pressure for the axion field or any similar pseudoscalar (ALP) or scalar field are given by

$$\rho_a = \frac{1}{2}\dot{\varphi}^2 + \frac{1}{2}m_a^2\varphi^2 \tag{3.12}$$

$$p_a = \frac{1}{2}\dot{\varphi}^2 - \frac{1}{2}m_a^2\varphi^2 \tag{3.13}$$

where φ is the axion field. The equation of motion for φ in a background Robertson-Walker metric, is

$$\ddot{\varphi} + 3H(t)\dot{\varphi} + m_a^2(t)\varphi = 0 \tag{3.14}$$

where $H(t)$ is the Hubble constant at time t. The equation of motion has solutions: $\varphi = constant$ and $\varphi \propto 1/a^3$ where a is the scale factor and $\varphi = constant$ is rejected on physical grounds. For $\varphi \propto 1/a^3$ and times when $H(t) \ll m_a(t)$ the energy density becomes

$$\rho_a \to \frac{1}{2} m_a^2 \varphi_1^2 \left(\frac{a(t_1)}{a(t)} \right)^3 \tag{3.15}$$

where φ_1 is a constant of order M, t_1 is the time at which $H(t_1) = m_{a0}$. The present axion density can be determined to be

$$\rho_a(t_0) \approx \frac{1}{2} m_a^{1/2} \mathcal{N}_1^{-1/4} \varphi_0^2 \left(\frac{4\pi^3 G}{45} \right)^{3/4} (k_b T_{\gamma 0})^3 \tag{3.16}$$

where $\mathcal{N}_\infty$ is the effective number of types of particles with masses much less than $k_b T(t_1)$, k_b is the Boltzmann constant, and $T_{\gamma 0}$ is the photon temperature at present time.

Assuming that $\varphi_0 \approx M$ and ignoring factors of order unity, the axion density can be shown to be a fraction Ω_a of the critical density:

$$\Omega_a h^2 \approx \left(m_a / 10^{-5} \text{ eV} \right)^{-3/2} \tag{3.17}$$

At the extreme, if axions constitute the entirety of dark matter, then $m_a \approx 10^{-5}$ eV. If axions are only a component of the dark matter density, then 10^{-5} serves as a lower bound on the axion mass. For ALPs, since the relationship between m_{ALP}, $g_{a\gamma}$ and M is broken, ALPs may or may not play a role as a component of dark matter depending on the value of the symmetry breaking scale, mass and other parameters.

3.4 Astrophysical Axion Constraints

The axion or axion-like particles could plausibly take on a wide range of values for their mass and coupling constants. Having many orders of magnitude in the parameter space to explore allows a variety of approaches to search for evidence of the existence of axions or ALPs. Axions could be produced in hot plasmas, such as those found in an abundance of astrophysical objects and the existence of axions would have affect well-studied astrophysical processes allowing a number of astrophysical constraints. Axions also convert to photons in the presence of strong magnetic or electric fields, providing for a mechanism of detection in terrestrial experiments. Parameters of axions and ALPs can be constrained by a combination of direct terrestrial searches and indirect astrophysical constraints. The following will discuss various bounds set on the axion/ALP parameter space by experiments and astrophysical observations.

3.4.1 Constraints from Globular Clusters

Globular clusters (GC) serve as an interesting astrophysical laboratory for searching for axion signatures. A GC is a gravitationally bound cluster of stars which formed at roughly the same time. GCs are important systems for testing theories on stellar evolution since the stars share the same age, but not necessarily other characteristics such as mass or surface temperature. One such test would be including axions in calculations of the rate of helium burning in horizontal branch stars. Observations of GCs have yielded the result that the theoretical helium-burning lifetime of low-mass stars is in agreement with observations to within 10%. The introduction of a nonstandard energy-loss rate accelerates the rate of nuclear fuel consumption while leaving the stellar structure largely unaffected. In helium burning stars the rate of helium consumption could be accelerated due to the presence of axions. Horizontal branch stars have a core mainly composed of He. As such, the accelerated consumption of He due to axions is easily calculated and found to reduce the lifetime of horizontal branch stars by a factor

$$\left[1 + \frac{3}{8}\left(\frac{g_{a\gamma}}{10^{-10}\ \mathrm{GeV}^{-1}}\right)^2\right]^{-1} \tag{3.18}$$

(Raffelt, 1996). A study conducted on the lifetime of horizontal branch stars in 15 GCs places a limit on on the axion-photon coupling constant at $g_{a\gamma} \lesssim 10^{-10}\ \mathrm{GeV}^{-1}$ for axion masses $m_a \gtrsim 30$ keV (Raffelt, 2008)

3.4.2 Constraints from White Dwarf Cooling Times

As a horizontal branch star reaches the late stage of its helium burning phase it enters the asymptotic giant branch (AGB) of the Hertzsprung-Russell diagram. AGB stars consist of a degenerate carbon-oxygen core and a helium burning shell. AGBs may later evolve into white dwarf star which cools first by neutrino emission and later surface photon emission. The existence of axions would allow an additional cooling channel for white dwarfs via axion bremsstrahlung:

$$e + Ze \rightarrow e + Ze + a.$$

This additional cooling channel would increase the cooling rate of white dwarfs. From observations, the white dwarf luminosity function shows an agreement between the cooling speed and the theoretical expectations allowing a constraint to placed on the axion-electron coupling $g_{ae} \lesssim 1.3 \times 10^{-13}$ for axion masses $m_a < 0.03$ eV (Raffelt, 1986).

A more recent method for constraining axion/ALP parameters using white dwarfs analyzes the level of linear polarization in radiation emitted from magnetic white dwarfs. Photon-axion oscillations in the magnetosphere of white dwarfs can enhance the level of linear polarization that is observed. Using this method, a constraint is placed on the axion-photon coupling constant $g_{a\gamma} < 10^{-10}$ GeV^{-1} for axion masses $10^{-6} < m_a < 10^{-3}$ eV (Gill and Heyl, 2011).

3.4.3 Constraints from SN 1987A

Observations of SN 1987A have had far reaching implications for astrophysics. SN 1987A confirmed many theories about core collapse supernovae and also provided the first evidence for astrophysical neutrinos (Bahcall, 1989; Arnett et al., 1989; Bionta et al., 1987; Hirata et al., 1987). In addition, SN 1987A provided an opportunity to study and constrain axion parameters. The existence of axions/ALPs would potentially play a prominent role in the cooling of the newly born neutron star which could have resulted in an observable effect on the duration of the neutrino flux from SN 1987A. Nucleon-nucleon axion bremsstrahlung would be the most relevant physical process for cooling. It has been shown in the literature that an axions with masses 10^{-3} eV $\lesssim m_a \lesssim 0.02$ eV would significantly affect the rate of cooling of the neutron star born in SN 1987A shortening the timescale of the neutrino burst and allowing for fewer neutrinos to be produced. With axion cooling incorporated into numerical models for SN 1987A it has been calculated that the number of neutrinos detected from SN 1987A would have been significantly lower than what was observed, thus essentially eliminating the possiblity of dark-matter axions/ALPs in the mass range 10^{-3} eV $\lesssim m_a \lesssim$ 0.02 eV are precluded (Burrows et al., 1989; Turner, 1988).

3.5 Searches for Axions/ALPs

A variety of experimental methods have been used to search for axions and ALPs. Fig. 3.2 shows current constraints placed on the axion/ALP coupling constant and the

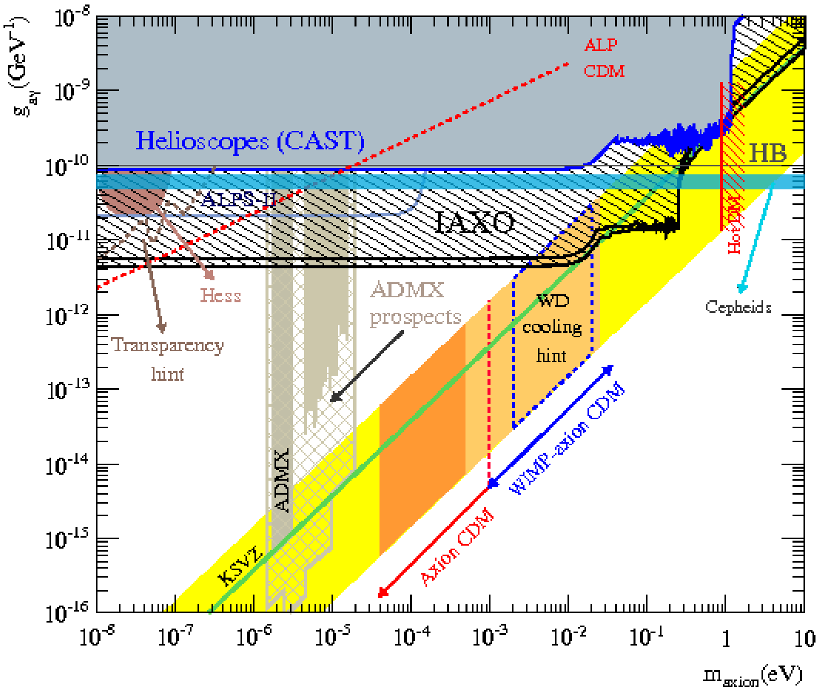

Figure 3.2: Summary of current constraints, future prospects and hints in axion/ALP parameter space. The classical QCD axion parameter space is shown by a yellow band. Axionic dark matter parameter space is shown by orange bands. In the region labeled "WIMP-axion CDM" axions would only comprise a fraction of the dark matter energy density. Prospects for IAXO and ADMX are shown by hatched regions. Figure taken from Carosi et al. (2013).

axion/ALP mass from a variety of search methods, many of which will be described in the following sections. Most searches for axions and ALPs are based on the same basic principle, the Primakoff effect. The Primakoff effect is the conversion of photons into axions by interacting with electric or magnetic fields acting as virtual photons. The effect arises from the $a\mathcal{F}^{\mu\nu}\tilde{\mathcal{F}}_{\mu\nu}$ term in the Lagrangian giving rise to a term $ga\vec{E}\cdot\vec{B}$. Not that this term represents the combined contribution of a direct coupling of axions to photons, or the coupling through fermion triangle diagrams (see Figure 3.1) a necessary consequence of the $aG^{\mu\nu}\tilde{G}_{\mu\nu}$ term in the Lagrangian. The Feynman diagram for this interaction is shown in Fig. 3.3.

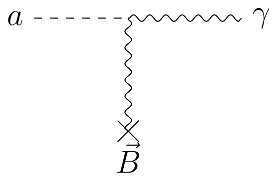

Figure 3.3: Feynmann diagram for the Primakoff effect.

3.5.1 Helioscope Searches

The Sun provides a good target for axion and ALP searches due to its proximity to Earth and its ability to produce axions within its core. Constraints on the axion/ALP coupling to photons have been determined by considering photon interactions via the Primakoff process with the Coulomb field of electrons or nuclei within the Sun. Bahcall et al. (1982) assume that Standard Solar Model (SSM) remains unchanged by the presence of axion mixing and determine the solar flux of axions to be

$$L_a = 1.7 \times 10^{-3} \left(\frac{g_{a\gamma}}{10^{-10}\ \mathrm{GeV}^{-1}} \right) L_\odot \tag{3.19}$$

where $L_\odot$ is the solar luminosity. Helioseismological sound-speed profiles have been used to constrain deviations from standard solar models leading to constraints on solar energy losses through the Primakoff emission of axions. This yields the constraint on the axion-photon coupling $g_{a\gamma} < 1.1 \times 10^{-9}\ \mathrm{GeV}^{-1}$ (Schlattl et al., 1999).

One type of direct search experiment technique used to search for these solar axions are Bragg scattering helioscopes. Typically these are not purpose-built experiments, but detectors constructed for WIMP dark matter detection, or more generally, the detection of ~keV energy deposition from rare events. The spectral energy distribution of solar axions is predicted to be peaked between $1 - 10$ keV corresponding to the solar core's temperature which puts the axion wavelength on the same order as the lattice spacing in a typical crystal. Crystalline detectors exploit the Coulomb field within a crystal to convert solar axions.

Characteristic Bragg scattering patterns would be produced, and the time variation of the signals would be distinctive due daily modulation from the relative diurnal movement of the Sun. Examples of this type of experiment include a sodium iodide crystal used in DAMA (Bernabei et al., 2001), a germanium crystal used in SOLAX (Avignone et al., 1998) and COSME (Morales et al., 2002), and germanium and silicon crystal used at CDMS (Ahmed et al., 2009). These experiments have found comparable limits $g \lesssim 2 \times 10^{-9}$ GeV^{-1}.

The other type of helioscope experiment use a powerful magnet to induce axion-photon mixing by the Primakoff process. The magnet is pointed at the Sun and is capable of converting solar axions into X-ray photons which can be observed by X-ray detectors in the instrument. The probability of axion-photon conversion in a homogeneous magnetic field, B, over a coherence length, L, is (van Bibber et al., 1989)

$$P_{a\to\gamma} = \frac{\left(g_{a\gamma}BL/2\right)^2}{L^2\left(q^2+\Gamma^2/4\right)}\left[1+e^{-\Gamma L}-2e^{-\Gamma L/2}\cos\left(qL\right)\right] \tag{3.20}$$

where Γ is the inverse absorption length for X-rays and q is a term for the momentum transferred in the axion-photon interaction.

The first generation of this type of purpose-built axion helioscope was built at Brookhaven National Laboratory in 1992 using a stationary dipole magnet with $B = 2.2$ T. This first axion helioscope set a 3σ limit on the axion coupling at $g_{a\gamma} = 3.6 \times 10^{-9}$ GeV^{-1} for masses $m_a < 0.03$ eV (Lazarus et al., 1992). A second generation of axion helioscope with a 4.4 T magnet was built at the University of Tokyo, the *Tokyo Axion Helioscope* (SUMICO). SUMICO also employed dynamic tracking of the sun. SUMICO set a limit on the axion coupling at $g_{a\gamma} = 6.0 \times 10^{-10}$ for masses $m_a < 0.03$ eV (Ohta et al., 2012). The third generation of axion helioscope is the CERN Axion Solar Telescope (CAST) which uses a dipole test magnet with $B = 9$ T from the Large Hadron Collider. As of this writing, CAST has set the best limits from axion helioscopes on the axion coupling, $g_{a\gamma} = 8.8 \times 10^{-11}$ for masses $m_a < 0.02$ eV (Andriamonje et al., 2007). The *International Axion Observatory* (IAXO) is a fourth generation helioscope that has been proposed. IAXO will use a large superconducting toroidal magnet with a maximum field strength of 5.4 T. The field strength is not as large as CAST, but the magnet is larger providing a larger distance over which an axion will travel through the strong magnetic field. IAXO is expected to have a signal to-background-ratio 4-5 orders of magnitude more sensitive than CAST allowing IAXO to reach the $\sim 2 \times 10^{-12}$ GeV^{-1} regime for the axion coupling constant for masses $m_a \lesssim 0.25$ eV (Armengaud et al., 2014).

3.5.2 Haloscopes

Axion haloscopes are used as a direct search method to detect galactic halo dark matter axions and ALPs. Sikivie proposed the first method for searching for dark matter (DM) axions (Sikivie, 1983) by using microwave cavities. Sikivie showed that an axion propagating through a microwave cavity in the presence of a strong magnetic field could resonantly convert into a monochromatic microwave signal (e.g. a 4.13μeV axion would convert into a 1 GHz photon). The size of the microwave cavity is designed to be adjustable to search over a range of possible axion masses.

The first generation of haloscope experiments were conducted at Brookhaven National Laboratory and the University of Florida in the 1980s. Brookhaven National Lab searched the mass range $4.5 - 16.3\mu$eV and set a limit on the axion coupling $g_{a\gamma} < 10^{-6}$ GeV^{-1} (Wuensch et al., 1989). The University of Florida experiment examined a much smaller mass range $5.4 - 5.9\mu$eV and set a comparable limit on the axion coupling (Hagmann et al., 1990). The second generation of haloscope is the *Axion Dark Matter eXperiment* (ADMX). The magnet for ADMX is a NbTi superconducting magnet that is 0.5 m in diameter and 1 m long. ADMX has explored the mass range $1.9 - 3.65\mu$eV (Asztalos et al., 2010). ADMX at

High Frequencies (ADMX-HF) is currently under development as an upgrade to ADMX that will allow for a microwave cavity search for axionic dark matter up to $\sim 100\mu\text{eV}$ (Shokair et al., 2014).

3.5.3 Light Shining Through Wall Searches

A different type of axion search is one which does not rely on astrophysical or cosmological sources of axions or ALPs. These searches are purely laboratory based. These experiments rely on the principle of photon regeneration. A polarized laser beam that propagates through a transverse magnetic field is blocked by some optical barrier, or wall. There is some probability of detecting photons on the other side of the barrier. This is possible if the photons have a probability, given by 3.20, to convert to weakly-interacting axions or ALPs that will pass through the optical barrier nearly unimpeded to the other side. If there is a second transverse magnetic field on the far side, these axions or ALPs can then reconvert to photons the same wavelength as those produced by the laser and can be detected. Such experiments are referred to as *light shining through walls* (LSW) experiments.

One such LSW experiment is the *Any-Light-Particle-Search* (ALPS) located at the DESY site. ALPS uses a superconducting HERA dipole magnet with $B = 5$ T over a length of 8.8. The light source for ALPS is a 35 W, 1064 nm laser. In 2010 the ALPS experiment reported constraints on the axion/ALP coupling $g_{a\gamma} \lesssim 7 \times 10^{-8}$ GeV^{-1} (Ehret et al., 2010). An upgrade to the experiment, ALPS-II, is currently under production. ALPS-II, amongst other upgrades, will include twenty straightened HERA dipole magnets with $B = 5.3$ T over a length of 100 m. With the upgrade ALPS-II is expected to probe the regime $g_{a\gamma} \sim 10^{-11}$ GeV^{-1} for a range of masses (Bähre et al., 2013).

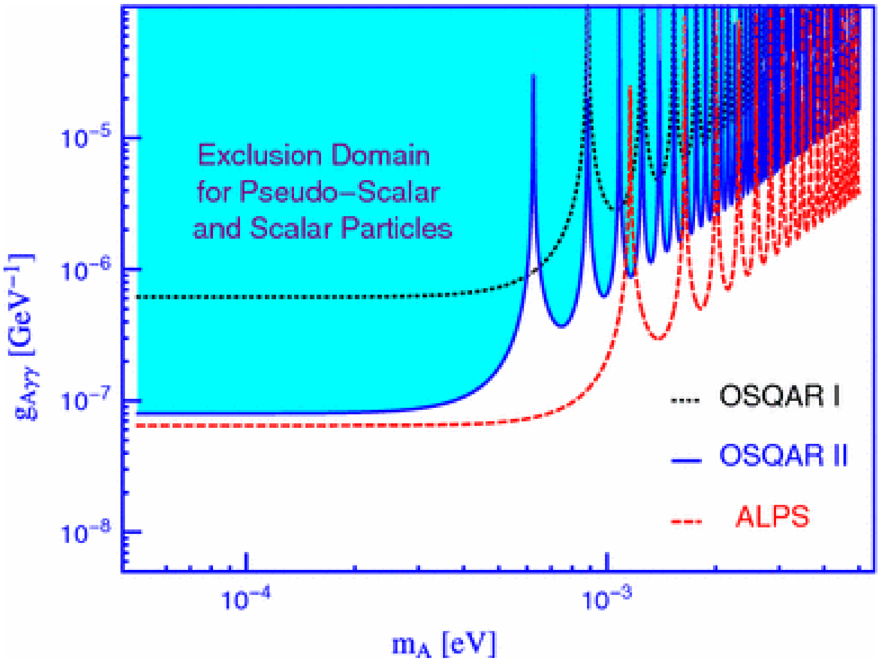

Figure 3.4: Exclusion limits on the axion/ALP coupling constant and mass from the first two OSQAR data runs. The exclusion limits from ALPS is shown for comparison in red. Figure taken from Pugnat et al. (2014).

Another such LSW experiment is located at CERN, the *Optical Search for QED vacuum birefringence, Axions and photon Regeneration* (OSQAR) experiment. OSQAR uses two LDC dipole magnets producing a transverse magnetic field $B = 9$ T over a distance of 14.3 m. The OSQAR light source is a multi-line mode ~ 3.3 W laser with (on average) 2/3 power at 514 nm and 1/3 power at 488 nm. In the second data run of the experiment, OSQAR was able to place a limit on the axion/ALP coupling $g_{a\gamma} \lesssim 8 \times 10^{-8}$ GeV^{-1} (Pugnat et al., 2014). A summary of the constraints in $g_{a\gamma}, m_a$ parameter space from OSQAR and ALPS is shown in Fig. 3.4

3.5.4 AGN/Blazar Searches

Another avenue for searching for evidence of ALPs makes use of observations of very high energy (VHE; $E > 100$ GeV) gamma rays emitted by active galactic nuclei (AGN).

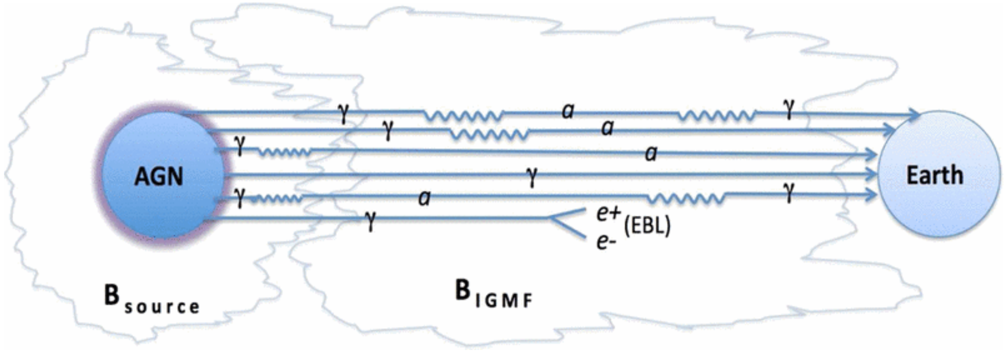

Figure 3.5: Illustration of ALP oscillation scenarios near the source and in the intergalactic magnetic field. Figure taken from Sánchez-Conde et al. (2009).

The gamma-ray emission from these cosmological sources is understood to be attenuated in an energy-dependent fashion by the extra-galactic background light (EBL) (Stecker et al., 1992). Gamma rays are absorbed via pair-production $\gamma\gamma \rightarrow e^{+}e^{-}$. Observations of many AGNs by imaging atmospheric Cherenkov telescopes (IACTs) such as HESS, MAGIC and VERITAS at high redshifts and in the VHE range seem to indicate that the universe is more transparent to VHE gamma rays than predicted by EBL models.

One possible explanation for this apparent transparency is that the oscillations of photons into ALPs in the extragalactic magnetic fields could allow for the avoidance of the EBL attenuation of the AGN spectra (de Angelis et al., 2007). The effect of these oscillations is more pronounced with magnetic fields at the nanoGauss (nG) scale, which is within present constraints but not observationally proven and oerhaos irders of magnitude larger than the values indicated by recent observations of pair halos (see e.g. Chen et al. (2015) and references therein). Another possibility proposed is that the ALP-photon oscillations occur within magnetic fields of the AGNs producing a substantial ALP-flux and then some fraction of the ALPs reconvert to gamma rays in the galactic magnetic field of the Milky Way and are observed by IACTs (Simet et al., 2008). Fig. 3.5 illustrates the different possible oscillation scenarios.

All of the previously described scenarios require ALP interaction with an external magnetic field via the Primakoff effect for oscillation to occur. The probability of ALP-photon oscillations in an external magnetic field is (Raffelt and Stodolsky, 1988):

$$P_0 = \sin^2 2\vartheta \sin^2 \left[\frac{Bdg_{a\gamma}}{2} \sqrt{1 + \left(\frac{E_{\text{crit}}}{E_\gamma} \right)^2} \right] \tag{3.21}$$

where d is the distance traveled, B is the magnetic field component along the polarization vector of the photon, θ is a mixing angle and E_{crit} is the critical energy, measured in GeV, above which mixing occurs. The mixing angle and critical energy are defined:

$$\sin^2 2\vartheta = \frac{1}{1 + \left(E_{\text{crit}}/E_\gamma \right)^2} \tag{3.22}$$

$$E_{\text{crit}} = \frac{5}{2} \frac{m_{\mu eV}^2}{g_{11} B_G} \tag{3.23}$$

where the subindices indicate the following dimensionless quantities: $m_{\mu eV} = m/\mu\text{eV}$, $g_{11} = g_{a\gamma}/10^{-11}\ \text{GeV}^{-1}$, and $B_G = B/\text{Gauss}$. The effective ALP mass is $m^2 \equiv |m_a^2 - \omega_{pl}^2|$ and the plasma frequency is $\omega_{pl} = \sqrt{4\pi\alpha n_e/m_e} = 0.37 \times 10^{-4} \mu\text{eV} \sqrt{n_e/\text{cm}^{-3}}$.

For intergalactic propagation of gamma rays, many coherent magnetic field domains will be traversed over a large distance, r. For a sufficiently large number of traversed domains the probability of oscillation becomes (Mirizzi et al., 2008):

$$P_{\gamma \to a} = \frac{1}{3} \left[1 - \exp\left(-\frac{3P_0 N}{2} \right) \right] \tag{3.24}$$

where P_0 is given by Equation 3.21 and N is the number of coherent domains.

The attenuation of gamma rays from AGNS via interaction with the EBL corresponds to an optical depth $\tau(E, z)$ such that $F = F_s e^{-\tau}$ where F_s is the photon flux at the source.

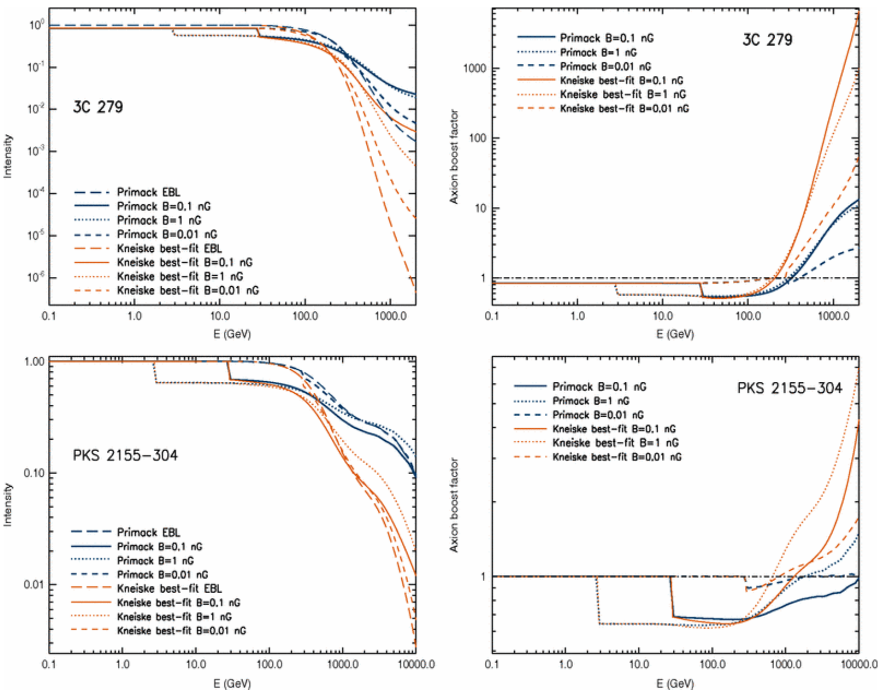

Figure 3.6: Left: Effect of ALP-photon oscillations inside source and in IGMF on the spectrum of 3C 279 and PKS 2155-304 for two EBL models: Kneiske (dashed line) and Primack (solid line). Expected photon flux without ALP mixing is shown for comparison (dotted line for Kneiske model and dot-dashed line for Primack model). Right: Boost in intensity of photon flux due to ALP mixing. Figure taken from Sánchez-Conde et al. (2009).

ALP-photon oscillations could lead to an alteration of this optical depth, as previously described, leading to a revised equation for the spectrum $F = F_S e^{-\tau}\phi_{ALP}$ where $\phi_{ALP} = e^{\pm\Delta\tau}$. The plus sign indicates an enchanced observed photon flux, since the optical depth is increased. The negative sign indicates an enhanced attenuation if more photons are lost via ALP mixing than predicted by the EBL model alone.

One study conducted by Sánchez-Conde et al. (2009) looked at modeled spectra of two AGNs, 3C 279 and PKS 2155-304. This study found extra attenuation of gamma rays in the energy range $200 - 300$ GeV, regardless of ALP or IGMF parameters. At ≥ 300 GeV energies an enhancement of the photon flux due to ALP oscillations is found. These findings are summarized in Fig. 3.6

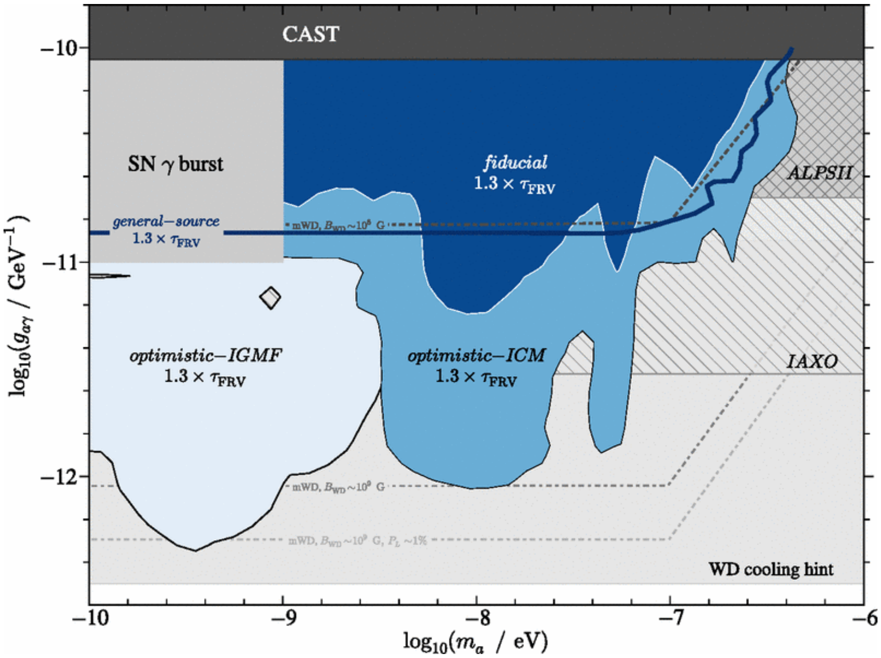

Figure 3.7: ALP parameter space with lower limits on the axion-photon coupling constant found by studying 15 AGNs with various ground-based gamma-ray telescopes. Several magnetic field scenarios are considered. Limits from each scenario are in different shades of blue. Only the FRV EBL model results are shown. Figure taken from Meyer et al. (2013).

In 2013, the first lower limits were placed on the axion/ALP coupling constant using AGN observations from several ground-based gamma-ray telescopes (Meyer et al., 2013). The study examined the very high energy spectra of 15 AGNs using data from HEGRA, H.E.S.S., CAT, MAGIC, VERITAS and Whipple. Several magnetic field scenarios were considered at the source, in the IGMF and in the Milky Way. The parameter space excluded for the various magnetic field scenarios can be seen in Fig. 3.7.

A more recent study (Ajello et al., 2016) used 6 years of observations of NGC 1275 from the *Fermi Large Area Telescope* (*Fermi-LAT*) to constrain ALP parameters. Given current constraints on the ALP-photon coupling and the relatively short distance to NGC 1275 (0.017559) no strong irregularities were expected. This source was investigated due to the bright gamma-ray flux and the presence of a relatively high magnetic field in the Perseus cluster where NGC 1275 is located. No irregularities due to ALP-mixing were detected and

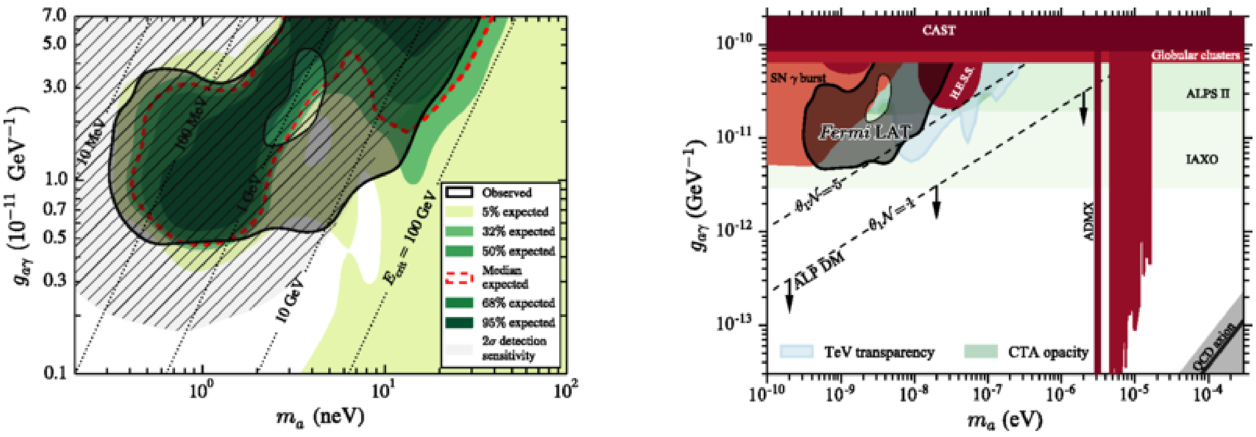

Figure 3.8: Left: Observed and expected 95% confidence limits on ALP mass and coupling derived from 6 years of *Fermi*-LAT observations of NGC 1275. Expected limits are from 400 Monte Carlo simulations. Right: Comparison of constraints from *Fermi*-LAT to other constraints from other works. Figure taken from Ajello et al. (2016).

ALP-photon couplings were ruled out between $0.5 < g_{11} < 3$ for ALP masses $0.5 < m_{neV} < 5$ and $g_{11} > 1$ for $5 < m_{neV} < 10$ as can be seen in Fig. 3.8.

3.5.5 Constraints from Neutron Stars

Neutron stars are another astrophysical laboratory that has been used to investigate the expansive parameter space of axions and ALPs. In 1984 Naoki Iwamoto considered the possibility of axion emission from neutron stars (Iwamoto, 1984). The emission of axions from neutron stars would provide another cooling mechanism and for some ranges of axion parameters, would be the dominant cooling mechanism allowing for constraints to be placed on axion parameter space from observations of the surface temperature of neutron stars. The two main processes considered were nucleon-nucleon axion bremsstrahlung

$$N + N \rightarrow N + N + a$$

and electron-nucleon axion bremsstrahlung

$$e + N \to e + N + a.$$

The case of a nonsuperfluid and a superfluid core for the neutron star were each considered. For the nonsuperfluid case, nucleon-nucleon axion bremsstrahlung was the most important process. For the superfluid core scenario electron-nucleon axion bremsstrahlung was found to dominate. After comparing the axion luminosity with the neutrino luminosity and the surface photon luminosity Iwamoto showed the time for cooling of a neutron star will be significantly shorten unless $m_a \lesssim 4 \times 10^{-2}$ eV.

In 1986 Donald Morris expanded on the work of Iwamoto and examined the interaction of the thermally emitted axions with the magnetic field in the pulsar magnetosphere via the Primakoff effect. Morris showed that thermal axions would be produced with energies to convert to x-ray photons in pulsar magnetospheres. Morris found that for axion parameters that allow efficient conversion in the magnetosphere, the observed x-ray flux would be enhanced. At the time the study was conducted the observational limits on the x-ray flux of the two pulsars considered, Vela and the Crab, were not sufficient to place constraints on the axion mass or coupling constant (Morris, 1986).

A more recent study published in 2016 examined 5 years of gamma-ray data from the *Fermi*-LAT on 4 neutron stars (Berenji et al., 2016). This study follows a similar methodology to the work of Iwamoto and Morris by considering the nucleon-nucleon axion bremsstrahlung in the neutron star core as the emission mechanism for axions. Then the conversion of the thermal axions to photons via the Primakoff process is considered. For the parameters used in the study the converted photons are expected to lie in the energy range observable by the *Fermi*-LAT. The excluded parameter space is shown in Fig. 3.9

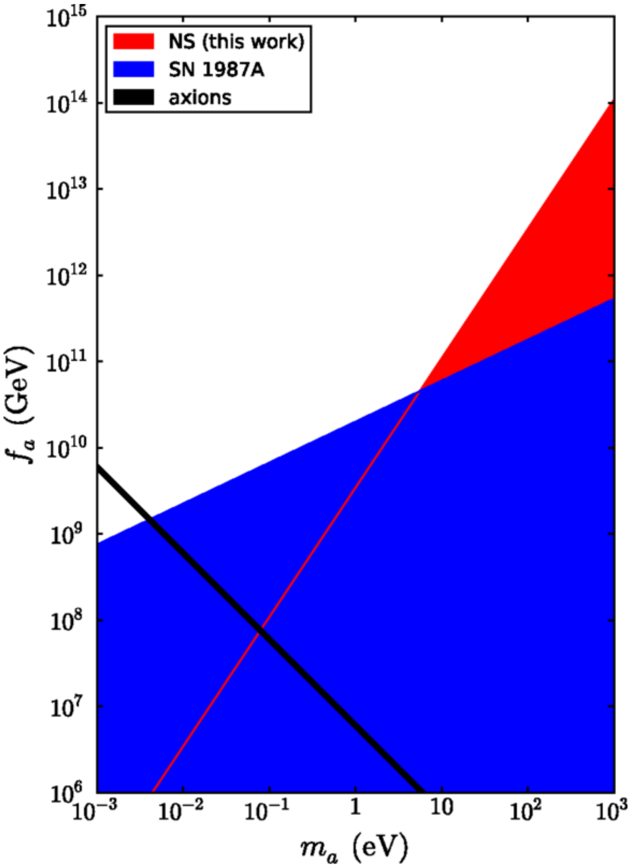

Figure 3.9: Excluded regions of ALP parameter space (m_a, f_a) from a study of 5 years of *Fermi*-LAT data for 4 neutron stars (labeled NS). Excluded parameter space from studies of SN 1987A are labeled SN 1987A. Allowed parameters for the classical Peccei-Quinn axion are shown with a black line. Figure taken from (Berenji et al., 2016).

Chapter 4

VERITAS Instrument and Analysis Techniques

The **V**ery **E**nergetic **R**adiation **I**maging **T**elescope **A**rray **S**ystem, VERITAS, is a high-energy gamma-ray observatory of an array of imaging atmospheric Cerenkov telescopes (IACT). The VERITAS array is located in southern Arizona, near Tucson (see Fig 4.1). The following chapter will discuss the VERITAS instrument, the standard analysis methods, and the periodic analysis methods used for pulsar observations.

4.1 Imaging Atmospheric Cherenkov Technique

Earth's atmosphere is completely opaque to very high energy (VHE; $E > 100$ GeV) gamma rays. However, in this energy range the interactions initiated by gamma rays in the Earth's atmosphere allow detection at the ground, via the imaging atmospheric Cherenkov technique proposed by Weekes and Turver (Weekes and Turver, 1977). When a gamma ray or charged cosmic-ray enters the atmosphere it will induce an extensive air shower. Fig. 4.2 depicts the electromagnetic cascade induced by a gamma ray.

Figure 4.1: The VERITAS array located at the Fred Lawrence Whipple Observatory near Tucson, AZ

The electromagnetic cascade induced by a gamma-ray photon begins with the production of on electron-positiron pair by the photon's interaction with the Coulomb field of nearby atmospheric particles. The produced pair of charged particles radiate gamma rays via bremsstrahlung as they are slowed by the Coulomb field of atmospheric particles. These secondary gamma rays further pair produce leading to an avalanche of particles and gamma rays. This cascade grows exponentially and is eventually halted when the electrons rapidly lose their energy by ionization loss (climbing up the Bethe-Bloch dE/dx curve) and the photons produced via bremsstrahlung no longer have the requisite energy for pair production. All along the cascade the electrons and positrons (often moving faster than the speed of light for the local medium) radiate Cherenkov light. The resultant flash of Cherenkov emission lasts 10 ns and is spread over an area of $\sim$ 130 m in radius.

The hadronic cascade induced by a charged cosmic ray, typically a proton, is distinguishable from the electromagnetic cascades. A hadronic cascade results in the production of many secondary particles: pions ($\pi^{\pm}, \pi^{0}$), neutrinos, muons, electrons and positrons. The inelastic scattering of the secondary particles and the overlap of many induced electromagnetic cascades result in an image from the Cherenkov radiation that is broader and irregularly shaped in comparison to the image produced by the gamma ray-induced electromagnetic

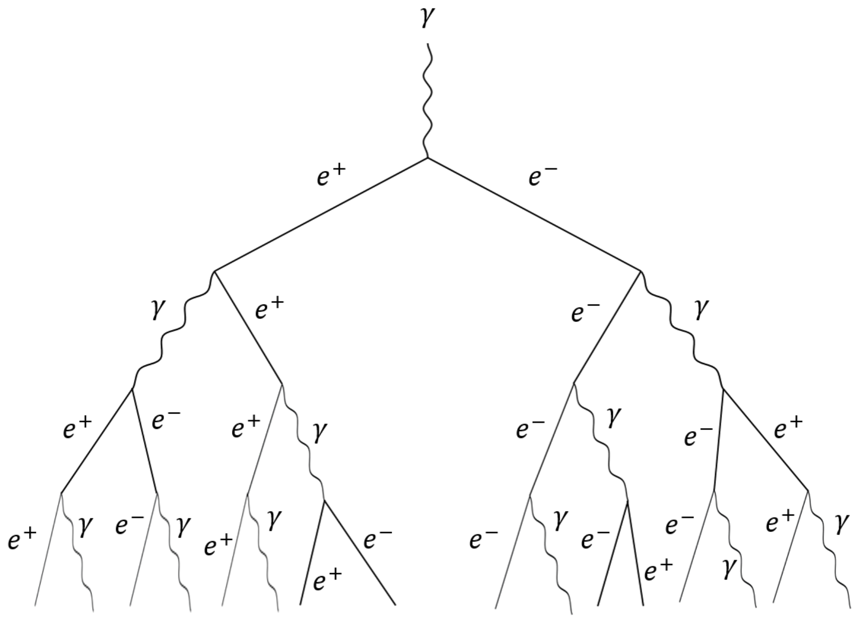

Figure 4.2: Model of electromagnetic cascade induced by VHE gamma ray interaction in the Earth's atmosphere

cascades. Hadronic showers are isotropically distributed in the sky and outnumber the gamma ray-induced electromagnetic cascades. The differences seen in the Cherenkov image provide a pathway to separate the hadronic background from gamma ray events. For a full description and details of extensive air showers see Longair (2011) and (Völk and Bernlöhr, 2009)

The technique used by IACTs is to employ large optical reflectors to focus the Cherenkov emission from air showers onto a pixelated camera comprised of many photomultiplier tubes (PMTs). The fast response time of the PMTs and electronics in the telescopes allow the faint Cherenkov images to be observed against the night-sky background. The telescopes can form images of the air showers from the collected Cherenkov emission. The Cherenkov signal produces a two-dimensional projection of the air shower in the shape of an ellipse. The orientation of the ellipse is used to determine the arrival direction of the air shower. The intensity of the Cherenkov signal is used to determine the energy of the initial particle or gamma ray. Other geometric properties of the image, known as the *Hillas* parameters

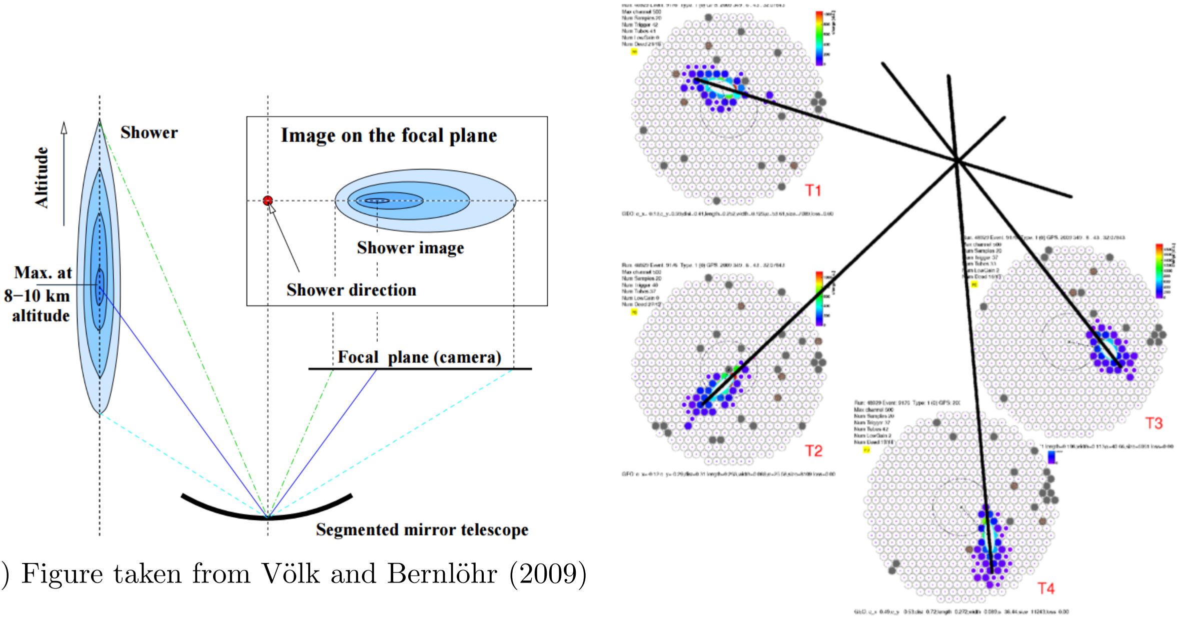

(a) Figure taken from Völk and Bernlöhr (2009)

(b)

Figure 4.3: Figures showing the shower geometry as an image in an IACT. (a) depicts how a shower forms a projection in the IACT camera. (b) is a schematic of a gamma ray shower imaged by 4 VERITAS telescopes and the geometry of the images is used to reconstruct the shower direction.

(see Section 4.2.1 for details), are used to separate hadronic signals from electromagnetic signals (Hillas, 1985). Modern IACTs use an array of telescopes to stereoscopically image air showers. Stereoscopic imaging provides better reconstruction of extensive air showers. In comparison to a single telescope, arrays allow for improved angular resolution, energy resolution, background rejection and increased sensitivity. Telescope arrays also allow for large effective areas providing an advantage over size-limited space-based observatories.

The VERITAS array consists of four identical 12-meter diameter Davies-Cotton design telescopes arranged in a quadrilateral footprint. Each telescope's optical reflectors consist of 350 hexagonal glass mirrors, each with area of 0.32 m^2, for a total area of 110 m^2 for each reflector. The mirrors direct light into a pixelated camera comprised of 499 UV-sensitive photomultiplier tubes with a total field of view of 3.5°. Further details of the VERITAS camera system can be found in Holder et al. (2006) and D. B. Kieda for the

VERITAS Collaboration (2013). Signals from the camera are sent to telescope trigger and data acquisition electronics systems which are discussed in detail in Buckley (1999), Holder et al. (2008), and Staszak et al. (2015). VERITAS has a collection area of approximately 10^5 m^2 (Krawczynski et al., 2006). VERITAS is sensitive in the energy range of 85 GeV to > 30 TeV, with an energy resolution of $15\% - 25\%$ at 1 TeV and a typical angular resolution of $< 0.1°$. For further information about VERITAS specifications refer to Holder et al. (2008).

4.2 Analysis Technique

4.2.1 Summary of Standard Data Analysis Methods

Data from the VERITAS telescopes consists of digitized PMT signal traces (from 500 MHz FADCs) and ancillary information such as GPS timestamps. The data is processed through an analysis pipeline which, among other things, separates gamma-ray signals from noise in the waveforms from Poisson fluctuations in the night-sky background, derives parameters for the air showers, determines strength and significance of the gamma-ray signal over the remaining cosmic-ray background and calculates the spectrum of the remaining gamma-ray excess. There are two standard analysis packages used for VERITAS data analysis: *EventDisplay* (Daniel, 2008) and the **VE**RITAS **G**amma Ray **A**nalysis **S**uite, *VEGAS* (Cogan, 2008). Both analysis suites are C++ object-based codes using the *ROOT* (Brun and Rademakers, 1997) data structures and libraries. Both employ similar methods of image cleaning (identifying true signals against the night-sky background), image parameterization and stereoscopic reconstruction, with some minor differences in the implementation (Daniel, 2008). The VERITAS data analysis presented in this work uses the *VEGAS* package. The standard analysis of VERITAS data proceeds as follows:

- calibration of pixel data and image cleaning,
- image parameterization and shower reconstruction,
- stereoscopic reconstruction,
- background rejection via gamma-hadron separation,
- significance calculation and reconstruction of spectrum.

In the first step of the analysis procedure, calibration parameters are calculated. The pedestal, pedestal variation and relative gains are calculated. LED flasher runs are used to calculate the relative gains between pixels and to calculate timing offsets in the different channels (more details on the flasher system and calibration methods can be found in Hanna et al. (2010)). Image cleaning is performed by selecting so-called picture pixels with signal pulse-height above a threshold. The threshold is typically given as the sum of the pedestal and 5 times the standard deviation of the pedestal variations. Pixels adjacent to these high threshold picture pixels that also are above a different threshold (2.5 times their pedestal standard deviation) are selected and designated "boundary" pixels. Pixels meeting these thresholds (both picture and boundary) are assigned to the image, while isolated pixels and pixels not meeting the criteria have their charge set to 0. The image produced is then parameterized with a moment analysis. The following parameters are most important for data analysis:

- *Size:* number of digital counts in the image providing a rough estimator of the shower energy,
- *Length:* determined from the second moments of the image this is the approximate length of the major axis of image ellipse,

- *Width:* determined from the second moments of the image this is the approximate length of the minor axis of image ellipse. and
- *Distance:* the angular separation from the image centroid to the center of field of view

Loose cuts on parameters such as *size* and *distance* are used as the first stage of analysis and constitute a set of cuts that form the standard "image quality" selection criteria. If quality criteria are met for a requisite number of images for an event then stereoscopic reconstruction is performed for the event. Image information is compared to lookup tables of parameters for simulated gamma ray showers. From these lookup tables the shower direction, the shower core impact location and energy of the air shower can be determined.

With the shower reconstructed, gamma-ray showers are separated from cosmic-ray showers. The standard method for gamma-hadron separation is to calculate geometric mean scaled parameters and make cuts based on these parameters. A mean scaled parameter (MSP) is given for some parameter, P, by:

$$MSP = \frac{1}{N_{\text{tel}}} \sum_{i=1}^{N_{\text{tel}}} \frac{P_i}{P_{\text{sim}}\left(\theta, Size, r\right)} \tag{4.1}$$

where N_{tel} is the number of telescope images, P_{sim} is the expected value of P found from a lookup table, θ is the zenith angle and r is the impact distance. More details of gamma-hadron separation methods can be found in Krawczynski et al. (2006).

Since analysis cuts still leave a substantial background of misidentified (gamma-like) cosmic-ray events this background must be measured and subtracted to find the excess number of gamma-ray like events from a particular direction in the sky. Thus VERITAS observations are typically conducting using the *wobble* mode where the observed source is kept in the field of view for the duration of observation but the telescope pointing is offset from the source position by a set amount (0.5° for VERITAS). The direction of the offset is alternated between the four cardinal directions (N, S, E, W) to reduce systematic errors. For this work the background model employed is the *ring-background method.* A second model commonly used is the *reflected-regions method.* For the ring-background method a model ring around a trial source position is used to provide a background estimate. Further details on the VERITAS background estimation methods can be found in Berge et al. (2007).

A gamma-ray signal is extracted from the data by calculating the number of excess gamma-ray events, $N_{\text{ex}} = N_{\text{on}} - \alpha N_{\text{off}}$. N_{on} is the number of counts within the defined ON source region, N_{off} is the number of counts within the defined OFF region as specified by the background model, and α is a relative normalization factor (details can be found in Berge et al. (2007)). Having a number of excess counts does not necessarily imply an actual signal from a gamma ray source. The significance of a detection is typically calculated using the method of Li & Ma (Li and Ma, 1983) where the significance S is defined as:

$$S = \sqrt{2}\left(N_{\text{on}} \ln\left[\frac{1+\alpha}{\alpha}\left(\frac{N_{\text{on}}}{N_{\text{on}}+N_{\text{off}}}\right)\right] + N_{\text{off}} \ln\left[(1+\alpha)\left(\frac{N_{\text{off}}}{N_{\text{on}}+N_{\text{off}}}\right)\right]\right)^{1/2} \tag{4.2}$$

A significance of $S = 5$ or 5σ is required to be considered a detection of a source by VERITAS. A variety of statistical methods are employed in different analyses, but the Li & Ma method is widely used and can be expressed in a relatively simple, closed-form as shown in Eq. 4.2.

4.2.2 Spectral Reconstruction

For a significant excess of gamma-ray events from a source the energy spectrum of that source can be reconstructed. For the spectral energy reconstruction it is first necessary to calculate the effective area of the telescope. The effective area A_{eff} is, in part, calculated from lookup tables of simulated gamma-ray showers created by Monte-Carlo methods using a procedure described in Kertzman and Sembroski (1994). The optical photons resulting from the simulated showers are then propagated through a detector model of the telescope array (Maier, 2008). A complication arises since effective areas are derived using true energies from the Monte Carlo simulations while only reconstructed energies are available for observational data. A given photon event may migrate from its true energy bin i to a different energy bin j for its reconstructed energy. To account for this a modified effective area is created by essentially smearing the distribution of events in each energy bin. A spectral function is defined (most sources are adequately described by a power law) and the simulations are re-weighted according to the defined spectral function. A migration matrix M_{ij} is defined to keep track of number of events migrating from some energy bin i into an energy bin j. The distribution of events from simulations is then adjusted using the known fraction of mis-reconstructed events in each energy bin from the migration matrix. The spectral energy distribution (SED) is defined as the number of events per unit area per unit time per unit energy:

$$\frac{dN}{dE}(E) = \frac{N_{\text{excess}}(E)}{A_{\text{eff}}(E)T_{\text{obs}}dE} \tag{4.3}$$

where T_{obs} is the dead-time corrected observation time and dE is the size of the reconstructed energy bins. Data analysis typically encompasses some number of data runs, n, and many different effective areas are needed. In such cases the previous equation becomes a summation with weighting factors of the time and area:

$$\frac{dN}{dE}(E) = \frac{\sum_{i=0}^{n} N^{i}_{\text{excess}}(E)}{\sum_{i=0}^{n} A^{i}_{\text{eff}}(E)T^{i}_{\text{obs}}dE}. \tag{4.4}$$

4.2.3 Periodic Analysis

In addition to the standard analysis procedures of looking for a significant gamma-ray signal and producing a SED for a given source, other features of a source may also be probed. In the case of pulsars, the focus is on the detection of the periodic signal from the pulsed emission. The following sections describe the steps in searching for periodic emission from a source.

Barycentering

The first step in searching for pulsed emission is applying a timing correction to account for the movement of Earth though the solar system. This process is known as *barycentering*. The time of arrival (TOA) of a photon at the VERITAS observatory is corrected to the nearly inertial solar system center of mass, also known as the solar system barycenter (SSB).

The process begins by calculating the Barycentric Dynamical Time (TDB) which is a linear scaling of Barycentric Coordinate Time (TCB) which is equivalent to the proper time experienced by an inertial clock in the a coordinate system co-moving with the SSB. TDB is defined as:

$$TDB = UTC + LS + 32.184 + 0.001658 \sin M + 0.000014 \sin(2M) \quad \text{(seconds)} \tag{4.5}$$

The quantities in the above equation are defined as follows:

- UTC: Coordinated Universal Time, the time standard used to tag the TOA of photons at VERITAS by GPS clocks.
- LS: Leap Seconds, one second corrections applied to UTC at irregular intervals to compensate for the slowing of Earth's rotation. The scheduling of leap seconds is handled by the International Earth Rotation and Reference Systems Service[3].

---

[3] LS update announcements are made every six months an published in IERS "Bulletin C" found at this website https://hpiers.obspm.fr/iers/bul/bulc/bulletinc.dat

- M: Earth's Orbit's Mean Anomaly, the ratio of the time since the last periapsis of Earth's orbit to the duration of the orbital period, times a factor of 2π.

  $$M = 6.24008 + 0.01720197\,(JD - 2451545) \quad \text{(radians)} \tag{4.6}$$

  where JD is the UTC expressed as the number of elapsed days since noon in Greenwich, London, January, 4713 BC.

After converting to TDB a time of flight correction must be applied to convert the photon TOA at Earth to the TOA at the SSB. First a correction is added for the time of flight from Earth's barycenter to the SSB and then an additional, smaller, correction for the time of flight from the observatory to Earth's barycenter. To make the conversion, the path length difference d of two photons (one arriving at the SSB from the pulsar and one arriving at Earth's barycenter) must be calculated: $\Delta t_{EC-SSB} = d/c$. The DE200 Planetary and Lunar Ephemeris from Jet Propulsion Laboratory[4] (Standish, 1982) is used to determine up Earth's position. The second correction, Δt_{Ob-EC} takes a similar form.

The previously described corrections are performed using the TEMPO2 package[5] (Edwards et al., 2006; Hobbs et al., 2006) implemented within VEGAS. These packages are used in the final stage of the VEGAS analysis pipeline. The final expression for the barycentered TOA, t_{bary} is:

$$\begin{aligned} t_{\text{bary}} = UTC + LS + 32.184 + 0.001658 \sin M \\ + 0.000014 \sin(2M) + \Delta t_{EC-SSB} + \Delta t_{Ob-EC} \quad \text{(seconds)} \end{aligned} \tag{4.7}$$

---

[4] ftp://ssd.jpl.nasa.gov/pub/eph/planets/ascii

[5] http://www.atnf.csiro.au/research/pulsar/tempo2/

Phase-folding

The next step in the pulsed analysis is phase-folding. Individual pulses from pulsars, especially in the VHE regime, do not have a sufficiently strong signal so observed pulses are folded, or averaged, by calculating the pulsar's phase for each observed photon allowing a light curve to be constructed from the data of many pulses. For a given pulsar the instantaneous pulse frequency is $f = 1/P$ and the instantaneous pulse phase, ϕ is defined by $d\phi/dt = f$. The pulse phase is measured in turns of 2π radians meaning $0 < \phi < 1$. In the SSB frame, the pulsar's rotational period is nearly constant so the phase, $\phi(t)$, can be represented as a Taylor expansion:

$$\phi(t) = \phi_0 + \left[f\left(t - t_0\right) + \frac{1}{2}\dot{f}\left(t - t_0\right)^2 + ... \right] \mathrm{mod} 1 \tag{4.8}$$

where ϕ_0 is some arbitrary phase offset, t_0 is some arbitrary reference epoch, and t is the arrival time of the photon. For known pulsar timing solutions (often determined by radio observations and referred to as the pulsar ephemerides) are often used to lookup the measurement for f and $\dot{f}$. These ephemerides have a limited period of validity determined by the accuracy of the timing solution and the stability of the pulsar's motion. For the analysis presented in this work on the Crab pulsar, timing solutions from the Jodrell Bank Observatory[6] (Lyne et al., 1993) were used in the phase-folding of data.

Statistical Analysis

Once the photon arrival times have been converted to phase values, the distribution of phase values can be tested for evidence of pulsed emission. For a steady-state source, the phase values will be evenly distributed. For a source with periodic emission, such as a

---

[6] http://www.jb.man.ac.uk/pulsar/crab.html

pulsar, the level of detected emission should increase during particular phases dependent on the exact source being examined. While several statistical tests exist to probe the existence of periodicity in a signal, this work uses two tests: an unbinned signal region test and the H-test (de Jager et al., 1989).

The unbinned signal region test relies on prior knowledge of the pulse emission phase regions within the light curve. For a known pulsar, signal and background regions can be defined. For a number of signal events, N_{on}, and a number of background events, N_{off}, the significance of an excess signal can be calculated using the Li & Ma formula from Section 4.2.1. This test for periodicity is limited to testing phase regions of known pulsed emission. The significance of any excess signal outside of the defined signal regions will not be tested using this method.

The second method, the H-test employed is best suited for weak signals and requires no prior knowledge of the pulse shape or location. The H-test is based upon a common test for periodicity, the Z_m^2-test (Buccheri et al., 1983). The Z_m^2-test involves the sum of the Fourier powers of the first m harmonics. This test, as with other tests, is limited to certain kinds of periodic shapes. The H-test was developed to be a more powerful test for a range of pulse shapes. The H-test is defined as:

$$H \equiv \max_{0\rightarrow 20}\left(Z_m^2 - 4m + 4\right) \tag{4.9}$$

where

$$Z_m^2 = \frac{2}{N}\sum_{k=1}^{m}\left[\sum_{j=1}^{N}\left(\cos k\phi_j\right)^2 + \left(\sum_{j=1}^{N}\sin k\phi_j\right)^2\right] \tag{4.10}$$

The probability of finding an H-test value H above some value h is given by (de Jager et al., 1989):

$$P\left(H > h\right) \simeq \left(1 + 0.45h\right)\exp\left(-0.398h\right) \tag{4.11}$$

The standard VERITAS analysis using the VEGAS analysis suite described in this chapter has been used to further examine the one known VHE emitting pulsar, the Crab pulsar. The specific details of the analysis of the Crab pulsar will be described in the following chapter.

Chapter 5

VERITAS Analysis of Crab Pulsar Up to TeV Energies

5.1 VERITAS Data on the Crab

In 2011 VERITAS published the first detection of a pulsar, the Crab pulsar, in the very high energy regime (VHE; $E > 100$ GeV) (VERITAS Collaboration et al., 2011). The detection came as a result of the analysis of 107 hours of observations on the Crab pulsar acquired between September 2007 and March 2011. Since 2011 the Crab Nebula has been a regular target of observation by VERITAS and the dataset from the 2011 publication has been expanded to ∼150 hours of quality-selected data as of June 2014. The analysis of the full ∼150 hour data set is presented in this chapter.

5.2 MAGIC Observations

The newest analysis of the Crab pulsar has been motivated in part by recent observations of the Crab from the MAGIC collaboration. MAGIC announced new results from its

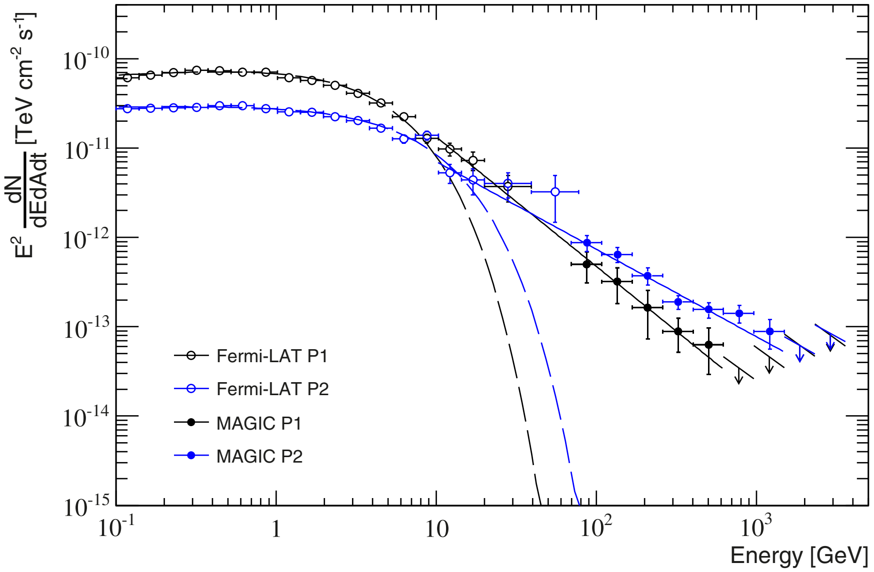

Figure 5.1: Phase-folded spectral energy distribution of the Crab pulsar for peaks P1 and P2 from MAGIC (closed circles) and *Fermi*-LAT (open circles). Dashed line shows power-law with exponential cut-off fit to *Fermi*-LAT data. Solid line shows fit using a broken power-law to *Fermi*-LAT and MAGIC data. Figure taken from (Ansoldi et al., 2016).

observations of the Crab at the *Fermi* Symposium in October 2014, showing evidence for pulsed emission reaching TeV energies (full details can be seen in (Ansoldi et al., 2016)). Results of the MAGIC analysis of $\sim$ 320 hours of good-quality data from February 2007 to April 2014 show pulsed emission up to 1.5 TeV (see Figure 5.1). The light curve, or phaseogram, from the MAGIC observations is shown in Fig. 5.2. The results of this study support the 2011 VERITAS observations of the Crab and provide further evidence that a broken power-law fit to the SED is preferred to a power-law with an exponential cutoff. The latter would be indicative of curvature radiation as the source of VHE emission; a spectrum consistent with a broken power-law function motivates a new explanation of VHE pulsed emission.

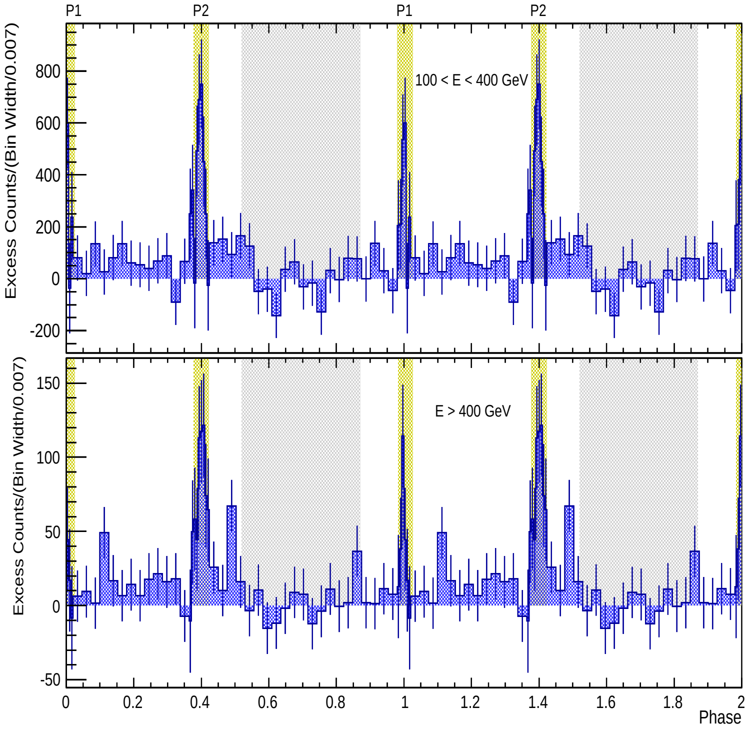

Figure 5.2: Phase-folded light curve, or phaseogram, of the Crab pulsar from MAGIC observations in the energy ranges $100 < E < 400$ GeV (top) and $E > 400$ GeV (bottom). The region used for background subtraction is shaded gray. The peak intervals are shown highlighted in yellow. Figure taken from (Ansoldi et al., 2016).

5.3 Data Selection

Since the original VERITAS results on the Crab in 2011, many more hours of observations have been collected. ~ 150 hours of observations are presented in this work. Much of the new data has been collected since a camera upgrade to the VERITAS array in 2012. This upgrade to the camera involved replacing the PMTs with higher quantum efficiency increasing the sensitivity and lowering the energy threshold of VERITAS (D. B. Kieda for the VERITAS Collaboration, 2013).

The full set of VERITAS observations of the Crab were pared down using a number of quality selection cuts based on constraints in the: number of participating telescopes, weather conditions, elevation angle of observations, and any abnormalities in trigger rates indicative of hardware problems. A minimum of four telescope participation was required for all data (i.e. any data with one or more telescopes not operational were excluded). The weather and environmental conditions are monitored at the observatory site using three far infra-red (FIR) cameras sensitive to atmospheric changes and capable of detecting overhead cloud cover. An automatic weather grading is applied based on the FIR cameras and observers manually assign a weather grade (A-D). To be used in this analysis weather must have been rated A or B during the collection of data and only good periods with no cloud cover (as indicated by the FIR cameras) are used in the analysis. For this analysis, only high elevation data (with zenith angles $< 35°$) are used to ensure a low trigger threshold. Different procedures are employed to (off-source) data while maximizing the on-source exposure. To minimize systematics or any artifacts in the time series, we only use data taken in the *wobble mode* with an offset of 0.5 degree. Diagnostic plots of data are checked to ensure no anomalies in the trigger rates during observations. A list of good data runs is given in Table A.1 in Appendix A.

Parameter	Cut Value
DistanceUpper	0/1.43
NTubesMin	0/5
SizeLower	0/200 d.c.
MSL	1.3
MSW	1.1
ShowerHeight	7 km
θ^2	$0.01^{\circ 2}$

Table 5.1: VERITAS Data Analysis Cuts

5.4 Cut Selection for Pulsed Analysis

Data quality selection cuts and event selection cuts (described in Chapter 4) are applied to the data set. The cuts used for the analysis of the Crab pulsar are given in Table 5.1. These cuts were determined by an optimization on the pulsed signal in the Crab phaseogram originally performed as part of the 2011 VERITAS analysis of the Crab. Originally an optimization strategy was employed based on analysis of the Crab Nebula spectrum due to the uncertainty in the expected pulsed emission flux at $E > 400$ GeV. The original strategy was to perform standard VERITAS analysis on the entire Crab data set using the three standard sets of VERITAS cuts for *soft, medium* and *hard* spectrum sources. The sensitivity of cuts to Crab flux levels at various energies would serve as an optimization to set cuts, *a priori*, without biasing the analysis. Ultimately, this strategy was abandoned in favor of optimization on an independent pulsed data set as the nebular flux is expected to have a different spectral shape and, in fact, is a dominant source of background signal for the pulsed signal. The analysis of the nebula is presented here in Fig 5.3 as a cross-check on the data quality with the spectra from the *soft, medium* and *hard* cuts analyses. The spectra are consistent in the separate analyses.

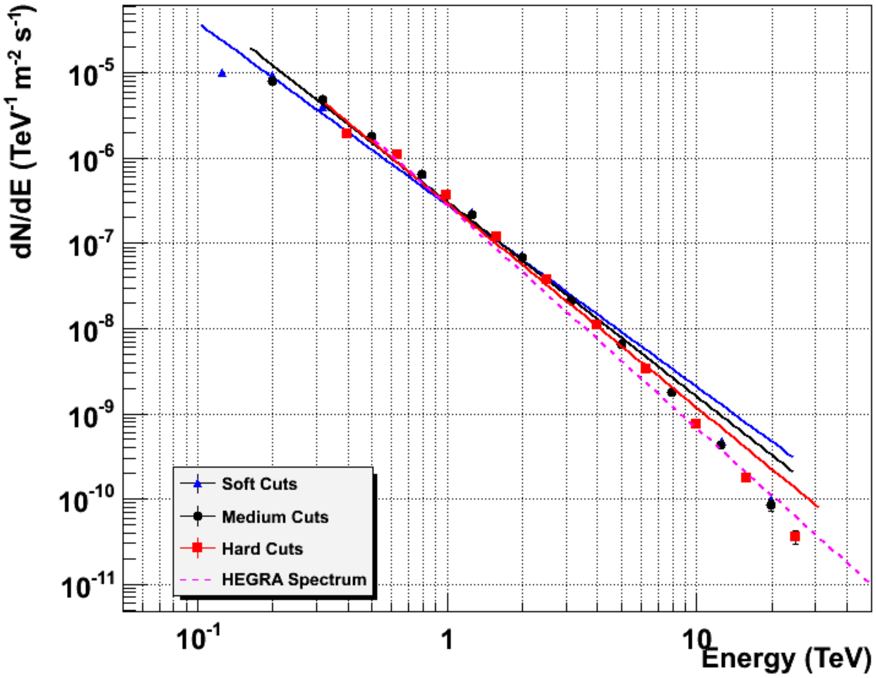

Figure 5.3: Crab Nebula differential spectrum for $100 < E < 30000$ GeV using the three standard VERITAS source cuts. *Soft*-source cuts are shown in blue. *Medium*-source cuts are shown in black. *Hard*-source cuts are shown in red. Each SED is fit using a power-law function shown as a solid line. The pink dashed line is the power-law function that was fit to HEGRA observations of the Crab Nebula and is shown for comparison (Aharonian et al., 2004).

5.5 Crab Pulsar Light Curve

After applying data quality selection and application of event selection cuts to candidate gamma-ray events, the arrival times of the remaining events are transformed to the solar system barycenter using *TEMPO2* as described in Chapter 4. The rotational phase of the Crab is then calculated for each event using the monthly ephemeris for the Crab pulsar published by the Jodrell Bank Observatory. After the phase-folding process is completed the light curve, or phaseogram, is constructed for the full range of energies. as shown in Figure 5.4.

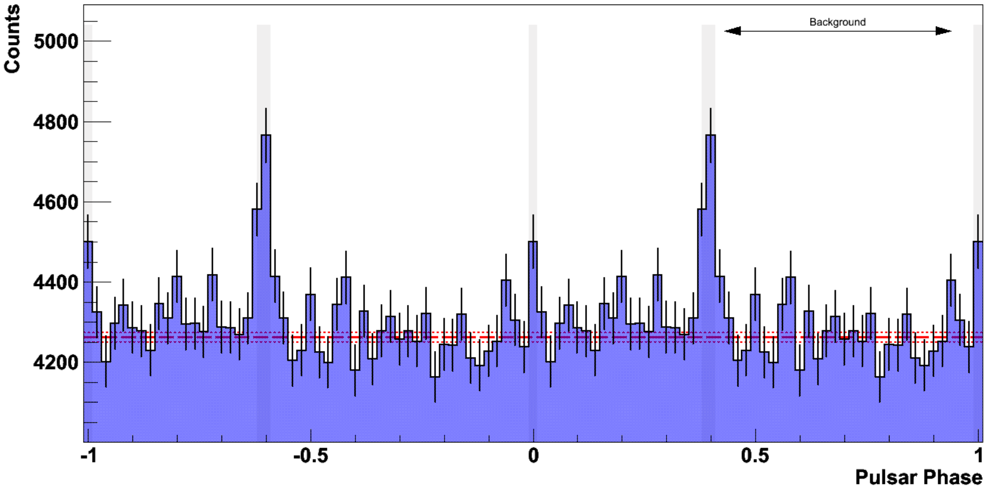

Figure 5.4: VERITAS phaseogram of the Crab pulsar plotted over two phase intervals for all energies observed. Two pulses can be seen at phases 0.0 and 0.4 and are referred to as P1 and P2, respectively. The highlighted regions are the signal regions used in the significance calculation for a pulsed signal. The signal regions were defined based on the previous 2011 VERITAS analysis of the Crab. The background region is indicated by black arrows. The red, dashed line indicates the background level estimated from the background region.

The significance of the pulsed signal is determined using the *H-Test* on the unbinned event times and the Li & Ma significance calculated from the excess number of counts of gamma-ray-like events at main pulse and interpulse, P1 and P2, centered at phase 0.0 and 0.4 in Figure 5.4, respectively. The signal region for P1 and P2, determined from the 2011 VERITAS analysis of the Crab, is defined as the phase interval -0.1 to 0.1 (P1) and 0.38 to 0.41 (P2). The signal region is highlighted in Figure 5.4. The background region, determined by the previous VERITAS analysis, is defined as the phase interval 0.43 to 0.94 and is indicated by black arrows in 5.4. The background region is used to estimate the background contamination due to cosmic rays and the steady-state flux of the Crab Nebula. An *H-Test* performed on the unbinned data gives a value of 57.3189. The probability of an *H-Test* value of 57.3189 by random chance is $1.10327e-10$. Using the phase intervals, for both P1 and P2, defined by the 2011 VERITAS analysis of the Crab, the statistical

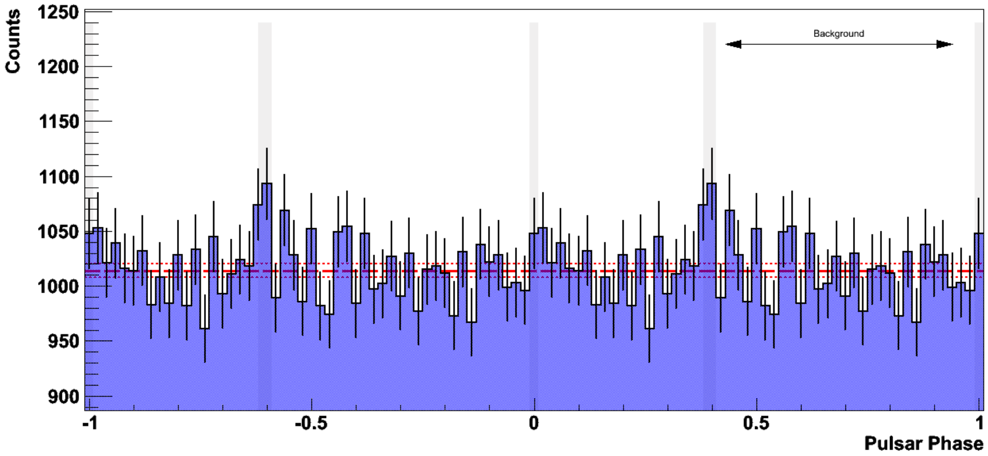

Figure 5.5: VERITAS integral phaseogram of Crab pulsar with an energy threshold of $E > 501$ GeV. Signal region (highlighted) and background region (indicated by arrows) are the same as Figure 5.4. The pulsed signal has a significance of 2.6σ as given by the Li & Ma formula.

significance of the number of excess events given by the Li & Ma formula 4.2 is 8.8σ. The growth of the significance from excess events can be seen in Figure 5.6.

Previous studies by VERITAS and MAGIC have already reported significant pulsed emission between 100 GeV and 400 GeV. This work is particularly focused on finding evidence for an extension of the pulsed emission spectrum and confirming the MAGIC collaboration's report of pulsed TeV emission. To that end, after initial analysis on the full energy range is performed, an energy cut is applied and a phaseogram is constructed from gamma-ray events with reconstructed energies $E > 500$ GeV. This phaseogram is shown in Figure 5.5. The significance of the pulsed signal at $E > 500$ GeV is calculated in the same fashion as previously described for the full energy range. The statistical significance of the number of excess events within the signal region for P1 and P2 combined, as given by the Li & Ma formula, is 2.6σ. Such a statistical significance is not sufficient to claim a VERITAS detection above 500 GeV with $\sim$150 hours of observations.

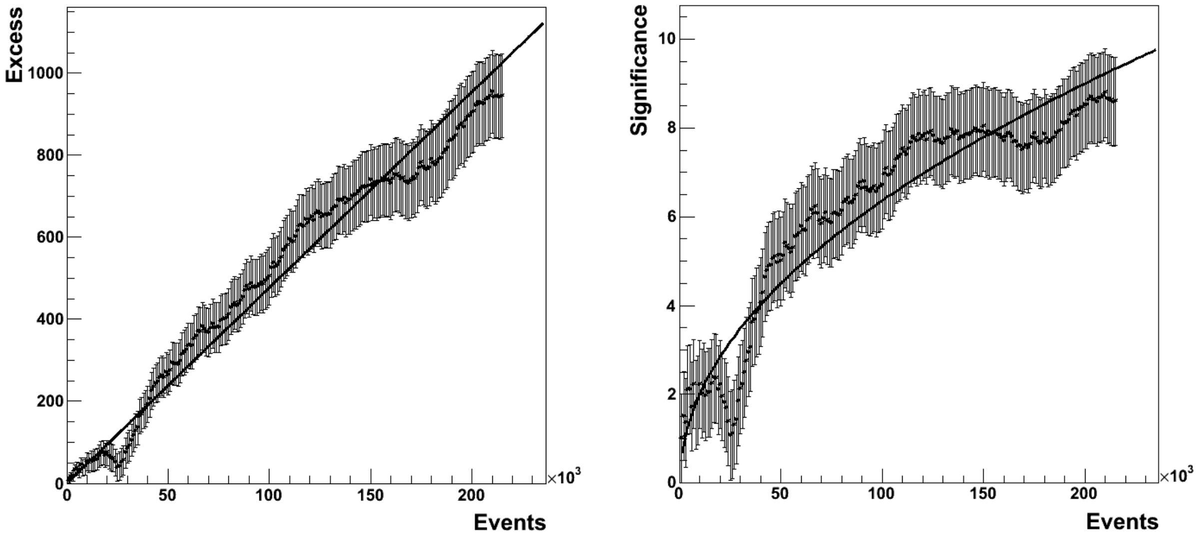

Figure 5.6: Growth of excess (left) and signifance (right) against cumulative photon events.

5.6 Crab Pulsar Spectrum

The differential energy spectrum of the pulsed Crab emission was reconstructed using the excess in the signal regions for P1 and P2 combined. Table 5.2 shows the details of the differential energy spectrum. The differential energy spectrum is shown in Figure 5.7 as well as the result of a fit with a power law spectrum of the form

$$\frac{dN}{dE} = N_0 \left(\frac{E}{E_0}\right)^{\Gamma} \tag{5.1}$$

where the normalization energy E_0 is set to 150 GeV. The best fit parameters, a flux normalization N_0 and spectral index Γ, are shown in Table 5.3 along with fit parameters from MAGIC observations for comparison. The VERITAS spectrum is limited by statistics and we are unable to reconstruct spectral points above 500 GeV. Due to statistical limitations we are unable to confirm the MAGIC detection of pulsed emission from the Crab at TeV energies.

$E_{\mathrm{low}} - E_{\mathrm{high}}$	dN/dE	N_{ON}	N_{OFF}	Significance
79-126	3.77e-07	358	314	2.3
126-200	1.95e-07	4175	3626	8.5
200-317	1.26e-08	3002	2770	4.1
316-501	6.03e-10	1736	1717	0.4
> 501	-	2780	1500	2.6

Table 5.2: Crab Pulsar Differential Energy Spectrum

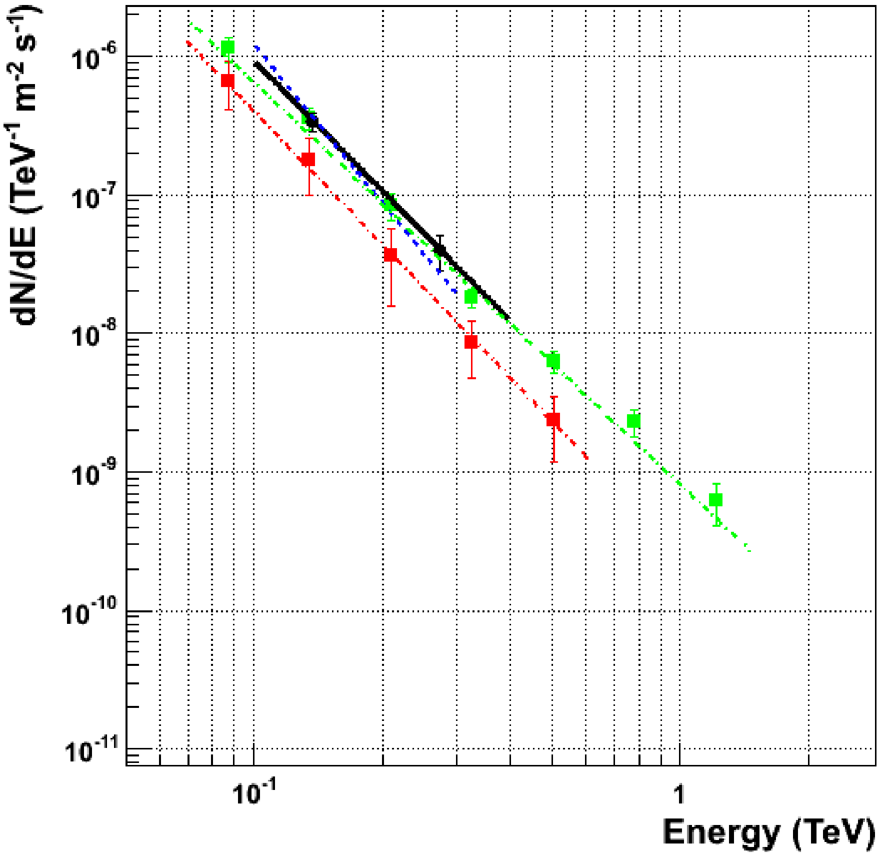

Figure 5.7: The phase-folded differential energy spectrum of the Crab pulsar for P1 and P2 combined measured by VERITAS between 100 GeV and 500 GeV. The Crab pulsar spectrum is well fit by a power law function (black line). The best-fit parameters are given in Table 5.3. The power law fit to the 2011 VERITAS observations is shown (dashed, blue) and the 2016 MAGIC observations are shown for P1 (dot-dashed, red) and P2 (dashed, green) for comparison.

		E_0 (GeV)	N_0 $\left(\text{TeV}^{-1}\ \text{m}^{-2}\ \text{s}^{-1}\right)$ $\times 10^{-7}$	Γ
MAGIC	P1	150	1.1 ± 0.3	-3.2 ± 0.4
MAGIC	P2	150	2.0 ± 0.3	-2.9 ± 0.2
VERITAS (2011)	P1+P2	150	$4.2 \pm 0.6_{\text{stat}}$	$-3.8 \pm 0.5_{\text{stat}}$
VERITAS (this work)	P1+P2	150	$2.62 \pm 0.35_{\text{stat}}$	$-3.1 \pm 0.45_{\text{stat}}$

Table 5.3: Results of Spectral Fit to Power Law Function

5.7 Height of Pulsed Emission Site

As discussed in Chapter 2, there exists a relation between the energy of an observed VHE photon from a pulsar and the minimum possible distance between the pulsar stellar surface and the emission location. This relation comes as a consequence of the interaction between photons and the strong magnetic fields of the magnetosphere leading to the absorption of some photons due to pair creation. VHE photons must be emitted beyond a certain distance to survive propagation through the magnetosphere to be observed. The restriction on the emission height is given by Equation 2.30. The relevant parameters for the Crab are: surface field strength $B_0 = 3.78 \times 10^{12}$ G and spin period $P = 33$ ms (Manchester et al., 2005). Using our results we find a minimum emission height of 12 R_s. This bound is not as restrictive as the limits that can be set using the MAGIC observations, which give a minimum emission height of 19.76 R_s for the highest energy point for P2 with an energy bin range of $965 - 1497$ GeV and centered at 2914 GeV.

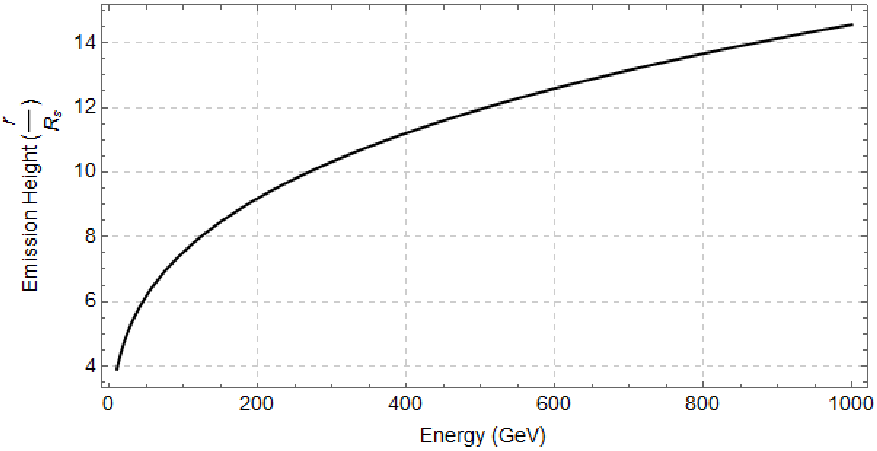

Figure 5.8: Plot of the minimum emission height (i.e. minimum distance between the Crab pulsar stellar surface and the emission location) of a VHE photon for a given energy. The strong magnetic fields in the magnetosphere allow the absorption of VHE photons due to pair creation. As a result of pair attenuation, photons observed at various energies must have been emitted a minimum distance above the stellar surface to survive propagation through the magnetosphere. The exact location of emission cannot be known but a bound may be set on the emission height. For the Crab pulsar, the spectrum is reconstructed up to 500 GeV by the analysis in this chapter. This yields a minimum emission height of 12 R_s.

5.8 Results Summary and Discussion

With ∼150 hours of observation we extend the Crab pulsar spectrum to 500 GeV. These results are in agreement with the MAGIC results up to 500 GeV. After ∼150 hours of observation we are unable to confirm the MAGIC detection of pulsed emission up to ∼2 TeV. The spectral shape further supports that view that curvature radiation only cannot explain the VHE emission. More data is needed to make definite conclusions about the spectral shape beyond 500 GeV. Extending the spectrum to higher energies will allow better understanding of the dominant emission mechanism(s) beyond the spectral break.

Our results further constrain the location of acceleration regions in the magnetosphere. At energies above 500 GeV the minimum emission height above the stellar surface is 12 R_s. This limit pushes the possible location of the acceleration region(s) further out in the magnetosphere.

VERITAS currently has plans to extend Crab observations up to 300 hours, which will enable analysis and results with the same or better sensitivity than MAGIC. Currently the Crab is still the only known VHE emitting pulsar. Adding to the VHE pulsar catalog will improve the understanding of emission mechanisms and acceleration region locations. VERITAS is currently analyzing archival data to search for pulsed emission from other known gamma-ray emitting pulsars. The location of 19 known pulsars have been observed by VERITAS. Each of these pulsars is a new candidate VHE source and most have not been observed by other VHE instruments. Many of these observations were obtained when the pulsar was in the field of view of another primary target. 11 of the locations have more than 20 hours of observations each. The top 10 pulsars, in terms of spin-down power divided by distance squared, detected in the Northern Hemisphere by *Fermi*-LAT are contained in this archival dataset (see Archer (2015)).

Chapter 6

Effect of Geometry and Pair Opacity on Light Curves

Observed pulsars exhibit a variety of features in their light curves (also referred to as phaseograms). Many studies have been conducted in attempts to understand what underlying physics is responsible for the variety of light curve shapes. This chapter discusses the basic physics and geometry that is used in simulations of photons propagating through a magnetosphere for a variety of physical scenarios. The simulations presented are intended to illustrate the effects of the geometry of the emission region and photon-magnetic field pair creation interactions. The methods and results are presented in detail in this chapter and help motivate the study of more exotic physics that may occur in the extreme environment of the pulsar magnetosphere. Chapter 7 will extend the discussion of the simulations described here to include considerations of axion-like particle models.

6.1 Simulation of Photon Propagation through Pulsar Magnetospheres

6.1.1 Pulsar Magnetosphere and Geometry

Since the first discovery of pulsars in 1967, numerous efforts have been put forth to provide a complete and accurate description of the magnetospheres of pulsars. The purpose of this work is not to study the intricate details of a realistic magnetosphere, but to examine physical processes within the magnetosphere and develop a simple model that can be used to understand the basic features of pair opacity and (in Chapter 7) photon-axion conversion. This work adopts a simple standard model for pulsars, treating the magnetic field geometry to be given by the retarded potential vacuum dipole solution (Deutsch, 1955) and adopt the formalism used in Michel and Li (1999):

$$\begin{aligned} B_r &= \frac{2M}{r^3}\left(\cos\xi\cos\theta + \sin\xi\sin\theta\left[d_1\cos\psi + d_2\sin\psi\right]\right) \\ B_\theta &= \frac{M}{r^3}\left(\cos\xi\sin\theta - \sin\xi\cos\theta\left[(q_1+d_3)\cos 2\theta + d_3\right]\sin\psi\right) \\ B_\phi &= \frac{M}{r^3}\sin\xi\left(-\left[q_2\cos 2\theta + d_4\right]\cos\psi + \left[q_1\cos 2\theta + d_3\right]\sin\psi\right) \end{aligned} \tag{6.1}$$

M is the magnetic dipole moment, ζ is the angle between the pulsar spin axis and the line of sight to the observer. ξ is the inclination angle of the magnetic dipole axis, and Ω is the angular velocity of the pulsar, $\psi = \phi - \Omega t + \rho - \alpha$, where $\rho = r\Omega/c$ and $\alpha = R_s\Omega/c$ and

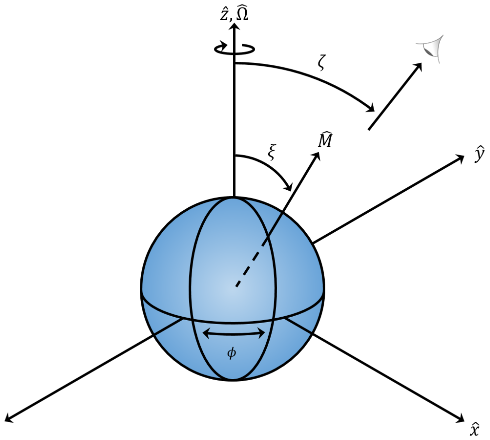

Figure 6.1: Schematic of the geometry used for pulsar simulations. The axis of rotation $\hat{\Omega}$ lies along the z-axis.

coefficients d_i, q_i are:

$$\begin{aligned}
d_1 &= \frac{\alpha\rho + 1}{\alpha^2 + 1} \\
d_2 &= \frac{\rho - \alpha}{\alpha^2 + 1} \\
d_3 &= \frac{1 + \alpha\rho - \rho^2}{\alpha^2 + 1} \\
d_4 &= \frac{\left(\rho^2 - 1\right)\alpha + \rho}{\alpha^2 + 1} \\
q_1 &= \frac{3\rho\left(6\alpha^3 - \alpha^5\right) + \left(3 - \rho^2\right)\left(6\alpha^2 - 3\alpha^4\right)}{\alpha^6 - 3\alpha^4 + 36} \\
q_2 &= \frac{\left(3 - \rho^2\right)\left(\alpha^5 - 6\alpha^3\right) + 3\rho\left(6\alpha^2 - 3\alpha^4\right)}{\alpha^6 - 3\alpha^4 + 36}
\end{aligned} \tag{6.2}$$

In the region near the stellar surface special relativistic effects are negligible and the near-field approximation ($\rho \sim \alpha$) for the magnetic field surrounding the pulsar simplifies to:

$$\begin{aligned}
B_r &= \frac{M}{r^3}\left(2\cos\xi\cos\theta + 2\sin\xi\sin\theta\cos\left(\phi - \Omega t\right)\right) \\
B_\theta &= \frac{M}{r^3}\left(\cos\xi\sin\theta - \sin\xi\cos\theta\cos\left(\phi - \Omega t\right)\right) \\
B_\phi &= \frac{M}{r^3}\sin\xi\sin\left(\phi - \Omega t\right)
\end{aligned} \tag{6.3}$$

As the light cylinder, R_{lc}, of the magnetosphere is approached the corotation velocity approaches the speed of light and special relativistic effects become prominent. The far-field approximation ($\rho \gg 1$) for the magnetic field surrounding the pulsar simplifies to:

$$
\begin{aligned}
B_r &= \frac{2M}{r^2}\frac{\Omega}{c}\sin\xi\sin\theta\sin\psi \\
B_\theta &= \frac{M}{r}\frac{\Omega^2}{c^2}\sin\xi\cos\theta\cos\psi \\
B_\phi &= -\frac{M}{r}\frac{\Omega^2}{c^2}\sin\xi\sin\psi
\end{aligned}
\tag{6.4}
$$

The full geometry of the model used is depicted in Fig. 6.1. The pulsar is centered at the origin and has a radius of 10 km $= R_s$. The rotation axis $\hat{\Omega}$ lies along the $z-$axis. The angle of inclination of the magnetic moment ξ is measured from the $z-$axis. The phase ϕ is defined to be zero when $\hat{M}$ is parallel to the $+\hat{x}$ direction.

6.1.2 Photon Emission

An array of n photons is generated for the simulation with some initial location x_i in the magnetosphere and some energy E. Because the precise nature of VHE emission from pulsars is not well-understood, few detailed assumptions are made about the emission mechanism(s) producing the photons for the simulation. We do assume that VHE photons are emitted through some relativistic process (e.g. curvature radiation or inverse Compton scattering), and thus photons are subject to relativistic beaming. As discussed in Chapter 2, the various possible VHE emission mechanisms are limited to occurring only within a few defined theoretical gap regions within the pulsar magnetosphere. As such, the photons generated have emission locations randomly distributed throughout the slot gap (SG) and outer gap (OG) regions, each considered as a separate case in the simulation studies.

The SG region (depicted in Figure 6.3) begins at the polar cap of the neutron star. The region then extends to higher altitudes in the magnetosphere along the outside of the last closed field line, $\sin^2\theta/r = 1/R_{lc}$ for an aligned dipole, and has some thickness ϵ. This emission region extends all the way out to the light cylinder R_{lc}. In many SG models the thickness of the SG region becomes smaller at higher altitudes. This condition is relaxed for our simulations and the thickness of the region matches that of the OG region.

The OG region is bounded at low altitudes on the inside by the null surface, where $\Omega \cdot B = 0$ and on the outside by the light cylinder. The region extends out to the light cylinder along the outside of the last closed field line with some thickness that is limited physically by pair creation in the region. In this simulation the thickness is set to an arbitrary value. The OG region used is depicted in Fig. 6.2. To ensure the simulation code is working properly the initial positions of photons generated are plotted and shown in Fig. 6.2 for comparison and the x, y, z position distributions are shown in Fig. 6.4.

The emitted phase angle value ϕ_i is given based on the geometric emission location and ϕ is the azimuthal angle measured in the xy-plane from the $x-$axis to the $+y-$axis with ϕ defined to be along the $+\hat{x}$ direction. The observer lies in the $x - z$ plane with an azimuthal angle $\phi = 0$. The phase angle is given in units of 2π such that one full rotation of the neutron star goes from $\phi = 0$ to $\phi = 1$. Given the periodic nature of pulsars, one might naively expect a light curve to be symmetric as is the one shown in the top of Fig. 6.5(a). Typically observed light curves are not perfectly symmetric and this is due, in part, to the difference in times of flight required for photons emitted at different locations in the magnetosphere. This difference in time of flight for photons is accounted for by subtracting a phase-correction factor $\phi_c = -\vec{r} \cdot \hat{k}/R_{lc}$ from the photons emission phase location ϕ_i to give the observed phase ϕ.

$$\phi = -\phi_i - \vec{r} \cdot \hat{k}/R_{lc} = -\phi_i - \phi_c \tag{6.5}$$

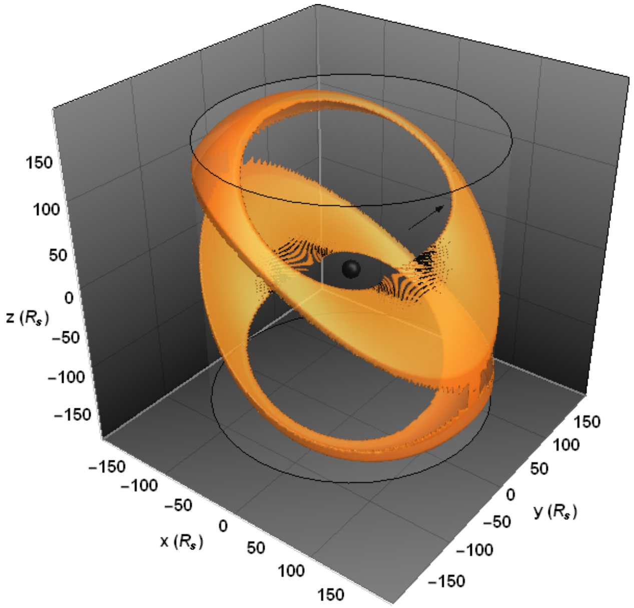

Figure 6.2: Outer gap region used for simulation shown in orange shaded region with the boundaries of the light cylinder shown. Photons are given randomly seeded initial positions throughout the OG region.

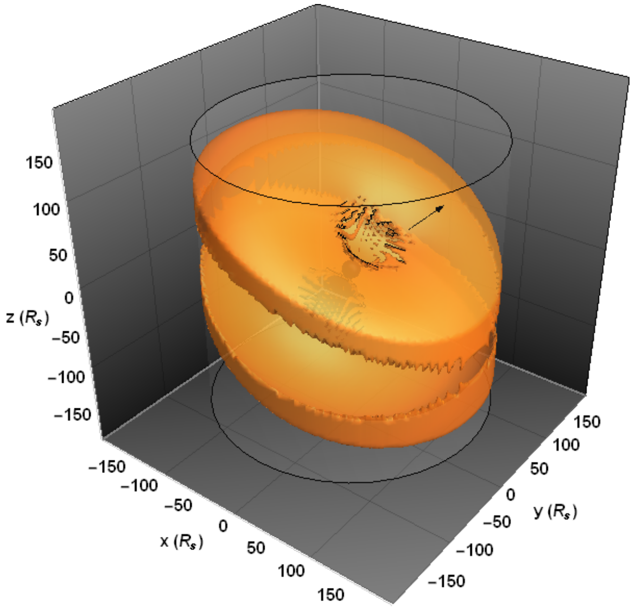

Figure 6.3: Slot gap region used for simulation shown in orange shaded region with the boundaries of the light cylinder shown. Photons are given randomly seeded initial positions throughout the SG region.

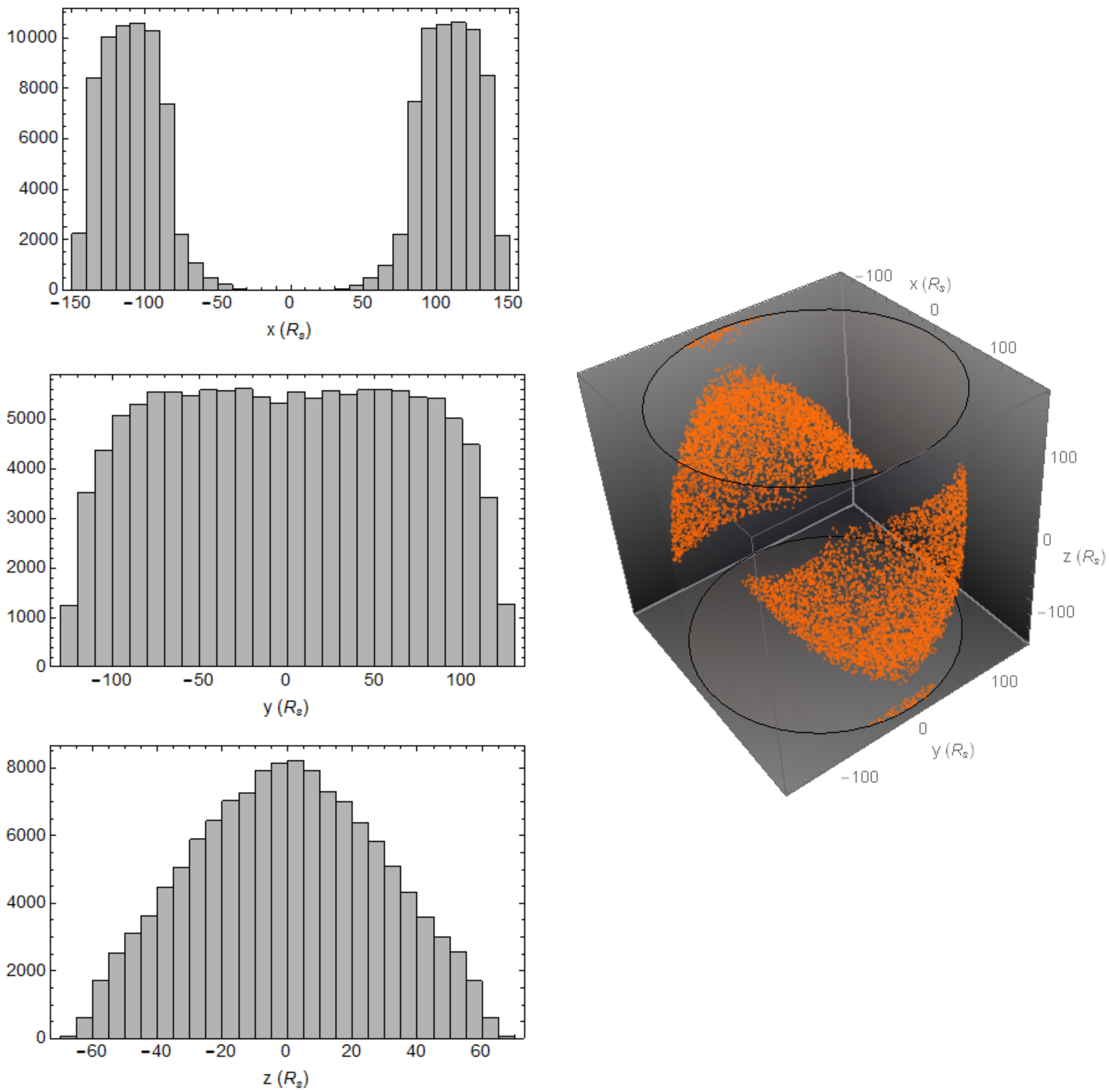

(a) Distributions of photon emission locations separated into x, y, z coordinates.

(b) Plot of photon positions. Each photon is represented by an orange point.

Figure 6.4: Example of the distributions of photon emission locations for one simulation with $\xi = \pi/4$.

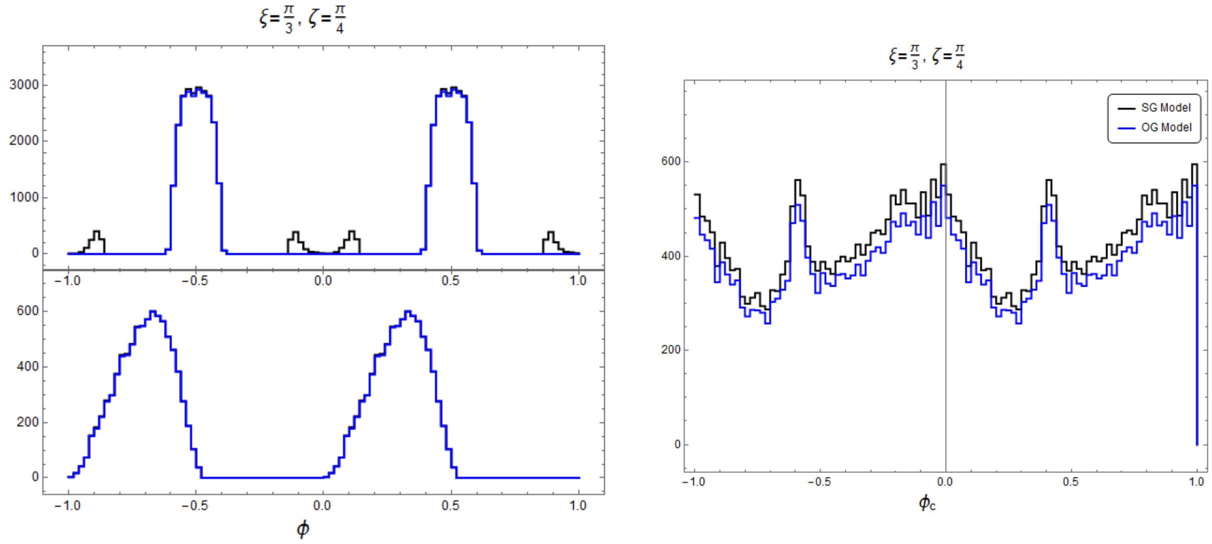

(a) (b)

Figure 6.5: (a) shows the light curves from one simulation with $\xi = \pi/3$ and $\zeta = \pi/4$ for both the SG model (black) and the OG model (blue). The top plot is the light curve before any time of flight corrections are applied to the emission phase ϕ_i. The bottom plot in (a) is the light curve for the same set of propagated photons with phase-corrections ϕ_c applied. (b) is the distribution of values for phase-corrections applied to the propagated photons.

where $\vec{k}$ is the photon wave vector and we consider photons where $\hat{k}$ points to the observer.

Fig. 6.5(b) shows the distribution of phase-correction factors applied to one simulation and the bottom plot in Fig. 6.5(a) shows the phase-corrected light curve.

While the emission mechanisms and emission regions are not fully understood, the energies of photons produced by pulsars can be defined using functions fit to observational data, with the caveat that the already observed spectrum includes the effects of pair absorption. For emission from pulsars in the 10 GeV to 300 GeV range, the spectral energy distribution is well-fit using a smoothly-broken power law of the form:

$$F(E) = A\left(\frac{E}{E_0}\right)^{\alpha}\left[1+\left(\frac{E}{E_0}\right)^{\alpha-\beta}\right]^{-1} \tag{6.6}$$

using the parameters $A = 1.45$, $E_0 = 4$, $\alpha = -1.96$, and $\beta = -3.52$ (VERITAS Collaboration et al., 2011). Photon energies are assigned using this distribution function for the range 100 GeV to 10 TeV. Frequency shifts due to relativistic effects are not considered. The distribution of energies for one simulation of 100000 photons is shown in Fig. 6.6. VHE

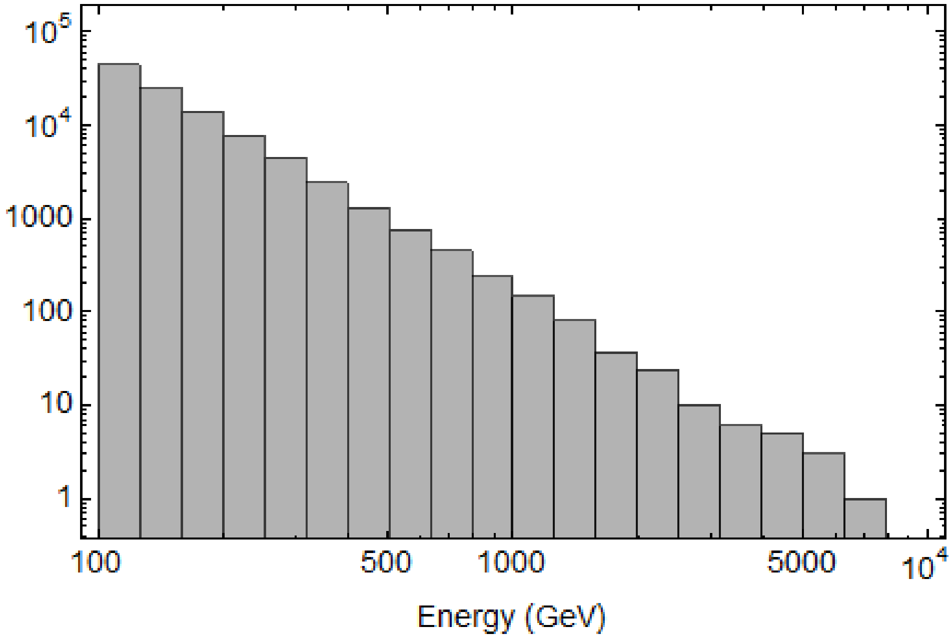

Figure 6.6: Distribution of photon energies used in simulations. Energies range from 100 GeV to 10 TeV. Photon energies are generated using a smoothly-broken power law function and parameters that have been fit to *Fermi*-LAT and VERITAS observations of the Crab Pulsar from VERITAS Collaboration et al. (2011).

photons in pulsar magnetospheres are not isotropically emitted. Due to the relativistic nature of the various particle acceleration processes that lead to the emission of VHE photons, these emitted photons are subject to relativistic beaming. This puts a constraint on the regions from which photons may reach an observer for various inclination angles ξ and observer angles ζ. It is assumed that emitted photons are beamed forward within a conical region centered along the magnetic field line at the photon's emission location. If this conical region overlaps with the unit vector to the observer then a photon may be observed. The precise physical processes that determine the opening angle (e.g. turbulent variations in the field about the mean dipole field) are unknown; we therefore treat the opening angle as a free parameter of the model to be determined empirically by matching the observed light curves. For the purposes of this study and partially due to limits of computational power, a wide beaming angle cut is applied, much larger than the naive $1/\gamma$ angle about the $B-$field direction.

6.2 Results

The simulation of very high energy photons propagating through a model pulsar magnetosphere is run for a variety of possible physical scenarios. As has been shown extensively in the literature (Ruderman and Sutherland, 1975; Romani, 1996; Dyks et al., 2004; Muslimov and Harding, 2003) the assumed location of particle acceleration resulting in VHE emission of photons has an effect on the observed light curve. The inclination angle of the magnetic pole and the observer angle also have clear affects on the observed light curves. VHE photons do not freely travel through strong magnetic fields as discussed in Chapter 2 and the inclusion of pair production physics restricts the regions from which VHE photons may escape the magnetosphere. The following sections will show the results of the various basic geometric and physical influences on the observed pulsar light curves.

6.2.1 Effects of Geometric Considerations on Simulated Light Curves

Two separate gap models are assumed for the purposes of this study. The first model considered is the SG model which is described in detail in Chapter 2. Photon emission is limited to the SG region as described.

The OG model is applied to the simulation to define the possible photon emission regions. Crab pulsar-like parameters are used for spin period and magnetic field strength

Parameter	Value(s)
M/R_s^3 (G)	10^{12}
P (s)	0.033
R_s (km)	10
ξ (rad)	$\pi/12, \pi/6, \pi/4, \pi/3, 5\pi/12$
ζ (rad)	$\pi/12, \pi/6, \pi/4, \pi/3, 5\pi/12, \pi/2$

Table 6.1: Pulsar Parameters Used in Simulations

and given in Table 6.1. A range of inclination angles ξ and observer angles ζ are used. For a given set of parameters, a set of n photons are generated randomly throughout the OG region. The angle between the magnetic field line along which a photon is generated and ζ is calculated. A selection cut is applied to this angle to account for beaming of the emission. If the angle is less than some value ϑ then the photon is "observed". No additional physics are considered at this time.

For both of these studies we use the spectrum assumed in Section 6.1.2 and plot results obtained by summing all photons above 100 GeV to simulate what would be observed by a VHE gamma-ray observatory like VERITAS. The results shown in Fig. 6.7 are light curves of "observed" photons only considering different geometries of gap regions.

6.2.2 Effect of Pair Creation on Simulated Light Curves

VHE photons traveling through a strong magnetic field interact with the field and may produce $e^{\pm}$ pairs, as discussed in Section 2.4.4. The attenuation of the VHE signal by photon-magnetic field interactions is considerable and therefore must be included to properly simulate photon propagation through the magnetosphere. The probability, per unit time, of producing an electron-positron pair by a photon with momentum $\vec{k}$ moving in a magnetic

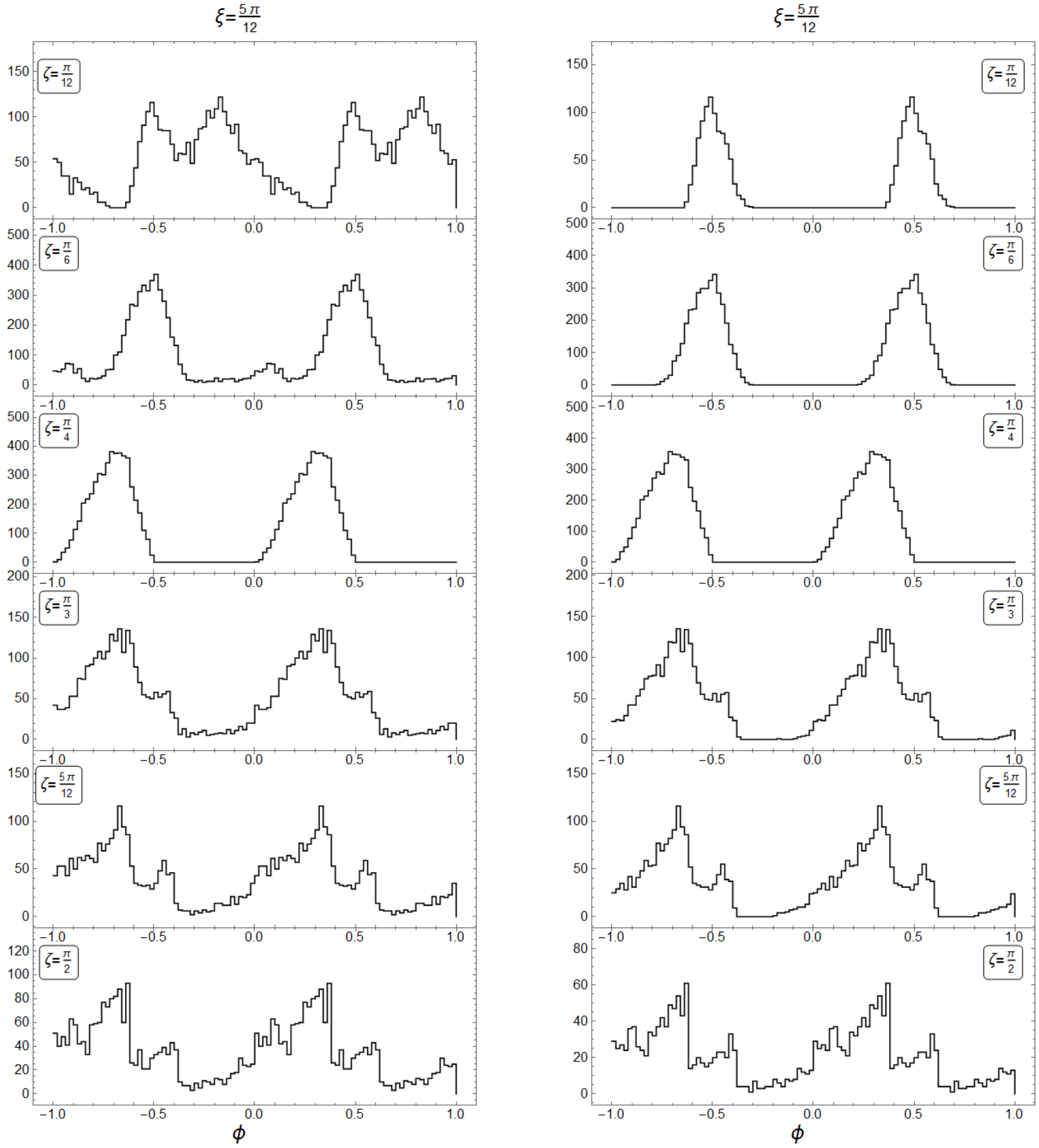

(a) Lightcurves using SG Model geometry (b) Lightcurves using OG Model geometry

Figure 6.7: Lightcurves from simulations for SG and OG models with inclination angle $\xi = 5\pi/12$ and a range of viewing angles ζ.

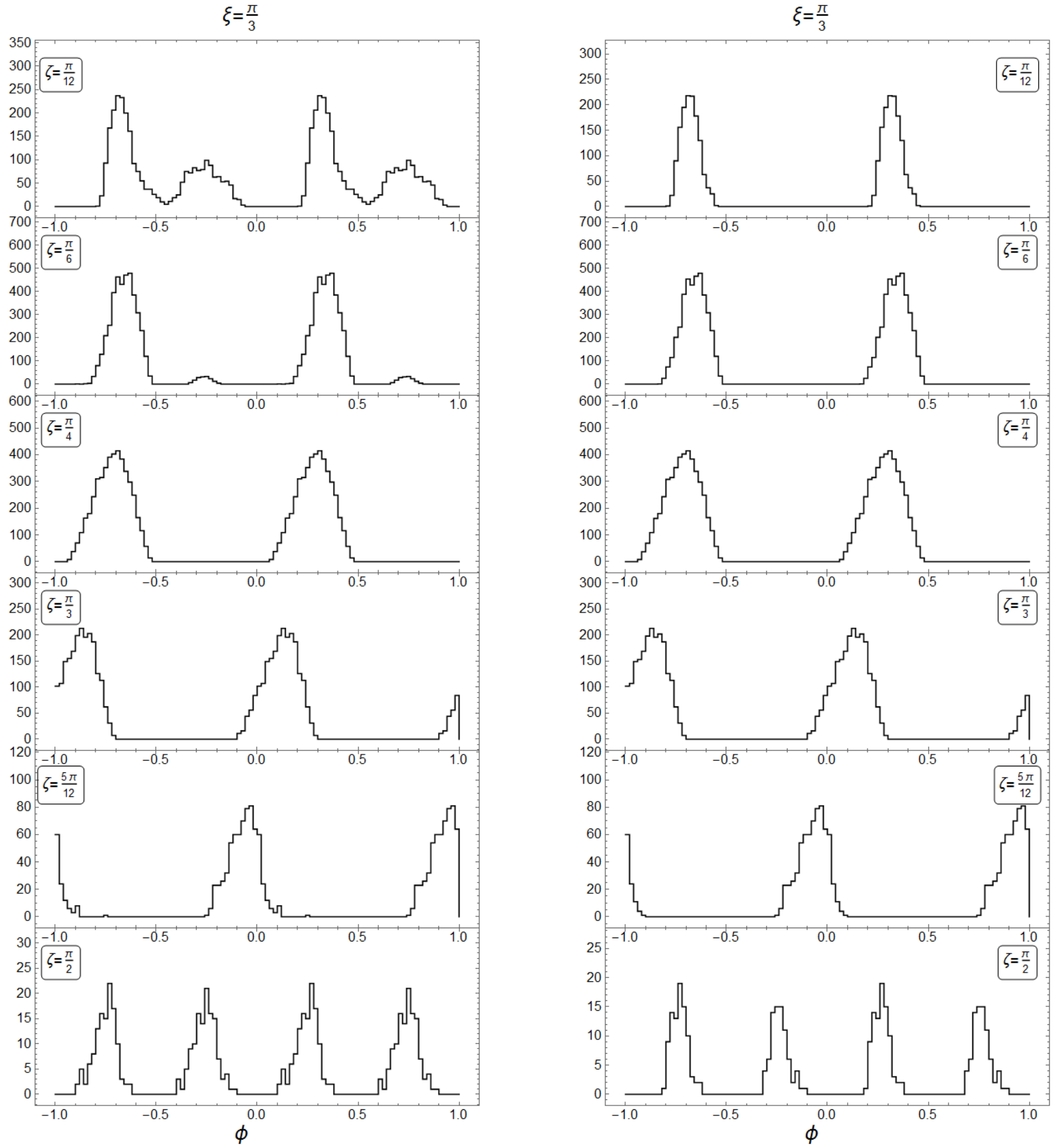

(a) Lightcurves using SG Model geometry (b) Lightcurves using OG Model geometry

Figure 6.8: Lightcurves from simulations for SG and OG models with inclination angle $\xi = \pi/3$ and a range of viewing angles ζ.

field $\vec{B}$ is given by the expression:

$$W\left(\vec{k}\right) = \frac{3^{3/2}}{2^{9/2}} \frac{\alpha_{\hbar} c}{\lambdabar} b_0 |\sin\beta_{ph}| \exp\left(-\frac{8}{3kb_0|\sin\beta_{ph}|}\right) \Theta\left[k|\sin\beta_{ph}| - k_{\perp 0}\right] \tag{6.7}$$

where $\alpha_{\hbar}$ is the fine-structure constant, $\lambdabar$ is the Compton wavelength, $b_0 = B/B_{\hbar}$, $\Theta(x)$ is a step-function and $k_{\perp 0}$ is the minimal value of the photon momentum component orthogonal to $\vec{B}$ for pair production to be possible (Beskin et al., 1993).

The optical depth for pair creation along some path out to a distance l, is obtained by integrating Eq. 6.7 over the photon propagation path s:

$$\tau\left(l\right) = \int_0^l W(\vec{k}) ds \tag{6.8}$$

The probability that a photon will survive along a given trajectory is $\exp\left\{-\tau\left(l\right)\right\}$. The mean free path L for a photon is defined by $l = L$ such that $\tau\left(L\right) = 1$. This function for photon survival is highly dependent on the photon energy and the strength of the magnetic field component perpendicular to the photon propagation direction. Fig. 6.9 depicts the mean free path for photons at different energies (100 GeV, 1 TeV and 10 TeV) at different locations in the magnetosphere. The mean free path was calculated assuming the inclination angle $\xi = \pi/4$ and photons travel along the $+\hat{x}$-direction. The plot shows that any photons in the VHE range will easily pair produce if the photons are emitted near the stellar surface.

The geometry used for the pulsar magnetosphere is shown in Fig. 6.1 and the geometry used for the calculation of the probability of pair production for photons is shown in Fig. 6.10. As with the simulations described in Section 6.2.1, photons are generated randomly throughout an emission region defined by two different theoretical models, the SG model and the OG model. The photon is assumed to propagate in a direction tangential to the magnetic field line at the emission location due to relativistic beaming, this defines the unit

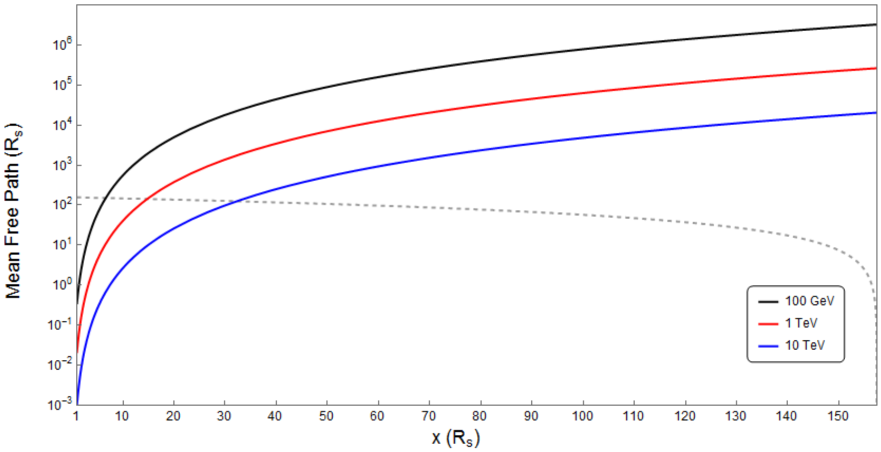

Figure 6.9: Plot of the mean free path of photons at various energies (100 GeV [black], 1 TeV [red] and 10 TeV [blue]) at any point from the stellar surface to the light cylinder. The mean free path was calculated for a pulsar with inclination angle $\xi = \pi/4$ and photons traveling along the $+\hat{x}$-direction. The mean free path changes as a function of distance from the pulsar due to the falling magnetic field strength. The x, y values are given in units of pulsar radii (R_s). The dashed gray line is the remaining distance to the light cylinder from a given $x-$coordinate. Once the mean free path value exceeds the distance to the light cylinder photons are expected to survive propagation. From this plot the one can get an idea of the distance from the stellar surface that higher energy photons must be emitted to be observed.

momentum vector $\hat{k}$. Due to uncertainty in the exact nature of the emission and the field geometry a loose restriction is placed on the required path for a photon to be observed. This comes in the form of a cut made on the angle ϑ between $\hat{k}$ and the direction to the observer. If ϑ is below the cut threshold the photon will be "observed" if it also survives propagation through the magnetosphere.

Photons that survive the ϑ-cut are then propagated through the magnetosphere. The photon follows a straight path in the observer frame (no general relativistic effects are considered). The path length is the distance between the photon emission point r_0 and the location at the light cylinder R_{lc} reached along $\hat{k}$. This path is used to calculate $\tau\left(l\right)$ for the photon. The probability of survival is then calculated using this value of τ. Light curves are created for the distribution of surviving photons and can be seen in Fig. 6.11 and 6.12. For comparison, light curves are also produced for the full initial distribution of photons

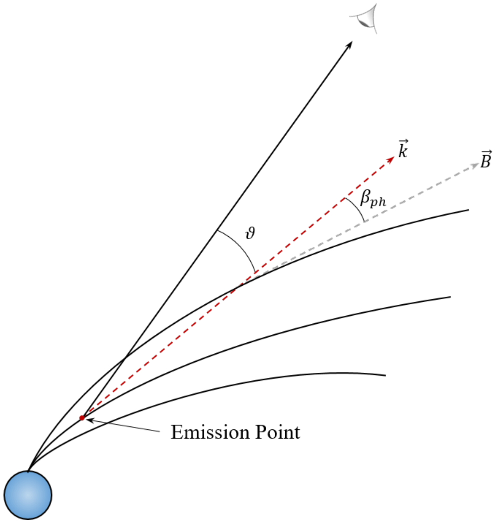

Figure 6.10: Schematic of the geometry used for calculation of pair production opacity. The emission point (red point) is identified in the diagram. The photon momentum vector $\vec{k}$ showing the direction of photon propagation is a dashed red arrow. Initially $\vec{k}$ is tangential to the field line but as the the photon propagates the angle β_{ph} between $\vec{k}$ and $\vec{B}$ increases. $\vec{B}$ is shown by a dashed gray arrow at one point along the photon's path. The line of sight to the observer is shown by the solid black arrow. An angle cut is applied for the angle ϑ to determine if a photon will be observed. The dipole magnetic field lines are shown as solid black lines.

assuming all survive showing the difference in peak strength and peak phase location when pair production is considered. The full set of light curves produced for all simulated ξ, ζ can be found in Appendix B.

Past studies on pulsar geometry and the influence of pair creation have put constraints on the possible theoretical emission regions for VHE photons. To demonstrate the effect of pair creation on the survival of VHE photons emitted near the stellar surface, Fig. 6.13(a) shows radial distance from the stellar surface to the emission locations of all photons simulated for one set of ξ, ζ values and Fig. 6.13 shows the energy distribution of emitted photons. The black distribution shows the full distribution of emitted photons. The blue distribution represents the distribution of photons that survive propagation through the

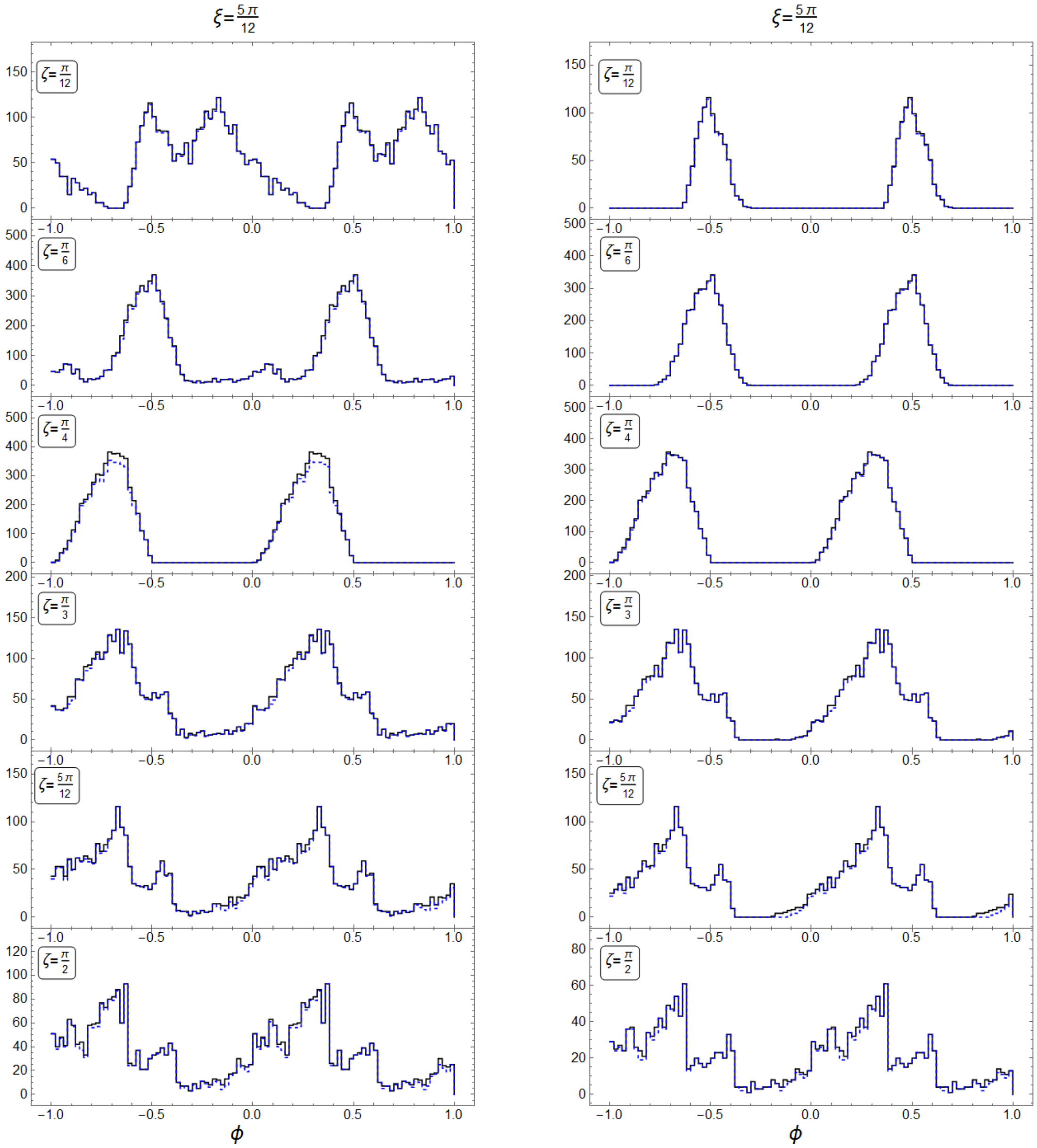

(a) Light curves using SG Model geometry (b) Light curves using OG Model geometry

Figure 6.11: Light curves from simulations for SG and OG models with inclination angle $\xi = 5\pi/12$, a range of viewing angles ζ and an energy threshold $E > 600$ GeV. The light curves resulting only from geometric considerations with no pair absorption are depicted in black for both SG and OG models. Some photons that are capable of being observed due to geometry are not observed due to pair attenuation in the strong magnetic fields of the magnetosphere. The light curves showing the effect of pair attenuation on VHE gamma rays are shown in blue. Light curves for some viewing angles, ζ, are more strongly affected than others. For viewing angles of similar value to the magnetic inclination angle the light curves are less affected as seen for both SG and OG models.

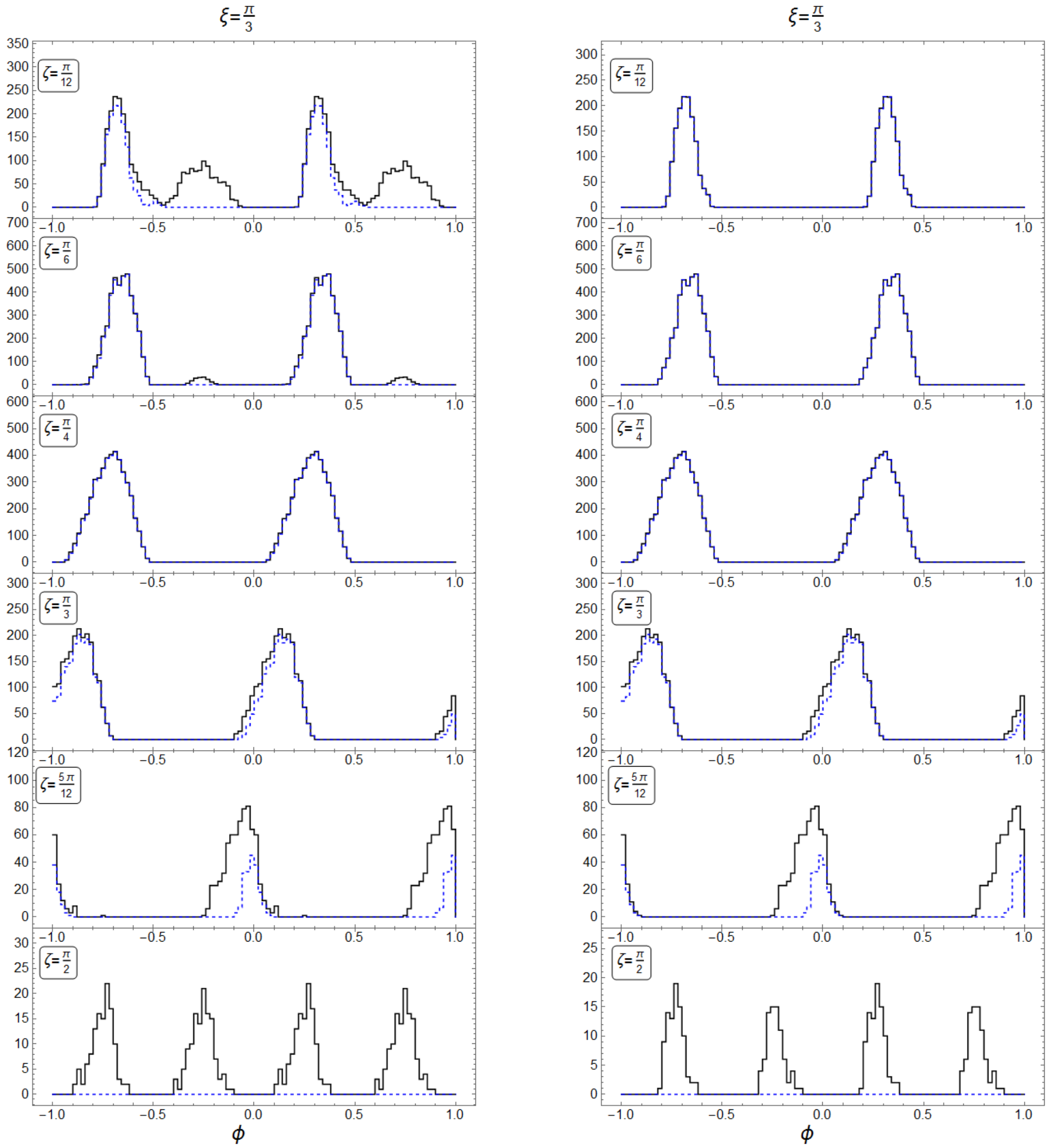

(a) Light curves using SG Model geometry

(b) Light curves using OG Model geometry

Figure 6.12: Light curves from simulations for SG and OG models with inclination angle $\xi = \pi/3$, a range of viewing angles ζ and an energy threshold $E > 600$ GeV. The light curves resulting only from geometric considerations with no pair absorption are depicted in black for both SG and OG models. Some photons that are capable of being observed due to geometry are not observed due to pair attenuation in the strong magnetic fields of the magnetosphere. The light curves showing the effect of pair attenuation on VHE gamma rays are shown in blue. Light curves for some viewing angles, ζ, are more strongly affected than others. For viewing angles of similar value to the magnetic inclination angle the light curves are less affected as seen for both SG and OG models.

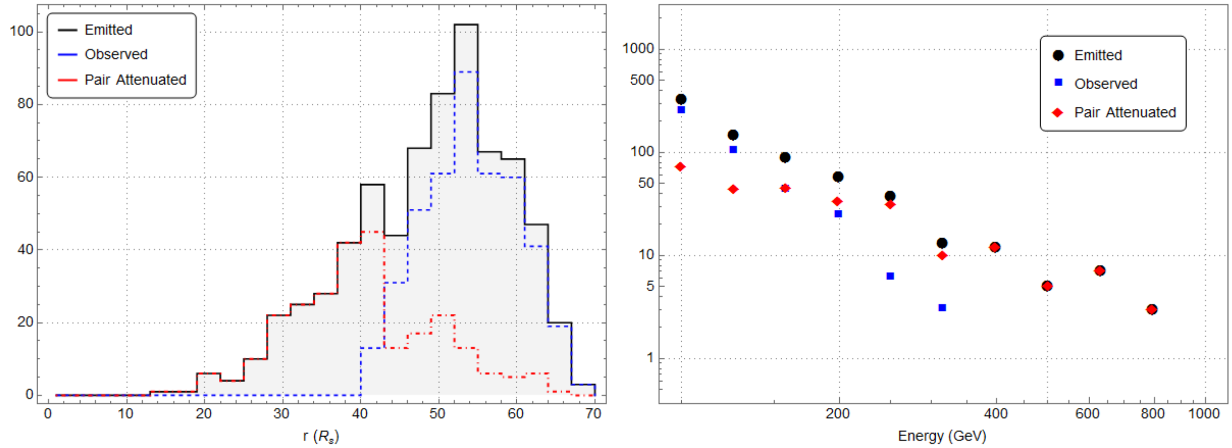

(a) Distribution of radial distance to emission location.

(b) Energy distribution of simulated photons.

Figure 6.13: Results of photon propagation with and without pair production. The distribution of radial distances to the emission location of photons is shown in (a). The energy distribution of simulated photons is shown in (b). The full distributions of emitted photons is shown in black with gray shading. The blue distributions shows “observed” photons. The red distribution shows photons that underwent pair production during propagation.

magnetosphere and are “observed”. The red distribution is the distribution of photons that pair produce and do not survive propagation through the magnetosphere. Fig. 6.14 is a 3D plot depicting the emission location of simulated photons. The black points represent the locations of photons that are “observed”, while the red points represent the emission location of photons that survive the ϑ-cut but have an optical depth $\tau \geq 1$ and therefore do not survive. The size of the points are weighted by the energy of the photon emitted. From Fig. 6.14 one can easily see that some higher energy photons pair produce even when emitted in regions where most lower photons survive propagation. The largest non-“observed” photon in Fig. 6.14 has an energy of ~ 4 TeV.

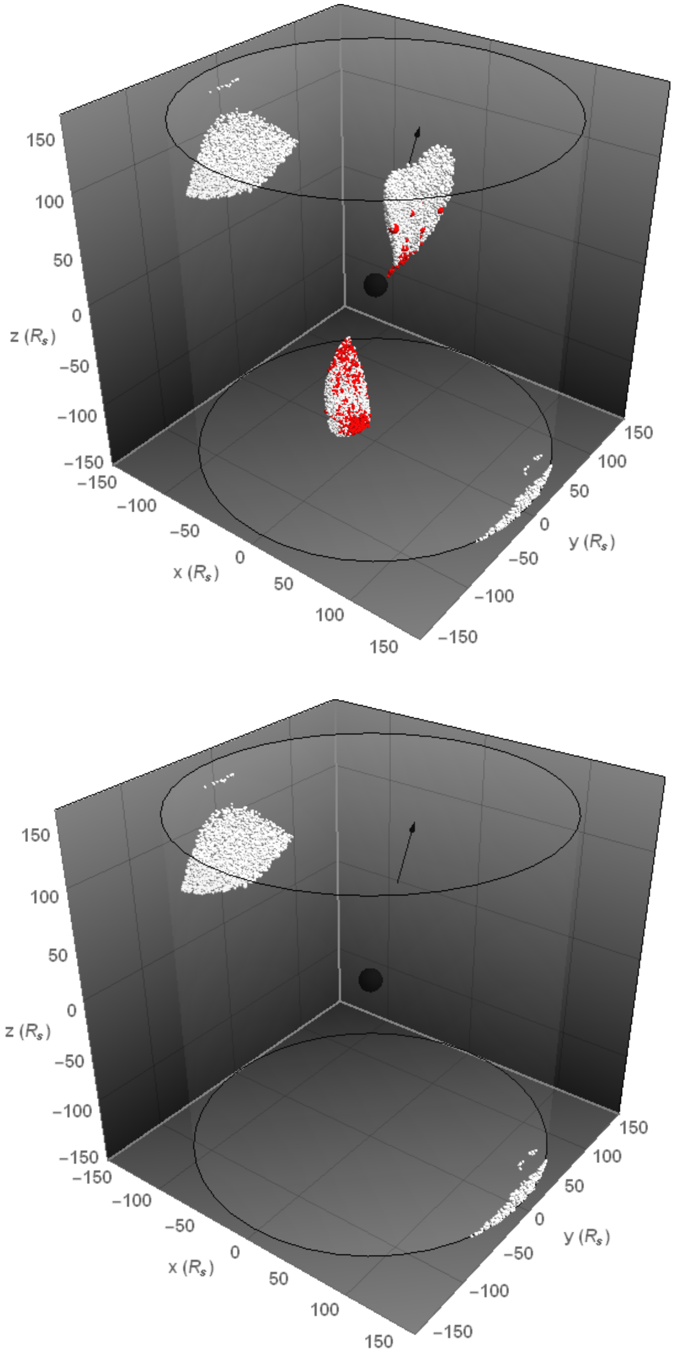

Figure 6.14: 3D visualization of the emission locations of simulated photons in the magnetosphere for SG (top) and OG (bottom) models where the inclination angle $\xi = \pi/3$. "Observed" photons are shown in white and pair-attenuated photons are depicted in red. The size of the points are weighted by the energy of the photon emitted. The light cylinder is shown as a nearly transparent cylinder. The pulsar is shown in black with an exaggerated size. The pulsar spin direction $\hat{\Omega}$ is along the $z-$axis. The line of sight to the observer is depicted by an arrow ($\zeta = \pi/12$).

Chapter 7

Axion-like Particle Oscillations in Pulsar Magnetospheres

Many avenues haven been pursued in the search for axions and axion-like particles, ranging from the terrestrial to the astrophysical and covering a large range of the available parameter space. In this chapter we present a new, the previously unexplored avenue of ALP-photon coupling in magnetosphere of pulsars. Pulsars provide an opportunity to probe new regions of the ALP mass-coupling constant parameter space through investigating the propagation of simulated VHE gamma rays in a model pulsar magnetosphere. The previous chapter discussed the effects of pair production of VHE gamma rays on the observed periodic signal from pulsars. Fewer photons at higher energies survive propagation and are more limited in the region from which they may be emitted and remain observable. This chapter discusses the physical implications of the existence of ALPs and the role ALP-photon coupling plays in allowing VHE photons to propagate through pulsar magnetospheres with a higher rate of survival.

7.1 Pair-Opacity of Pulsar Magnetospheres

Chapter 6 discusses a Monte Carlo simulation of VHE photon emission and propagation through a pulsar magnetosphere for a variety of geometries. The results of this study illustrate that in VHE regime, pulsar magnetospheres quickly become opaque to photons at higher energies and as the emission location nears the stellar surface. As ground-based gamma-ray observatories report increasing observed energies of the pulsed emission from pulsars, the opaqueness of the magnetosphere becomes an increasingly limiting constraint on potential emission regions.

Figures 7.1 and 7.2 illustrate the fraction of geometrically observable photons over a range of energies and emission locations that undergo pair production.Both figures show this fraction for simulations with pulsar magnetic inclination angles of $\pi/4$ and $\pi/3$, as well as a variety of viewing angles ζ. The bottom of Figure 7.1 shows a clear trend that as the photon energy increases a growing fraction of photons are attenuated and for many viewing angles nearly all photons above 300 GeV over the entire geometrically allowed gap region.

The opacity of the magnetosphere is dependent on the emission location since at smaller altitudes, near the stellar surface, the magnitude of the magnetic field is greater and the propagation distance through the magnetosphere is greater, both quantities increasing the probability of attenuation. Figure 7.2 illustrates the fraction of geometrically observable photons over a range of emission locations (measured as a radial distance from the stellar surface) that undergo pair production thereby preventing observation of these photons. Figure 7.2 shows this fraction for simulations with pulsar magnetic inclination angles of $\pi/4$ and $\pi/3$, as well as a variety of viewing angles ζ. For both inclination angles shown, all photons emitted (at any energy) between the stellar surface out to an altitude of 30 R_s are attenuated. A significant fraction are attenuated at higher altitudes, but the general trend

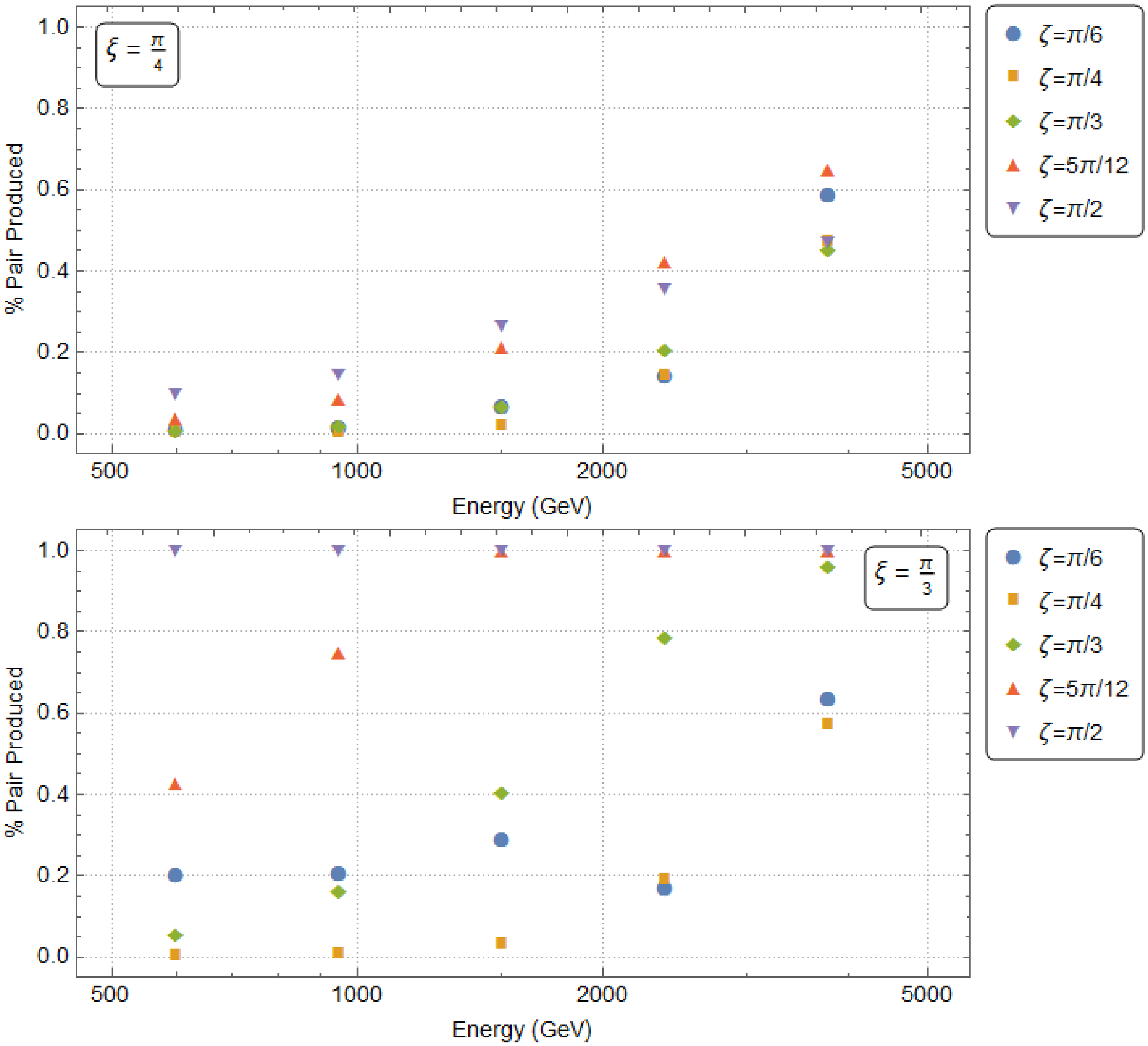

Figure 7.1: Plot of the fraction of simulated, emitted VHE photons that undergo pair production while propagating through the pulsar magnetosphere for $\xi = \pi/4$ (top), $\xi = \pi/4$ (bottom) and the range of simulated ζ values over the range of energies used. The plots demonstrate the range in effects of pair attenuation on the propagation of photons. For $\xi = \pi/4$ most photons do not pair produce until high energies are reached. For $\xi = \pi/3$ between $0-20\%$ of photons in the 600 GeV energy bin are attenuated (for $\zeta \leq \pi/3$) while at higher energies, for some viewing angles, all photons are attenuated.

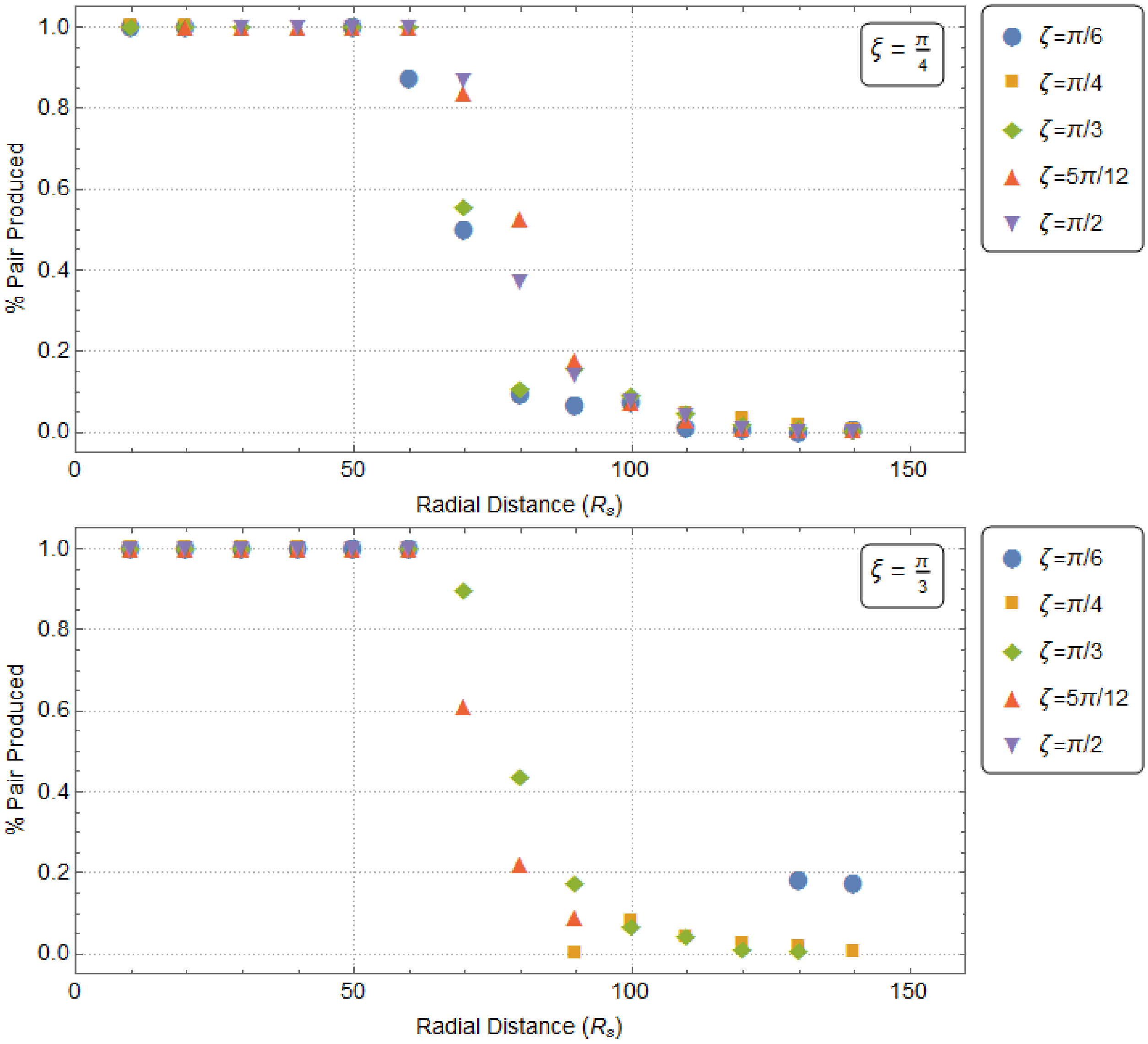

Figure 7.2: Plot of the fraction of simulated, emitted VHE photons that undergo pair production while propagating through the pulsar magnetosphere for $\xi = \pi/4$ (top), $\xi = \pi/4$ (bottom) and the range of simulated ζ values over the range of emission location radial distances. The plots demonstrate the range in effects of pair attenuation on the propagation of photons.

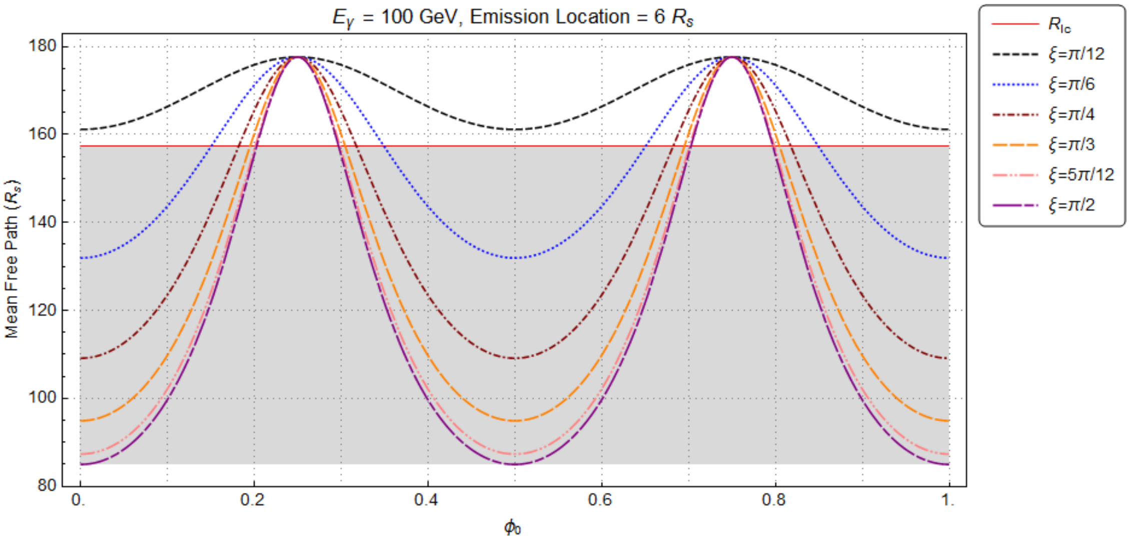

Figure 7.3: The mean free path of a 100 GeV photon emitted at a distance $6R_s$ (in the $\hat{x}-$direction) above the stellar surface is shown for the full range of phase values. The mean free path is calculated for several possible inclination angles to illustrate the range of phase dependence for all simulated inclination angles. The photons are assumed to propagate in the $+\hat{x}-$direction. The distance to the light cylinder R_{lc} is shown (red). Photons with mean free path values less than this distance imply (gray region) the photons will be attenuated. Photons with mean free path values greater than R_{lc} will be observed.

is not clear beyond 50 R_s as a result of limited statistics and the energy dependence of pair production that is not fully captured in this figure.

The probability of pair production is not wholly determined by the magnitude of the magnetic field, but rather the magnitude of the perpendicular component of the magnetic field. For the misaligned rotating dipole field of a pulsar this implies that a photon emitted at some location and with some energy will have different probabilities of undergoing pair production depending on the rotational phase at the time of emission. In certain cases this can be the difference between the survival or attenuation of a photon. Figure 7.3 shows the mean free path (given by Equation 7.1) for a 100 GeV photon emitted at 6 R_s for various pulsar inclination angles as a function of rotational phase. Figure 7.3 demonstrates that for some phases the simulated photon will be attenuated while for other phases the photon will be observed.

7.2 Distance Scales

As an initial step to gauge the efficacy of using pulsar magnetospheres to search for signatures of ALPs the relevant distance scales of pair production and ALP-photon oscillations are considered. If one physical process dominates for the energy range considered it is unlikely to find an observable effect on the propagation of VHE photons. The two process need to be competitive for similar distance scales to expect an appreciable effect on the light curves and/or energy spectrum of pulsars. For pair production the mean free path, L, derived from Equation 6.7 serves as the relevant distance scale. This mean free path for the case of a photon with momentum k moving in a magnetic field with a constant curvature radius ρ_c is given by:

$$L = \frac{8\rho_c}{3kb_0}\left(\ln\left[\frac{\alpha_\hbar \rho_c}{2\sqrt{6}\lambda\!\!\!^{-} k^2 b_0}\right] - 3\ln\left[\frac{1}{2}\ln\left(\frac{\alpha_\hbar \rho_c}{2\sqrt{6}\lambda\!\!\!^{-} k^2 b_0}\right)\right]\right) \tag{7.1}$$

where b_0 is $B/B_\hbar$, k is the momentum of the gamma ray and the other quantities are defined in Chapter 6.

The mean free path for photons emitted on the $x-$axis, traveling in the $+\hat{x}-$direction with an energy of 100 GeV, 1 TeV and 10 TeV were calculated and plotted shown in Figure 6.9. The range of energies considered in our simulations and the associated range of mean free paths are shown again in Figure 7.4 in blue to compare directly with the relevant distance scale for ALP-photon oscillations (to be described later in this chapter). From the formula for the probability of conversion of an ALP to a photon given by 7.6 it is clear the probability of conversion is maximal at some path distance $d = d_{\max}$ where $d_{\max} = \pi/\left(Bg\right)$ for a given magnetic field strength and coupling constant. This quantity $d_{\max}$ becomes the relevant length scale to consider and is calculated using ALP-photon coupling constant values $g = 10^{-7}$ GeV^{-1} to $g = 10^{-11}$ GeV^{-1} over the range of values of B encountered throughout the magnetosphere. Figure 7.4 shows that there is significant overlap in the distance scales for pair production and ALP-photon oscillations throughout the entire magnetosphere. The

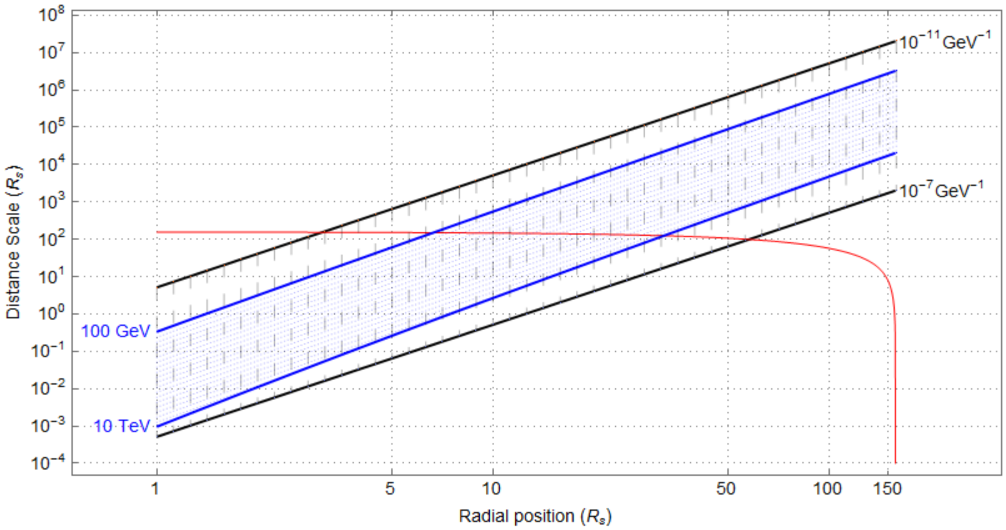

Figure 7.4: Comparison of relevant distance scales for pair-production and ALP oscillation probability for a pulsar with $\xi = \pi/4, \zeta = \pi/2$. The horizontal axis is the emission location of photons in units of stellar radii (R_s) and goes from the stellar surface out to the light cylinder radius. The vertical axis is the distance scale for the two considered physical processes in units of stellar radii (R_s). The mean free path for the range of energies considered (100 GeV to 10 TeV) is bounded by blue lines and shaded. The distance scale that maximizes ALP oscillation probability ($d = \pi/(Bg)$ for the relevant range of coupling constant, g, (10^{-11} to 10^{-7}) is bounded by black lines and hashed. The distance from the radial position to the light cylinder R_{lc} is shown in red to indicate what distance scales are of interest for pulsar magnetospheres. From this figure it can be seen that there is a range of photon energies and coupling constants for which the distance scale relevant to pair production and ALP oscillation probability are comparable. This range lies naturally in the VHE regime for photon energies.

figure also demonstrates that the distance scales for the two physical process are, for some photon emission locations, less than the distance to the light cylinder which is important for either process to take place while a photon propagates through the magnetosphere. At distant regions of the magnetosphere approaching the light cylinder the mean free path of pair production is sufficiently large for all considered energies that photons are expected to propagate without pair producing. Likewise the distance scale for ALP-photon oscillations increases to large enough values that no oscillation is expected beyond a certain radial distance.

7.3 ALP-Photon Mixing in Pulsar Magnetospheres

As discussed in Chapter 3, axions and ALPs are predicted to couple to photons in the presence of a magnetic field. The production of axions by high-energy photons is referred to as the Primakoff effect. The inverse process of producing high-energy photons from the decay of axions in the presence of a magnetic field is aptly named, the inverse Primakoff effect. Figure 7.5 shows the Feynman diagrams for both processes. In a plasma, the photon acquires an effective mass, and one can consider these Primakoff processes to be analogous to the neutrino mixing problem as pointed out by Raffelt (1996). The Primakoff effects shows up as off-diagonal elements in the mass matrix for a considered photon-ALP system. Consideration of the propagation of a monochromatic, photon/ALP beam of energy E_γ has been shown to take the form of a three-state nonrelativistic quantum system where there are two photon-polarization states and one ALP state (de Angelis et al., 2011). For propagation of VHE photons in a pulsar, the process of pair production must be considered as well. This physical process comes in the form of an absorption term in the mixing matrix for ALP-photon mixing. The following sections will discuss ALP-photon mixing first without consideration of pair production and then including the absorption term from pair production. The following sections make use of natural units with $\hbar = c = k_B = 1$ unless explicitly stated otherwise.

7.3.1 Mixing without Pair Production

For the general case of a monochromatic, unpolarized photon beam propagating though a magnetic field, $\vec{B}$, in which $\vec{B}$ is misaligned from the $\hat{z}-$axis by an angle ψ, ALP-photon conversion can be described by a Schrödinger-like equation of motion[7] (Raffelt and Stodolsky,

---

[7] This follows by starting with the Dirac or Klein-Gordon equation then making the approximation that $\partial_t^2 + k^2 \approx 2k\left(-i\partial_t + k\right)$ if $\omega_i \approx k \gg m_i$.

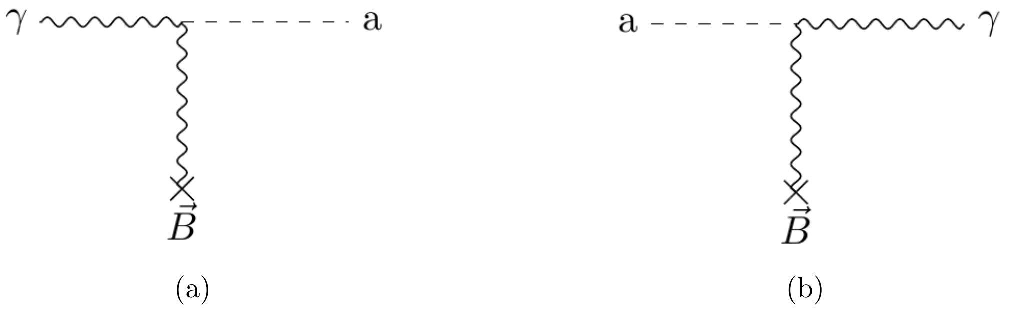

Figure 7.5: Feynman diagrams of the Primakoff effect (a) and the inverse Primakoff effect (b). Axions and ALPs are coupled to photons and in the presence of an external magnetic field, an ALP may convert into a photon. This interaction is key for many searches for ALPs including the work presented in this chapter.

1988):

$$\left(i\frac{d}{dy} + E + \mathcal{M}\right)\Psi(y) = 0. \tag{7.2}$$

where the mixing matrix $\mathcal{M} = M^2/(2k)$ and M^2 is the mass matrix.

$$\Psi(y) = \begin{pmatrix} A_x(y) \\ A_z(y) \\ a(y) \end{pmatrix} \tag{7.3}$$

where $A_x(y)$ and $A_z(y)$ are the amplitudes of photon polarization along the $x-$axis and $z-$axis, respectively and $a(y)$ is the ALP amplitude. The mixing matrix $\mathcal{M}$ can be written as

$$\mathcal{M} = \begin{pmatrix} \Delta_{pl} & 0 & \Delta_{a\gamma}\sin\psi \\ 0 & \Delta_{pl} & \Delta_{a\gamma}\cos\psi \\ \Delta_{a\gamma}\sin\psi & \Delta_{a\gamma}\cos\psi & \Delta_a \end{pmatrix} \tag{7.4}$$

where $\Delta_{pl} = -\omega_{pl}^2/\left(2E_\gamma\right)$, $\Delta_{a\gamma} \equiv Bg/2$, and $\Delta_a = -m_a^2/\left(2E_\gamma\right)$. The Δ_{pl} term arises from properties of the medium producing an effective photon mass.

The probability of ALP-photon oscillation can be determined in an analogous fashion to neutrino oscillations. For the simplified case where $\psi = 0$ the probability of ALP-photon oscillation after propagation over a distance d can be written in the compact form

$$P_{a\gamma} = \sin^2 2\vartheta \sin^2 \left[\frac{\Delta_{osc} d}{2}\right] \tag{7.5}$$

where $\Delta_{osc} = \sqrt{(\Delta_{pl} - \Delta_a)^2 + 4\Delta_{a\gamma}^2}$ and ϑ is the ALP-photon mixing angle that diagonalizes the mixing matrix $\tan 2\vartheta = 2\Delta_{a\gamma}/\left(\Delta_{pl} - \Delta_a\right)$. Equation 7.5 can be simplified to

$$P_{a\gamma} = \frac{1}{1 + \left(E_{\text{crit}}/E_\gamma\right)^2} \sin^2 \left[\frac{B d g_{a\gamma}}{2} \sqrt{1 + \left(\frac{E_{\text{crit}}}{E_\gamma}\right)^2}\right] \tag{7.6}$$

where E_{crit} is the energy threshold above which oscillation probability is maximal and independent of E_γ.

$$E_{\text{crit}}\,(\text{GeV}) \equiv \frac{5}{2} \frac{m_{\mu eV}^2}{B_G g_{11}} \tag{7.7}$$

This regime where $\Delta_{a\gamma} \gg \Delta_{pl} - \Delta_a$ is referred to as the *strong-mixing regime.* The subindices indicate the following dimensionless quantities: $m_{\mu eV} = m/\mu\text{eV}$ where $m^2 \equiv |m_a^2 - \omega_{pl}^2|$, $g_{11} = g_{a\gamma}/10^{-11}\ \text{GeV}^{-1}$, and $B_G = B/\text{Gauss}$. The plasma frequency is $\omega_{pl} = \sqrt{4\pi\alpha n_e/m_e} = 0.37 \times 10^{-4} \mu\text{eV}\sqrt{n_e/\text{cm}^{-3}}$ and plays the role of mass in the dispersion relationship for radiation propagating in a polarizeable medium. n_e for pulsars is taken to be the Goldreich-Julian density $n_{GJ} = \left|\rho_{GJ}\right|/e$, though this likely underestimates the particle density in some regions, and overestimates the density in the acceleration regions[8] allowing axions to be efficiently produced and to escape before regenerating gamma rays. The particle density is then $n_{GJ} \sim 10^{12}\ \text{cm}^{-3}$ near the stellar surface and drops to $n_{GJ} \sim 10^5\ \text{cm}^{-3}$ near the light cylinder. From plasma frequency and Equation 7.6, the effective ALP mass will not be less than $\sim 10\mu\text{eV}$ if ALP-photon oscillations are to occur near the stellar surface and the effective ALP mass will not be less than $\sim 0.01\mu\text{eV}$ if ALP-photon oscillations are to occur near the light cylinder.

---

[8] This detail could play a roll if the density crosses a value yielding an enhancement due to resonant conversion

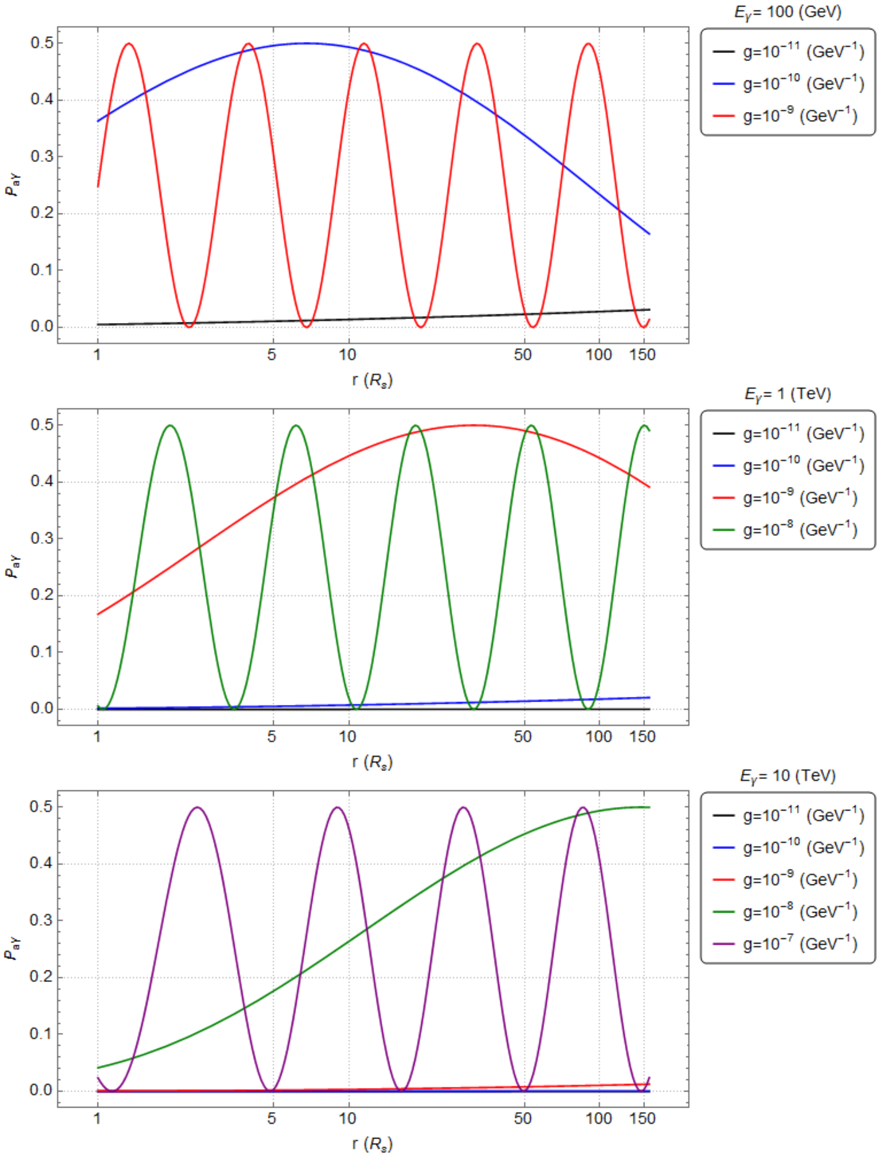

Figure 7.6: Probability of photon-ALP oscillation at locations through a pulsar magnetosphere calculated using Equation 7.6 where $m_a = 10^{-4}$ eV, $d = L$. $P_{a\gamma}$ is shown for $E_\gamma = 100$ GeV (top), $E_\gamma = 1$ TeV (center) and $E_\gamma = 10$ TeV (bottom) and various values of g. The $x-$axis gives the emission location of the considered photon, d is measured from this distance. Not all values of g are shown for each energy due to the rapid oscillations of the function that obscure the graph. For each considered energy, smaller values of g give lower frequencies of oscillation for the probability function. For any values of g, E_γ the probability of oscillation never exceeds 0.5.

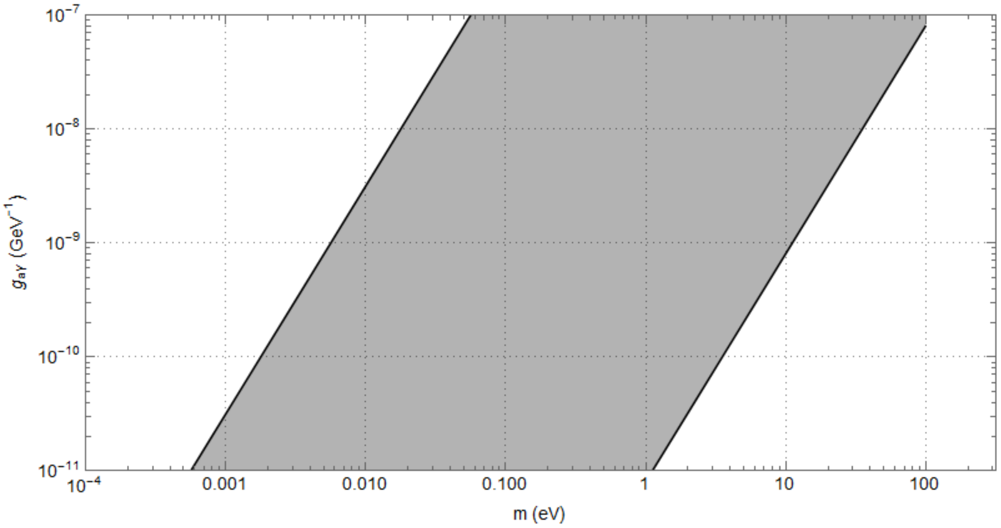

Figure 7.7: ALP parameter space relevant to pulsar magnetospheres where we fix $E_{\text{crit}} = 10$ GeV to allow for strong mixing to occur in the VHE regime. The effective axion mass is limited, in part, by the particle density, n_{GJ}, in the magnetosphere. The coupling constant range is limited to values where ALP-photon oscillation distance scales are comparable to the pair-attenuation mean free path of VHE photons (as seen in Figure 7.4). The left and right edges of the parameter space are determined by the magnitude of the magnetic field at the stellar surface (right) and the light cylinder (left).

The parameter space considered in this work consists of values for g, m such that VHE photons are within the strong mixing regime. Figure 7.7 shows the relevant parameter space, given by Equation 7.7, for $g_{a\gamma}$ and m given the range $\vec{B}-$field magnitudes encountered in a pulsar magnetosphere and with critical energy threshold set to 10 GeV, allowing the entire VHE regime to be in the strong ALP-photon mixing regime. The range of masses considered comes from limitations due to the plasma frequency of the magnetosphere.

The probability of ALP-photon oscillation in a pulsar magnetosphere is calculated and shown in Figure 7.6 using Equation 7.6 with the ALP mass fixed at $m_a = 10^{-4}$ eV and the path distance $d = L$ where L is the mean free path for pair creation for a VHE photon with energy E_γ at a distance r from the star (Equation 7.1). The path distance in the mixing equation is set to the mean free path of a VHE photon to illustrate regions where one expects measurable effects from the interplay of these two processes as will be discussed in Section 7.2.

Figure 7.6 shows that $P_{a\gamma}$ varies greatly depending on the value of the coupling constant, the photon energy and the initial location of the photon. For no considered parameters does the of $P_{a\gamma}$ exceed 0.5. The sensitivity of $P_{a\gamma}$ to the value of the coupling constant can be seen clearly for $E_\gamma = 100$ GeV where a value $g = 10^{-11}$ GeV^{-1} gives a probability of oscillation < 0.1 for any location in the magnetosphere. For $g = 10^{-10}$ GeV^{-1} the probability of oscillation is > 0.3 for a large fraction of the pulsar magnetosphere and for $g = 10^{-9}$ GeV^{-1} the probability of oscillation oscillates between 0.0 and 0.5 depending on the location of emission.

7.3.2 Mixing with Pair Production

The attenuation of VHE photons in pulsar magnetospheres due to pair production is understood to play a large role in the observed light curves of pulsars. Due to the strength of the magnetic field and the very high energy of photons considered in this work, pair production can not be excluded when formulating the mixing matrix. The addition of pair production effects to the ALP-photon mixing calculation comes in the form of an imaginary absorption term that is added to the plasma term of the mixing matrix $\mathcal{M}$ so that $\Delta_{pl} \rightarrow \Delta_{pl} + i/(2L)$, where L is the mean free path of pair production. The mixing matrix then takes the form

$$\mathcal{M} = \begin{pmatrix} \Delta_{pl} + \frac{i}{2L} + \Delta_{\text{QED}} & 0 & \Delta_{a\gamma} \sin\psi \\ 0 & \Delta_{pl} + \frac{i}{2L} + \Delta_{\text{QED}} & \Delta_{a\gamma} \cos\psi \\ \Delta_{a\gamma} \sin\psi & \Delta_{a\gamma} \cos\psi & \Delta_a \end{pmatrix} \tag{7.8}$$

Here we have an included the additional term $\Delta_{\rm QED}$ which comes from QED vacuum polarization. Typically for ALP-photon mixing problems this term can be ignored due to the weak magnetic fields considered in other astrophysical or experimental environments. For the case of a pulsar magnetosphere this term is non-negligible in comparison to the other mixing matrix terms. Unfortunately, there is no complete theory for the complex refactive index that combines the effects of vacuum polarization and pair production. The most careful studies of QED effects (to two loops) reproduce the famous result of Euler and Heisenberg (Heisenberg and Euler, 1936) or more recently by (Adler, 1971), but allow one to relax the assumption that $E \ll m_e$. The use of Kramers–Kronig relations might provide a way of relating the real part of the refractive index to the imaginary part near threshold. But, at gamma-ray energies well below the pair production threshold the QED vacuum polarization term is well-approximated by the expression $\Delta_{\rm QED} = (\alpha/45\pi)\,(B_\perp/B_\hbar)^2$. $\Delta_{\rm QED}$ has a magnitude $\mathcal{O}(10^{-9})$ near the stellar surface and $\mathcal{O}(10^{-22})$ near the light cylinder, while the ALP-photon mixing term, $\Delta_{a\gamma}$ has the magnitudes $\mathcal{O}(10^{-15})$ and $\mathcal{O}(10^{-22})$ near the stellar surface and near the light cylinder, respectively, for an assumed coupling constant $g_{a\gamma} = 10^{-7}$.

Equation 7.2 can be written in terms of the density matrix

$$\rho = \begin{pmatrix} A_x \\ A_y \\ a \end{pmatrix} \otimes (A_x A_y a)^* \tag{7.9}$$

as $i\partial_z \rho(z) = [\mathcal{U}, \rho(z)]$. The solution of this equation gives

$$\mathcal{U} = e^{i\mathcal{M}z} \tag{7.10}$$

and

$$\rho(z) = \mathcal{U}_0^\dagger(z)\rho_0\mathcal{U}_0(z) \tag{7.11}$$

But somce $\mathcal{U}_0$ is no longer unitary, it is convenient to first find a new set of basis functions that diagonalize the mixing matrix in order to evaluate $\mathcal{U}$. Diagonalization of this mixing matrix yields a transfer matrix $\mathcal{U}$ of the form

$$\mathcal{U} = e^{i\lambda_1 d}\mathcal{T}_1 + e^{i\lambda_2 d}\mathcal{T}_2 + e^{i\lambda_3 d}\mathcal{T}_3 \tag{7.12}$$

with eigenvalues λ_i:

$$\begin{aligned}
\lambda_1 &= \Delta_{pl} + \tfrac{i}{2L} + \Delta_{\mathrm{QED}} \\
\lambda_2 &= \tfrac{1}{2}\left(\Delta_a + \Delta_{pl} + \tfrac{i}{2L} + \Delta_{\mathrm{QED}} - \sqrt{\left[\Delta_a - \left(\Delta_{pl} + \tfrac{i}{2L} + \Delta_{\mathrm{QED}}\right)\right]^2 + 4\Delta_{a\gamma}^2}\right) \\
\lambda_3 &= \tfrac{1}{2}\left(\Delta_a + \Delta_{pl} + \tfrac{i}{2L} + \Delta_{\mathrm{QED}} + \sqrt{\left[\Delta_a - \left(\Delta_{pl} + \tfrac{i}{2L} + \Delta_{\mathrm{QED}}\right)\right]^2 + 4\Delta_{a\gamma}^2}\right)
\end{aligned} \tag{7.13}$$

For notational simplicity we introduce δ such that

$$\delta = 2\Delta_{a\gamma}L \tag{7.14}$$

Using the mixing angle notation, the matrices $\mathcal{T}_i$ can be written

$$\mathcal{T}_1 = \begin{pmatrix} \cos^2\psi & -\sin\psi\cos\psi & 0 \\ -\sin\psi\cos\psi & \sin^2\psi & 0 \\ 0 & 0 & 0 \end{pmatrix}$$

$$\mathcal{T}_2 = \begin{pmatrix} \frac{-1+\sqrt{1-4\delta^2}}{2\sqrt{1-4\delta^2}}\sin^2\psi & \frac{-1+\sqrt{1-4\delta^2}}{2\sqrt{1-4\delta^2}}\sin\psi\cos\psi & \frac{i\delta}{\sqrt{1-4\delta^2}}\sin\psi \\ \frac{-1+\sqrt{1-4\delta^2}}{2\sqrt{1-4\delta^2}}\sin\psi\cos\psi & \frac{-1+\sqrt{1-4\delta^2}}{2\sqrt{1-4\delta^2}}\cos^2\psi & \frac{i\delta}{\sqrt{1-4\delta^2}}\cos\psi \\ \frac{i\delta}{\sqrt{1-4\delta^2}}\sin\psi & \frac{i\delta}{\sqrt{1-4\delta^2}}\cos\psi & \frac{1+\sqrt{1-4\delta^2}}{2\sqrt{1-4\delta^2}} \end{pmatrix}$$

$$\mathcal{T}_3 = \begin{pmatrix} \frac{1+\sqrt{1-4\delta^2}}{2\sqrt{1-4\delta^2}}\sin^2\psi & \frac{1+\sqrt{1-4\delta^2}}{2\sqrt{1-4\delta^2}}\sin\psi\cos\psi & \frac{-i\delta}{\sqrt{1-4\delta^2}}\sin\psi \\ \frac{1+\sqrt{1-4\delta^2}}{2\sqrt{1-4\delta^2}}\sin\psi\cos\psi & \frac{1+\sqrt{1-4\delta^2}}{2\sqrt{1-4\delta^2}}\cos^2\psi & \frac{-i\delta}{\sqrt{1-4\delta^2}}\cos\psi \\ \frac{-i\delta}{\sqrt{1-4\delta^2}}\sin\psi & \frac{-i\delta}{\sqrt{1-4\delta^2}}\cos\psi & \frac{-1+\sqrt{1-4\delta^2}}{2\sqrt{1-4\delta^2}} \end{pmatrix}$$

The probability that a photon beam initially in some state ρ_i will be found in the ρ_f state after propagating some distance d is

$$P_{\rho_i \to \rho_f} = \mathrm{Tr}\left[\rho_{\mathrm{f}}\mathcal{U}\rho_{\mathrm{i}}\mathcal{U}^\dagger\right] \tag{7.15}$$

The density matrix for an unpolarized beam ρ_{unpol} and the density matrix for an ALP state ρ_a are

$$\rho_{\mathrm{unpol}} = \frac{1}{2}\begin{pmatrix} 1 & 0 & 0 \\ 0 & 1 & 0 \\ 0 & 0 & 0 \end{pmatrix}$$

$$\rho_a = \begin{pmatrix} 0 & 0 & 0 \\ 0 & 0 & 0 \\ 0 & 0 & 1 \end{pmatrix}$$

We are interested in the case of an unpolarized beam of VHE photons propagating through a pulsar magnetosphere and the rate at which such photons convert to ALPs. The probability of ALP-photon oscillations is given by

$$P_{\gamma \to a} = \mathrm{Tr}\left[\rho_{\mathrm{a}}\mathcal{U}\rho_\gamma\mathcal{U}^\dagger\right] \tag{7.16}$$

The probability of ALP-photon oscillation is calculated for positions throughout a pulsar magnetosphere for a photon beam with energy $E_\gamma = 100$ GeV and for $E_\gamma = 1$ TeV, with the ALP-photon coupling taking a range of values. The results are shown in Figure 7.8

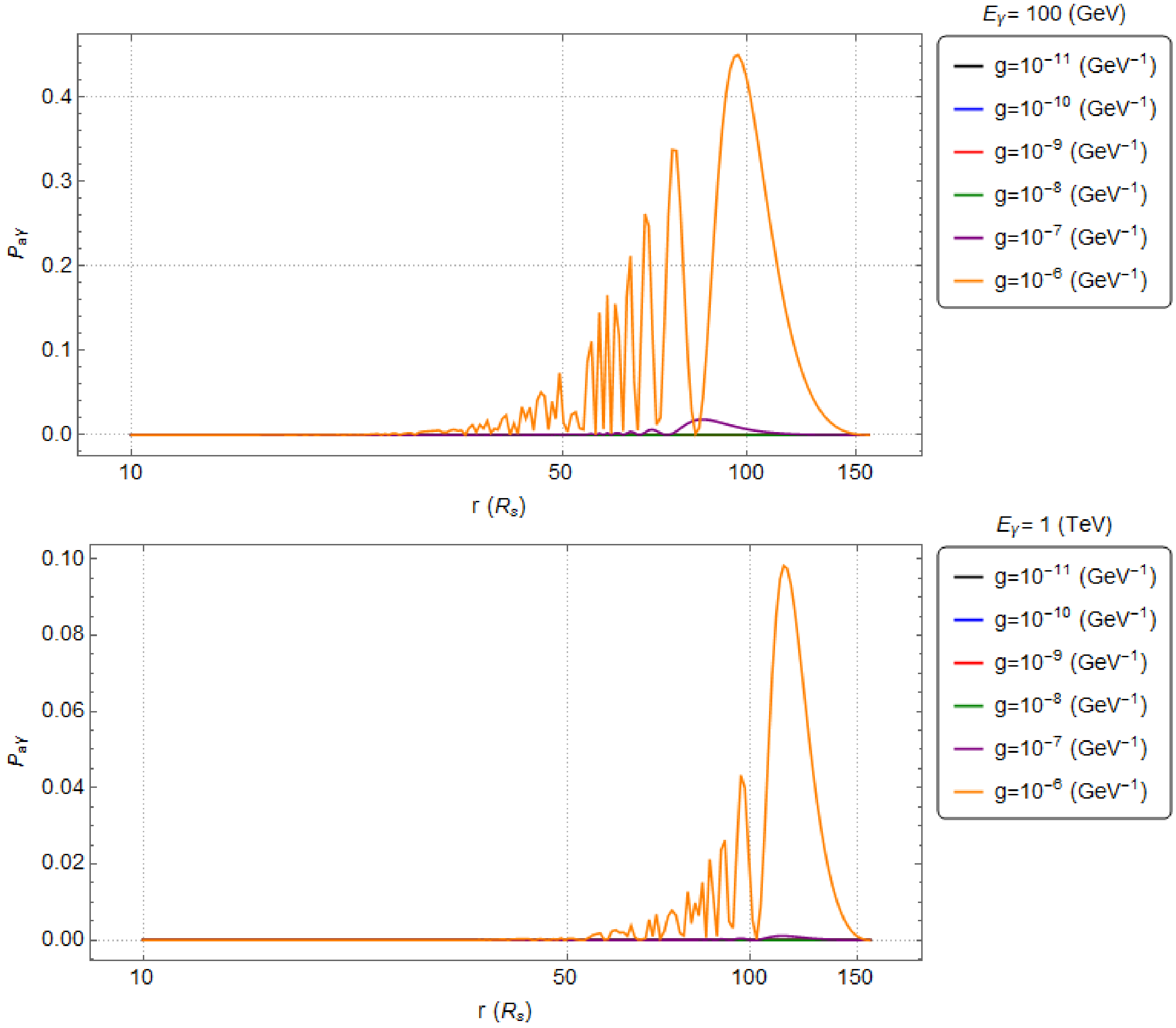

Figure 7.8: Probability of photon-ALP oscillation at locations through a pulsar magnetosphere calculated using Equation 7.16 where $m_a = 10^{-4}$ eV and d is the distance to the light cylinder from the initial position. $P_{a\gamma}$ is shown for $E_\gamma = 100$ GeV (top), $E_\gamma = 1$ TeV (bottom) with various values of g. The $x-$axis gives the emission location of the considered photon, d is measured from this distance. Both graphs show that the probability of oscillation is negligible until beyond $10R_s$. In general lower energy photons have a larger probability of oscillation for the parameters considered. The suppression of the ALP-photon oscillations near the stellar surface is due to inclusion of the vacuum polarization term, Δ_{QED}, and the oscillation probability becomes nonnegligible once the other terms are of the same order of magnitude as Δ_{QED}. Including Δ_{QED} inside of the pair producing region is clearly not rigorously correct, but is shown here to bound the possible effects of vacuum polarization.

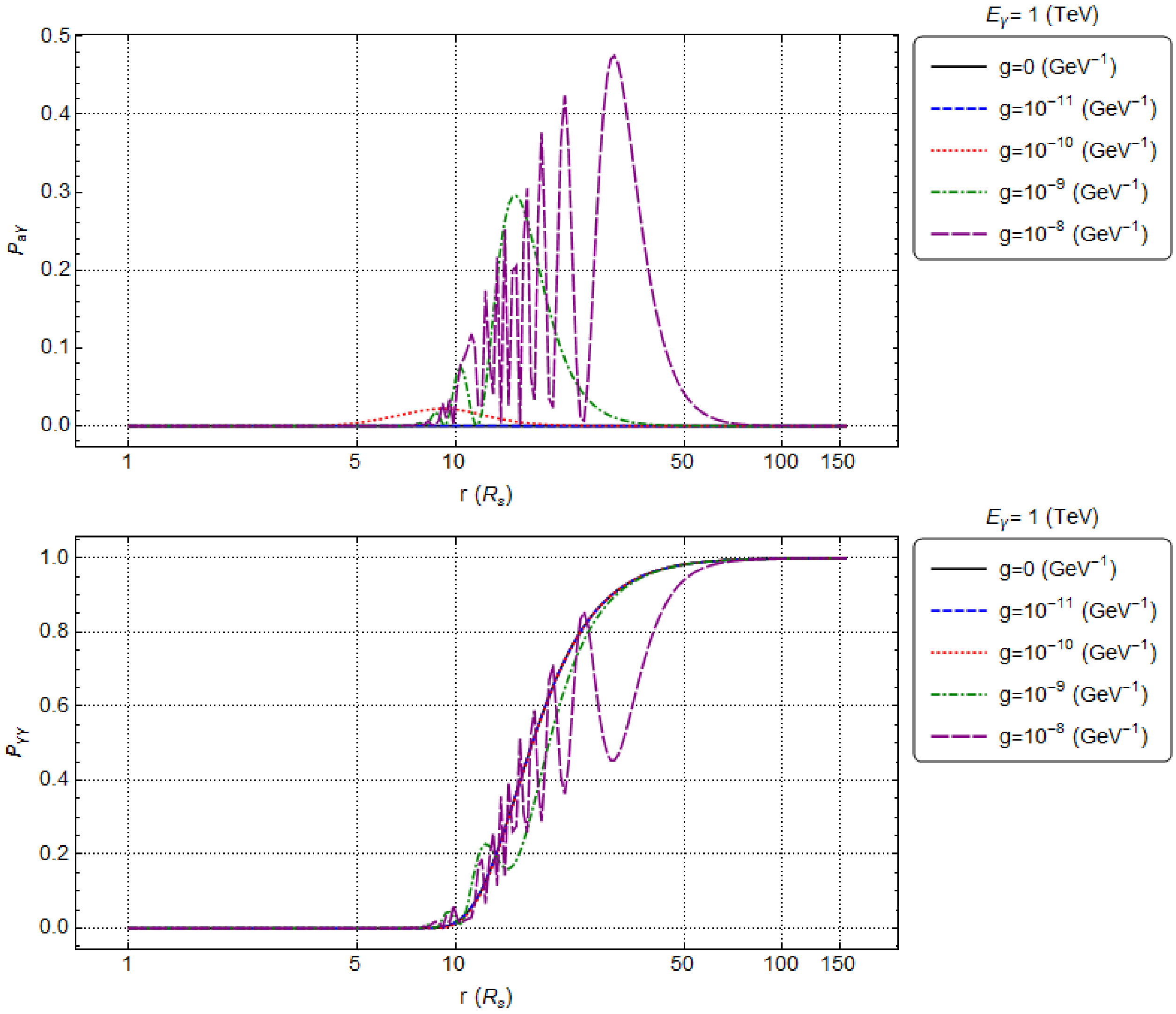

Figure 7.9: Probability of photon-ALP oscillation (top) and probability of photon survival (bottom) at locations through a pulsar magnetosphere calculated using Equation 7.15 with Δ_{QED} set to zero where $m_a = 10^{-4}$ eV, $E_\gamma = 1$ TeV d is the distance to the light cylinder from the initial position. The $x-$axis gives the emission location of the considered photon. The graph of $P_{a\gamma}$ shows that the probability of oscillation negligible until beyond $5R_s$. The suppression of ALP-photon oscillations near the stellar surface is due to the strength of the pair absorption term in this region. ALP-photon oscillations are limited to a narrow region of the magnetosphere.

7.3.3 Monte Carlo Simulation of Photons

The recent observations by VERITAS and MAGIC of the Crab pulsar up to > 400 GeV energies and the analysis presented in Chapter 5, paired with the natural overlap in $d_{\max}$ and L at these energies motivates a more careful examination of ALP-photon oscillations on observable quantities like the light curves and spectra of the VHE emission. To study this effect, a Monte Carlo simulation of the emission and propagation of VHE photons is performed. The generation of a distribution of VHE photons throughout the theoretical emission regions in a pulsar magnetosphere is described in Chapter 6. The same algorithm is applied here.

Photon distributions are simulated for each combination of pulsar parameters given in 6.1. The parameters for each photon (initial position, energy, phase position, path to observer) are then used with Equation 7.16 to calculate the probability of ALP-photon oscillation and the probability of photons surviving in either polarization state. Rather than directly using the probability in a Monte Carlo calculation to accept or reject individual events, the probability of photon survival $P_{\gamma\gamma}$ for an individual photon position and energy is used as a weighting factor for the produced light curve and differential energy spectrum to preserve computational resources.

7.4 Results

The results of the Monte Carlo simulations of photon emission and propagation in pulsar magnetospheres are presented for each of the viewing geometries discussed in Chapter 6. Photon distributions are generated for $500,000$ photons uniformly distributed throughout the emission region as described in Chapter 6. Energies are assigned to the photons using a power-law spectrum with parameters from the 2011 VERITAS observations of the Crab with

Viewing Angle (ζ)	Geometry Spectral Index (Γ_G)	Pair Attenuation Spectral Index (Γ_{pp})	ALP-mixing Spectral Index ($\Gamma_{a\gamma}$)
$\pi/12$	-2.36 ± 0.03	-2.45 ± 0.04	-2.36 ± 0.04
$\pi/6$	-2.38 ± 0.02	-2.40 ± 0.02	-2.40 ± 0.02
$\pi/4$	-2.40 ± 0.01	-2.41 ± 0.01	-2.41 ± 0.01
$\pi/3$	-2.37 ± 0.02	-2.64 ± 0.05	-2.64 ± 0.05
$5\pi/12$	-2.45 ± 0.02	-3.73 ± 0.11	-3.73 ± 0.11
$\pi/2$	-2.56 ± 0.05	–	–

Table 7.1: Results of Spectral Fit with Power Law Function

a threshold energy of 600 GeV. Photons are then propagated through the magnetosphere and the probability of ALP-mixing, $P_{a\gamma}$,; the probability of photon survival, $P_{\gamma\gamma}$,; and the probability of pair attenuation are calculated.

Figure 7.10 shows the light curves (a) and the SEDs (b) for each simulated viewing angle for one selected pulsar inclination angle $\xi = \pi/3$. The full results for all simulated values of ξ are shown in Appendix C. Very little effect on the spectrum is seen from ALP-photon oscillations. However, Figure 7.11 shows a small but significant difference in the light curve. Three physical scenarios are considered:

1. the geometric effects of the pulsar magnetosphere and viewing angles
2. the geometric effects and the effects of pair attenuation
3. the geometric effects, the effects of pair attenuation and the effects of ALP-photon oscillations

The three scenarios are shown in the same plots for comparison. Figure 7.10a shows light curves for the three physical scenarios considered. Four of the six viewing angles have negligible differences between the “observed” light curves with and without pair creation

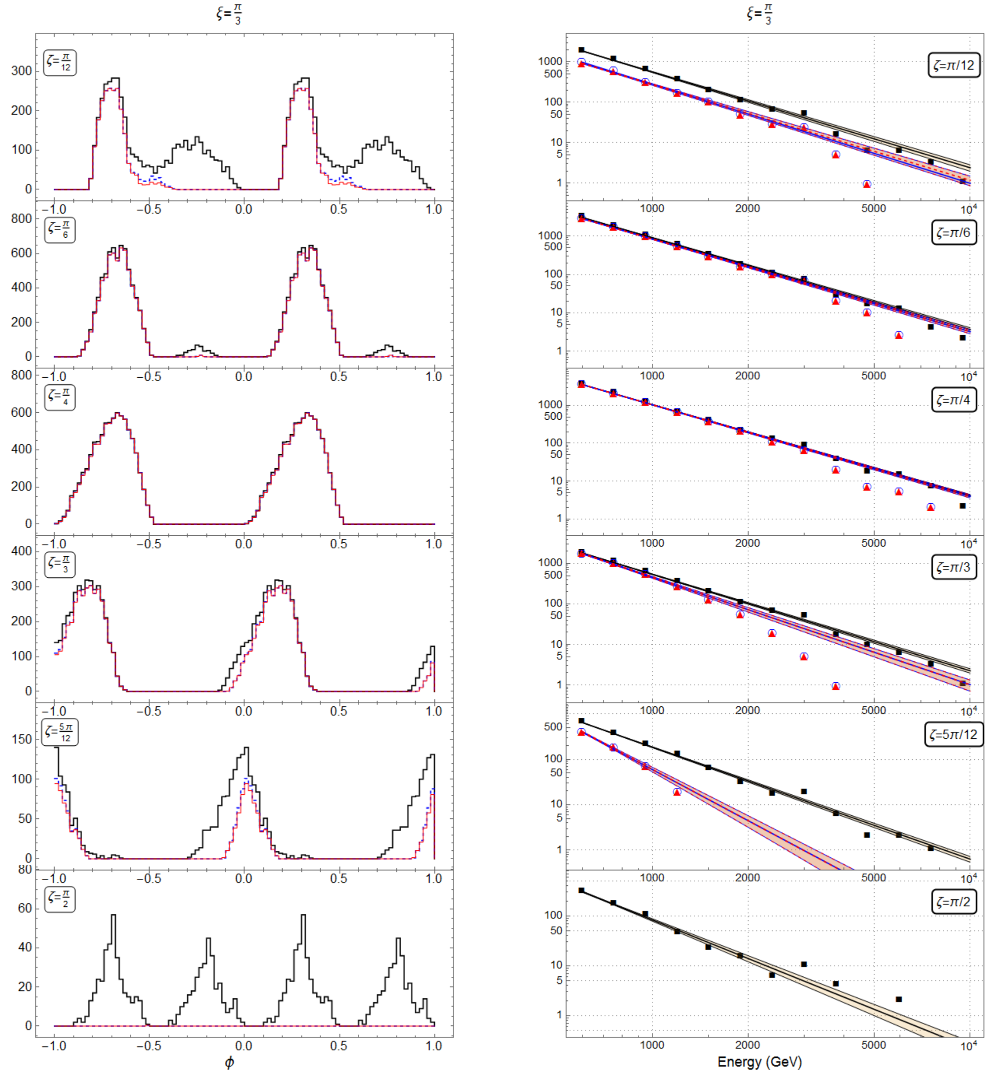

(a) Light Curves

(b) SEDs

Figure 7.10: Results of simulations of photon emission and propagation in a pulsar magnetosphere with inclination angle $\xi = \pi/3$ and various viewing angles. Light curves are shown (left) for the observed photons with considerations for geometry only (black), geometry and pair attenuation (red) and geometry, pair attenuation and ALP-photon mixing (blue). For many viewing angles variations in light curves are negligible. More pronounced effects are seen for $\zeta = \pi/12$ and $\zeta = \pi/2$. Differential spectra are shown (right) for the observed photons with consideration for geometry only (black), geometry and pair attenuation (red) and geometry, pair attenuation and ALP-photon mixing (blue). Each distribution is fit with a power law function (solid line) and 95% confidence bands (dotted line) are shown. The best-fit spectral indices for each viewing angle are shown in Table 7.1.

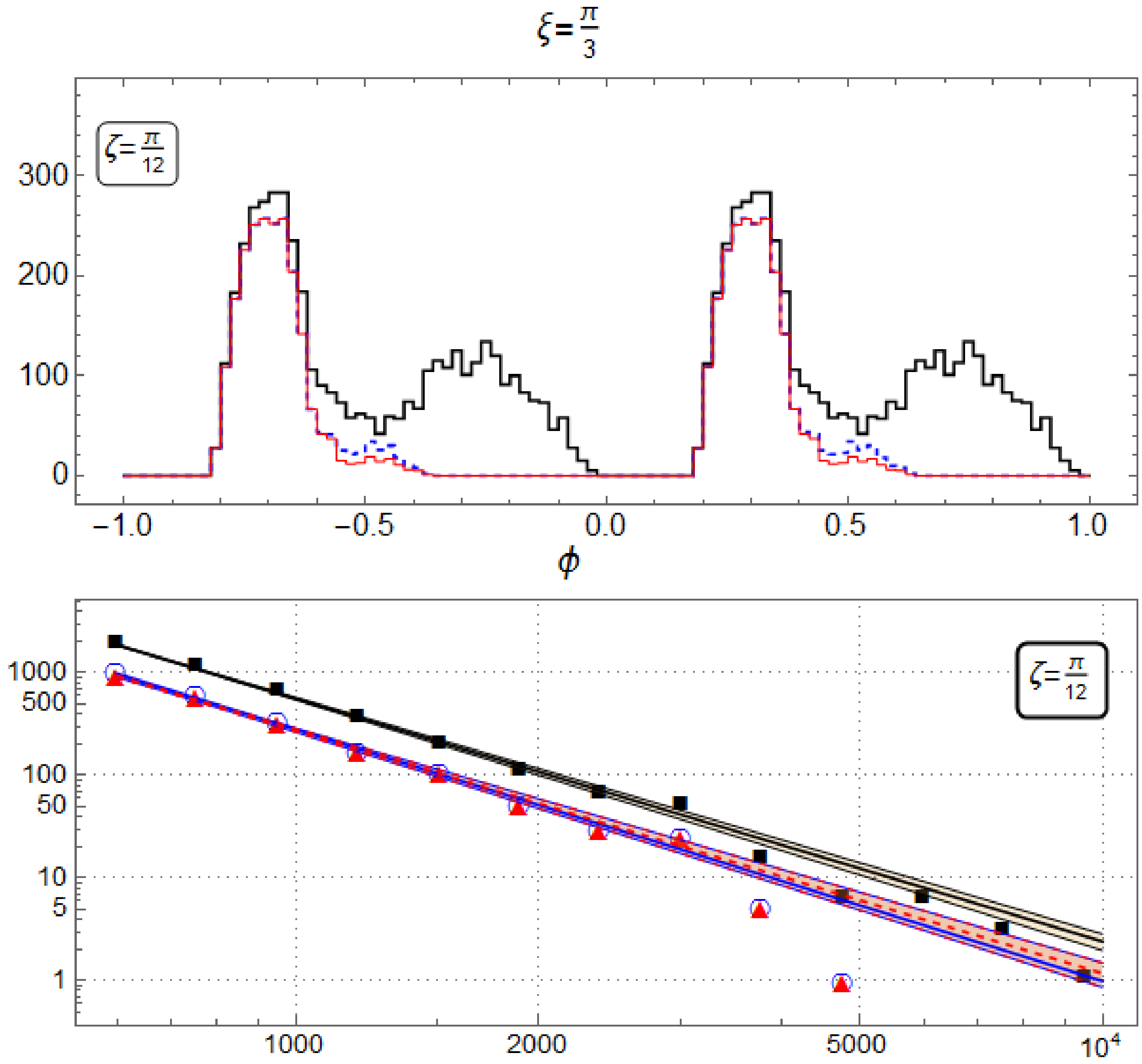

Figure 7.11: Results of simulations of photon emission and propagation in a pulsar magnetosphere with inclination angle $\xi = \pi/3$ and $\zeta = \pi/12$. The light curve is shown (above) for the observed photons with considerations for geometry only (black), geometry and pair attenuation (red) and geometry, pair attenuation and ALP-photon mixing (blue). The differential spectrum is shown (bottom) for the observed photons with consideration for geometry only (black), geometry and pair attenuation (red) and geometry, pair attenuation and ALP-photon mixing (blue). Each distribution is fit with a power law function (solid line) and 95% confidence bands (dotted line) are shown. The best-fit spectral indices are shown in Table 7.1.

and do not hold promising outlooks for observational constraints. The two extremes of viewing angles $\zeta = \pi/12$ and $\zeta = \pi/2$ show some visible differences between the light curve for scenarios (1),(2) and (3) (see expanded view Figure 7.11). In scenario (1) photons survival is dependent only on the angle between propagation and the line of sight to the observer. In scenario (2) photons have an addition dependency on pair attenuation. Any discrepancies between (1) and (2) are solely the result of pair attenuation. In scenario (3) photons that may be "observed" in scenario (1) may oscillate into an ALP state and not survive or they may oscillate in a fashion that allows the photon to survive propagation when otherwise the photon would undergo pair production. Photons emitted in the observed phases $0.0 - 0.25$ are highly attenuated in scenario (2) with few to no photons surviving propagation. In scenarios (1) and (3) the light curves are identical, demonstrating that for some geometries ALP-mixing allows for the survival of photons that would otherwise be attenuated. While Figure 7.10a shows that there may be a difference in the light curve from pulsars due to ALP mixing, there are many complicating factors to explaining particular light curve shapes and a minor variation in light curve shape could be explained using one of many other models or factors that determine light curve shapes.

The 2011 VERITAS observations of VHE pulsed emission from the Crab and the following 2015 MAGIC observations of TeV pulsed emission from the Crab came as somewhat of a surprise because VHE photons are expected to be heavily attenuated in the strong magnetic fields of pulsar magnetospheres. The precise nature of the VHE emission is not yet understood or agreed upon, but current models do not allow for such high-energy emission near the stellar surface. Figure 7.10b shows varying influence of ALP-mixing on the spectral shape of a pulsar for different viewing angles. The spectral points are determined from the simulated photon distribution and consideration of physical effects from scenarios (1), (2) and (3). For scenario (1) a simple beaming angle cut is applied. For scenario (2) the optical depth is calculated and photons in the optically thick regime are not "observed" following the prescription in Chapter 6. For scenario (3) the probability of photon survival is calculated using Equation 7.16 and this probability is applied as a weighting factor. A best fit is performed using a power law on the resulting energy distributions of surviving photons. The power law function has the form:

$$F(E) = F_0 \left(E/E_0\right)^{\Gamma} \tag{7.17}$$

The energy E_0 is set to 150 GeV for all cases. The results of the fit for each viewing angle and physical scenario are shown in Table 7.1. Pair attenuation is expected to primarily affect the spectral index due the energy dependence of attenuation. If ALP-mixing allows for an increased survival rate for VHE photons, then the spectral index of the power law fits are expected to be more similar for (1) and (3) than (1) and (2). For viewing angles $\zeta = \pi/6$, $\zeta = \pi/4$, and $\zeta = \pi/3$ the SEDs are nearly indistinguishable. The spectral indices from the power law fit are all within agreement for these viewing angles. For viewing angles $\zeta = \pi/12$, $\zeta = 5\pi/12$, and $\zeta = \pi/2$ the SEDs are visually distinct for scenario (2) compared to scenarios (1) and (3). The spectral indices Γ_G and $\Gamma_{a\gamma}$ are in agreement within the best-fit errors. The spectral index Γ_{pp} is not in agreement with Γ_G nor $\Gamma_{a\gamma}$ for these viewing angles.

These differences in spectral indices can serve as a key metric to constrain the ALP parameter space using VHE observations of pulsars. In addition to the difference in spectral index amongst the physical scenarios considered, all photons above 500 GeV are attenuated for the case $\xi = \pi/3$ and $\zeta = \pi/2$. For some geometries VHE emission will be exteremely weak or nonexistent without the inclusion of ALP-photon mixing.

Currently the Crab pulsar is the only known VHE pulsar. With new generation experiments such as Cherenkov Telescope Array, which will have a greater sensitivity to gamma rays than current generation telescopes, more VHE pulsars may be added to the catalog. With a population of VHE pulsars the ALP parameter space can be probed using the methods described in this work and constraints can be placed on the ALP mass and coupling constant. These constraints will complement the constraints from other astrophysical studies and experimental searches.

Chapter 8

Conclusion

In this dissertation, the VHE photon emission and propagation from pulsars are studied in detail. Several theoretical models (polar cap, slot gap and outer gap models) have been proposed to explain radiative emission from pulsars. One distinguishing factor of these models is the location of emission regions. With new observations from the VHE band better constraints are placed on the theoretical models. New results from ∼150 hours of VERITAS observations of the Crab are presented in Chapter 5. Significant pulsed emission is seen up to 400 GeV extending the Crab spectrum. The MAGIC detection of pulsed emission up to ∼2 TeV cannot be confirmed by the VERITAS results; a deeper exposure is necessary to further extend the spectrum of the Crab. The highest energies from the Crab observed by VERITAS place a limit on the minimum height above the stellar surface of VHE emission at $12R_s$. The energy spectrum observed by VERITAS cannot be reproduced by curvature radiation alone. Additional emission mechanisms such as inverse Compton scattering are likely needed to account for the VHE pulsed emission beyond the spectral break. In addition to ongoing observations of the Crab, the detection of other VHE pulsars would also greatly aid in the understanding of these emission mechanisms.

The observed light curves of pulsars are heavily impacted by geometry. The Monte Carlo simulations described in Chapter 6 demonstrate the range of light curves produced by different geometries. Consideration of special relativistic effects is required to produce light curves similar to observed pulsar light curves. Time-of-flight and aberration effects drastically shift the distribution of photons to produce the observed asymmetric light curves. Photons in the VHE regime are subject to pair production interactions when propagating through strong magnetic fields. Pulsar magnetospheres can even become completely opaque to VHE photons for some geometries. For one considered geometry all simulated photons above 400 GeV were absorbed. In other cases, for example for a pulsar with magnetic inclination angle $\xi = \pi/3$, there exist viewing angles at which few VHE photons are attenuated. There also exist misalignment and viewing angles at which pair attenuation significantly alters the observed pulsed signal and could result in significant differences in the GeV and several-hundred GeV emission. The VHE spectrum of pulsars is also strongly modified due to pair attenuation at higher energies. The suppression of the highest energy signals by pair attenuation limits the possibility of ground-based detection to certain geometries and should be taken into account in the selection of new source candidates. I investigated the possibility that ALP-photon oscillations might change the observed lightcurves or spectrum of gamma rays by either allowing more VHE gamma rays to escape pair creation or to convert to axions without reconverting to gamma rays.

A theoretical solution to the strong CP problem of QCD, the axion, is considered in this work as a possible means of decreasing the opacity of pulsar magnetospheres to VHE photons. Axions, psuedo-Nambu Goldstone bosons, have been proposed as a solution to the strong CP problem and by virtue of their coupling to quarks must also couple to photons allowing for axion-photon oscillations. A broader class of pseudo-scalar, axion-like particles that share the coupling with electromagnetism could arise from other extensions to the Standard Model. Chapter 7 describes Monte Carlo simulations of ALP-photon mixing as VHE photons propagate through pulsar magnetospheres. This dissertation demonstrates that for ALP masses 10^{-4} eV $< m_a <$ 10 eV and coupling constants 10^{-11} GeV^{-1} $< g_{a\gamma} <$ 10^{-6} GeV^{-1}

ALP-mixing can occur in some regions of pulsar magnetospheres. This mixing allows for photons to survive propagation that would otherwise be attenuated or for photons to convert to axions and escape from the outer magnetosphere. ALP-mixing is shown to have some small effect on the spectrum of pulsars at TeV energies and some effect on the shape of light curves. The effects of QED vacuum polarization dominate mixing at distances from the stellar surface just beyond the regime of strong pair attenuation out to near the light cylinder. The strength of the magnetic fields of pulsars warrants consideration of QED vacuum polarization effects, but the precise nature of these effects at photon energies $E_\gamma \gg m_e c^2$ are not well understood. For future work, one could follow the methodology of to use the Kramers-Kronig relationship between the real and imaginary (pair abosrption) part of the index of refraction to better characterize the transition region, between the low energy cauum polarization regime and the high energy pair production regime. Future investigations of the QED vacuum polarization effects near the pair threshold will provide a more realistic model to test ALP-photon mixing in pulsar magnetospheres. Better understanding of the possible effects of ALP-photon mixing on pulsar observations could yet result in methods to constrain the axion-ALP parameter space. The powerful magnetic fields of pulsars allow for a unique astrophysical laboratory to study possible signals from axions and ALPs. Even if ALP oscillations produce small effects on observables, the interplay between pair creation and geometry shown in this work underscores the unique role that can be played by VHE observations of pulsars.

Appendix A

List of Crab Data Run

Table A.1 Contains the full list of 422 quality-selected data observation runs used in the analysis of the Crab nebula and pulsar in Chapter 5. Descriptions of the quality-selection criteria used to generate this list of runs is described in Chapter 5. The 422 data runs used total ~ 150 hours of observations from 2007 to 2014.

Run ID										
36604	41727	44096	52128	53172	53490	54619	55128	64110	69915	70356
36634	41794	44097	52129	53205	53491	54645	55129	64257	69916	70373
37009	41851	44326	52141	53206	53519	54646	55130	64258	69979	70381
37010	41876	44327	52155	53207	53520	54679	55131	64259	70351	70438
37195	41877	44531	52173	53208	53521	54680	55139	64325	70355	70439
37230	41879	44549	52175	53209	53581	54681	55140	64326	70357	70441
37231	41925	44566	52390	53210	53582	54682	55141	64378	70458	70458
37266	41926	44684	52391	53263	53703	54683	55142	64379	70530	70461
37267	41988	44862	52419	53264	53704	54684	55143	64380	70996	70463
37297	42032	43754	52446	53265	53705	54685	55160	64443	70997	70487
37298	42438	43766	52447	53266	53734	54738	55161	64759	71223	70488
37945	42439	44098	52448	53267	53735	54739	55162	64760	71224	70489
37946	42440	48394	52449	53268	53736	54740	55163	65255	71247	70490
37947	42510	48395	52450	53269	53737	54741	55164	65311	71347	70532
37948	42553	48396	52477	53290	53738	54743	55186	65312	71348	70533
37949	42854	48397	52478	53291	53739	54744	55187	65370	71375	70690
37950	42893	48398	52479	53292	53740	54745	55188	65371	71454	70754
38032	42894	48399	52480	53294	53772	54772	55189	65404	71455	70755
38033	42895	48400	52481	53302	53811	54773	55212	65474	71477	71197
38034	42928	48401	52507	53304	54501	54774	55213	65776	71802	71198
38035	42948	48402	52508	53305	54502	54775	55214	65777	38753	71523
38061	42949	48403	52592	53306	54503	54776	55215	65778	38762	71524
38062	43366	48578	52593	53307	54519	54781	55243	65779	41793	71547
38063	43367	48579	52594	53317	54520	54782	55244	66002	57993	71916
38064	43464	48580	52595	53318	54521	54783	55272	66003	58193	
38200	43465	48581	53047	53319	54522	54806	55273	66534	58861	
38273	43757	48582	53048	53320	54550	54807	55301	67044	58862	
38405	43758	48583	53049	53332	54551	54808	55302	67071	58892	
38523	43759	48584	53075	53338	54554	54809	55303	67135	58893	
38722	43760	48585	53076	53420	54556	54810	55304	67137	58932	
38759	43761	48854	53109	53421	54558	54811	55332	67138	58933	
38764	43763	48921	53110	53422	54586	54813	55361	67251	58934	
38957	43764	48923	53111	53423	54587	54882	55362	67252	58935	
38958	43465	48924	53112	53424	54611	54883	55363	67271	58969	
39035	43757	48925	53166	53454	54612	54884	55392	67272	58970	
39036	43758	48926	53167	53455	54613	54886	55467	67292	58995	
39072	43759	48927	53168	53486	54614	54915	55468	67293	58996	
39073	43760	48928	53169	53487	54615	54916	55469	67332	70322	
39109	44015	48929	53170	53488	54616	54917	64108	69884	70323	
39459	44052	48930	53171	53489	54618	55127	64109	69914	70324	

Table A.1: Crab Pulsar Run List

Appendix B

Monte Carlo Simulations of VHE Emission and Propagation Results

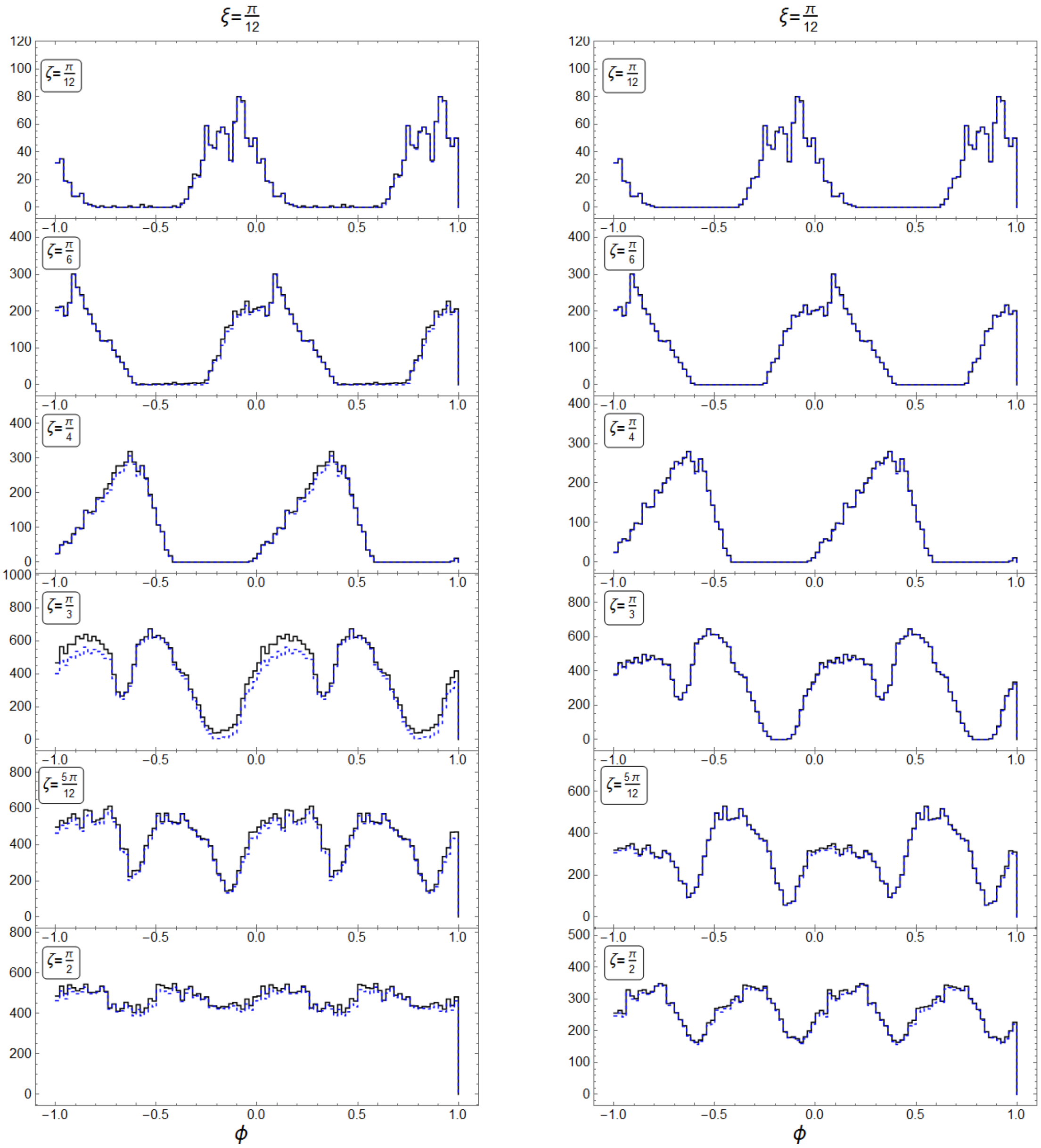

(a) Light curves using SG Model geometry (b) Light curves using OG Model geometry

Figure B.1: Light curves from simulations for SG and OG models with inclination angle $\xi = \pi/12$ and a range of viewing angles ζ. The light curves with only resulting only from geometric considerations are depicted in black for both SG and OG models. Some photons that are capable of being observed due to geometry are not observed due to pair attenuation in the strong magnetic fields of the magnetosphere. The light curves showing the effect of pair attenuation on VHE gamma rays are shown in blue. Some the light curves for some viewing angles, ζ, are more strongly affected than others. For viewing angles of similar value to the magnetic inclination angle the light curves are less affected as seen for both SG and OG models.

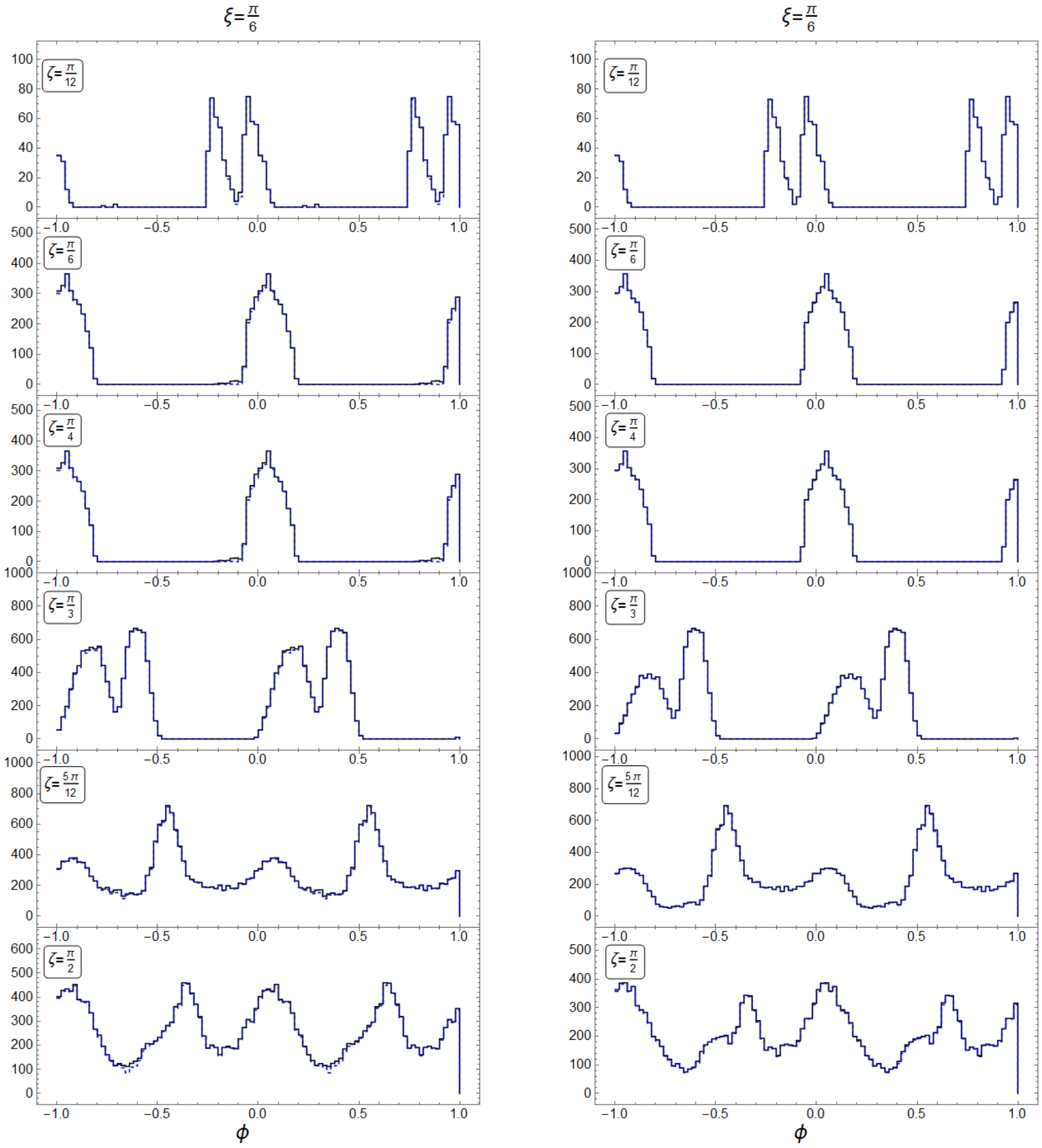

(a) Light curves using SG Model geometry (b) Light curves using OG Model geometry

Figure B.2: Light curves from simulations for SG and OG models with inclination angle $\xi = \pi/6$ and a range of viewing angles ζ. The light curves with only resulting only from geometric considerations are depicted in black for both SG and OG models. Some photons that are capable of being observed due to geometry are not observed due to pair attenuation in the strong magnetic fields of the magnetosphere. The light curves showing the effect of pair attenuation on VHE gamma rays are shown in blue. Some the light curves for some viewing angles, ζ, are more strongly affected than others. For viewing angles of similar value to the magnetic inclination angle the light curves are less affected as seen for both SG and OG models.

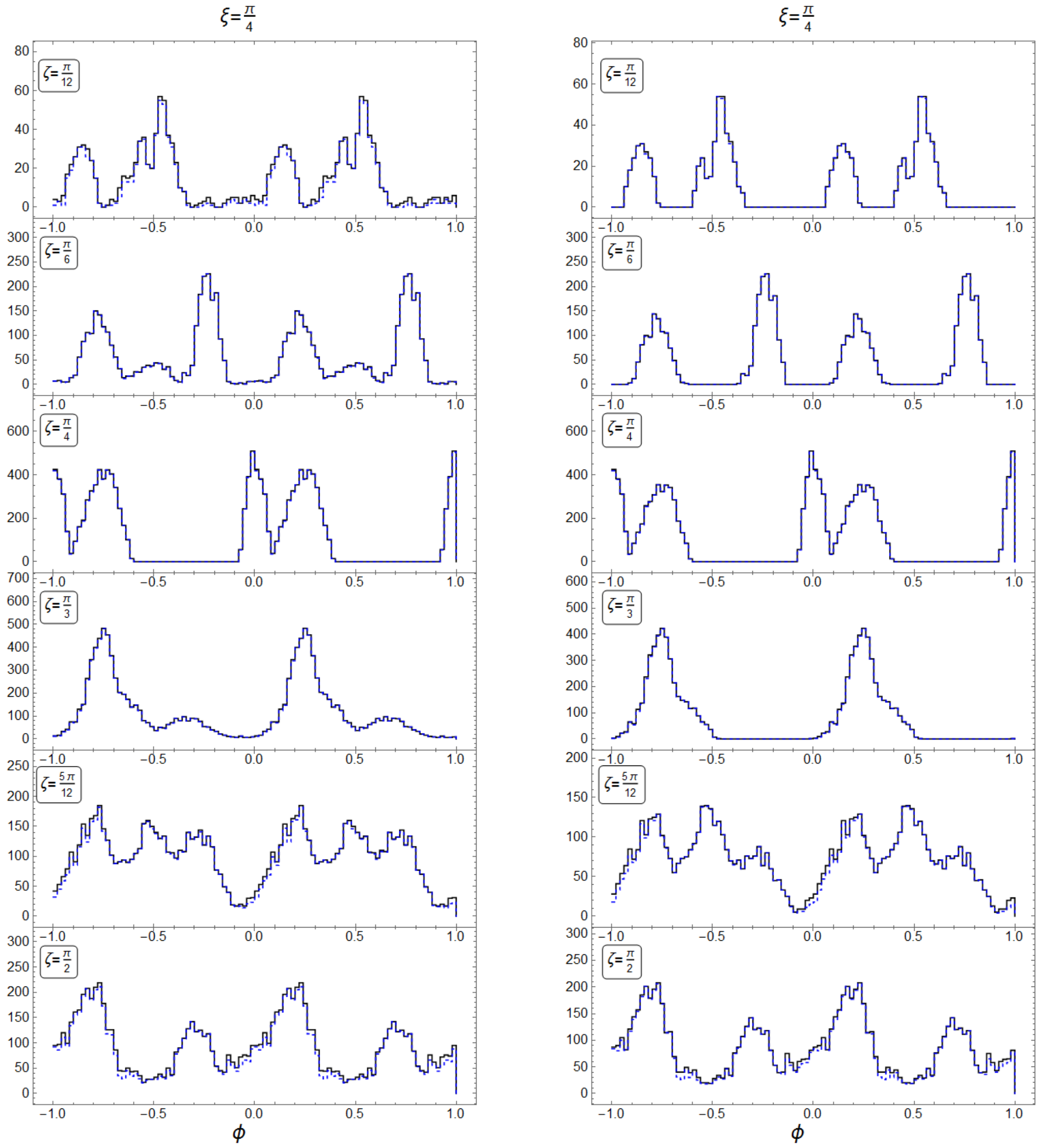

(a) Light curves using SG Model geometry (b) Light curves using OG Model geometry

Figure B.3: Light curves from simulations for SG and OG models with inclination angle $\xi = \pi/4$ and a range of viewing angles ζ. The light curves with only resulting only from geometric considerations are depicted in black for both SG and OG models. Some photons that are capable of being observed due to geometry are not observed due to pair attenuation in the strong magnetic fields of the magnetosphere. The light curves showing the effect of pair attenuation on VHE gamma rays are shown in blue. Some the light curves for some viewing angles, ζ, are more strongly affected than others. For viewing angles of similar value to the magnetic inclination angle the light curves are less affected as seen for both SG and OG models.

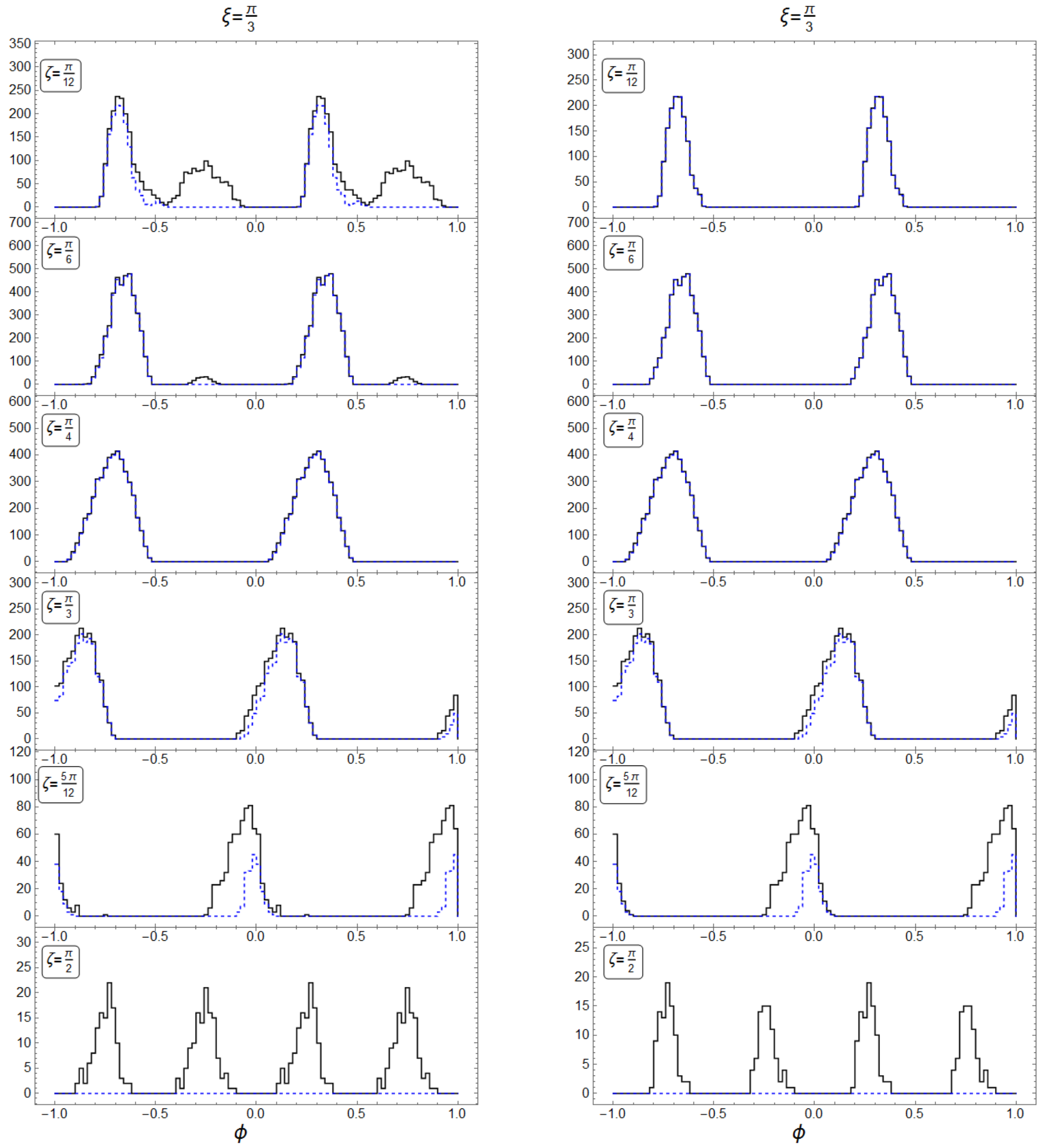

(a) Light curves using SG Model geometry (b) Light curves using OG Model geometry

Figure B.4: Light curves from simulations for SG and OG models with inclination angle $\xi = \pi/3$ and a range of viewing angles ζ. The light curves with only resulting only from geometric considerations are depicted in black for both SG and OG models. Some photons that are capable of being observed due to geometry are not observed due to pair attenuation in the strong magnetic fields of the magnetosphere. The light curves showing the effect of pair attenuation on VHE gamma rays are shown in blue. Some the light curves for some viewing angles, ζ, are more strongly affected than others. For viewing angles of similar value to the magnetic inclination angle the light curves are less affected as seen for both SG and OG models.

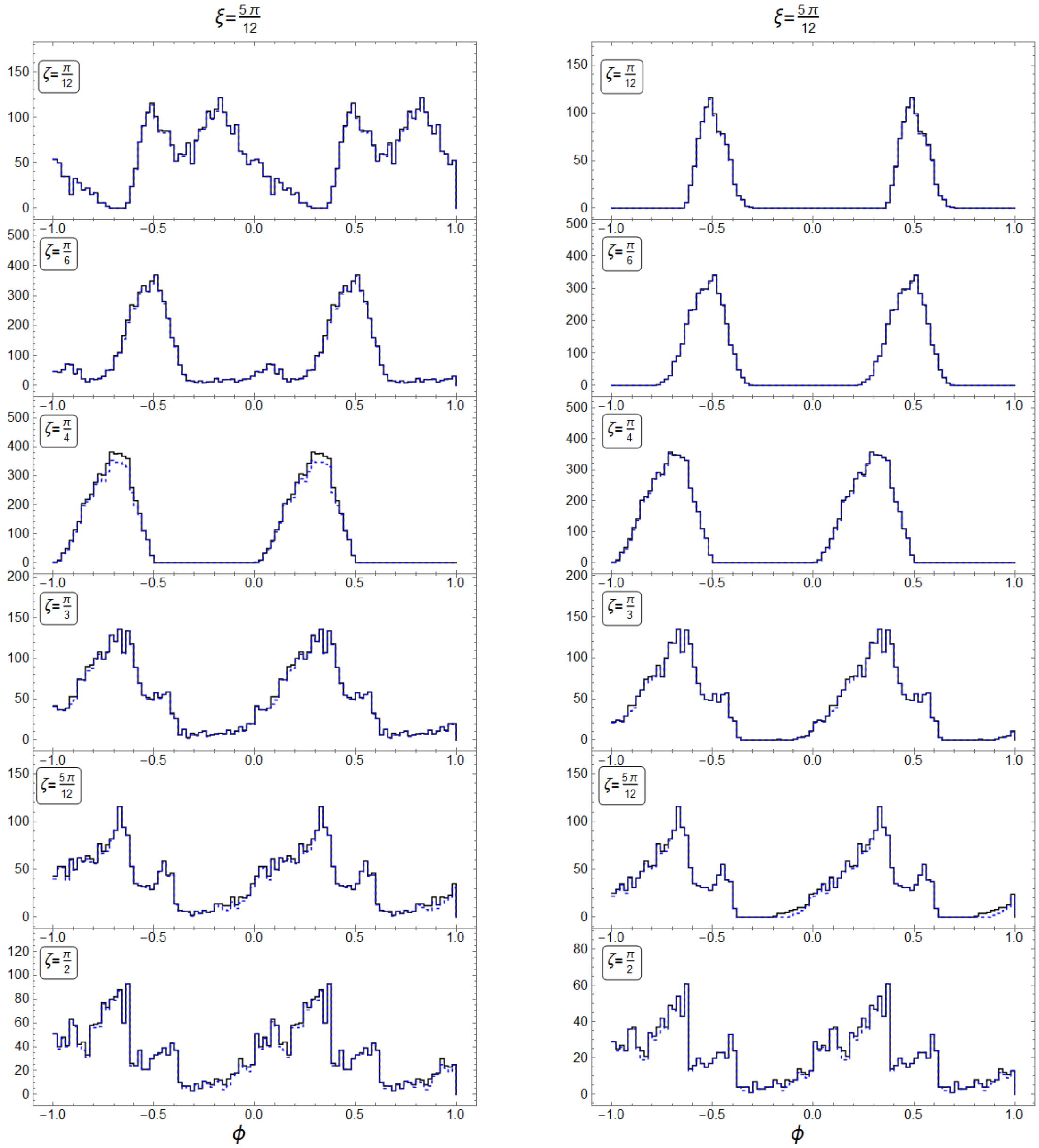

(a) Light curves using SG Model geometry (b) Light curves using OG Model geometry

Figure B.5: Light curves from simulations for SG and OG models with inclination angle $\xi = 5\pi/12$ and a range of viewing angles ζ. The light curves with only resulting only from geometric considerations are depicted in black for both SG and OG models. Some photons that are capable of being observed due to geometry are not observed due to pair attenuation in the strong magnetic fields of the magnetosphere. The light curves showing the effect of pair attenuation on VHE gamma rays are shown in blue. Some the light curves for some viewing angles, ζ, are more strongly affected than others. For viewing angles of similar value to the magnetic inclination angle the light curves are less affected as seen for both SG and OG models.

Appendix C

ALP-mixing Results

Some text about the results presented here in this appendix

Viewing Angle (ζ)	Geometry Spectral Index (Γ_G)	Pair Attenuation Spectral Index (Γ_{pp})	ALP-mixing Spectral Index ($\Gamma_{a\gamma}$)
$\pi/12$	–	–	–
$\pi/6$	–	–	–
$\pi/4$	-2.51 ± 0.01	-2.61 ± 0.01	-2.60 ± 0.01
$\pi/3$	–	–	–
$5\pi/12$	-2.51 ± 0.01	-2.54 ± 0.01	-2.54 ± 0.01
$\pi/2$	-2.51 ± 0.01	-2.53 ± 0.01	-2.53 ± 0.01

Table C.1: Results of Spectral Fit with Power Law Function ($\xi = \pi/12$)

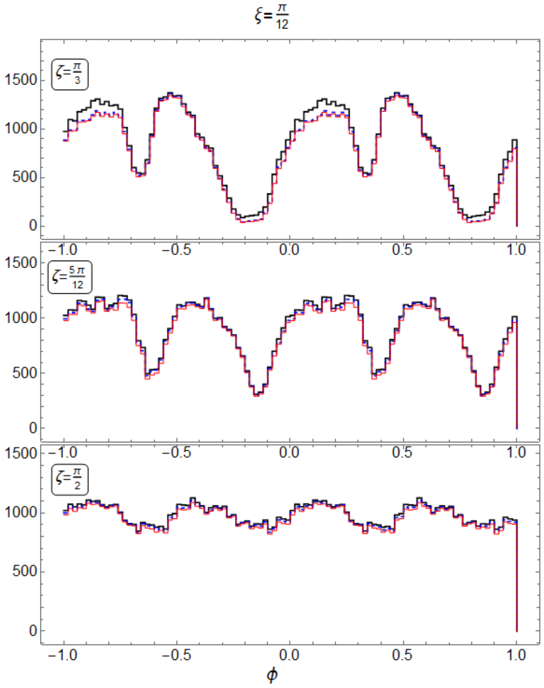

(a) Light Curves

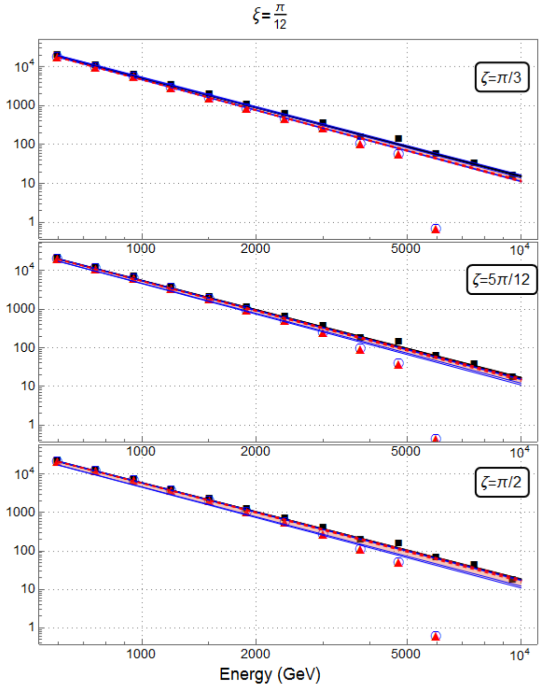

(b) SEDs

Viewing Angle (ζ)	Geometry Spectral Index (Γ_G)	Pair Attenuation Spectral Index (Γ_{pp})	ALP-mixing Spectral Index ($\Gamma_{a\gamma}$)
$\pi/12$	$-$	$-$	$-$
$\pi/6$	-2.49 ± 0.02	-2.53 ± 0.02	-2.51 ± 0.02
$\pi/4$	-2.49 ± 0.02	-2.53 ± 0.02	-2.51 ± 0.02
$\pi/3$	-2.53 ± 0.01	-2.54 ± 0.01	-2.54 ± 0.01
$5\pi/12$	-2.50 ± 0.01	-2.50 ± 0.01	-2.50 ± 0.01
$\pi/2$	-2.50 ± 0.01	-2.51 ± 0.01	-2.50 ± 0.01

Table C.2: Results of Spectral Fit with Power Law Function ($\xi = \pi/6$)

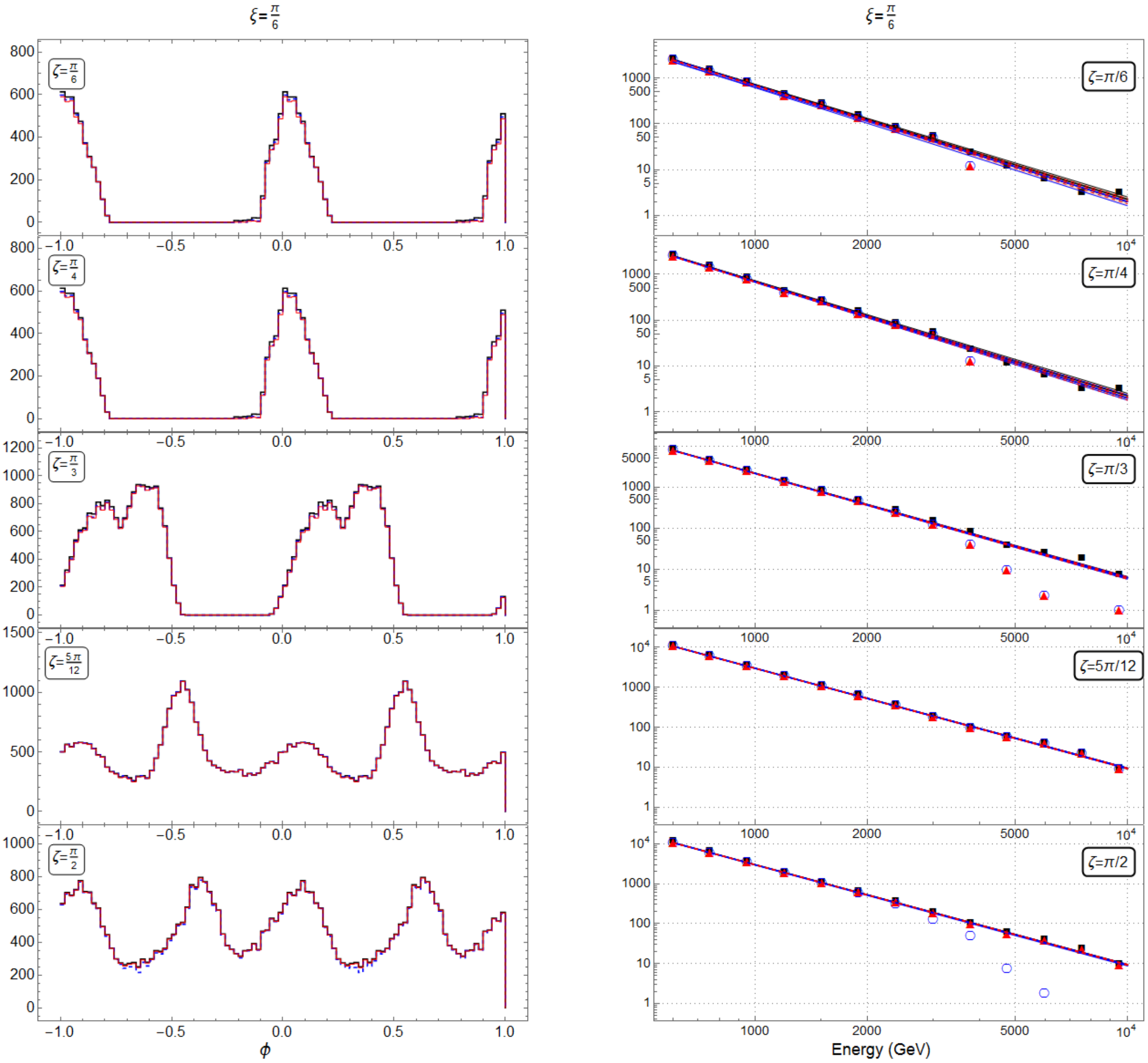

(a) Light Curves

(b) SEDs

Viewing Angle (ζ)	Geometry Spectral Index (Γ_G)	Pair Attenuation Spectral Index (Γ_{pp})	ALP-mixing Spectral Index ($\Gamma_{a\gamma}$)
$\pi/12$	-2.57 ± 0.04	-2.62 ± 0.04	-2.61 ± 0.04
$\pi/6$	-2.52 ± 0.02	-2.53 ± 0.02	-2.53 ± 0.02
$\pi/4$	-2.52 ± 0.02	-2.52 ± 0.02	-2.52 ± 0.02
$\pi/3$	-2.51 ± 0.01	-2.53 ± 0.01	-2.53 ± 0.01
$5\pi/12$	-2.55 ± 0.01	-2.61 ± 0.01	-2.61 ± 0.01
$\pi/2$	-2.54 ± 0.01	-2.58 ± 0.01	-2.58 ± 0.01

Table C.3: Results of Spectral Fit with Power Law Function ($\xi = \pi/4$)

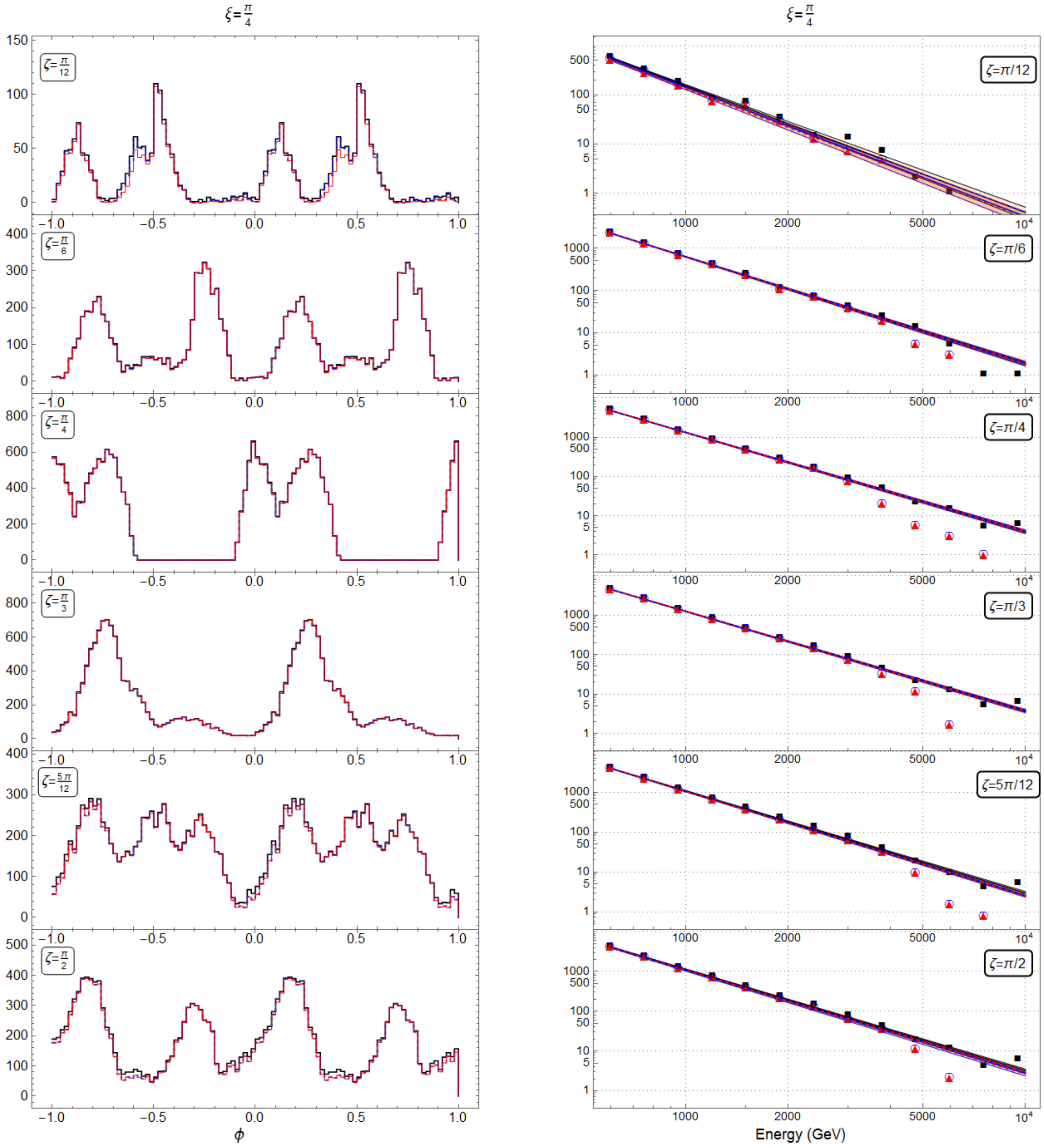

(a) Light Curves (b) SEDs

Viewing Angle (ζ)	Geometry Spectral Index (Γ_G)	Pair Attenuation Spectral Index (Γ_{pp})	ALP-mixing Spectral Index ($\Gamma_{a\gamma}$)
$\pi/12$	-2.63 ± 0.01	-2.86 ± 0.04	-2.62 ± 0.01
$\pi/6$	-2.49 ± 0.01	-2.50 ± 0.01	-2.49 ± 0.01
$\pi/4$	-2.52 ± 0.01	-2.53 ± 0.01	-2.52 ± 0.01
$\pi/3$	-2.51 ± 0.04	-2.51 ± 0.04	-2.50 ± 0.04
$5\pi/12$	-2.65 ± 0.02	-2.82 ± 0.03	-2.65 ± 0.02
$\pi/2$	-2.78 ± 0.11	-3.77 ± 0.04	-2.79 ± 0.11

Table C.4: Results of Spectral Fit with Power Law Function ($\xi = \pi/3$)

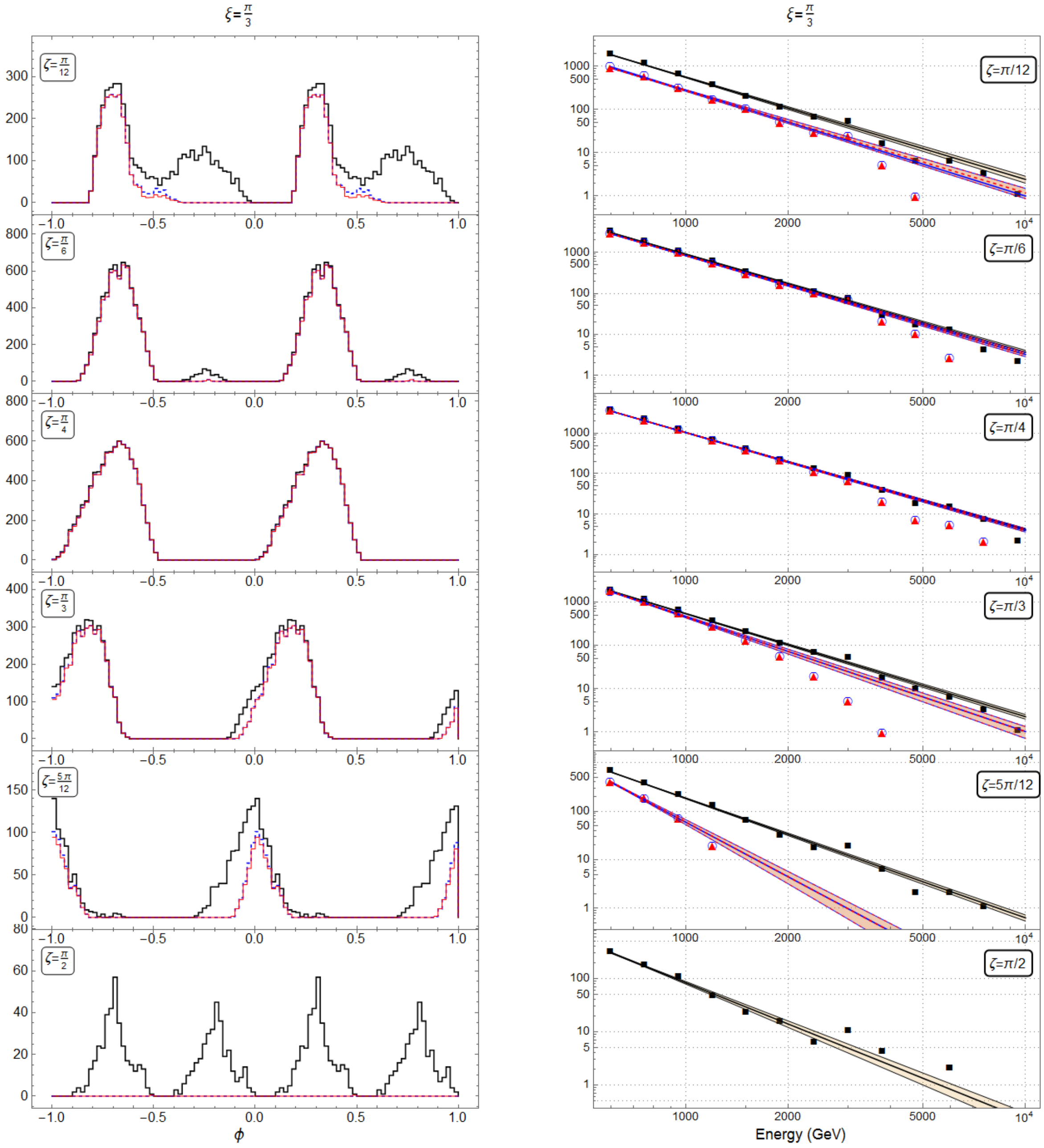

(a) Light Curves

(b) SEDs

Viewing Angle (ζ)	Geometry Spectral Index (Γ_G)	Pair Attenuation Spectral Index (Γ_{pp})	ALP-mixing Spectral Index ($\Gamma_{a\gamma}$)
$\pi/12$	–	–	–
$\pi/6$	–	–	–
$\pi/4$	-2.50 ± 0.02	-2.55 ± 0.02	-2.54 ± 0.02
$\pi/3$	-2.60 ± 0.02	-2.62 ± 0.03	-2.62 ± 0.03
$5\pi/12$	-2.54 ± 0.04	-2.60 ± 0.05	-2.59 ± 0.05
$\pi/2$	-2.58 ± 0.03	-2.61 ± 0.04	-2.60 ± 0.04

Table C.5: Results of Spectral Fit with Power Law Function ($\xi = 5\pi/12$)

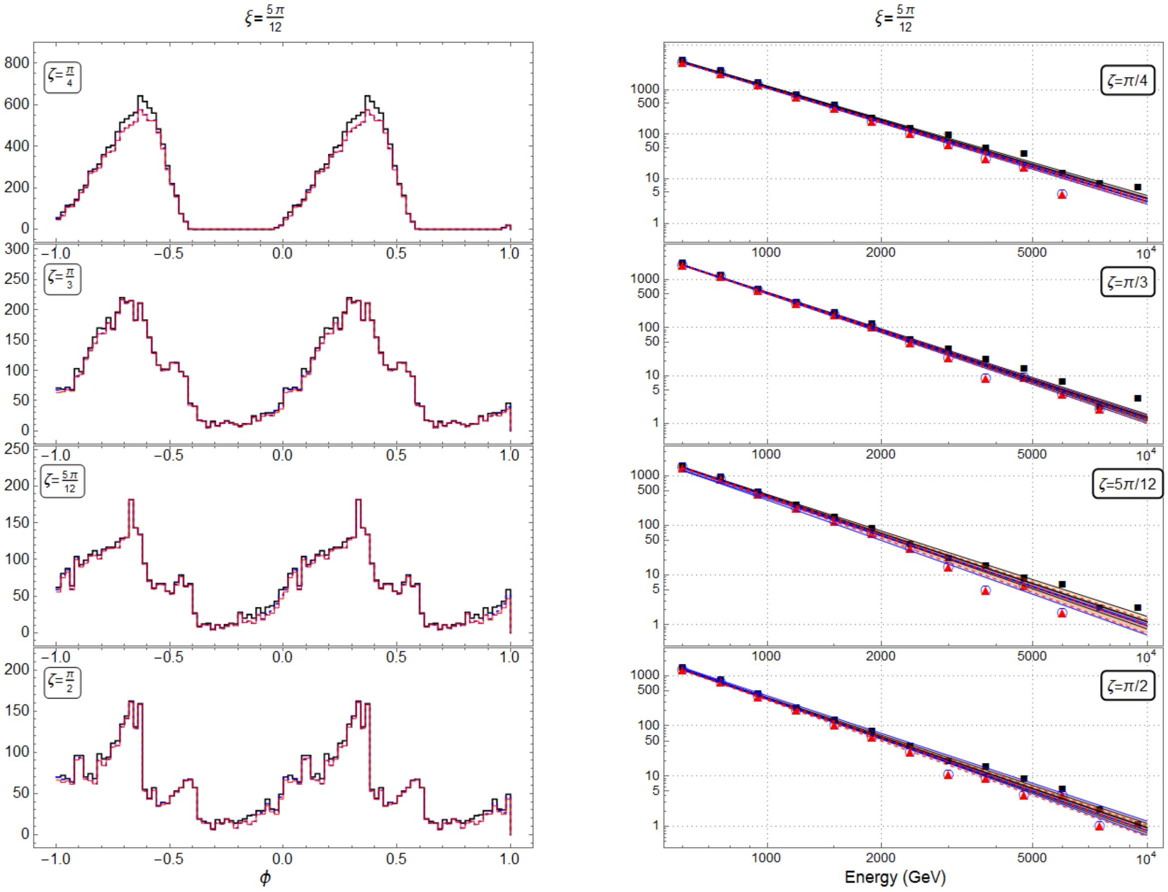

(a) Light Curves (b) SEDs

References

A. A. Abdo, M. Ackermann, W. B. Atwood, R. Bagagli, L. Baldini, J. Ballet, D. L. Band, G. Barbiellini, M. G. Baring, J. Bartelt, D. Bastieri, B. M. Baughman, K. Bechtol, F. Bellardi, R. Bellazzini, B. Berenji, D. Bisello, R. D. Blandford, E. D. Bloom, J. R. Bogart, E. Bonamente, A. W. Borgland, A. Bouvier, J. Bregeon, A. Brez, M. Brigida, P. Bruel, T. H. Burnett, G. A. Caliandro, R. A. Cameron, F. Camilo, P. A. Caraveo, J. M. Casandjian, M. Ceccanti, C. Cecchi, E. Charles, A. Chekhtman, C. C. Cheung, J. Chiang, S. Ciprini, R. Claus, I. Cognard, J. Cohen-Tanugi, L. R. Cominsky, J. Conrad, R. Corbet, L. Corucci, S. Cutini, D. S. Davis, M. DeKlotz, C. D. Dermer, A. de Angelis, F. de Palma, S. W. Digel, M. Dormody, E. do Couto e Silva, P. S. Drell, R. Dubois, D. Dumora, C. Espinoza, C. Farnier, C. Favuzzi, D. L. Flath, P. Fleury, W. B. Focke, M. Frailis, P. C. C. Friere, Y. Fukazawa, S. Funk, P. Fusco, F. Gargano, D. Gasparrini, N. Gehrels, S. Germani, R. Giannitrapani, B. Giebels, N. Giglietto, F. Giordano, T. Glanzman, G. Godfrey, E. V. Gotthelf, I. A. Grenier, M.-H. Grondin, J. E. Grove, L. Guillemot, S. Guiriec, G. Haller, A. K. Harding, P. A. Hart, R. C. Hartman, E. Hays, G. Hobbs, R. E. Hughes, G. Jhannesson, A. S. Johnson, R. P. Johnson, T. J. Johnson, W. N. Johnson, S. Johnston, T. Kamae, G. Kanbach, V. M. Kaspi, H. Katagiri, J. Kataoka, A. Kavelaars, N. Kawai, H. Kelly, M. Kerr, B. Kiziltan, W. Klamra, J. Kndlseder, M. Kramer, F. Kuehn, M. Kuss, J. Lande, D. Landriu, L. Latronico, B. Lee, S.-H. Lee, M. Lemoine-Goumard, M. Livingstone, F. Longo, F. Loparco, B. Lott, M. N. Lovellette, P. Lubrano, A. G. Lyne, G. M. Madejski, A. Makeev, R. N. Manchester, B. Marangelli, M. Marelli, M. N. Mazziotta, J. E. McEnery, S. McGlynn, M. A. McLaughlin, N. Menon, C. Meurer, P. F. Michelson, T. Mineo, N. Mirizzi, W. Mitthumsiri, T. Mizuno, A. A. Moiseev, M. Mongelli, C. Monte,

M. E. Monzani, E. Moretti, A. Morselli, I. V. Moskalenko, S. Murgia, T. Nakamori, P. L. Nolan, A. Noutsos, E. Nuss, T. Ohsugi, N. Omodei, E. Orlando, J. F. Ormes, M. Ozaki, A. Paccagnella, D. Paneque, J. H. Panetta, D. Parent, M. Pearce, M. Pepe, M. Perchiazzi, M. Pesce-Rollins, L. Pieri, M. Pinchera, F. Piron, T. A. Porter, S. Rain, R. Rando, S. M. Ransom, E. Rapposelli, M. Razzano, A. Reimer, O. Reimer, T. Reposeur, L. C. Reyes, S. Ritz, L. S. Rochester, A. Y. Rodriguez, R. W. Romani, M. Roth, F. Ryde, A. Sacchetti, H. F.-W. Sadrozinski, N. Saggini, D. Sanchez, A. Sander, P. M. Saz Parkinson, K. N. Segal, A. Sellerholm, C. Sgr, E. J. Siskind, D. A. Smith, P. D. Smith, G. Spandre, P. Spinelli, M. Stamatikos, J.-L. Starck, F. W. Stecker, T. E. Stephens, M. S. Strickman, A. W. Strong, D. J. Suson, H. Tajima, H. Takahashi, T. Takahashi, T. Tanaka, A. Tenze, J. B. Thayer, J. G. Thayer, G. Theureau, D. J. Thompson, S. E. Thorsett, L. Tibaldo, O. Tibolla, D. F. Torres, A. Tramacere, M. Turri, T. L. Usher, L. Vigiani, N. Vilchez, V. Vitale, A. P. Waite, P. Wang, K. Watters, P. Weltevrede, B. L. Winer, K. S. Wood, T. Ylinen, and M. Ziegler. Fermi large area telescope observations of the vela pulsar. *The Astrophysical Journal*, 696 (2):1084, 2009. URL `http://stacks.iop.org/0004-637X/696/i=2/a=1084`.

A. A. Abdo, M. Ackermann, M. Ajello, W. B. Atwood, M. Axelsson, L. Baldini, J. Ballet, G. Barbiellini, M. G. Baring, D. Bastieri, and et al. The First Fermi Large Area Telescope Catalog of Gamma-ray Pulsars. *The Astrophysical Journal Supplement*, 187:460–494, April 2010a. doi: 10.1088/0067-0049/187/2/460.

A. A. Abdo, M. Ackermann, M. Ajello, W. B. Atwood, M. Axelsson, L. Baldini, J. Ballet, G. Barbiellini, M. G. Baring, D. Bastieri, and et al. The First Fermi Large Area Telescope Catalog of Gamma-ray Pulsars. *The Astrophysical Journal Supplement Series*, 187:460–494, April 2010b. doi: 10.1088/0067-0049/187/2/460.

A. A. Abdo, M. Ajello, A. Allafort, L. Baldini, J. Ballet, G. Barbiellini, M. G. Baring, D. Bastieri, A. Belfiore, R. Bellazzini, and et al. The Second Fermi Large Area Telescope

Catalog of Gamma-Ray Pulsars. *The Astrophysical Journal Supplement*, 208:17, October 2013. doi: 10.1088/0067-0049/208/2/17.

S. L. Adler. Photon splitting and photon dispersion in a strong magnetic field. *Annals of Physics*, 67:599–647, 1971. doi: 10.1016/0003-4916(71)90154-0.

F. Aharonian, A. Akhperjanian, M. Beilicke, K. Bernlhr, H.-G. Brst, H. Bojahr, O. Bolz, T. Coarasa, J. L. Contreras, J. Cortina, S. Denninghoff, M. V. Fonseca, M. Girma, N. Gtting, G. Heinzelmann, G. Hermann, A. Heusler, W. Hofmann, D. Horns, I. Jung, R. Kankanyan, M. Kestel, A. Kohnle, A. Konopelko, D. Kranich, H. Lampeitl, M. Lopez, E. Lorenz, F. Lucarelli, O. Mang, D. Mazin, H. Meyer, R. Mirzoyan, A. Moralejo, E. Oa-Wilhelmi, M. Panter, A. Plyasheshnikov, G. Phlhofer, R. de los Reyes, W. Rhode, J. Ripken, G. Rowell, V. Sahakian, M. Samorski, M. Schilling, M. Siems, D. Sobzynska, W. Stamm, M. Tluczykont, V. Vitale, H. J. Vlk, C. A. Wiedner, and W. Wittek. The crab nebula and pulsar between 500 gev and 80 tev: Observations with the hegra stereoscopic air cerenkov telescopes. *The Astrophysical Journal*, 614(2):897, 2004. URL `http://stacks.iop.org/0004-637X/614/i=2/a=897`.

Z. Ahmed, D. S. Akerib, S. Arrenberg, C. N. Bailey, D. Balakishiyeva, L. Baudis, D. A. Bauer, J. Beaty, P. L. Brink, T. Bruch, R. Bunker, B. Cabrera, D. O. Caldwell, J. Cooley, P. Cushman, F. Dejongh, M. R. Dragowsky, L. Duong, E. Figueroa-Feliciano, J. Filippini, M. Fritts, S. R. Golwala, D. R. Grant, J. Hall, R. Hennings-Yeomans, S. Hertel, D. Holmgren, L. Hsu, M. E. Huber, O. Kamaev, M. Kiveni, M. Kos, S. W. Leman, R. Mahapatra, V. Mandic, D. Moore, K. A. McCarthy, N. Mirabolfathi, H. Nelson, R. W. Ogburn, M. Pyle, X. Qiu, E. Ramberg, W. Rau, A. Reisetter, T. Saab, B. Sadoulet, J. Sander, R. W. Schnee, D. N. Seitz, B. Serfass, K. M. Sundqvist, M. Tarka, G. Wang, S. Yellin, J. Yoo, and B. A. Young. Search for Axions with the CDMS Experiment. *Physical Review Letters*, 103(14):141802, October 2009. doi: 10.1103/PhysRevLett.103.141802.

M. Ajello, A. Albert, B. Anderson, L. Baldini, G. Barbiellini, D. Bastieri, R. Bellazzini, E. Bissaldi, R. D. Blandford, E. D. Bloom, R. Bonino, E. Bottacini, J. Bregeon, P. Bruel, R. Buehler, G. A. Caliandro, R. A. Cameron, M. Caragiulo, P. A. Caraveo, C. Cecchi, A. Chekhtman, S. Ciprini, J. Cohen-Tanugi, J. Conrad, F. Costanza, F. D'Ammando, A. de Angelis, F. de Palma, R. Desiante, M. Di Mauro, L. Di Venere, A. Domínguez, P. S. Drell, C. Favuzzi, W. B. Focke, A. Franckowiak, Y. Fukazawa, S. Funk, P. Fusco, F. Gargano, D. Gasparrini, N. Giglietto, T. Glanzman, G. Godfrey, S. Guiriec, D. Horan, G. Jóhannesson, M. Katsuragawa, S. Kensei, M. Kuss, S. Larsson, L. Latronico, J. Li, L. Li, F. Longo, F. Loparco, P. Lubrano, G. M. Madejski, S. Maldera, A. Manfreda, M. Mayer, M. N. Mazziotta, M. Meyer, P. F. Michelson, N. Mirabal, T. Mizuno, M. E. Monzani, A. Morselli, I. V. Moskalenko, S. Murgia, M. Negro, E. Nuss, C. Okada, E. Orlando, J. F. Ormes, D. Paneque, J. S. Perkins, M. Pesce-Rollins, F. Piron, G. Pivato, T. A. Porter, S. Rainò, R. Rando, M. Razzano, A. Reimer, M. Sánchez-Conde, C. Sgrò, D. Simone, E. J. Siskind, F. Spada, G. Spandre, P. Spinelli, H. Takahashi, J. B. Thayer, D. F. Torres, G. Tosti, E. Troja, Y. Uchiyama, K. S. Wood, M. Wood, G. Zaharijas, and S. Zimmer. Search for spectral irregularities due to photon˘axionlike-particle oscillations with the fermi large area telescope. *Physical Review Letters*, 116:161101, Apr 2016. doi: 10.1103/PhysRevLett.116.161101. URL `http://link.aps.org/doi/10.1103/PhysRevLett.116.161101`.

S. Andriamonje, S. Aune, D. Autiero, K. Barth, A. Belov, B. Beltrán, H. Bräuninger, J. M. Carmona, S. Cebrián, J. I. Collar, T. Dafni, M. Davenport, L. Di Lella, C. Eleftheriadis, J. Englhauser, G. Fanourakis, E. Ferrer Ribas, H. Fischer, J. Franz, P. Friedrich, T. Geralis, I. Giomataris, S. Gninenko, H. Gómez, M. Hasinoff, F. H. Heinsius, D. H. H. Hoffmann, I. G. Irastorza, J. Jacoby, K. Jakovcic, D. Kang, K. Königsmann, R. Kotthaus, M. Krcmar, K. Kousouris, M. Kuster, B. Lakic, C. Lasseur, A. Liolios, A. Ljubicic, G. Lutz, G. Luzón, D. Miller, A. Morales, J. Morales, A. Ortiz, T. Papaevangelou,

A. Placci, G. Raffelt, H. Riege, A. Rodríguez, J. Ruz, I. Savvidis, Y. Semertzidis, P. Serpico, L. Stewart, J. Vieira, J. Villar, J. Vogel, L. Walckiers, K. Zioutas, and CAST Collaboration. An improved limit on the axion photon coupling from the CAST experiment. *Journal of Cosmology and Astroparticle Physics*, 4:010, April 2007. doi: 10.1088/1475-7516/2007/04/010.

S. Ansoldi, L. A. Antonelli, P. Antoranz, A. Babic, P. Bangale, U. Barres de Almeida, J. A. Barrio, J. Becerra González, W. Bednarek, E. Bernardini, B. Biasuzzi, A. Biland, O. Blanch, S. Bonnefoy, G. Bonnoli, F. Borracci, T. Bretz, E. Carmona, A. Carosi, P. Colin, E. Colombo, J. L. Contreras, J. Cortina, S. Covino, P. Da Vela, F. Dazzi, A. De Angelis, G. De Caneva, B. De Lotto, E. de Oña Wilhelmi, C. Delgado Mendez, F. Di Pierro, D. Dominis Prester, D. Dorner, M. Doro, S. Einecke, D. Eisenacher Glawion, D. Elsaesser, A. Fernández-Barral, D. Fidalgo, M. V. Fonseca, L. Font, K. Frantzen, C. Fruck, D. Galindo, R. J. García López, M. Garczarczyk, D. Garrido Terrats, M. Gaug, N. Godinović, A. González Muñoz, S. R. Gozzini, Y. Hanabata, M. Hayashida, J. Herrera, K. Hirotani, J. Hose, D. Hrupec, G. Hughes, W. Idec, H. Kellermann, M. L. Knoetig, K. Kodani, Y. Konno, J. Krause, H. Kubo, J. Kushida, A. La Barbera, D. Lelas, N. Lewandowska, E. Lindfors, S. Lombardi, F. Longo, M. López, R. López-Coto, A. López-Oramas, E. Lorenz, M. Makariev, K. Mallot, G. Maneva, K. Mannheim, L. Maraschi, B. Marcote, M. Mariotti, M. Martínez, D. Mazin, U. Menzel, J. M. Miranda, R. Mirzoyan, A. Moralejo, P. Munar-Adrover, D. Nakajima, V. Neustroev, A. Niedzwiecki, M. Nevas Rosillo, K. Nilsson, K. Nishijima, K. Noda, R. Orito, A. Overkemping, S. Paiano, M. Palatiello, D. Paneque, R. Paoletti, J. M. Paredes, X. Paredes-Fortuny, M. Persic, J. Poutanen, P. G. Prada Moroni, E. Prandini, I. Puljak, R. Reinthal, W. Rhode, M. Ribó, J. Rico, J. Rodriguez Garcia, T. Saito, K. Saito, K. Satalecka, V. Scalzotto, V. Scapin, C. Schultz, T. Schweizer, S. N. Shore, A. Sillanpää, J. Sitarek, I. Snidaric, D. Sobczynska, A. Stamerra, T. Steinbring, M. Strzys, L. Takalo, H. Takami, F. Tavecchio,

P. Temnikov, T. Terzić, D. Tescaro, M. Teshima, J. Thaele, D. F. Torres, T. Toyama, A. Treves, J. Ward, M. Will, and R. Zanin. Teraelectronvolt pulsed emission from the Crab Pulsar detected by MAGIC. *Astronomy and Astrophysics*, 585:A133, January 2016. doi: 10.1051/0004-6361/201526853.

A. Archer. Search for Pulsed Emission in Archival VERITAS Data. *ArXiv e-prints*, September 2015.

E. Armengaud, F. T. Avignone, M. Betz, P. Brax, P. Brun, G. Cantatore, J. M. Carmona, G. P. Carosi, F. Caspers, S. Caspi, S. A. Cetin, D. Chelouche, F. E. Christensen, A. Dael, T. Dafni, M. Davenport, A. V. Derbin, K. Desch, A. Diago, B. Döbrich, I. Dratchnev, A. Dudarev, C. Eleftheriadis, G. Fanourakis, E. Ferrer-Ribas, J. Galán, J. A. García, J. G. Garza, T. Geralis, B. Gimeno, I. Giomataris, S. Gninenko, H. Gómez, D. González-Díaz, E. Guendelman, C. J. Hailey, T. Hiramatsu, D. H. H. Hoffmann, D. Horns, F. J. Iguaz, I. G. Irastorza, J. Isern, K. Imai, A. C. Jakobsen, J. Jaeckel, K. Jakovčić, J. Kaminski, M. Kawasaki, M. Karuza, M. Krčmar, K. Kousouris, C. Krieger, B. Lakić, O. Limousin, A. Lindner, A. Liolios, G. Luzón, S. Matsuki, V. N. Muratova, C. Nones, I. Ortega, T. Papaevangelou, M. J. Pivovaroff, G. Raffelt, J. Redondo, A. Ringwald, S. Russenschuck, J. Ruz, K. Saikawa, I. Savvidis, T. Sekiguchi, Y. K. Semertzidis, I. Shilon, P. Sikivie, H. Silva, H. ten Kate, A. Tomas, S. Troitsky, T. Vafeiadis, K. van Bibber, P. Vedrine, J. A. Villar, J. K. Vogel, L. Walckiers, A. Weltman, W. Wester, S. C. Yildiz, and K. Zioutas. Conceptual design of the International Axion Observatory (IAXO). *Journal of Instrumentation*, 9:T05002, May 2014. doi: 10.1088/1748-0221/9/05/T05002.

W. D. Arnett, J. N. Bahcall, R. P. Kirshner, and S. E. Woosley. Supernova 1987A. *Annual Review of Astronomy and Astrophysics*, 27:629–700, 1989. doi: 10.1146/annurev.aa.27.090189.003213.

J. Arons. Pair creation above pulsar polar caps - Geometrical structure and energetics of slot gaps. *The Astrophysical Journal*, 266:215–241, March 1983. doi: 10.1086/160771.

J. Arons and E. T. Scharlemann. Pair formation above pulsar polar caps - Structure of the low altitude acceleration zone. *The Astrophysical Journal*, 231:854–879, August 1979. doi: 10.1086/157250.

S. J. Asztalos, G. Carosi, C. Hagmann, D. Kinion, K. van Bibber, M. Hotz, L. J. Rosenberg, G. Rybka, J. Hoskins, J. Hwang, P. Sikivie, D. B. Tanner, R. Bradley, J. Clarke, and ADMX Collaboration. SQUID-Based Microwave Cavity Search for Dark-Matter Axions. *Physical Review Letters*, 104(4):041301, January 2010. doi: 10.1103/PhysRevLett.104.041301.

F. T. Avignone, D. Abriola, R. L. Brodzinski, J. I. Collar, R. J. Creswick, D. E. Digregorio, H. A. Farach, A. O. Gattone, C. K. Guérard, F. Hasenbalg, H. Huck, H. S. Miley, A. Morales, J. Morales, S. Nussinov, A. Ortiz de Solórzano, J. H. Reeves, J. A. Villar, and K. Zioutas. Experimental Search for Solar Axions via Coherent Primakoff Conversion in a Germanium Spectrometer. *Physical Review Letters*, 81:5068–5071, December 1998. doi: 10.1103/PhysRevLett.81.5068.

W. Baade and F. Zwicky. On super-novae. *Proceedings of the National Academy of Science*, 20:254–259, May 1934. doi: 10.1073/pnas.20.5.254.

J. N. Bahcall. *Neutrino astrophysics*. 1989.

J. N. Bahcall, W. F. Huebner, S. H. Lubow, P. D. Parker, and R. K. Ulrich. Standard solar models and the uncertainties in predicted capture rates of solar neutrinos. *Reviews of Modern Physics*, 54:767–799, July 1982. doi: 10.1103/RevModPhys.54.767.

R. Bähre, B. Döbrich, J. Dreyling-Eschweiler, S. Ghazaryan, R. Hodajerdi, D. Horns, F. Januschek, E.-A. Knabbe, A. Lindner, D. Notz, A. Ringwald, J. E. von Seggern,

R. Stromhagen, D. Trines, and B. Willke. Any light particle search II—Technical Design Report. *Journal of Instrumentation*, 8:T09001, September 2013. doi: 10.1088/1748-0221/8/09/T09001.

C. A. Baker, D. D. Doyle, P. Geltenbort, K. Green, M. G. D. van der Grinten, P. G. Harris, P. Iaydjiev, S. N. Ivanov, D. J. R. May, J. M. Pendlebury, J. D. Richardson, D. Shiers, and K. F. Smith. Improved Experimental Limit on the Electric Dipole Moment of the Neutron. *Physical Review Letters*, 97(13):131801, September 2006. doi: 10.1103/PhysRevLett.97.131801.

M. G. Baring. Perspectives on Gamma-Ray Pulsar Emission. In E. Göğüş, T. Belloni, and Ü. Ertan, editors, *American Institute of Physics Conference Series*, volume 1379 of *American Institute of Physics Conference Series*, pages 74–81, September 2011. doi: 10.1063/1.3629488.

K. Bennett, G. F. Bignami, G. Boella, R. Buccheri, W. Hermsen, G. G. Kanbach, G. G. Lichti, J. L. Masnou, H. A. Mayer-Hasselwander, J. A. Paul, L. Scarsi, B. N. Swanenburg, B. G. Taylor, and R. D. Wills. COS-B observations of pulsed gamma-ray emission from PSR 0531 plus 21 and PSR 0833-45. *Astronomy and Astrophysics*, 61:279–284, October 1977.

B. Berenji, J. Gaskins, and M. Meyer. Constraints on axions and axionlike particles from fermi large area telescope observations of neutron stars. *Physical Review D*, 93:045019, Feb 2016. doi: 10.1103/PhysRevD.93.045019. URL `http://link.aps.org/doi/10.1103/PhysRevD.93.045019`.

D. Berge, S. Funk, and J. Hinton. Background modelling in very-high-energy γ-ray astronomy. *AStronomy and Astrophysics*, 466:1219–1229, May 2007. doi: 10.1051/0004-6361:20066674.

R. Bernabei, P. Belli, R. Cerulli, F. Montecchia, F. Nozzoli, A. Incicchitti, D. Prosperi, C. J. Dai, H. L. He, H. H. Kuang, J. M. Ma, and S. Scopel. Search for solar axions by Primakoff effect in NaI crystals. *Physics Letters B*, 515:6–12, August 2001. doi: 10.1016/S0370-2693(01)00840-1.

V. S. Beskin, A. V. Gurevich, and Y. N. Istomin. *Physics of the pulsar magnetosphere.* January 1993.

R. M. Bionta, G. Blewitt, C. B. Bratton, D. Casper, and A. Ciocio. Observation of a neutrino burst in coincidence with supernova 1987A in the Large Magellanic Cloud. *Physical Review Letters*, 58:1494–1496, April 1987. doi: 10.1103/PhysRevLett.58.1494.

R. Brun and F. Rademakers. ROOT—An object oriented data analysis framework. *Nuclear Instruments and Methods in Physics Research A*, 389:81–86, February 1997. doi: 10.1016/S0168-9002(97)00048-X.

R. Buccheri, K. Bennett, G. F. Bignami, J. B. G. M. Bloemen, V. Boriakoff, P. A. Caraveo, W. Hermsen, G. Kanbach, R. N. Manchester, J. L. Masnou, H. A. Mayer-Hasselwander, M. E. Ozel, J. A. Paul, B. Sacco, L. Scarsi, and A. W. Strong. Search for pulsed gamma-ray emission from radio pulsars in the COS-B data. *Astronomy and Astrophysics*, 128:245–251, November 1983.

J. Buckley. High Speed Electronics for Atmospheric Cherenkov Detectors. *International Cosmic Ray Conference*, 5:267, 1999.

A. Burrows, M. S. Turner, and R. P. Brinkmann. Axions and SN 1987A. *Physical Review D*, 39:1020–1028, February 1989. doi: 10.1103/PhysRevD.39.1020.

G. Carosi, A. Friedland, M. Giannotti, M. J. Pivovaroff, J. Ruz, and J. K. Vogel. Probing the axion-photon coupling: phenomenological and experimental perspectives. A snowmass white paper. *ArXiv e-prints*, September 2013.

W. Chen, J. H. Buckley, and F. Ferrer. Search for GeV γ -Ray Pair Halos Around Low Redshift Blazars. *Physical Review Letters*, 115(21):211103, November 2015. doi: 10.1103/PhysRevLett.115.211103.

K. S. Cheng, C. Ho, and M. Ruderman. Energetic radiation from rapidly spinning pulsars. I - Outer magnetosphere gaps. II - VELA and Crab. *The Astrophysical Journal*, 300: 500–539, January 1986. doi: 10.1086/163829.

P. Cogan. VEGAS, the VERITAS Gamma-ray Analysis Suite. *International Cosmic Ray Conference*, 3:1385–1388, 2008.

J. M. Comella, H. D. Craft, R. V. E. Lovelace, and J. M. Sutton. Crab Nebula Pulsar NP 0532. *Nature*, 221:453–454, February 1969. doi: 10.1038/221453a0.

D. B. Kieda for the VERITAS Collaboration. The Gamma Ray Detection sensitivity of the upgraded VERITAS Observatory. *ArXiv e-prints*, August 2013.

M. K. Daniel. The VERITAS standard data analysis. *International Cosmic Ray Conference*, 3:1325–1328, 2008.

A. de Angelis, M. Roncadelli, and O. Mansutti. Evidence for a new light spin-zero boson from cosmological gamma-ray propagation? *Physical Review D*, 76(12):121301, December 2007. doi: 10.1103/PhysRevD.76.121301.

A. de Angelis, G. Galanti, and M. Roncadelli. Relevance of axionlike particles for very-high-energy astrophysics. *Physical Review D*, 84(10):105030, November 2011. doi: 10.1103/PhysRevD.84.105030.

O. C. de Jager, B. C. Raubenheimer, and J. W. H. Swanepoel. A poweful test for weak periodic signals with unknown light curve shape in sparse data. *Astronomy and Astrophysics*, 221:180–190, August 1989.

A. J. Deutsch. The electromagnetic field of an idealized star in rigid rotation in vacuo. *Annales d'Astrophysique*, 18:1, January 1955.

J. Dyks and B. Rudak. Two-Pole Caustic Model for High-Energy Light Curves of Pulsars. *The Astrophysical Journal*, 598:1201–1206, December 2003. doi: 10.1086/379052.

J. Dyks, Alice K. Harding, and B. Rudak. Relativistic effects and polarization in three high-energy pulsar models. *The Astrophysical Journal*, 606(2):1125, 2004. URL `http://stacks.iop.org/0004-637X/606/i=2/a=1125`.

R. T. Edwards, G. B. Hobbs, and R. N. Manchester. TEMPO2, a new pulsar timing package - II. The timing model and precision estimates. *Monthly Notices of the Royal Astronomical Society*, 372:1549–1574, November 2006. doi: 10.1111/j.1365-2966.2006.10870.x.

K. Ehret, M. Frede, S. Ghazaryan, M. Hildebrandt, E.-A. Knabbe, D. Kracht, A. Lindner, J. List, T. Meier, N. Meyer, D. Notz, J. Redondo, A. Ringwald, G. Wiedemann, and B. Willke. New ALPS results on hidden-sector lightweights. *Physics Letters B*, 689: 149–155, May 2010. doi: 10.1016/j.physletb.2010.04.066.

C. E. Fichtel, R. C. Hartman, D. A. Kniffen, D. J. Thompson, H. Ogelman, M. E. Ozel, T. Tumer, and G. F. Bignami. High-energy gamma-ray results from the second small astronomy satellite. *The Astrophysical Journal*, 198:163–182, May 1975. doi: 10.1086/153590.

R. Gill and J. S. Heyl. Constraining the photon-axion coupling constant with magnetic white dwarfs. *Physical Review D*, 84(8):085001, October 2011. doi: 10.1103/PhysRevD.84.085001.

P. Goldreich and W. H. Julian. Pulsar Electrodynamics. *The Astrophysical Journal*, 157: 869, August 1969. doi: 10.1086/150119.

C. Hagmann, P. Sikivie, N. S. Sullivan, and D. B. Tanner. Results from a search for cosmic axions. *Physical Review D*, 42:1297–1300, August 1990. doi: 10.1103/PhysRevD.42.1297.

D. Hanna, A. McCann, M. McCutcheon, and L. Nikkinen. An LED-based flasher system for VERITAS. *Nuclear Instruments and Methods in Physics Research A*, 612:278–287, January 2010. doi: 10.1016/j.nima.2009.10.107.

A. K. Harding. Gamma-ray pulsars: Models and predictions. In F. A. Aharonian and H. J. Völk, editors, *American Institute of Physics Conference Series*, volume 558 of *American Institute of Physics Conference Series*, pages 115–126, April 2001. doi: 10.1063/1.1370785.

A. K. Harding. Pulsar High-Energy Emission From the Polar Cap and Slot Gap. *ArXiv e-prints*, October 2007.

R. C. Hartman, D. L. Bertsch, S. D. Bloom, A. W. Chen, P. Deines-Jones, J. A. Esposito, C. E. Fichtel, D. P. Friedlander, S. D. Hunter, L. M. McDonald, P. Sreekumar, D. J. Thompson, B. B. Jones, Y. C. Lin, P. F. Michelson, P. L. Nolan, W. F. Tompkins, G. Kanbach, H. A. Mayer-Hasselwander, A. Mücke, M. Pohl, O. Reimer, D. A. Kniffen, E. J. Schneid, C. von Montigny, R. Mukherjee, and B. L. Dingus. The Third EGRET Catalog of High-Energy Gamma-Ray Sources. *The Astrophysical Journal Supplement Series*, 123:79–202, July 1999. doi: 10.1086/313231.

W. Heisenberg and H. Euler. Folgerungen aus der diracschen theorie des positrons. *Zeitschrift für Physik*, 98(11):714–732, 1936. ISSN 0044-3328. doi: 10.1007/BF01343663. URL `http://dx.doi.org/10.1007/BF01343663`.

A. Hewish, S. J. Bell, J. D. H. Pilkington, P. F. Scott, and R. A. Collins. Observation of a Rapidly Pulsating Radio Source. *Nature*, 217:709–713, February 1968. doi: 10.1038/217709a0.

A. M. Hillas. Cerenkov light images of EAS produced by primary gamma. *International Cosmic Ray Conference*, 3, August 1985.

K. Hirata, T. Kajita, M. Koshiba, M. Nakahata, and Y. Oyama. Observation of a neutrino burst from the supernova SN1987A. *Physical Review Letters*, 58:1490–1493, April 1987. doi: 10.1103/PhysRevLett.58.1490.

G. B. Hobbs, R. T. Edwards, and R. N. Manchester. TEMPO2, a new pulsar-timing package - I. An overview. *Monthly Notices of the Royal Astronomical Society*, 369:655–672, June 2006. doi: 10.1111/j.1365-2966.2006.10302.x.

J. Holder, R. W. Atkins, H. M. Badran, G. Blaylock, S. M. Bradbury, J. H. Buckley, K. L. Byrum, D. A. Carter-Lewis, O. Celik, Y. C. K. Chow, P. Cogan, W. Cui, M. K. Daniel, I. de la Calle Perez, C. Dowdall, P. Dowkontt, C. Duke, A. D. Falcone, S. J. Fegan, J. P. Finley, P. Fortin, L. F. Fortson, K. Gibbs, G. Gillanders, O. J. Glidewell, J. Grube, K. J. Gutierrez, G. Gyuk, J. Hall, D. Hanna, E. Hays, D. Horan, S. B. Hughes, T. B. Humensky, A. Imran, I. Jung, P. Kaaret, G. E. Kenny, D. Kieda, J. Kildea, J. Knapp, H. Krawczynski, F. Krennrich, M. J. Lang, S. LeBohec, E. Linton, E. K. Little, G. Maier, H. Manseri, A. Milovanovic, P. Moriarty, R. Mukherjee, P. A. Ogden, R. A. Ong, D. Petry, J. S. Perkins, F. Pizlo, M. Pohl, J. Quinn, K. Ragan, P. T. Reynolds, E. T. Roache, H. J. Rose, M. Schroedter, G. H. Sembroski, G. Sleege, D. Steele, S. P. Swordy, A. Syson, J. A. Toner, L. Valcarcel, V. V. Vassiliev, S. P. Wakely, T. C. Weekes, R. J. White, D. A. Williams, and R. Wagner. The first VERITAS telescope. *Astroparticle Physics*, 25: 391–401, July 2006. doi: 10.1016/j.astropartphys.2006.04.002.

J. Holder, V. A. Acciari, E. Aliu, T. Arlen, M. Beilicke, W. Benbow, S. M. Bradbury, J. H. Buckley, V. Bugaev, Y. Butt, K. L. Byrum, A. Cannon, O. Celik, A. Cesarini, L. Ciupik, Y. C. K. Chow, P. Cogan, P. Colin, W. Cui, M. K. Daniel, T. Ergin, A. D. Falcone, S. J. Fegan, J. P. Finley, G. Finnegan, P. Fortin, L. F. Fortson, A. Furniss,

G. H. Gillanders, J. Grube, R. Guenette, G. Gyuk, D. Hanna, E. Hays, D. Horan, C. M. Hui, T. B. Humensky, A. Imran, P. Kaaret, N. Karlsson, M. Kertzman, D. B. Kieda, J. Kildea, A. Konopelko, H. Krawczynski, F. Krennrich, M. J. Lang, S. Lebohec, G. Maier, A. McCann, M. McCutcheon, P. Moriarty, R. Mukherjee, T. Nagai, J. Niemiec, R. A. Ong, D. Pandel, J. S. Perkins, M. Pohl, J. Quinn, K. Ragan, L. C. Reyes, P. T. Reynolds, H. J. Rose, M. Schroedter, G. H. Sembroski, A. W. Smith, D. Steele, S. P. Swordy, J. A. Toner, L. Valcarcel, V. V. Vassiliev, R. Wagner, S. P. Wakely, J. E. Ward, T. C. Weekes, A. Weinstein, R. J. White, D. A. Williams, S. A. Wissel, M. Wood, and B. Zitzer. Status of the VERITAS Observatory. In F. A. Aharonian, W. Hofmann, and F. Rieger, editors, *American Institute of Physics Conference Series*, volume 1085 of *American Institute of Physics Conference Series*, pages 657–660, December 2008. doi: 10.1063/1.3076760.

Naoki Iwamoto. Axion emission from neutron stars. *Physical Review Letters*, 53:1198–1201, Sep 1984. doi: 10.1103/PhysRevLett.53.1198. URL `http://link.aps.org/doi/10.1103/PhysRevLett.53.1198`.

M. P. Kertzman and G. H. Sembroski. Computer simulation methods for investigating the detection characteristics of TeV air Cherenkov telescopes. *Nuclear Instruments and Methods in Physics Research A*, 343:629–643, April 1994. doi: 10.1016/0168-9002(94)90247-X.

H. Krawczynski, D. A. Carter-Lewis, C. Duke, J. Holder, G. Maier, S. Le Bohec, and G. Sembroski. Gamma hadron separation methods for the VERITAS array of four imaging atmospheric Cherenkov telescopes. *Astroparticle Physics*, 25:380–390, July 2006. doi: 10.1016/j.astropartphys.2006.03.011.

M. I. Large, A. E. Vaughan, and B. Y. Mills. A Pulsar Supernova Association? *Nature*, 220:340–341, October 1968. doi: 10.1038/220340a0.

D. M. Lazarus, G. C. Smith, R. Cameron, A. C. Melissinos, G. Ruoso, Y. K. Semertzidis, and F. A. Nezrick. Search for solar axions. *Physical Review Letters*, 69:2333–2336, October 1992. doi: 10.1103/PhysRevLett.69.2333.

T.-P. Li and Y.-Q. Ma. Analysis methods for results in gamma-ray astronomy. *The Astrophysical Journal*, 272:317–324, September 1983. doi: 10.1086/161295.

M. S. Longair. *High Energy Astrophysics*. February 2011.

A. G. Lyne, R. S. Pritchard, and F. Graham-Smith. Twenty-Three Years of Crab Pulsar Rotational History. *Monthly Notices of the Royal Astronomical Society*, 265:1003, December 1993. doi: 10.1093/mnras/265.4.1003.

M. Lyutikov, N. Otte, and A. McCann. The Very High Energy Emission from Pulsars: A Case for Inverse Compton Scattering. *The Astrophysical Journal*, 754:33, July 2012a. doi: 10.1088/0004-637X/754/1/33.

M. Lyutikov, N. Otte, and A. McCann. The Very High Energy Emission from Pulsars: A Case for Inverse Compton Scattering. *The Astrophysical Journal*, 754:33, July 2012b. doi: 10.1088/0004-637X/754/1/33.

G. Maier. Monte Carlo studies of the VERITAS array of Cherenkov telescopes. *International Cosmic Ray Conference*, 3:1413–1416, 2008.

R. N. Manchester, G. B. Hobbs, A. Teoh, and M. Hobbs. The australia telescope national facility pulsar catalogue. *The Astronomical Journal*, 129(4):1993, 2005. URL `http://stacks.iop.org/1538-3881/129/i=4/a=1993`.

E. Massó and R. Toldrà. Light spinless particle coupled to photons. *Physical Review D*, 52: 1755–1763, August 1995. doi: 10.1103/PhysRevD.52.1755.

Manuel Meyer, Dieter Horns, and Martin Raue. First lower limits on the photon-axion-like particle coupling from very high energy gamma-ray observations. *Physical Review D*, 87:

035027, Feb 2013. doi: 10.1103/PhysRevD.87.035027. URL `http://link.aps.org/doi/10.1103/PhysRevD.87.035027`.

F. C. Michel and H. Li. Electrodynamics of neutron stars. *Physics Reports*, 318:227–297, September 1999. doi: 10.1016/S0370-1573(99)00002-2.

A. Mirizzi, G. G. Raffelt, and P. D. Serpico. Photon-Axion Conversion in Intergalactic Magnetic Fields and Cosmological Consequences. In M. Kuster, G. Raffelt, and B. Beltrán, editors, *Axions*, volume 741 of *Lecture Notes in Physics, Berlin Springer Verlag*, page 115, 2008.

A. Morales, F. T. Avignone, III, R. L. Brodzinski, S. Cebrián, E. García, D. González, I. G. Irastorza, H. S. Miley, J. Morales, A. O. de Solórzano, J. Puimedón, J. H. Reeves, M. L. Sarsa, S. Scopel, and J. A. Villar. Particle dark matter and solar axion searches with a small germanium detector at the Canfranc Underground Laboratory. *Astroparticle Physics*, 16:325–332, January 2002. doi: 10.1016/S0927-6505(01)00117-7.

D. E. Morris. Axion mass limits may be improved by pulsar x-ray measurements. *Physical Review D*, 34:843–848, Aug 1986. doi: 10.1103/PhysRevD.34.843.

A. G. Muslimov and A. K. Harding. Extended Acceleration in Slot Gaps and Pulsar High-Energy Emission. *The Astrophysical Journal*, 588:430–440, May 2003. doi: 10.1086/368162.

R. Ohta, Y. Akimoto, Y. Inoue, M. Minowa, T. Mizumoto, S. Moriyama, T. Namba, Y. Takasu, and A. Yamamoto. The Tokyo axion helioscope. *Nuclear Instruments and Methods in Physics Research A*, 670:73–78, April 2012. doi: 10.1016/j.nima.2011.12.027.

R. D. Peccei and H. R. Quinn. CP conservation in the presence of pseudoparticles. *Physical Review Letters*, 38:1440–1443, June 1977. doi: 10.1103/PhysRevLett.38.1440.

P. Pugnat, R. Ballou, M. Schott, T. Husek, M. Sulc, G. Deferne, L. Duvillaret, M. Finger, M. Finger, L. Flekova, J. Hosek, V. Jary, R. Jost, M. Kral, S. Kunc, K. Macuchova, K. A. Meissner, J. Morville, D. Romanini, A. Siemko, M. Slunecka, G. Vitrant, and J. Zicha. Search for weakly interacting sub-eV particles with the OSQAR laser-based experiment: results and perspectives. *European Physical Journal C*, 74:3027, August 2014. doi: 10.1140/epjc/s10052-014-3027-8.

G. Raffelt and L. Stodolsky. Mixing of the photon with low-mass particles. *Physical Review D*, 37:1237–1249, March 1988. doi: 10.1103/PhysRevD.37.1237.

G. G. Raffelt. Axion constraints from white dwarf cooling times. *Physics Letters B*, 166: 402–406, January 1986. doi: 10.1016/0370-2693(86)91588-1.

G. G. Raffelt. Astrophysical methods to constrain axions and other novel particle phenomena. *Physics Reports*, 198:1–113, December 1990. doi: 10.1016/0370-1573(90)90054-6.

G. G. Raffelt. *Stars as laboratories for fundamental physics : the astrophysics of neutrinos, axions, and other weakly interacting particles.* 1996.

G. G. Raffelt. Astrophysical Axion Bounds. In M. Kuster, G. Raffelt, and B. Beltrán, editors, *Axions*, volume 741 of *Lecture Notes in Physics, Berlin Springer Verlag*, page 51, 2008.

R. W. Romani. Gamma-Ray Pulsars: Radiation Processes in the Outer Magnetosphere. *The Astrophysical Journal*, 470:469, October 1996. doi: 10.1086/177878.

M. A. Ruderman and P. G. Sutherland. Theory of pulsars - Polar caps, sparks, and coherent microwave radiation. *The Astrophysical Journal*, 196:51–72, February 1975. doi: 10.1086/153393.

M. A. Sánchez-Conde, D. Paneque, E. Bloom, F. Prada, and A. Domínguez. Hints of the existence of axionlike particles from the gamma-ray spectra of cosmological sources. *Physical Review D*, 79(12):123511, June 2009. doi: 10.1103/PhysRevD.79.123511.

Norbert Schartel. Old Pulsars Still Have New Tricks to Teach Us. URL `http://www.esa.int/Our_Activities/Space_Science/Old_pulsars_still_have_new-_tricks_to_teach_us`.

H. Schlattl, A. Weiss, and G. Raffelt. Helioseismological constraint on solar axion emission. *Astroparticle Physics*, 10:353–359, May 1999. doi: 10.1016/S0927-6505(98)00063-2.

T. M. Shokair, J. Root, K. A. van Bibber, B. Brubaker, Y. V. Gurevich, S. B. Cahn, S. K. Lamoreaux, M. A. Anil, K. W. Lehnert, B. K. Mitchell, A. Reed, and G. Carosi. Future directions in the microwave cavity search for dark matter axions. *International Journal of Modern Physics A*, 29:1443004, July 2014. doi: 10.1142/S0217751X14430040.

P. Sikivie. Experimental tests of the 'invisible' axion. *Physical Review Letters*, 51:1415–1417, October 1983. doi: 10.1103/PhysRevLett.51.1415.

P. Sikivie. Axion Cosmology. In M. Kuster, G. Raffelt, and B. Beltrán, editors, *Axions*, volume 741 of *Lecture Notes in Physics, Berlin Springer Verlag*, page 19, 2008.

M. Simet, D. Hooper, and P. D. Serpico. Milky Way as a kiloparsec-scale axionscope. *Physical Review D*, 77(6):063001, March 2008. doi: 10.1103/PhysRevD.77.063001.

E. M. Standish, Jr. Orientation of the JPL Ephemerides, DE 200/LE 200, to the dynamical equinox of J 2000. *Astronomy and Astrophysics*, 114:297–302, October 1982.

D. Staszak, A. U. Abeysekara, S. Archambault, A. Archer, A. Barnacka, W. Benbow, R. Bird, J. Biteau, M. Buchovecky, J. H. Buckley, V. Bugaev, K. Byrum, J. V Cardenzana, M. Cerruti, X. Chen, J. L. Christiansen, L. Ciupik, E. Collins-Hughes, M. P. Connolly, P. Coppi, W. Cui, V. V. Dwarkadas, J. D. Eisch, M. Errando, A. Falcone, Q. Feng,

M. Fernandez Alonso, J. P. Finley, H. Fleischhack, A. Flinders, P. Fortin, L. Fortson, A. Furniss, G. H. Gillanders, S. Griffin, S. T. Griffiths, G. Gyuk, M. Hütten, D. Hanna, J. Holder, T. B. Humensky, C. A. Johnson, P. Kaaret, P. Kar, M. Kertzman, Y. Khassen, D. Kieda, M. Krause, F. Krennrich, S. Kumar, M. J. Lang, G. Maier, S. McArthur, A. McCann, K. Meagher, P. Moriarty, R. Mukherjee, T. Nguyen, D. Nieto, A. O'Faoláin de Bhróithe, R. A. Ong, A. N. Otte, D. Pandel, N. Park, V. Pelassa, J. S. Perkins, M. Pohl, A. Popkow, E. Pueschel, J. Quinn, K. Ragan, P. T. Reynolds, G. T. Richards, E. Roache, A. C. Rovero, M. Santander, S. Schlenstedt, G. H. Sembroski, K. Shahinyan, A. W. Smith, I. Telezhinsky, J. V. Tucci, J. Tyler, V. V. Vassiliev, S. Vincent, S. P. Wakely, O. M. Weiner, A. Weinstein, A. Wilhelm, D. A. Williams, and B. Zitzer. Science Highlights from VERITAS. *ArXiv e-prints*, October 2015.

F. W. Stecker, O. C. de Jager, and M. H. Salamon. TeV gamma rays from 3C 279 - A possible probe of origin and intergalactic infrared radiation fields. *The Astrophysical Journal*, 390: L49–L52, May 1992. doi: 10.1086/186369.

P. A. Sturrock. A Model of Pulsars. *The Astrophysical Journal*, 164:529, March 1971. doi: 10.1086/150865.

D. J. Thompson. Gamma ray astrophysics: the EGRET results. *Reports on Progress in Physics*, 71(11):116901, November 2008. doi: 10.1088/0034-4885/71/11/116901.

D. J. Thompson, C. E. Fichtel, D. A. Kniffen, and H. B. Ogelman. SAS-2 high-energy gamma-ray observations of the VELA pulsar. *The Astrophysical Journal*, 200:L79–L82, September 1975. doi: 10.1086/181902.

M. S. Turner. Axions from 1987A. *Physical Review Letters*, 60:1797–1800, May 1988. doi: 10.1103/PhysRevLett.60.1797.

K. van Bibber, P. M. McIntyre, D. E. Morris, and G. G. Raffelt. Design for a practical laboratory detector for solar axions. *Physical Review D*, 39:2089–2099, April 1989. doi: 10.1103/PhysRevD.39.2089.

VERITAS Collaboration, E. Aliu, T. Arlen, T. Aune, M. Beilicke, W. Benbow, A. Bouvier, S. M. Bradbury, J. H. Buckley, V. Bugaev, K. Byrum, A. Cannon, A. Cesarini, J. L. Christiansen, L. Ciupik, E. Collins-Hughes, M. P. Connolly, W. Cui, R. Dickherber, C. Duke, M. Errando, A. Falcone, J. P. Finley, G. Finnegan, L. Fortson, A. Furniss, N. Galante, D. Gall, K. Gibbs, G. H. Gillanders, S. Godambe, S. Griffin, J. Grube, R. Guenette, G. Gyuk, D. Hanna, J. Holder, H. Huan, G. Hughes, C. M. Hui, T. B. Humensky, A. Imran, P. Kaaret, N. Karlsson, M. Kertzman, D. Kieda, H. Krawczynski, F. Krennrich, M. J. Lang, M. Lyutikov, A. S. Madhavan, G. Maier, P. Majumdar, S. McArthur, A. McCann, M. McCutcheon, P. Moriarty, R. Mukherjee, P. Nuñez, R. A. Ong, M. Orr, A. N. Otte, N. Park, J. S. Perkins, F. Pizlo, M. Pohl, H. Prokoph, J. Quinn, K. Ragan, L. C. Reyes, P. T. Reynolds, E. Roache, H. J. Rose, J. Ruppel, D. B. Saxon, M. Schroedter, G. H. Sembroski, G. D. Şentürk, A. W. Smith, D. Staszak, G. Tešić, M. Theiling, S. Thibadeau, K. Tsurusaki, J. Tyler, A. Varlotta, V. V. Vassiliev, S. Vincent, M. Vivier, S. P. Wakely, J. E. Ward, T. C. Weekes, A. Weinstein, T. Weisgarber, D. A. Williams, and B. Zitzer. Detection of Pulsed Gamma Rays Above 100 GeV from the Crab Pulsar. *Science*, 334:69, October 2011. doi: 10.1126/science.1208192.

H. J. Völk and K. Bernlöhr. Imaging very high energy gamma-ray telescopes. *Experimental Astronomy*, 25:173–191, August 2009. doi: 10.1007/s10686-009-9151-z.

T. C. Weekes and K. E. Turver. Gamma-ray astronomy from 10-100 GeV: A new approach. In R. D. Wills and B. Battrick, editors, *Recent Advances in Gamma-Ray Astronomy*, volume 124 of *ESA Special Publication*, July 1977.

S. Weinberg. A new light boson? *Physical Review Letters*, 40:223–226, January 1978. doi: 10.1103/PhysRevLett.40.223.

S. Weinberg. *Cosmology*. Cosmology. OUP Oxford, 2008. ISBN 9780191523601. URL `https://books.google.com/books?id=nqQZdg020fsC`.

F. Wilczek. Problem of strong P and T invariance in the presence of instantons. *Physical Review Letters*, 40:279–282, January 1978. doi: 10.1103/PhysRevLett.40.279.

W. U. Wuensch, S. de Panfilis-Wuensch, Y. K. Semertzidis, J. T. Rogers, A. C. Melissinos, H. J. Halama, B. E. Moskowitz, A. G. Prodell, W. B. Fowler, and F. A. Nezrick. Results of a laboratory search for cosmic axions and other weakly coupled light particles. *Physical Review D*, 40:3153–3167, November 1989. doi: 10.1103/PhysRevD.40.3153.

V. V. Zheleznyakov, editor. *Radiation in Astrophysical Plasmas*, volume 204 of *Astrophysics and Space Science Library*, February 1996. doi: 10.1007/978-94-009-0201-5.